

UNIVERSITÀ DEGLI STUDI DI MODENA E REGGIO EMILIA

Dipartimento di Scienze Fisiche, Informatiche e Matematiche

Corso di Dottorato di Ricerca in Physics and Nanosciences

Ciclo XXXIV

**Continuous-time quantum walks for
quantum technology: Quantum estimation
and modeling of transport phenomena**

Relatore:

Prof. Paolo BORDONE

Candidato:

Luca RAZZOLI

Correlatore:

Prof. Matteo G. A. PARIS

Coordinatore del Corso di Dottorato:

Prof. Stefano FRABBONI

Anno Accademico 2020-2021

The Road Not Taken

Two roads diverged in a yellow wood,
And sorry I could not travel both
And be one traveler, long I stood
And looked down one as far as I could
To where it bent in the undergrowth;

Then took the other, as just as fair,
And having perhaps the better claim,
Because it was grassy and wanted wear;
Though as for that the passing there
Had worn them really about the same,

And both that morning equally lay
In leaves no step had trodden black.
Oh, I kept the first for another day!
Yet knowing how way leads on to way,
I doubted if I should ever come back.

I shall be telling this with a sigh
Somewhere ages and ages hence:
Two roads diverged in a wood, and I—
I took the one less traveled by,
And that has made all the difference.

– Robert Frost

A single atom can travel down both roads in Frost's yellow wood... no regrets for atoms; they can sample all possible experiences simultaneously. Indeed, they follow the advice of the great American baseball player, Yogi Berra, who said, "If you come to a fork in the road, take it."

– Jim Al-Khalili

(from *Quantum: A Guide for the Perplexed*)

Acknowledgments

I wish to express my gratitude to my supervisors, Prof. Paolo Bordone and Prof. Matteo G. A. Paris, for being a beacon for me in the quantum world, where *uncertainty* reigns, and for guiding me with competence and experience through it. For their patience and kindness, constant help and suggestions. For offering me the best opportunities of growth, professional and human, in these challenging years. I can never thank them enough for what they have taught me during these years. I would like to thank Alessandro Candeloro for his friendship, and the fruitful collaborations we had. I am deeply grateful to my family and to my friends, for their closeness and support.

Summary

Quantum walks are the quantum counterpart of classical random walks and describe the motion of a quantum walker when confined to discrete spatial locations. The quantum nature of the walker gives them peculiar features, totally different from the classical ones. In the continuous-time quantum walk (CTQW) the state of the walker obeys the Schrödinger equation and evolves under a Hamiltonian typically given by the Laplacian matrix. The latter is the mathematical representation of a graph, whose vertices are the allowed positions, and the edges the allowed paths. Actually, any Hamiltonian which respects the topology of the graph defines a CTQW, thus making CTQWs extremely versatile.

CTQWs are investigated in several research areas, ranging from modeling of physical phenomena to quantum communication, from universal quantum computation to the development of quantum algorithms. Experimentally, they can be implemented on different platforms, e.g., NMR quantum computers, optical lattices of ultracold Rydberg atoms, photonic chips, spin chains, and superconducting qubits.

This thesis is a theoretical study on CTQWs, with a focus on their dynamics, free or in the presence of external perturbations, and on their potential use as probes in quantum estimation problems. A quantum probe is a physical system prepared in a quantum state sensitive to fluctuations affecting one or more parameters of interest. The quantum Fisher information (QFI) is the central quantity in quantum metrology, as it establishes the ultimate bound on the achievable precision in estimating a parameter of interest. Diverging QFI corresponds to optimal estimability.

We studied CTQWs generated by the Laplacian matrix and perturbed by its square, as this term introduces next-nearest-neighbor hopping. After investigating the evolution of a walker on paradigmatic graphs for connectivity and symmetry, we determined the walker preparations and the graphs that maximize the QFI for estimating the perturbation parameter.

Moreover, we investigated CTQWs on the regular tessellations of the Euclidean plane, showing that the spread is not universally ballistic. Then, assuming a charged walker, we inserted a perpendicular uniform magnetic field and compared two approaches to define the CTQW Hamiltonian: (i) Introducing the Peierls phase-factors and (ii) spatially discretizing the original Hamiltonian in the continuum.

Based on this, we used a charged (spinless) particle on a finite square lattice as a probe to detect a locally static transverse magnetic field, putting forward the idea of lattice quantum magnetometry. Our scheme finds its root in CTQWs, but it does not exploit their dynamical properties, being based on ground-state measurements. The system turned out to be of interest as a quantum magnetometer, providing non-negligible QFI with relevant peaks in a large range of configurations.

Employing the concept of QFI and graph theory, we assessed the role of topology on the thermometric performance of a given system. Upon modeling the thermometer as a set of vertices for the CTQW of an excitation at thermal equilibrium, we found that low connectivity is a resource to build precise thermometers working at low temperatures, whereas highly connected systems

are suitable for higher temperatures.

Graphs with different topology also exhibit different transport properties. To correlate them, we modeled transport processes as coherent CTQWs of an excitation and we analytically assessed the transport efficiency for different initial states and graphs. Our results suggest that, in general, connectivity is a poor indicator for transport efficiency.

Sommario

I quantum walk sono la controparte quantistica dei random walk classici e descrivono il moto di un walker quantistico confinato su posizioni discrete. La natura quantistica del walker conferisce loro caratteristiche peculiari, totalmente diverse da quelle classiche. Nel quantum walk continuo nel tempo (CTQW) lo stato del walker soddisfa l'equazione di Schrödinger ed evolve secondo l'Hamiltoniana data, tipicamente, dalla matrice Laplaciana. Quest'ultima è la rappresentazione matematica di un grafo, i cui vertici sono le posizioni permesse e gli archi i cammini consentiti. In realtà, qualsiasi Hamiltoniana che rispetta la topologia del grafo definisce un CTQW.

I CTQW sono studiati in diverse aree di ricerca, dalla modellizzazione di fenomeni fisici alla comunicazione quantistica, dalla computazione quantistica universale allo sviluppo di algoritmi quantistici. Sperimentalmente, possono essere implementati su diverse piattaforme, quali computer quantistici NMR, atomi di Rydberg ultrafreddi in reticoli ottici, chip fotonici, catene di spin e qubit superconduttori.

Questa tesi è uno studio teorico sui CTQW focalizzato sulla loro dinamica, libera o in presenza di perturbazioni esterne, e sul loro potenziale utilizzo come sonde in problemi di stima quantistica. Una sonda quantistica è un sistema fisico preparato in uno stato quantistico sensibile alle fluttuazioni di uno o più parametri. L'informazione di Fisher quantistica (QFI) è la quantità centrale della metrologia quantistica, in quanto stabilisce il limite ultimo alla precisione ottenibile nella stima di un parametro di interesse. Una QFI divergente corrisponde alla stimabilità ottimale.

Abbiamo studiato CTQW generati dalla matrice Laplaciana e perturbati dal suo quadrato, in quanto questo termine introduce hopping a secondi vicini. Dopo aver analizzato l'evoluzione di un walker su grafi paradigmatici per connettività e simmetria, abbiamo determinato le preparazioni del walker e i grafi che massimizzano la QFI per la stima del parametro perturbativo.

Inoltre, abbiamo analizzato i CTQW sulle tassellature regolari del piano Euclideo, mostrando che la propagazione non è universalmente balistica. Assumendo poi un walker dotato di carica, abbiamo inserito un campo magnetico uniforme perpendicolare e confrontato due definizioni dell'Hamiltoniana del CTQW: (i) l'introduzione dei fattori di fase di Peierls e (ii) la discretizzazione spaziale dell'Hamiltoniana originale nel continuo.

Quindi, abbiamo utilizzato una particella carica (senza spin) su un reticolo quadrato finito come sonda per rilevare un campo magnetico localmente statico e perpendicolare, avanzando l'idea di magnetometria quantistica reticolare. Il nostro schema deriva dai CTQW, ma non ne sfrutta le proprietà dinamiche, basandosi su misure di stato fondamentale. Il sistema è di interesse come magnetometro quantistico, poiché fornisce una QFI non trascurabile e con picchi rilevanti per numerose configurazioni.

Utilizzando il concetto di QFI e la teoria dei grafi, abbiamo valutato il ruolo della topologia sulle prestazioni termometriche di un dato sistema. Modellizzando il termometro come un insieme di vertici per il CTQW di un'eccitazione all'equilibrio termico, abbiamo trovato che una bassa connettività è una risorsa per realizzare termometri precisi a basse temperature, mentre sistemi altamente connessi sono adatti per temperature più elevate.

Grafi con diversa topologia presentano anche proprietà diverse di trasporto. Per correlarle, abbiamo modellizzato i processi di trasporto come CTQW coerenti di un'eccitazione ed abbiamo calcolato analiticamente l'efficienza di trasporto per diversi stati iniziali e grafi. I nostri risultati suggeriscono che in generale la connettività non è un buon indice per l'efficienza di trasporto.

Contents

Introduction	3
I <i>Overture</i>	5
1 Theoretical background	7
1.1 Quantum walks	7
1.1.1 Discrete-time quantum walks	7
1.1.2 Continuous-time quantum walks	9
1.2 Quantum estimation theory	12
1.2.1 Local quantum estimation theory	13
1.2.2 Asymptotically efficient estimators	15
1.2.3 Geometry of quantum estimation	16
1.2.4 Quantum Fisher information for pure states	17
II <i>Allegro non troppo. Perturbed dynamics</i>	21
2 Continuous-time quantum walks in the presence of a quadratic perturbation	23
2.1 Introduction	23
2.2 Dynamics	24
2.2.1 Cycle graph	25
2.2.2 Complete graph	30
2.2.3 Star graph	32
2.3 Characterization	36
2.3.1 Localized states	37
2.3.2 States maximizing the QFI	39
2.4 Discussion and Conclusions	44
Appendices	46
2.A Analytical derivation of the results for the dynamics	46
2.A.1 Cycle Graph	46
2.A.2 Complete Graph	47
2.A.3 Star graph	48
2.B Fisher Information and Quantum Fisher Information for localized states and states maximizing the QFI	50
2.B.1 Cycle graph	50
2.B.2 Complete graph	52
2.B.3 Star graph	53

2.B.4	Maximum QFI states: the role of the phase factor in the superposition of energy eigenstates	54
3	Continuous-time quantum walks on planar lattices and the role of the magnetic field	55
3.1	Introduction	55
3.2	CTQW on planar lattice graphs	56
3.2.1	Planar lattice graph	56
3.2.2	The CTQW Hamiltonian on PLGs	57
3.2.3	Numerical simulation	62
3.3	A charged quantum walker in a magnetic field	67
3.3.1	The Hamiltonian of the system: The issue of the spatial discretization	67
3.3.2	Numerical simulation: Parameter setting	68
3.4	CTQW under magnetic field: The Peierls model	69
3.4.1	The Peierls phase-factors	69
3.4.2	The CTQW Hamiltonian	71
3.4.3	Numerical simulation: results	72
3.5	CTQW under magnetic field: the spatial discretization of the Hamiltonian	77
3.5.1	Finite-difference formulas with Taylor expansion	77
3.5.2	Conservative finite-difference methods	78
3.5.3	The CTQW Hamiltonian	82
3.5.4	Numerical simulation: results	84
3.6	Conclusions	89
	Appendices	91
3.A	Mathematical tools and discretization of the space	91
3.A.1	Green's theorem in a plane	91
3.A.2	Spatial discretization	92
3.A.3	Discrete differential operators	93
3.A.4	Linear momentum operator	94
3.A.5	Derivation of the discrete Hamiltonian: details	95
3.B	Computational details	97
3.B.1	Plotting the maps	97
3.B.2	Indexing and coordinates of vertices	98
3.B.3	Boundary conditions	101
3.C	Units	102

III *Adagio.* Quantum estimation 105

4	Lattice quantum magnetometry	107
4.1	Introduction	107
4.2	The probing system	108
4.3	The estimation procedure	112
4.4	Ground-state quantum magnetometry	114
4.4.1	Homogeneous magnetic field	114
4.4.2	Inhomogeneous magnetic field	115
4.5	Conclusions	119
	Appendices	119
4.A	The role of the lattice size	119

5	Role of topology in determining the precision of a finite thermometer	121
5.1	Introduction	121
5.2	Equilibrium Thermometry	122
5.2.1	Estimation Theory	122
5.2.2	Quantum Fisher Information	123
5.2.3	Fisher Information for a position measurement	124
5.3	Network Thermometry	124
5.3.1	Low-temperature regime	125
5.3.2	High-temperature regime	125
5.3.3	Fisher Information for circulant graphs	127
5.4	Results	128
5.4.1	Complete graph	128
5.4.2	Cycle graph	129
5.4.3	Complete Bipartite Graph	130
5.4.4	Path graph	132
5.4.5	Lattices	133
5.5	Role of coherence	136
5.6	Conclusions	137
	Appendices	138
5.A	Sum of the Laplacian eigenvalues and sum of their square	138
5.B	Fisher Information for a position measurement	139
5.C	QFI and FI for the Cartesian product of two graphs	140
5.C.1	Cartesian product of two graphs	140
5.C.2	Quantum Fisher Information	140
5.C.3	Fisher Information for position measurement	140
5.C.4	Grid graph and torus grid graph	141
5.D	Exact QFI for the complete bipartite graph	141

IV Presto. Modeling of transport phenomena **143**

6	Transport efficiency of continuous-time quantum walks on graphs	145
6.1	Introduction	145
6.2	Dimensionality reduction method	146
6.3	Quantum transport	147
6.3.1	Complete bipartite graph	150
6.3.2	Strongly regular graph	152
6.3.3	Joined complete graphs	153
6.3.4	Simplex of complete graphs	155
6.4	Measures of connectivity	159
6.5	Conclusions	161
	Appendices	162
6.A	Subspace of the eigenstates of the Hamiltonian with non-zero overlap with the trap	162
6.B	Basis of $\mathcal{I}(H, w\rangle)$ for each graph	163
6.B.1	Complete bipartite graph	163
6.B.2	Strongly regular graph	164
6.B.3	Joined complete graphs	165
6.B.4	Simplex of complete graphs	166

V	<i>Finale</i>	169
7	Concluding remarks and perspectives	171
	List of publications	175
	Bibliography	189

Introduction

The so-called first quantum revolution began in the early 20th century and allowed scientists to understand and apply physical laws in the microscopic realm, i.e., to understand and use quantum effects. Such a revolution resulted in groundbreaking technologies that brought many devices to the market, such as transistors and microprocessors, solid-state lighting and lasers, and medical imaging scanners. The second quantum revolution began at the beginning of the 21st century. The way was paved by our ability to use quantum effects in customized systems and materials. Scientists can now manipulate and perceive individual particles, measuring and exploiting their properties. This has led to significant development of quantum technologies and technological advances in computing, sensors, simulations, cryptography, and telecommunications. In 2018 the European Commission launched the FET¹ Flagship on Quantum Technologies, a 10-year research programme that aims to put Europe at the forefront of the second quantum revolution. The call to support the flagship was made through the *Quantum Manifesto* [1], which identifies four leading areas of quantum technologies:

- i. **Quantum communication** A global quantum-safe communication network—a quantum internet combining quantum with classical information and encryption—offers security for internet transactions against the threat of a quantum computer breaking purely classical encryption schemes.
- ii. **Quantum simulation** Quantum simulators can be viewed as analogue versions of quantum computers, constructed with the special purpose of simulating the behavior of materials and chemical reactions at very low temperatures, where quantum phenomena arise. Simulation allows new processes or properties to be explored before the material exists, offering the key to design new materials and chemicals.
- iii. **Quantum metrology and sensing** Quantum sensors exploit quantum superposition and/or entanglement (naturally very sensitive to the environment) to achieve a higher sensitivity and resolution, and to provide the most accurate measurements. In addition to quantum communication, quantum sensors will arguably be the basis for the first applications of quantum technologies.
- iv. **Quantum computing** Quantum computers are built from “quantum bits”, *qubits*, and exploit superposition and entanglement to solve certain problem classes that would otherwise be unsolvable, even for the supercomputers of today and tomorrow. Universal quantum computers will be reprogrammable machines used to solve demanding computational problems, such as optimization tasks, database searches, machine learning, and image recognition.

Quantum walks are the quantum analog of classical random walks. As such, their behavior is utterly different from the classical one, due to the superposition of the quantum walker in

¹Future and Emerging Technologies.

their path. The position space of the quantum walker is discrete, but with respect to time we distinguish *discrete-time* quantum walks (DTQWs) [2–4], in which the motion of the quantum walker is ruled by a quantum coin tossed at discrete time steps, and *continuous-time* quantum walks (CTQWs) [5, 6], in which the quantum walker evolves continuously in time according to the Schrödinger equation and no coin is involved. We recommend Refs. [7–9] as comprehensive reviews on quantum walks, and Ref. [10] for their physical implementations. This thesis focuses on CTQWs, which describe the propagation of a quantum particle on a graph. The state of a walker with only kinetic energy evolves under the Hamiltonian $H = \gamma L$, where $\gamma \in \mathbb{R}^+$ is the hopping amplitude of the walk, and L is the Laplacian matrix which encodes the connectivity of the graph. This is the prototype of CTQW but any Hermitian operator which respects the topology of the graph defines a CTQW [11, 12]. This is what makes CTQWs a powerful tool, since one can devise and design a Hamiltonian for a specific task with that one constraint. Experimentally, CTQWs can be implemented on different platforms, e.g., on nuclear-magnetic-resonance quantum computers [13], ultracold Rydberg ^{87}Rb atoms in optical lattices [14, 15], optical waveguides [16, 17], and photonic chips [18, 19]. Recently, they have been demonstrated for one and two strongly correlated microwave photons in a 1D array of 12 superconducting qubits [20] and on a programmable 2D 62-qubit superconducting processor [21].

Quantum walks inherit the versatility of application from their classical ancestors, but the peculiar features arising from their quantum nature make them suitable candidates not only for modeling physical processes but also for application in quantum technologies, e.g., in the four pillars previously mentioned. The task of perfect state transfer is of utmost importance for quantum communication and it has often been modeled in terms of CTQWs in quantum spin networks [22–25]. CTQWs are universal for quantum computation [26–29]. They offer a versatile paradigm for quantum computing, based on discrete data encoding and continuous data processing [30]. The vertices in a graph serve to model the computational basis states, while the edges between vertices the connectivity between computational basis states. Moreover, CTQWs are employed to develop quantum algorithms, e.g., spatial search [12, 31–34], graph isomorphism [35, 36], image segmentation [37], and to solve K -SAT problems² [38]. DTQW is a validated quantum simulation scheme for the Dirac equation, it is a simple, discrete toy model of relativistic particles [39]. Models of quantum walks which admit continuous-time and continuous-spacetime limits have recently led to quantum simulation schemes for simulating fermions in relativistic and non-relativistic regimes [40]. CTQWs are of use to model and simulate other physical phenomena, such as quantum transport [41, 42], even in biological system [43, 44], and to characterize many-body systems [45, 46]. CTQWs may also be of use in quantum chaos studies, as the CTQW on the line, under appropriate conditions, is equivalent to the quantum kicked rotor³ at resonance conditions [48]. Regarding quantum metrology, quantum-limited measurements on the walker performing a CTQW on a graph may provide information on the tunnelling amplitude between the nodes of the graph, and the amount of extractable information strongly depends on the underlying topology [49]. Moreover, there is a proposal of addressing the scattering as a quantum metrology problem based on CTQWs [50].

In this thesis we propose some potential applications of CTQWs to quantum metrology, i.e., their potential use as probes in quantum estimation problems, and address fundamental aspects

² K -SAT is one of the most important problems in computer science, known to be NP-Complete for $K > 2$. It is a constraint satisfaction problem where a Boolean formula has to be satisfied (true). A K -SAT instance is written in conjunctive normal form, that is, a conjunction of clauses, where a clause is a disjunction of K literals, and a literal can be a logical variable or its negation.

³By definition, the kicked rotor is a point particle that moves freely on a circle. The particle is kicked periodically in time, where the kick strength depends on the angular position. When a kick strength parameter exceeds a certain threshold value, the dynamics becomes globally chaotic [47].

of their dynamics, free or in the presence of external perturbations. A quantum probe is a physical system prepared in a quantum state sensitive to fluctuations affecting one or more parameters of interest and the ultimate bound on the achievable precision in estimating them is provided by the quantum Fisher information (QFI), which is therefore the central quantity in quantum metrology. Diverging QFI corresponds to optimal estimability. On the other hand, besides fundamental interest, understanding and characterizing the CTQW dynamics beyond the prototypical model may pave the way to further applications in quantum technologies, e.g., enhanced quantum algorithms, and in modeling physical processes. The studies presented in this thesis are theoretical, supported by analytical results and numerical evidence from originally developed codes. Due to the variety of topics considered, the thesis is structured in five parts, in the spirit of musical *movements*. Each chapter presenting our original results has its own conclusions and appendices.

Part I, i.e., Chapter 1, is a theoretical introduction to quantum walks and quantum estimation theory which provides the main concepts used in the next chapters.

Part II is devoted to the perturbed dynamics of CTQWs. In Chapter 2 we study CTQWs generated by the Laplacian matrix and perturbed by its square, as this term introduces next-nearest-neighbor hopping. After investigating the evolution of a walker on paradigmatic graphs for connectivity and symmetry, we determine the walker preparations and the graphs that maximize the QFI for estimating the perturbation parameter. In Chapter 3 we investigate CTQWs on the regular tessellations of the Euclidean plane, showing that the spread is not universally ballistic. Then, assuming a (spinless) charged walker, we insert a perpendicular uniform magnetic field and compare two approaches to define the CTQW Hamiltonian: (i) Introducing the Peierls phase-factors and (ii) spatially discretizing the original Hamiltonian in the continuum.

Part III is devoted to quantum estimation problems. In Chapter 4 we use a charged (spinless) particle on a finite square lattice as a probe to detect a locally static transverse magnetic field, putting forward the idea of lattice quantum magnetometry. Our scheme finds its root in CTQWs, but it does not exploit their dynamical properties, being based on ground-state measurements. In Chapter 5 we assess the role of topology on the thermometric performance of a given system, upon modeling the thermometer as a set of vertices for the CTQW of an excitation at thermal equilibrium.

Part IV is devoted to modeling transport phenomena. Graphs with different topology exhibit different transport properties. To correlate them, in Chapter 6 we model transport processes as coherent CTQWs of an excitation and we analytically assess the transport efficiency for different initial states and graphs.

Part V, i.e., Chapter 7, is devoted to final remarks and future perspectives of CTQWs.

Part I

Overture

Chapter 1

Theoretical background

In this chapter we present the theoretical background on which this work is based. We review the quantum counterpart of classical random walk, namely the quantum walks, which are either discrete or continuous in time. Then, we report some elements of quantum estimation theory, with particular attention to the definition of the quantum Fisher information.

1.1 Quantum walks

Quantum walks (QWs) are the quantum counterpart of classical random walks [8, 9] and describe the motion of a *walker* (usually a quantum particle) on a graph, i.e., on a discrete space made of vertices connected by edges. These processes can be either *discrete* or *continuous* in time. Discrete-time QWs were formally introduced by Aharonov et al. [2, 3] and by Ambainis et al. [4], whereas continuous-time QWs were developed from Farhi and colleagues' works [5, 6].

1.1.1 Discrete-time quantum walks

In a discrete-time quantum walk (DTQW) the motion of the particle is governed by the toss of a so-called quantum *coin*, an ancillary quantum system whose state determines the discrete spatial translations of the particle. The system is thus bipartite and the Hilbert space of the composite system $\mathcal{H} = \mathcal{H}_c \otimes \mathcal{H}_p$ is the tensor product of the subspace \mathcal{H}_c of the coin and the subspace \mathcal{H}_p of the particle. It is customary to initialize the system into a state like

$$|\Psi\rangle = |\phi_c\rangle \otimes |\psi_p\rangle, \quad (1.1)$$

where $|\phi_c\rangle \in \mathcal{H}_c$ is the coin state, and $|\psi_p\rangle \in \mathcal{H}_p$ is the (position) state of the particle.

We can understand the fundamental features of this system just by considering the one-dimensional model. The space of the particle \mathcal{H}_p is spanned by the basis states describing the particle localized at the n -th site of the lattice, $\{|n\rangle \mid n \in \mathbb{Z}\}$, whereas the two-dimensional coin space \mathcal{H}_c is spanned by the basis states $\{|\uparrow\rangle, |\downarrow\rangle\}$. The evolution of the walk depends on the state of the quantum coin. If one obtains “heads”, $|\uparrow\rangle$, after tossing the coin and the walker is in the state $|n\rangle$, then in the next step it will be in $|n+1\rangle$. If it is “tails”, $|\downarrow\rangle$, then the walker will be in $|n-1\rangle$. The key point is that since both the particle and the coin are quantum, even the coin can be in a superposition of states. Therefore, having a superposition of “heads” and “tails” allows the walker to simultaneously explore the two corresponding different paths. This results in a probability distribution with no classical analog, due to the self-interference effects.

The conditional shift from $|n\rangle$ to $|n \pm 1\rangle$ must be described by a unitary operator, the so-called (conditional) shift operator \hat{S} , which operates as follows

$$\begin{aligned}\hat{S}|\uparrow\rangle|n\rangle &= |\uparrow\rangle|n+1\rangle, \\ \hat{S}|\downarrow\rangle|n\rangle &= |\downarrow\rangle|n-1\rangle.\end{aligned}\tag{1.2}$$

Hence, we can explicitly write the expression of this operator as follows

$$\hat{S} = |\uparrow\rangle\langle\uparrow| \otimes \sum_{n \in \mathbb{Z}} |n+1\rangle\langle n| + |\downarrow\rangle\langle\downarrow| \otimes \sum_{n \in \mathbb{Z}} |n-1\rangle\langle n|.\tag{1.3}$$

We have just shown the working principle of a DTQW, i.e., how the walker moves according to the coin state, but now we need to understand how to quantumly toss a coin. The quantum analog of tossing a coin in the classical case is the application of a coin operator \hat{C} to the coin state. The operator \hat{C} is unitary and describes a rotation in the coin space \mathcal{H}_c . The arbitrariness in choosing it allows us to define and to study a wide range of DTQWs, phenomenologically different. A commonly used coin is the *Hadamard coin*,

$$\hat{C}_H = \frac{1}{\sqrt{2}} \begin{pmatrix} 1 & 1 \\ 1 & -1 \end{pmatrix},\tag{1.4}$$

which, acting on a given coin basis state, results in a superposition of the two coin basis states. The evolution operator \hat{U} of single time step is thus

$$\hat{U} = \hat{S} \cdot (\hat{C}_H \otimes \hat{I}_p),\tag{1.5}$$

where \hat{I}_p is the identity for \mathcal{H}_p . In other words, first $\hat{C}_H \otimes \hat{I}_p$ acts on the state of the composite system, tossing the quantum coin. This changes the coin state, leaving the particle state unchanged. Then \hat{S} acts, and this changes the particle state according to the coin state, leaving the latter unchanged. It is worth noticing that the evolution operator (1.5) generates entanglement between the coin state and the particle state. After $t \in \mathbb{N}$ time steps the state of the composite system is $\hat{U}^t|\Psi\rangle$.

To highlight how the quantum nature of these walks results in a radically different behavior compared to the classical case, we compare the probability distribution of the walker in a classical random walk with that in a symmetric DTQW [9], i.e., a DTQW involving the Hadamard coin and the following initial state

$$|\Psi_{sym}\rangle = \frac{1}{\sqrt{2}} (|\uparrow\rangle + i|\downarrow\rangle) \otimes |0\rangle.\tag{1.6}$$

In both cases the walker moves on a line (one-dimensional lattice) and starts in $n = 0$. The probability distribution in the classical random walk has a Gaussian shape peaked in the center of the line, $n = 0$, while in the DTQW it shows increasing peaks towards the extremes of the line, several local maxima and minima due to the self-interference effects, and low probability in the initial position. It can be proved [4] that in this case the DTQW is characterized by a variance which scales quadratically with the number of time steps, $\sigma^2 \propto t^2$ (*ballistic spread*), and the expected value for the distance of the walker from the origin is therefore $\sigma \propto t$. Hence, a DTQW spreads faster than a classical random walk, for which $\sigma^2 \propto t$ (*diffusive spread*).

As a final remark, it is worth noticing that measuring the coin state at each iteration of the walk reproduces the classical behavior of a random walk on a line. Indeed, because of this measurement, correlations between different positions are deleted. In this case, the limiting distribution,

for large number of iterations t , approaches a Gaussian distribution with mean zero and variance $\sigma^2 = t$. In a DTQW the coin state is not measured at each iteration, and so quantum correlations between different positions are preserved and are allowed to interfere at subsequent steps, thus resulting in the peculiar behavior previously outlined.

1.1.2 Continuous-time quantum walks

The model of continuous-time quantum walks (CTQWs) was developed by Farhi and Gutmann [5] on the basis of continuous-time classical Markov chains, which are described by the simple model of a continuous-time classical random walk on a graph. So, before presenting CTQWs, we will briefly review the concepts of graph and of continuous-time classical random walk following Ref. [7].

A graph G is defined as a pair $G := (V, E)$, where V denotes the non-empty set of vertices, whose cardinality $|V| = N$ is the number of vertices (order of the graph), and E the set of edges. An undirected graph¹ is mathematically represented by the Laplacian matrix (also known as graph Laplacian or Kirchhoff matrix)

$$L = D - A, \quad (1.7)$$

where the adjacency matrix

$$A_{jk} = \begin{cases} 1 & \text{if } (j, k) \in E, \\ 0 & \text{otherwise,} \end{cases} \quad (1.8)$$

is symmetric and describes the connectivity of G (nonzero entry only if the vertices j and k are connected by an edge), while D is the diagonal degree matrix whose general element $D_{jj} = \text{deg}(j)$ is the degree of vertex j , i.e., the number of incident edges in j [51]. According to this definition, L is real, symmetric, positive semidefinite,² and singular.³

The continuous-time random walk on G is a Markov process with a fixed probability per unit time γ of jumping from a vertex to an adjacent one. The transition matrix M is what makes the probability distribution over V evolve at each time step. To make this process continuous in time, we assume that transitions can occur at any time with a transition rate given by γ which is constant for all vertices (homogeneous rate) and for all times (uniform rate). Given an infinitesimal time interval τ , the probability of the walker to jump from the vertex j to the vertex k is $\gamma\tau$. If $d_j = \text{deg}(j)$ is the degree of the vertex j , i.e., j has d_j neighbors, then the walker has an overall probability $d_j\gamma\tau$ of exiting j , and so a probability $1 - d_j\gamma\tau$ of remaining on it. According to this, the elements of the transition matrix at time t are defined as the transition probabilities during

¹Undirected graphs have edges that do not have a direction. An undirected edge is defined by an unordered pair of vertices and can be traversed in both directions (two-way relationship). Directed graphs, instead, have edges with direction. A directed edge is defined by an ordered pair of vertices and can only be traversed in a single direction (one-way relationship).

²A $n \times n$ real symmetric matrix M is positive semidefinite (PSD) if

$$\mathbf{v}^T M \mathbf{v} \geq 0 \quad \forall \mathbf{v} \in \mathbb{R}^n.$$

A matrix M is PSD iff all eigenvalues $\lambda_j \geq 0$. The Laplacian matrix is PSD since it can be written as $L = N^T N$, where N is the directed incidence matrix of the directed graph obtained by orienting its edges in an arbitrary way. It follows that for any vector v we have $\mathbf{v}^T L \mathbf{v} = \sum_{(j,k) \in E} (v_j - v_k)^2 \geq 0$ [52].

³A singular matrix is a square matrix that does not have a matrix inverse. A matrix is singular if and only if its determinant is 0. The determinant of the Laplacian is 0 because it always admits the null eigenvalue. Indeed, every row sum and column sum of L is zero, and so the vector $\mathbf{v} = (1, \dots, 1)$ satisfies $L\mathbf{v} = 0$.

the time interval t . Thus, for the infinitesimal time interval we have

$$M_{jk}(\tau) = \begin{cases} \gamma\tau + O(\tau^2) & \text{if } j \neq k \text{ and } (j, k) \in E, \\ 0 & \text{if } j \neq k \text{ and } (j, k) \notin E, \\ 1 - d_j\gamma\tau + O(\tau^2) & \text{if } j = k. \end{cases} \quad (1.9)$$

Notice that $M_{jk}(\tau) = 0$ if vertices j and k are not adjacent. Indeed, if there is no edge connecting two vertices, the transition between them can not occur. The element $M_{jk}(\tau)$ is the transition probability from the j -th to k -th vertex⁴ during τ . The (infinitesimal) generator of such a process is the following matrix:

$$\mathcal{H}_{jk} = \gamma L_{jk} = \begin{cases} -\gamma & \text{if } j \neq k \text{ and } (j, k) \in E, \\ 0 & \text{if } j \neq k \text{ and } (j, k) \notin E, \\ d_j\gamma & \text{if } j = k. \end{cases} \quad (1.10)$$

In a Markov chain the next state only depends on the current one. The state is the probability distribution at the current time t , and, in our case, this is the probability distribution over the vertices V of G

$$\mathbf{p}(t) = \begin{pmatrix} p_1(t) \\ p_2(t) \\ \vdots \\ p_{|V|}(t) \end{pmatrix}. \quad (1.11)$$

The element $p_j(t)$ is the probability of finding the walker in the vertex j at time t . Just like the probability of two independent events is the product of the probability of each event, we can write⁵

$$M_{jk}(t + \tau) = \sum_l M_{jl}(\tau) M_{lk}(t). \quad (1.12)$$

The index l runs over all the vertices, but, according to the definition of M_{jk} , this is equivalent to summing only over the vertices adjacent to k . Using the definition (1.10) and isolating the term $l = j$, we have

$$\begin{aligned} M_{jk}(t + \tau) &= M_{jj}(\tau) M_{jk}(t) - \sum_{l \neq j} M_{jl}(\tau) M_{lk}(t) \\ &= (1 - d_j\gamma\tau) M_{jk}(t) - \tau \sum_{l \neq j} \mathcal{H}_{jl} M_{lk}(t), \end{aligned} \quad (1.13)$$

from which

$$\lim_{\tau \rightarrow 0} \frac{M_{jk}(t + \tau) - M_{jk}(t)}{\tau} = \frac{dM_{jk}(t)}{dt} = - \sum_l \mathcal{H}_{jl} M_{lk}(t). \quad (1.14)$$

⁴The convention is actually to read M_{jk} as the transition probability from j to k . Here we made a different choice to be more consistent to the quantum formalism. Hence, when comparing the following discussion with the literature about Markov chains, be aware of the different conventions. A transposition is involved.

⁵This equation is known as the Chapman-Kolmogorov Equation (time-homogeneous)

$$M(t + s) = M(s)M(t) \Leftrightarrow M(t + s) = \sum_{l \in S} M_{jl}(s) M_{lk}(t),$$

where S is the discrete state space.

Given the initial condition $M_{jk}(0) = \delta_{jk}$, the solution of this differential equation is

$$M(t) = e^{-\mathcal{H}t}. \quad (1.15)$$

Now that we know the transition matrix, we can obtain the probability distribution at time t , given the initial distribution $\mathbf{p}(0)$, according to

$$\mathbf{p}(t) = M(t)\mathbf{p}(0) = e^{-\mathcal{H}t}\mathbf{p}(0). \quad (1.16)$$

Indeed, the probability distribution satisfies the following first-order linear differential equation

$$\frac{dp_j(t)}{dt} = -\sum_k \mathcal{H}_{jk}p_k(t) = -\gamma \sum_k L_{jk}p_k(t). \quad (1.17)$$

The probability is conserved since the columns of L sum to zero. Indeed, to be a valid probability-conserving classical Markov process, the above differential equation requires⁶ $\sum_j L_{jk} = 0$.

Farhi and Gutmann's idea is to extend such a model to the quantum case, so that the matrix \mathcal{H} generating the process is a Hamiltonian. The CTQW on a graph takes place in a N -dimensional Hilbert space spanned by states $|j\rangle$, where $j \in V$ is a vertex in G . A state $|j\rangle$ describes a walker localized on the j -th vertex. These position states form an orthonormal basis, so we can write a general state $|\psi(t)\rangle$ in terms of the N complex amplitudes $q_j(t) = \langle j|\psi(t)\rangle$, i.e., $|\psi(t)\rangle = \sum_{j \in V} q_j(t)|j\rangle$. Given the Hamiltonian \mathcal{H} , the dynamics of the system obeys the Schrödinger equation $i\frac{d}{dt}|\psi(t)\rangle = \mathcal{H}|\psi(t)\rangle$, which, written in the vertex basis, reads as

$$i\frac{dq_j(t)}{dt} = \sum_k \mathcal{H}_{jk}q_k(t), \quad (1.18)$$

in the units in which $\hbar = 1$. As known, according to Eq. (1.18), an initial quantum state $|\psi(0)\rangle$ evolves in time as

$$|\psi(t)\rangle = \mathcal{U}(t)|\psi(0)\rangle = e^{-i\mathcal{H}t}|\psi(0)\rangle. \quad (1.19)$$

The evolution is unitary and the probability to find the walker in a given vertex j is therefore

$$p_j(t) = |q_j(t)|^2 = |\langle j|\psi(t)\rangle|^2. \quad (1.20)$$

The CTQW is defined by letting $\mathcal{H} = \gamma L$, i.e., by promoting the Laplacian matrix to Hamiltonian of a quantum system. However, it is worth noticing that not only the graph Laplacian, but also any Hermitian operator \mathcal{H} that respects the locality of the graph defines a CTQW [11]. Indeed, Eq. (1.18) requires $\mathcal{H} = \mathcal{H}^\dagger$ to be a valid unitary quantum process [31]. As an example, often CTQWs are generated by the adjacency matrix A . For regular graphs,⁷ $D_{jj} = \text{deg}(j) =: d$ is independent of j , thus $L = dI - A$, where I is the identity matrix, and A generate the same CTQW, the same quantum dynamics. For non-regular graphs, instead, the two choices provide different results.

To conclude, we stress that passing from the continuous-time Markov chain to the CTQW model,

⁶We know that probabilities must satisfy $\sum_j p_j(t) = 1$, from which

$$\frac{d}{dt} \sum_j p_j(t) = \sum_j \frac{dp_j(t)}{dt} = -\gamma \sum_j \sum_k L_{jk}p_k(t) = 0.$$

Since $\gamma > 0$, we have $\sum_j L_{jk} = 0$. Indeed, the conservation of probability can not be ensured, in general, by $\sum_k L_{jk}p_k(t) = 0$ because the latter depends on the particular probability distribution $\{p_k(t)\}_k$.

⁷A graph is said to be regular if all its vertices have the same degree.

- we pass from the vector \mathbf{p} , which describes the probability distribution, to a quantum state vector $|\psi\rangle$ (i.e., given the vertex basis, the vector \mathbf{q} whose elements are the probability amplitudes);
- the probability distribution satisfies the differential equation (1.17), while the quantum state vector satisfies the Schrödinger equation (1.18);
- we pass from the transition matrix $M(t)$, which is not unitary in general, to a unitary time-evolution operator $\mathcal{U}(t)$.

The physical meaning of the graph Laplacian

The graph Laplacian has its roots in the discretization of the space. The Hamiltonian characterizes the total energy of the system, and, for a particle of mass m , it includes a kinetic energy term

$$\mathcal{T} = -\frac{1}{2m}\nabla^2, \quad (1.21)$$

where $\hbar = 1$ and $\nabla^2 = \partial_x^2 + \partial_y^2 + \partial_z^2$ is the Laplace operator (in the three-dimensional Euclidean space). If the particle is confined to discrete spatial locations, then ∇^2 is replaced by the graph Laplacian⁸ $L = A - D$. For example, for a one-dimensional grid with lattice spacing a , note the similarities between the continuous-space Laplacian

$$\nabla^2\psi(x) = \frac{d^2\psi(x)}{dx^2} = \lim_{a \rightarrow 0} \frac{\psi(x+a) + \psi(x-a) - 2\psi(x)}{a^2} \quad (1.22)$$

and the discrete-space analog

$$\langle x|L|\psi\rangle = \langle x|(A - D)|\psi\rangle = \psi_{x+1} + \psi_{x-1} - 2\psi_x, \quad (1.23)$$

where $\psi_x := \langle x|\psi\rangle$ and $x \in \mathbb{Z}$. Now letting $\gamma = 1/2ma^2$, the kinetic energy operator becomes

$$\mathcal{T} = -\gamma L. \quad (1.24)$$

This defines the prototypical CTQW, the propagation of a quantum particle with kinetic energy when confined to a lattice. Unlike the Markov process, now the parameter $\gamma \in \mathbb{R}^+$ is the hopping amplitude, i.e., the amplitude rate of the walk. A higher rate corresponds to a particle with a smaller mass, since a less massive particle scatters more readily [12].

1.2 Quantum estimation theory

Measuring is one of the key aspects of physics. In a classical context, we have to associate to each outcome an error, which might be of random or systematic nature. In a quantum context the uncertainty of a measurement is intrinsically related to the system under investigation. However, unlike its classical counterpart, quantum mechanics allows us to establish the ultimate bound to the precision of any measurement. In this case, furthermore, it is of particular interest the concept of estimation of a parameter, since parameters of a system are not always physical observables and

⁸The proper mathematical definition of the Laplacian matrix is $L = D - A$. The definition $L = A - D$ is sometimes preferred because closer to the Laplace operator ∇^2 , as in the present case. The reason is that, for a lattice, L is the discrete approximation of the continuum operator ∇^2 . Both definitions of L generate the same CTQW, as in the former case the Hamiltonian is defined as $\mathcal{H} = \gamma L$, while in the latter as $\mathcal{H} = -\gamma L$.

hence not accessible with direct measurements. *Quantum estimation theory* (QET) [53–55] allows us to identify the best strategy for estimating an unknown parameter in a quantum system, even if this is not accessible through a direct measurement. In particular, it is possible to write an estimator to assess the value of the unknown parameter with the maximum precision allowed by quantum mechanics by means of a suitable elaboration of the outcomes of a properly optimized measurement of an observable. In general there are two paradigms in QET:

- (i) *Global QET* looks for the positive operator-valued measure⁹ (POVM) minimizing a suitable cost functional, averaged over all possible values of the parameter to be estimated. The result of a global optimization is thus a single POVM, independent of the value of the parameter.
- (ii) *Local QET* looks for the POVM maximizing the Fisher information, thus minimizing the variance of the estimator, at a fixed value of the parameter [58–62].

In this work we will adopt the latter paradigm, the local QET, which is usually applied to the estimation of quantum phase [63] and to estimation problems with open quantum systems and non-unitary processes [64–71]. In the following we briefly review the main concepts of local QET according to Ref. [55].

1.2.1 Local quantum estimation theory

Solving a parameter estimation problem amounts to finding an *estimator*, i.e., a mapping $\hat{\lambda} = \hat{\lambda}(x_1, x_2, \dots)$ from the set $\{x_i\}$ of measurement outcomes, which depend on some parameter λ , into the space of parameters. Purpose of *classical* estimation theory is to find an estimator that gives the most precise estimate of such parameter λ . Optimal estimators in classical estimation theory are those saturating the Cramér-Rao inequality [72–74]

$$V(\lambda) \geq \frac{1}{M\mathcal{F}_c(\lambda)}, \quad (1.25)$$

where M is the number of measurements and $\mathcal{F}_c(\lambda)$ is the so-called Fisher information (FI)

$$\mathcal{F}_c(\lambda) = \int dx p(x|\lambda) \left(\frac{\partial \ln p(x|\lambda)}{\partial \lambda} \right)^2 = \int dx \frac{1}{p(x|\lambda)} \left(\frac{\partial p(x|\lambda)}{\partial \lambda} \right)^2, \quad (1.26)$$

where $p(x|\lambda)$ is the conditional probability of obtaining the value x when the parameter takes the value λ . The Cramér-Rao inequality (1.25) establishes a lower bound on the mean square error

$$V(\lambda) = \mathbb{E}_\lambda \left[\left(\hat{\lambda}(\{x\}) - \lambda \right)^2 \right] \quad (1.27)$$

for each estimator of the parameter λ , where $\mathbb{E}_\lambda[\cdot]$ denotes the expectation value. A particular class of $\hat{\lambda}$ are the *unbiased estimators*, for which the mean square error is equal to the variance

$$\text{Var}(\hat{\lambda}) = \mathbb{E}_\lambda[\hat{\lambda}^2] - \mathbb{E}_\lambda[\hat{\lambda}]^2, \quad (1.28)$$

⁹A measure is a function which assigns a number, in this case a probability, to the subsets of a given set. The elements of the measure are the probability operators and this is the reason for calling it a probability operator measure (POM). The most often used expression ‘positive operator-valued measure’ expresses the fact that the elements of the measure, the probability operators, are positive operators. Calling the set of operators a POM reminds us of their physical significance, while the term POVM recalls their mathematical properties [56]. The POVM consists of a set of non-negative quantum-mechanical Hermitian operators that add up to the identity. The probability that a quantum system is in a particular state is given by the expectation value of the POVM operator corresponding to that state [57].

and the expectation value is the actual value of the parameter λ , $E_\lambda[\hat{\lambda}] = \int dx p(x|\lambda) \hat{\lambda}(x) \equiv \lambda$. The variance is the usual figure of merit that quantifies the precision of an estimator: The lower the variance, the closer the outcomes are spread around the expected value of the estimator. In the present work we will always deal with unbiased estimators. The Cramér-Rao bound (1.25) sets a lower bound on the variance of any unbiased estimator $\hat{\lambda}$, provided that the family of distribution $p(x|\lambda)$ realizes a so-called *regular statistical model*. Regular models are those with a constant support, i.e., the region in which $p(x|\lambda) \neq 0$ does not depend on the parameter λ , and with non-singular FI. If these hypotheses are not satisfied, estimators with vanishing variance may be easily found. The FI for the statistical model $p(x|\lambda)$ quantifies how much information on λ is encoded in the probability distribution: A large FI means that the outcomes carry significant information on the parameter, which is reflected by the possibility of having more precise estimators, see Eq. (1.25). The attainability of the Cramér-Rao bound (1.25) is the fundamental problem of classical estimation theory. Indeed, it is known that the lower bound can be saturated by the maximum likelihood estimator in the limit of infinite set of measurements $M \rightarrow +\infty$ [75].

When quantum systems are involved, any estimation problem may be stated by considering a family of quantum states $\{\rho_\lambda\}$, defined on a given finite-dimensional Hilbert space and parametrized by λ , living on a d -dimensional manifold, with the mapping $\lambda \mapsto \rho_\lambda$ providing a coordinate system. This is sometimes referred to as a *quantum statistical model*. The parameter λ does not, in general, correspond to a quantum observable and our aim is to estimate its values through the measurement of some observable on ρ_λ . In turn, a quantum estimator for λ is a self-adjoint operator, which describes a quantum measurement followed by any classical data processing performed on the outcomes. The indirect procedure of parameter estimation implies an additional uncertainty for the measured value, that cannot be avoided even in optimal conditions. The aim of QET is to optimize the inference procedure by minimizing this additional uncertainty. As known, in quantum mechanics, probability distributions naturally arise according to the Born rule $p(x|\lambda) = \text{tr}[\Pi_x \rho_\lambda]$, where $\{\Pi_x\}$ are the elements of a POVM and ρ_λ is the density operator parametrized by the quantity we want to estimate. Notice that the measurement, the POVM, is independent of λ , while the information of the parameter λ is encoded in the density matrix. Unlike the classical regime, the probability distribution depends both on the state and on the measurement, so we can suitably choose them to get better estimates. In particular, given ρ_λ , there is arbitrariness in the choice of the POVM: Different choices of POVM result in different probability distributions. To evaluate the ultimate bounds to precision, we have to maximize the FI over all the possible quantum measurements. The FI of any quantum measurement is bounded by the so-called *quantum Fisher information* (QFI), $\mathcal{F}_q(\lambda)$, according to

$$\mathcal{F}_c(\lambda) \leq \mathcal{F}_q(\lambda) \equiv \text{tr}[\rho_\lambda L_\lambda^2], \quad (1.29)$$

where L_λ is the symmetric logarithmic derivative (SLD), defined as the self-adjoint operator satisfying the Lyapunov equation

$$\frac{L_\lambda \rho_\lambda + \rho_\lambda L_\lambda}{2} = \frac{\partial \rho_\lambda}{\partial \lambda}. \quad (1.30)$$

The maximum of the FI among all the possible POVMs is the QFI [76], $\mathcal{F}_q(\lambda) = \max_{\Pi_x} \{\mathcal{F}_c(\lambda)\}$. Therefore, an optimal quantum measurement for the estimation of λ is the POVM that maximizes the FI and thus makes $\mathcal{F}_c(\lambda) = \mathcal{F}_q(\lambda)$, saturating the inequality (1.29). One can prove that the optimal POVM is given by the set of projectors onto the eigenstates of the SLD L_λ [55]. It is worth noticing, however, that L_λ itself may not be the optimal observable to be measured, i.e., it may not be easy to implement in practice.

Since the FI is upper bounded by the QFI, we have a more precise bound on $\text{Var}(\hat{\lambda})$, the quantum Cramér-Rao inequality [61]

$$\text{Var}(\hat{\lambda}) \geq \frac{1}{M \mathcal{F}_q(\lambda)}. \quad (1.31)$$

The quantum version of the Cramér-Rao inequality provides the ultimate lower bound of the precision in estimating a parameter λ encoded in a quantum state: It does depend on the geometrical structure of the quantum statistical model and does not depend on the measurement. Notice that the quantum Cramér-Rao inequality is valid for *regular quantum statistical model*, i.e., families of quantum states made of density matrices with constant rank (i.e., the rank does not depend on the parameter) and leading to a non-singular QFI [77–79].

In conclusion, the QFI sets the minimum attainable error among the sets of all probing schemes in the estimation problem of λ , since

$$\text{Var}(\hat{\lambda}) \geq \frac{1}{M\mathcal{F}_c(\lambda)} \geq \frac{1}{M\mathcal{F}_q(\lambda)}. \quad (1.32)$$

1.2.2 Asymptotically efficient estimators

An estimator of a parameter λ is a mapping $\hat{\lambda} = \hat{\lambda}(x_1, x_2, \dots, x_M)$ from the set $\{x_k\}$ of measurement outcomes (M is the number of measurements) into the space of parameters Λ . As discussed in Sec. 1.2.1, for unbiased estimators the mean square error is equal to the variance $\text{Var}(\hat{\lambda})$ and the expectation value is the actual value of the parameter λ . The variance quantifies the precision of an estimator. In the present work we consider unbiased estimators. The variance has a classical lower bound (Cramér-Rao inequality) and a ultimate quantum lower bound (quantum Cramér-Rao inequality), summarized in Eq. (1.32).

Optimal estimators in classical estimation theory are those saturating the Cramér-Rao inequality, $\text{Var}(\hat{\lambda}) = (M\mathcal{F}_c(\lambda))^{-1}$. Optimal *quantum* measurements for the estimation of λ correspond to POVM with $\mathcal{F}_c(\lambda) = \mathcal{F}_q(\lambda)$. In quantum mechanics, probability distributions arise according to the Born rule $p(x|\lambda) = \text{tr}[\Pi_x \rho_\lambda]$, where $\{\Pi_x\}$ are the elements of a POVM, ρ_λ is the density operator parametrized by the quantity we want to estimate, and $p(x|\lambda)$ is the conditional probability of obtaining the value x when the parameter takes the value λ .

Let $\{x_k\}$, with $k = 1, \dots, M$, be an experimental set of outcomes of size M with probability distribution $p(x_k|\lambda) = \text{tr}[\Pi_{x_k} \rho_\lambda]$. An estimator is *asymptotically efficient* if it attains the Cramér-Rao bound asymptotically, $\text{Var}(\hat{\lambda}) = (M\mathcal{F}_c(\lambda))^{-1}$ for $M \rightarrow +\infty$. This is the case, e.g., of the Bayes estimator [80, 81] and the maximum likelihood estimator [82]. In the present thesis we assume to always use the Bayes estimator. The asymptotic limit (infinite number of measurements) is unfeasible. However, for the finite systems we will consider, the Cramér-Rao bound is approximately attained, $\text{Var}(\hat{\lambda}) \approx (M\mathcal{F}_c(\lambda))^{-1}$, performing a relatively low but sufficiently large number of measurements, $1 \ll M < +\infty$.

Bayes estimator The Bayes' theorem states that

$$p(x|\lambda)p(\lambda) = p(\lambda|x)p(x), \quad (1.33)$$

where $p(\cdot|\cdot)$ are the conditional probabilities, $p(\lambda)$ is the prior assuming no *a priori* information and $p(x)$ is the overall probability to observe the outcome x . Upon inverting the above equation, we obtain the conditional *a posteriori* probability $p(\lambda|x)$ of having λ given the outcome x . After M independent measurements the *a posteriori* probability is

$$p_M(\lambda|\{x_1, \dots, x_M\}) = \frac{1}{\mathcal{N}} \prod_{k=1}^M p(x_k|\lambda), \quad (1.34)$$

where \mathcal{N} is the normalization factor. The Bayes estimator is

$$\hat{\lambda}_B = \int d\lambda \lambda p_M(\lambda|\{x_1, \dots, x_M\}), \quad (1.35)$$

the mean of the posterior distribution.

Maximum likelihood estimator Purpose maximum likelihood estimation is to make inferences about the population that is most likely to have generated the sample $\{x_1, \dots, x_M\}$, in particular the joint probability distribution. Evaluating the joint probability distribution at the observed data sample $\{x_1, \dots, x_M\}$ we obtain the likelihood function

$$\mathcal{L}_M(\lambda) = \mathcal{L}_M(\lambda|\{x_1, \dots, x_M\}) = p_M(\{x_1, \dots, x_M\}|\lambda) \quad (1.36)$$

where

$$p_M(\{x_1, \dots, x_M\}|\lambda) = \prod_{k=1}^M p(x_k|\lambda) \quad (1.37)$$

for statistically independent individual observations, x_k 's, as in our case. Maximum likelihood estimation aims at finding the values of the model's parameter λ that maximize the likelihood function over the parameter space Λ , therefore

$$\hat{\lambda}_{ML} = \arg \max_{\lambda \in \Lambda} \mathcal{L}_M(\lambda), \quad (1.38)$$

where $\arg \max$, arguments of the maximum, returns the set of elements in Λ for which the function $\mathcal{L}_M(\lambda)$ attains the global maximum in Λ .

1.2.3 Geometry of quantum estimation

In situations where more than a parameter is involved, the family of quantum states ρ_λ depends on a set $\lambda = \{\lambda_\mu\}, \mu = 1, \dots, N$. In these cases the relevant object in the estimation problem is the so-called quantum Fisher information matrix, whose elements are denoted with $\mathcal{F}_{q,\mu\nu}$. From the geometrical point of view, the estimability of a set of parameters labeling the family of quantum states ρ_λ is naturally related to the distinguishability of the states within the quantum statistical model, i.e., with the notion of distance. On the manifold of quantum states, however, different distances may be defined and a question arises on which of them captures the notion of estimation measure. As it can be easily proved, the Bures distance D_B [83–90] is the proper quantity to be taken into account, and between two density matrices ρ and σ it is defined as

$$D_B^2(\rho, \sigma) = 2 \left[1 - \sqrt{F(\rho, \sigma)} \right], \quad (1.39)$$

where $F(\rho, \sigma) = (\text{tr} [\sqrt{\sqrt{\rho}\sigma\sqrt{\rho}}])^2$ is the fidelity.¹⁰ The Bures metric $g_{\mu\nu}$ is obtained upon considering the distance between two states obtained by an infinitesimal change in the value of the parameter

$$d_B^2 = D_B^2(\rho_\lambda, \rho_{\lambda+d\lambda}) = g_{\mu\nu} d\lambda_\mu d\lambda_\nu. \quad (1.40)$$

By explicitly evaluating the Bures distance we find [91]

$$g_{\mu\nu} = \frac{1}{4} \mathcal{F}_{q,\mu\nu}(\lambda). \quad (1.41)$$

The Bures metric is proportional to the QFI, which itself is symmetric, real, and positive semidefinite, i.e., it represents a metric for the manifold underlying the quantum statistical model. Indeed,

¹⁰The fidelity $F(\rho, \sigma)$ tells us how much similar the two quantum states are and it takes value in $[0,1]$. In particular it is 1 if ρ and σ coincide and it is 0 if they represent completely different states.

a large QFI for a given λ implies that the quantum states ρ_λ and $\rho_{\lambda+d\lambda}$ should be statistically distinguishable more effectively than the same pair of states for a value λ corresponding to smaller QFI. In other words, one confirms the intuitive picture in which optimal estimability (that is, a diverging QFI) corresponds to quantum states that are sent far apart upon infinitesimal variations of the parameters.

1.2.4 Quantum Fisher information for pure states

In the present work, we will consider pure states. Below, we specify the general discussion carried on so far for pure states, obtaining a very simple expression for the QFI. Pure states are represented by density matrices $\rho = |\psi\rangle\langle\psi|$ and $\sigma = |\phi\rangle\langle\phi|$, thus the fidelity is simply¹¹

$$F(\rho, \sigma) = |\langle\psi|\phi\rangle|^2. \quad (1.42)$$

Then, the Bures distance (1.39) is

$$D_B^2(\rho_\lambda, \rho_{\lambda+d\lambda}) = 2[1 - |\langle\psi_\lambda|\psi_{\lambda+d\lambda}\rangle|], \quad (1.43)$$

from which, by using Eq. (1.40), we get the following expression for the Bures metric

$$g_{\mu\nu} = \frac{2(1 - |\langle\psi_\lambda|\psi_{\lambda+d\lambda}\rangle|)}{d\lambda_\mu d\lambda_\nu}. \quad (1.44)$$

Therefore, from Eq. (1.41), the QFI matrix element is

$$\mathcal{F}_{q,\mu\nu}(\lambda) = 4g_{\mu\nu} = \frac{8(1 - |\langle\psi_\lambda|\psi_{\lambda+d\lambda}\rangle|)}{d\lambda_\mu d\lambda_\nu}, \quad (1.45)$$

but if we are interested in estimating a single parameter, as in the present work, the QFI is just

$$\mathcal{F}_q(\lambda) = \frac{8(1 - |\langle\psi_\lambda|\psi_{\lambda+d\lambda}\rangle|)}{(d\lambda)^2}. \quad (1.46)$$

We can also prove the above result, Eq. (1.46), from nongeometric point view as follows.

Proof. The density operator of the state $\rho_\lambda = |\psi_\lambda\rangle\langle\psi_\lambda|$ is idempotent, $\rho_\lambda^2 = \rho_\lambda$, so if we take a derivative with respect to λ , then

$$(\partial_\lambda \rho_\lambda) \rho_\lambda + \rho_\lambda (\partial_\lambda \rho_\lambda) = \partial_\lambda \rho_\lambda. \quad (1.47)$$

Comparing Eq. (1.47) to the SLD L_λ in Eq. (1.30), we obtain

$$L_\lambda = 2\partial_\lambda \rho_\lambda = 2(|\psi_\lambda\rangle\langle\partial_\lambda \psi_\lambda| + |\partial_\lambda \psi_\lambda\rangle\langle\psi_\lambda|), \quad (1.48)$$

where we assume the Leibniz's rule holds for $\rho_\lambda = |\psi_\lambda\rangle\langle\psi_\lambda|$. We have already seen that the QFI is defined as $\mathcal{F}_q(\lambda) = \text{Tr} [\rho_\lambda L_\lambda^2]$. For sake of simplicity, since we are interested in a single parameter

¹¹*Proof.* The density matrix is idempotent, $\rho^2 = \rho$, thus $\rho = \sqrt{\rho}$ and so

$$\begin{aligned} F(\rho, \sigma) &= \left(\text{tr} \left[\sqrt{\sqrt{\rho}\sigma\sqrt{\rho}} \right] \right)^2 = \left(\text{tr} [\sqrt{\rho\sigma\rho}] \right)^2 = \left(\text{tr} \left[\sqrt{|\psi\rangle\langle\psi|\sigma|\psi\rangle\langle\psi|} \right] \right)^2 \\ &= \left(\text{tr} \left[\sqrt{\langle\psi|\sigma|\psi\rangle\sqrt{\rho}} \right] \right)^2 = \langle\psi|\sigma|\psi\rangle (\text{tr} [\rho])^2 = |\langle\psi|\phi\rangle|^2, \end{aligned}$$

since $\text{tr} [\rho] = 1$ and $\langle\psi|\sigma|\psi\rangle$ is a multiplicative constant. \square

λ , we omit such label in states and derivatives, which we assume to take always with respect to λ . So we have to compute

$$L_\lambda^2 = 4(|\psi\rangle\langle\partial\psi|\partial\psi\rangle\langle\psi| + |\partial\psi\rangle\langle\psi|\partial\psi\rangle\langle\psi| + |\psi\rangle\langle\partial\psi|\psi\rangle\langle\partial\psi| + |\partial\psi\rangle\langle\partial\psi|) , \quad (1.49)$$

since $\langle\psi|\psi\rangle = 1$, but $\langle\partial\psi|\partial\psi\rangle \neq 1$ in general, from which¹²

$$\mathcal{F}_q(\lambda) = 4(\langle\partial\psi|\partial\psi\rangle + \langle\psi|\partial\psi\rangle^2 + \langle\partial\psi|\psi\rangle^2 + |\langle\partial\psi|\psi\rangle|^2) . \quad (1.50)$$

Because of normalization,

$$\partial\langle\psi|\psi\rangle = 0 = \langle\partial\psi|\psi\rangle + \langle\psi|\partial\psi\rangle = z + z^* , \quad (1.51)$$

after introducing $z := \langle\partial\psi|\psi\rangle \in \mathbb{C}$. Such equality holds iff z is purely imaginary. Hence, since $z^2 + (z^*)^2 + |z|^2 = -|z|^2$, the QFI for pure states reduces to

$$\mathcal{F}_q(\lambda) = 4(\langle\partial\psi|\partial\psi\rangle - |\langle\partial\psi|\psi\rangle|^2) . \quad (1.52)$$

Now we consider how an infinitesimal variation of the parameter λ affects the state $|\psi_\lambda\rangle$. We expand $|\psi_{\lambda+d\lambda}\rangle$ about $|\psi_\lambda\rangle$ up to the second order

$$|\psi_{\lambda+d\lambda}\rangle = |\psi_\lambda\rangle + |\partial\psi\rangle d\lambda + \frac{1}{2}|\partial^2\psi\rangle d\lambda^2 + O(d\lambda^3) , \quad (1.53)$$

and we project it onto the original state

$$\begin{aligned} \langle\psi_\lambda|\psi_{\lambda+d\lambda}\rangle &= 1 + \langle\psi|\partial\psi\rangle d\lambda + \frac{1}{2}\langle\psi|\partial^2\psi\rangle d\lambda^2 + O(d\lambda^3) \\ &= 1 + z^* d\lambda + \frac{1}{2}w^* d\lambda^2 + O(d\lambda^3) , \end{aligned} \quad (1.54)$$

where $w^* := \langle\psi|\partial^2\psi\rangle \in \mathbb{C}$. Then

$$\begin{aligned} |\langle\psi_\lambda|\psi_{\lambda+d\lambda}\rangle|^2 &= \left(1 + z^* d\lambda + \frac{1}{2}w^* d\lambda^2 + O(d\lambda^3)\right) \left(1 + z d\lambda + \frac{1}{2}w d\lambda^2 + O(d\lambda^3)\right) \\ &= 1 + (z + z^*) d\lambda + \left[|z|^2 + \frac{1}{2}(w + w^*)\right] d\lambda^2 + O(d\lambda^3) \\ &= 1 + \left[|z|^2 + \frac{1}{2}(w + w^*)\right] d\lambda^2 + O(d\lambda^3) , \end{aligned} \quad (1.55)$$

where the last equality holds because of Eq. (1.51). Again, from Eq. (1.51), if we take a further derivative, then we get

$$\partial^2\langle\psi|\psi\rangle = 2\langle\partial\psi|\partial\psi\rangle + \langle\partial^2\psi|\psi\rangle + \langle\psi|\partial^2\psi\rangle = 0 , \quad (1.56)$$

from which

$$\langle\partial\psi|\partial\psi\rangle = -\frac{1}{2}(\langle\partial^2\psi|\psi\rangle + \langle\psi|\partial^2\psi\rangle) = -\frac{1}{2}(w + w^*) . \quad (1.57)$$

¹²If we assume an orthonormal basis set $\{|\alpha\rangle\}$, $\sum_\alpha |\alpha\rangle\langle\alpha| = \mathbb{I}$, then

$$\text{Tr}[\rho_\lambda L_\lambda^2] = \sum_\alpha \langle\alpha|\psi\rangle\langle\psi|L_\lambda^2|\alpha\rangle = \sum_\alpha \langle\psi|L_\lambda^2|\alpha\rangle\langle\alpha|\psi\rangle = \langle\psi|L_\lambda^2|\psi\rangle ,$$

from which Eq. (1.50) follows.

In the light of this result and the definition of z and w , we can rewrite Eq. (1.55) as

$$|\langle \psi_\lambda | \psi_{\lambda+d\lambda} \rangle|^2 \approx 1 + (|\langle \partial\psi | \psi \rangle|^2 - \langle \partial\psi | \partial\psi \rangle) d\lambda^2. \quad (1.58)$$

If we consider the square root of this quantity, then we get

$$\begin{aligned} |\langle \psi_\lambda | \psi_{\lambda+d\lambda} \rangle| &= \sqrt{1 + (|\langle \partial\psi | \psi \rangle|^2 - \langle \partial\psi | \partial\psi \rangle) d\lambda^2} \\ &\approx 1 + \frac{1}{2} (|\langle \partial\psi | \psi \rangle|^2 - \langle \partial\psi | \partial\psi \rangle) d\lambda^2 \\ &= 1 - \frac{1}{8} \mathcal{F}_q(\lambda) d\lambda^2, \end{aligned} \quad (1.59)$$

because of Eq. (1.52) and since $\sqrt{1+x} \approx 1 + \frac{1}{2}x$ for $x \ll 1$, from which

$$\mathcal{F}_q(\lambda) = \frac{8(1 - |\langle \psi_\lambda | \psi_{\lambda+d\lambda} \rangle|)}{d\lambda^2}. \quad (1.60)$$

□

Part II

Allegro non troppo.
Perturbed dynamics

Chapter 2

Continuous-time quantum walks in the presence of a quadratic perturbation

In this chapter we address the properties of continuous-time quantum walks with Hamiltonians of the form $\mathcal{H} = L + \lambda L^2$, with L the Laplacian matrix of the underlying graph and the perturbation λL^2 motivated by its potential use to introduce next-nearest-neighbor hopping. We consider cycle, complete, and star graphs as paradigmatic models with low/high connectivity and/or symmetry. First, we investigate the dynamics of an initially localized walker. Then, we devote attention to estimating the perturbation parameter λ using only a snapshot of the walker dynamics. Our analysis shows that a walker on a cycle graph spreads ballistically independently of the perturbation, whereas on complete and star graphs one observes perturbation-dependent revivals and strong localization phenomena. Concerning the estimation of the perturbation, we determine the walker preparations and the simple graphs that maximize the quantum Fisher information. We also assess the performance of position measurement, which turns out to be optimal, or nearly optimal, in several situations of interest. Besides fundamental interest, our study may find applications in designing enhanced algorithms on graphs.

2.1 Introduction

In a CTQW the graph Laplacian L plays the role of the free particle Hamiltonian, i.e., it corresponds to the kinetic energy of the particle. Perturbations to ideal CTQW have been investigated earlier [29, 33, 92–98], however with the main focus being on the decoherence effects of stochastic noise, rather than the quantum effects induced by a perturbing Hamiltonian. A notable exception exists, though, given by the quantum spatial search, where the perturbation induced by the so-called oracle Hamiltonian has been largely investigated as a tool to induce localization on a desired site [31, 99–103].

In the present chapter, we investigate the dynamics of an initially localized quantum walker propagating on cycle, complete, and star graphs (see Fig. 2.1) under perturbed Hamiltonians of the form $\mathcal{H} = L + \lambda L^2$. Characterizing these Hamiltonians amounts to determining the value of the coupling parameter λ , which quantifies the effects of the quadratic term. For this purpose, we investigate whether and to what extent a snapshot of the walker dynamics at a given time suffices to estimate the value of λ .

Besides the fundamental interest, there are a few reasons to address these particular systems. The topologies of these graphs describe paradigmatic situations with low (cycle and star) or

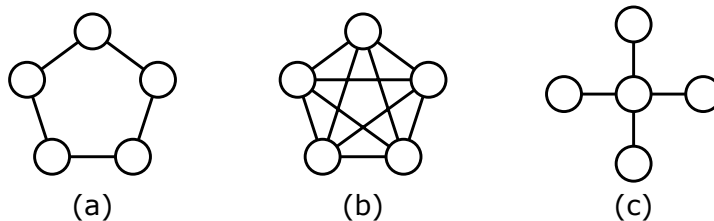


Figure 2.1. The three types of graphs considered in the present work: (a) cycle, (b) complete, and (c) star graphs. Examples are for $N = 5$ vertices.

high (complete) connectivity, as well as low (star) and high (cycle and complete) symmetry. At the same time, CTQW Hamiltonians with quadratic perturbation of the form λL^2 are of interest, e.g., because they represent a physically motivated and convenient way to introduce next-nearest-neighbor hopping in one-dimensional lattices, or intrinsic spin-orbit coupling in two-dimensional lattices. Moreover, considering such perturbations is the first step towards the description of dephasing and decoherence processes, which result from making the parameter λ a stochastic process.

To analyze both semiclassical and genuinely quantum features of the dynamics, we employ a set of different quantifiers, including site distribution, mixing, inverse participation ratio, and coherence. In this framework, mixing has been studied for CTQWs on some circulant graphs [104], e.g., the cycle and the complete graph, and also employed together with the temporal standard deviation to study the dynamics of CTQWs on the cycle graph [105]. Moreover, a spectral method has been introduced to investigate CTQWs on graphs [106, 107]. Coherent transport has been analytically analyzed for CTQWs on star graphs [108], showing the occurrence of perfect revivals and strong localization on the initial node.

2.2 Dynamics

Given a graph $G = (V, E)$, with $|V| = N$ vertices, which we index from 0 to $N - 1$, with Laplacian matrix $L = D - A$, the kinetic energy term ($\hbar = 1$) $T = -\nabla^2/2m$ of a particle on the graph is replaced by $T = \gamma L$. The hopping amplitude $\gamma \in \mathbb{R}^+$ plays the role of a time-scaling factor, thus the time dependence of the results is significant when expressed in terms of the dimensionless time γt . In the following we set $\gamma = \hbar = 1$, and, as a consequence, hereafter time and energy will be dimensionless.

We focus on the dynamics of a walker whose initial state $|\psi(0)\rangle$ is a vertex of the graph, i.e., the walker is initially localized. We consider the Hamiltonian

$$\mathcal{H} = \mathcal{H}_0 + \lambda \mathcal{H}_1 = L + \lambda L^2, \quad (2.1)$$

where λ is a dimensionless perturbation parameter. Because of this choice, the eigenproblem of \mathcal{H} is basically the eigenproblem of L . The Laplacian eigenvalue $\varepsilon = 0$ is common to all simple graphs, it is not degenerate for connected graphs, like cycle, complete, and star graph, and the corresponding eigenvector is $(1, \dots, 1)/\sqrt{N}$. The time evolution of the system is coherent and ruled by the unitary time-evolution operator

$$\mathcal{U}_\lambda(t) = e^{-i\mathcal{H}t} = \sum_{n=0}^{N-1} e^{-i(\varepsilon_n + \lambda \varepsilon_n^2)t} |e_n\rangle \langle e_n|, \quad (2.2)$$

where the second equality follows from the spectral decomposition of L . To study the dynamics of the walker, we consider the following quantities, which basically arise from the density matrix $\rho(t) = |\psi(t)\rangle\langle\psi(t)|$.

The (*instantaneous*) probability of finding the walker in the vertex k at time t is

$$P(k, t|\lambda) = |\langle k|\mathcal{U}_\lambda(t)|\psi(0)\rangle|^2, \quad (2.3)$$

whereas the *average* probability is

$$\bar{P}(k|\lambda) = \lim_{T \rightarrow +\infty} \frac{1}{T} \int_0^T P(k, t|\lambda) dt. \quad (2.4)$$

There are two main notions of mixing in quantum walks [3, 104, 109]. A graph has the *instantaneous exactly uniform mixing* property if there are times when the probability distribution $P(t)$ of the walker is exactly uniform; it has the *average uniform mixing* property if the average probability distribution \bar{P} is uniform.

In addition, we consider the inverse participation ratio (IPR) [95, 110, 111]

$$\mathcal{I}(t) = \sum_{k=0}^{N-1} \langle k|\rho(t)|k\rangle^2 = \sum_{k=0}^{N-1} P^2(k, t|\lambda), \quad (2.5)$$

which allows us to assess the amount of localization in position space of the walker. Indeed, the IPR is bounded from below by $1/N$ (complete delocalization) and from above by 1 (localization on a single vertex). In this sense, the IPR is an alternative quantity to study the instantaneous exactly uniform mixing. The inverse of the IPR indicates the number of vertices over which the walker is distributed [112].

Finally, to further analyze the quantum features of the dynamics, we consider the quantum coherence. A proper measure is provided by the l_1 norm of coherence [113]

$$\mathcal{C}(t) = \sum_{\substack{j,k=0, \\ j \neq k}}^{N-1} |\rho_{j,k}(t)| = \sum_{j,k=0}^{N-1} |\rho_{j,k}(t)| - 1. \quad (2.6)$$

Refer to Appendix 2.A for details about the analytical derivation of the results shown in the following.

2.2.1 Cycle graph

In the cycle graph each vertex is adjacent to two other vertices, so its degree is 2. Hence, the graph Laplacian is

$$L = 2I - \sum_{k=0}^{N-1}' (|k-1\rangle\langle k| + |k+1\rangle\langle k|). \quad (2.7)$$

The primed summation symbol means that we look at the cycle graph as a path graph provided with periodic boundary conditions, thus the terms $|-1\rangle\langle 0|$ and $|N\rangle\langle N-1|$ are $|N-1\rangle\langle 0|$ and $|0\rangle\langle N-1|$, respectively. The matrix representation of this Laplacian is symmetric and circulant (a special case of Toeplitz matrix), and the related eigenproblem is analytically solved in Ref. [114] and reported in Table 2.1.

The ground state ($n = 0$) is unique and equal to

$$\varepsilon_{min} = 0, \quad (2.8)$$

$$|e_{min}\rangle = \frac{1}{\sqrt{N}} \sum_{k=0}^{N-1} |k\rangle. \quad (2.9)$$

$ e_n\rangle$	ε_n	μ_n
$ e_n\rangle = \frac{1}{\sqrt{N}} \sum_{k=0}^{N-1} e^{-i\frac{2\pi n}{N}k} k\rangle$	$2 \left[1 - \cos\left(\frac{2\pi n}{N}\right)\right]$	*
with $n = 0, \dots, N-1$		

Table 2.1. Eigenvectors $|e_n\rangle$ and eigenvalues ε_n of the graph Laplacian in the cycle graph. The asterisk denotes that the multiplicity of the eigenvalues depends on the parity of N . In particular, the ground state $n = 0$ is always unique, whereas the highest energy level is unique for even N and doubly degenerate for odd N . Independently of the parity of N , the remaining eigenvalues have multiplicity 2, since $\varepsilon_n = \varepsilon_{N-n}$.

Instead, the highest-energy level depends on the parity of N and is unique for even N ($n = N/2$),

$$\varepsilon_{max} = 4, \quad (2.10)$$

$$|e_{max}\rangle = \frac{1}{\sqrt{N}} \sum_{k=0}^{N-1} (-1)^k |k\rangle, \quad (2.11)$$

and has degeneracy 2 for odd N ($n = (N \pm 1)/2$),

$$\varepsilon_{max} = 2 \left[1 + \cos\left(\frac{\pi}{N}\right)\right], \quad (2.12)$$

$$|e_{max}\rangle = \frac{1}{\sqrt{N}} \sum_{k=0}^{N-1} (-1)^k e^{\pm i(\pi/N)k} |k\rangle, \quad (2.13)$$

where the phase factors are all either with the plus sign or with the minus sign.

Since for odd N the highest energy level is doubly degenerate, we may be interested in finding the corresponding orthonormal eigenstates having real components.¹ Therefore, we define the following states by linearly combining the two eigenstates in Eq. (2.13) in one case with the plus sign and with the minus sign in the other,² respectively:

$$|e_{max}^+\rangle = \sqrt{\frac{2}{N}} \sum_{k=0}^{N-1} (-1)^k \cos\left(\frac{\pi}{N}k\right) |k\rangle, \quad (2.14)$$

$$|e_{max}^-\rangle = \sqrt{\frac{2}{N}} \sum_{k=0}^{N-1} (-1)^k \sin\left(\frac{\pi}{N}k\right) |k\rangle. \quad (2.15)$$

The perturbation involves

$$L^2 = 6I + \sum_{k=0}^{N-1} (|k-2\rangle\langle k| - 4|k-1\rangle\langle k| + \text{H.c.}), \quad (2.16)$$

¹The further reason is that some numerical routines solving the eigenproblem for real symmetric matrices may return orthonormal eigenvectors with real components.

²The linear combination leading to Eq. (2.15) introduces also an imaginary unit. However, this is a global phase factor, and, as such, we neglect it.

where the Hermitian conjugate of $|k - n\rangle\langle k|$ is a hopping term of $+n$ vertices, and as such should be $|k + n\rangle\langle k|$. Hence, the perturbed Hamiltonian (2.1) reads as follows:

$$\mathcal{H} = (2 + 6\lambda)I + \sum_{k=0}^{N-1} [\lambda |k - 2\rangle\langle k| - (1 + 4\lambda) |k - 1\rangle\langle k| + \text{H.c.}] . \quad (2.17)$$

The perturbation λL^2 thus introduces the next-nearest-neighbor hopping and affects the nearest-neighbor one and also the on-site energies proportional to I .

In a cycle graph all the vertices are equivalent, so an initially localized walker will show the same time evolution independently of the starting vertex chosen. We denote the initial state by $|j\rangle$. The probability of finding the walker in the vertex k at time t for a given value of λ is (Fig. 2.2)

$$P_j(k, t|\lambda) = \frac{1}{N} + \frac{2}{N^2} \sum_{\substack{n=0, \\ m>n}}^{N-1} \cos \left[(E_n^\lambda - E_m^\lambda)t - \frac{2\pi}{N}(n - m)(j - k) \right] , \quad (2.18)$$

which is symmetric with respect to the starting vertex j , i.e., $P_j(j + k, t|\lambda) = P_j(j - k, t|\lambda)$ (proof in Appendix 2.A.1). The average probability distribution is the same as the one reported in [105], which is basically our unperturbed CTQW.³

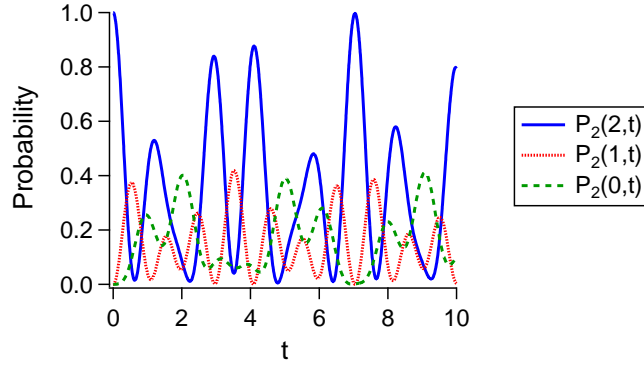


Figure 2.2. Probability distribution $P_j(k, t|\lambda)$ of the walker as a function of time in the cycle graph. The walker is initially localized in the vertex $|j = 2\rangle$. The probability distribution is symmetric with respect to the starting vertex, i.e., $P_j(j + k, t|\lambda) = P_j(j - k, t|\lambda)$. Numerical results suggest that revivals in the starting vertex are most likely not exact. Indeed, to be exact, the periods of the cosine functions entering the definition of the probability (2.18) have to be commensurable and such periods strongly depend on the choice of N and λ . Results are for $N = 5$ and $\lambda = 0.2$.

The solution of the time-dependent Schrödinger equation of the unperturbed system ($\lambda = 0$) can be expressed in terms of Bessel functions [104]. This allows us to analytically prove the ballistic spreading in a one-dimensional infinite lattice [115], i.e., that the variance of the position is $\sigma^2(t) = \langle \hat{x}(t)^2 \rangle - \langle \hat{x}(t) \rangle^2 \propto t^2$. We expect the same ballistic spreading to characterize the CTQW on a finite cycle at short times, i.e., as long as the walker does not feel the topology of the cycle graph.

³The CTQW Hamiltonian in [105] is $\mathcal{H} = A/d$, instead of being the Laplacian. In regular graphs d , the degree of the vertex, is the same for all the vertices. The diagonal degree matrix D is thus proportional to the identity, and this introduces an irrelevant phase factor in the time evolution of the quantum state. The timescale of the evolutions under the Hamiltonians A and A/d is clearly different, but the resulting time-averaged probability distribution is the same.

We can find a simple expression describing the variance of the position for $\lambda \neq 0$ at short times. The variance is meaningful if we consider sufficiently large N , and the assumption $t \ll 1$ ensures that the wave function does not reach the vertices $|0\rangle$ and $|N-1\rangle$. Indeed, the position on the graph is the corresponding vertex, but the topology of the cycle graph allows the walker to jump from $|0\rangle$ to $|N-1\rangle$ and vice versa. This in turn affects the computation of the variance. To ensure the maximum distance from the extreme vertices, we consider a walker initially localized in the central vertex. We assume even N , so the starting vertex is $|j = N/2\rangle$. Under these assumptions, we have that

$$\sigma^2(t) \approx \left[40(\lambda - \lambda_0)^2 + \frac{2}{5} \right] t^2, \quad (2.19)$$

with $\lambda_0 = -1/5$ (see Appendix 2.A.1). The spreading of the walker is ballistic in spite of the perturbation. Nevertheless, increasing $|\lambda - \lambda_0|$ makes the walker spread faster by affecting the factor in front of t^2 . Indeed, such a factor is related to the square of the parameter characterizing the speed of the walker [115]. The lowest variance is for $\lambda = \lambda_0$, which is the value for which the nearest-neighbor hopping $-(1 + 4\lambda)$ equals the next-nearest-neighbor one λ (see Eq. (2.17)). Numerical simulations of the CTQW provide evidence that the same behavior in Eq. (2.19) characterizes also the CTQW on the cycle with odd N or when the starting vertex is not the central one, again assuming that the wave function does not reach the extreme vertices.

For completeness, we report in Fig. 2.3 the numerical results for the probability distribution (2.18) at a given time and at varying λ . The pattern of the probability distribution is not symmetric with respect to λ_0 . Nevertheless, at short times the resulting variance of the position (2.19) turns out to be symmetric with respect to λ_0 .

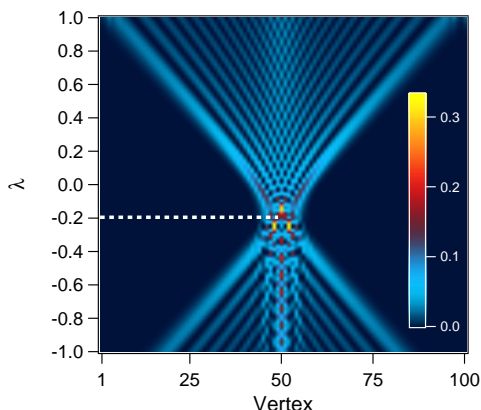


Figure 2.3. Map of the probability distribution (2.18) as a function of the position (vertex) and λ at $t = 4$. The walker is initially localized in the center of the cycle graph ($N = 100$). The horizontal dashed white line highlights $\lambda_0 = -1/5$, the value at which the variance of the position is minimum. For clarity, here vertices are indexed from 1 to N .

Next we numerically evaluate the IPR (2.5) for the probability distribution in Eq. (2.18); the results are shown in Fig. 2.4. As expected from the previous results about the probability distribution (see also Fig. 2.2), the IPR does not show a clear periodicity, it strongly fluctuates, and there are instants of time when it gets closer to 1, meaning that the walker is more localized. The numerical results also suggest that the instantaneous exactly uniform mixing is achievable for $N \leq 4$, while there is no exact delocalization for $N > 4$, as already conjectured [104]. However, for large N the probability distribution (2.18) approaches the uniform one, and so the IPR approaches $1/N$.

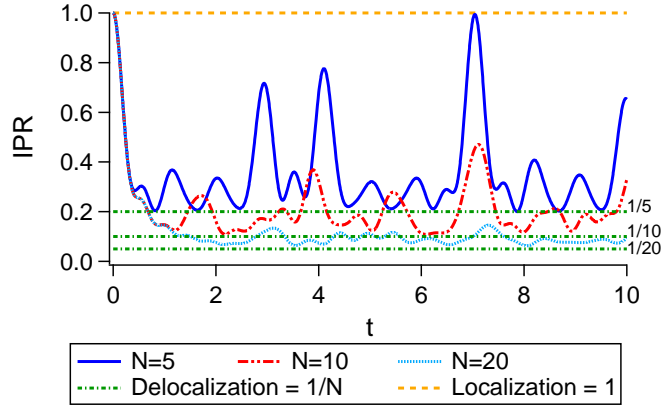


Figure 2.4. Inverse participation ratio for a walker initially localized in the cycle graph. Numerical results suggest that for $t > 0$ the IPR reaches neither the lower bound $1/N$ (green dashdotted line), i.e., the delocalization, nor the upper bound 1 (orange dashed line), i.e., the localization. Whether or not the (de)localization is achievable is most likely related to the choice of N and λ . This choice, in turn, might result in the commensurability or incommensurability of the periods of the cosine functions entering the definition of the probability (2.18). For large N the IPR approaches $1/N$, since the probability distribution approaches the uniform one. Results are for $\lambda = 0.2$.

Finally, we focus on the time dependence of the coherence (2.6) for an initially localized walker. The exact numerical results are shown in Fig. 2.5. Under the assumption $t \ll 1$, we can find a simple expression. We Taylor expand the time-evolution operator up to the first order, so the density matrix is approximated as $\rho(t) = \rho(0) - it [\mathcal{H}, \rho(0)] + O(t^2)$. Then, with the Hamiltonian (2.17), the behavior characterizing the earlier steps of the time evolution of the coherence is

$$\mathcal{C}(t, \lambda) \approx 4(|\lambda| + |1 + 4\lambda|)t, \quad (2.20)$$

consistently with the results shown in Fig. 2.5. Hence, at short times the coherence is minimum for $\lambda = -1/4$. For such a value the nearest-neighbor hopping $-(1 + 4\lambda)$ is null, while the next-nearest-neighbor hopping λ is nonzero (see Eq. (2.17)).

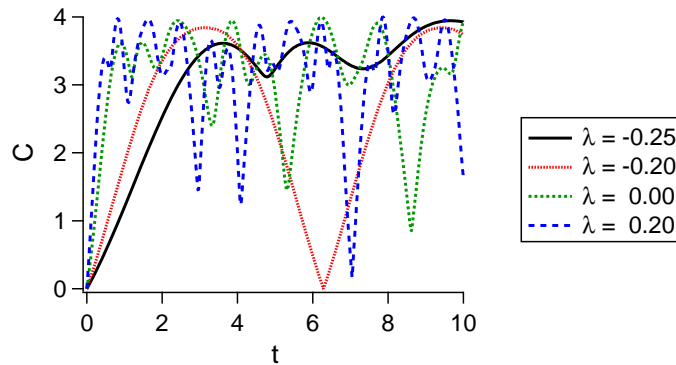


Figure 2.5. Coherence for a walker initially localized in the cycle graph with $N = 5$. For $t \ll 1$ the minimum is for $\lambda = -1/4$, as expected from the linear approximation in Eq. (2.20).

2.2.2 Complete graph

In the complete graph each vertex is adjacent to all the others, so its degree is $N - 1$. Hence, the graph Laplacian is

$$L = (N - 1)I - \sum_{\substack{j,k=0, \\ j \neq k}}^{N-1} |j\rangle\langle k|, \quad (2.21)$$

and has the property

$$L^n = N^{n-1}L. \quad (2.22)$$

The eigenproblem related to Eq. (2.21) is solved in Table 2.2. The graph Laplacian has two energy levels: the level $\varepsilon_0 = 0$, having eigenstate $|e_0\rangle$, and the $(N - 1)$ -degenerate level $\varepsilon_1 = N$, having orthonormal eigenstates $|e_1^l\rangle$, with $l = 1, \dots, N - 1$.

n	$ e_n\rangle$	ε_n	μ_n
0	$ e_0\rangle = \frac{1}{\sqrt{N}} \sum_{k=0}^{N-1} k\rangle$	0	1
1	$ e_1^l\rangle = \frac{1}{\sqrt{l(l+1)}} \left(\sum_{k=0}^{l-1} k\rangle - l l\rangle \right)$ with $l = 1, \dots, N - 1$	N	$N - 1$

Table 2.2. Eigenvectors $|e_n\rangle$ and eigenvalues ε_n with multiplicity μ_n of the graph Laplacian in the complete graph.

The perturbed Hamiltonian is therefore

$$\mathcal{H} = (1 + N\lambda)L, \quad (2.23)$$

i.e., it is basically the CTQW Hamiltonian of the complete graph multiplied by a constant which linearly depends on λ . We observe that the value $\lambda^* = -1/N$ makes the Hamiltonian null and so it makes this case trivial. The perturbation affects the energy scale of the unperturbed system and thus its timescale. Therefore, we can directly compare the next results with the well-known ones concerning the unperturbed system [104].

The time-evolution operator (2.2) is

$$e^{-i\mathcal{H}t} = I + \frac{1}{N} \left[e^{-i2\omega_N(\lambda)t} - 1 \right] L, \quad (2.24)$$

where we have Taylor expanded the exponential, used Eq. (2.22), and defined the angular frequency

$$\omega_N(\lambda) = \frac{N}{2}(1 + \lambda N), \quad (2.25)$$

which depends on λ . For large N , the time evolution basically results in adding a phase to the initial state, since $\lim_{N \rightarrow +\infty} \mathcal{U}_\lambda(t) = \exp[-i2\omega_N(\lambda)t] I$.

In a complete graph all the vertices are equivalent, so an initially localized walker will show the same time evolution independently of the starting vertex chosen. We denote the initial state by $|0\rangle$. The probabilities of finding the walker in $|0\rangle$ or elsewhere, $|1 \leq i \leq N - 1\rangle$, at time t for a

given value of λ are periodic (Fig. 2.6),

$$P_0(0, t|\lambda) = 1 - \frac{4(N-1)}{N^2} \sin^2(\omega_N(\lambda)t), \quad (2.26)$$

$$P_0(i, t|\lambda) = \frac{4}{N^2} \sin^2(\omega_N(\lambda)t). \quad (2.27)$$

Hence, the walker returns periodically to the starting vertex and can be found in it with certainty. This occurs for $t_k = 2k\pi/(N + \lambda N^2)$, with $k \in \mathbb{N}$. Increasing the order of the graph makes the angular frequency higher, and $\lim_{N \rightarrow +\infty} P_0(0, t|\lambda) = 1$, while $\lim_{N \rightarrow +\infty} P_0(i, t|\lambda) = 0$. The perturbation only affects the periodicity of the probabilities. The probability distribution is symmetric with respect to λ^* , since $\omega_N(\lambda^* \pm \lambda) = \pm \lambda N^2/2$ and $\sin^2(\lambda N^2/2) = \sin^2(-\lambda N^2/2)$. As expected, for λ^* the walker remains in the starting vertex all the time, since $\omega_N(\lambda^*) = 0$ and so $P_0(0, t|\lambda^*) = 1 \forall t$. The average probability distribution is the same as the one reported in [104], which is basically our unperturbed CTQW.⁴

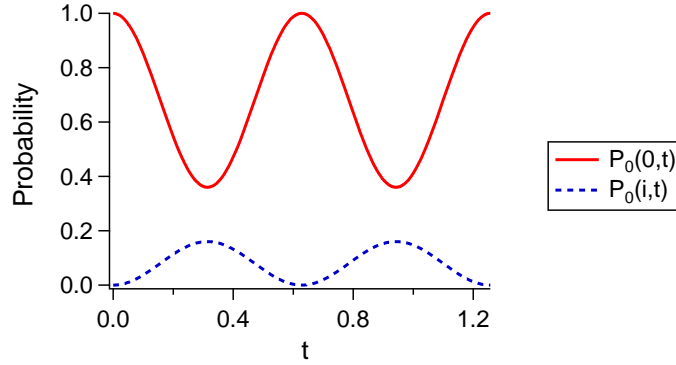


Figure 2.6. Probability of finding the walker in the starting vertex $P_0(0, t|\lambda)$ (red solid line) or in any other vertex $P_0(i, t|\lambda)$ (blue dashed line) as a function of time in the complete graph. The walker is initially localized at the vertex $|0\rangle$. Results are for $N = 5$ and $\lambda = 0.2$.

Next the IPR (2.5) for the probability distribution in Eqs. (2.26) and (2.27) reads

$$\mathcal{I}(t) = 1 - \frac{8(N-1)}{N^2} \sin^2(\omega_N(\lambda)t) + \frac{16(N-1)}{N^3} \sin^4(\omega_N(\lambda)t). \quad (2.28)$$

The IPR has the same properties of the probability distribution: it is periodic, reaches the upper bound 1 (localization of the walker) for t_k such that $P_0(0, t_k|\lambda) = 1$, and $\lim_{N \rightarrow +\infty} \mathcal{I} = 1$, since for large N the walker tends to be localized in the starting vertex (Fig. 2.7). The lower bound $\mathcal{I}_m := \min_t \mathcal{I}$ actually depends on N :

$$\mathcal{I}_m = \mathcal{I}(t_l) = \begin{cases} \frac{1}{N} & \text{for } N \leq 4, \\ 1 - \frac{8}{N} + \frac{24}{N^2} - \frac{16}{N^3} & \text{for } N > 4, \end{cases} \quad (2.29)$$

⁴The CTQW Hamiltonian in [104] is $\mathcal{H} = A/d$. See also footnote 3.

where

$$t_l = \begin{cases} \frac{2[\pm \arcsin(\sqrt{N}/2) + \pi l]}{N + \lambda N^2} & \text{for } N \leq 4, \\ \frac{2\pi(1/2 + l)}{N + \lambda N^2} & \text{for } N > 4, \end{cases} \quad (2.30)$$

with $l \in \mathbb{N}$. Please notice that the two definitions of \mathcal{I}_m match in $N = 4$. For $N \leq 4$ there are instants of time when the walker is delocalized ($\mathcal{I}_m = 1/N$) and there is instantaneous exactly uniform mixing. Instead, for $N > 4$ the walker is never delocalized, since $\mathcal{I}_m > 1/N$.

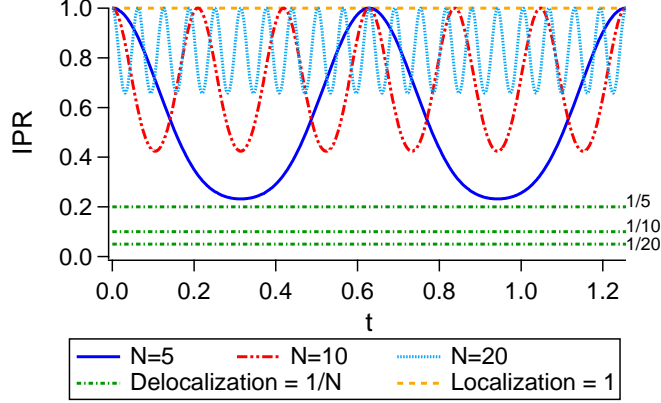


Figure 2.7. Inverse participation ratio for a walker initially localized in the complete graph. The IPR periodically reaches the upper bound 1 (orange dashed line), i.e., the localization, but for $N > 4$ does not reach the value $1/N$ (green dashdotted line), i.e., the delocalization. The lower bound of the IPR is defined in Eq. (2.29). For $N \rightarrow +\infty$ the IPR approaches 1, since the probability of finding the walker at the starting vertex approaches 1 (see Eqs. (2.26) and (2.27)). Results are for $\lambda = 0.2$.

Finally, we focus on the time dependence of the coherence, which we derive in Appendix 2.A.2 and show in Fig. 2.8. The modulus of the off-diagonal elements of the density matrix can be expressed in terms of the square root of probabilities (see Appendix 2.A); thus the coherence is periodic and it is symmetric with respect to λ^* , as well as the probability distribution. As expected, the dependence on the perturbation is encoded only in the angular frequency $\omega_n(\lambda)$, and the coherence is identically null, thus minimum, for λ^* . For $\lambda \neq \lambda^*$, the coherence periodically reaches the extrema

$$\max C = \frac{8(N-1)(N-2)}{N^2} \quad \text{for } t_k = \frac{(2k+1)\pi}{N + \lambda N^2}, \quad (2.31)$$

$$\min C = 0 \quad \text{for } t_k = \frac{2k\pi}{N + \lambda N^2}, \quad (2.32)$$

with $k \in \mathbb{N}$ and assuming $N \geq 2$.

2.2.3 Star graph

In the star graph, the central vertex is adjacent to all the others, so its degree is $N - 1$. On the other hand, the other vertices are only connected to the central one, so their degree is 1. Hence, the graph Laplacian is

$$L = I + (N-2)|0\rangle\langle 0| - \sum_{k=1}^{N-1} (|k\rangle\langle 0| + |0\rangle\langle k|), \quad (2.33)$$

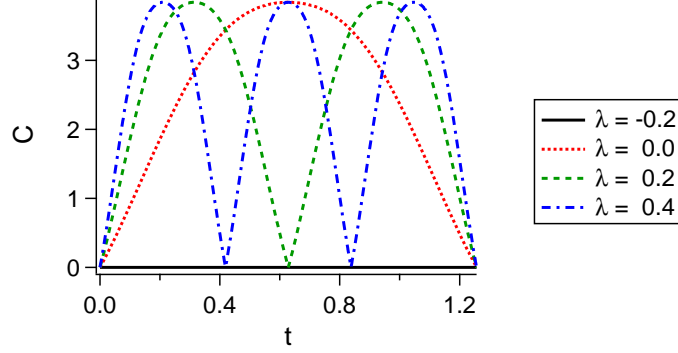


Figure 2.8. Coherence for a walker initially localized in the complete graph with $N = 5$. The coherence is null, thus minimum, for $\lambda^* = -1/N$ and it is symmetric with respect to λ^* , so only the data for $\lambda \geq \lambda^*$ are shown.

where $|0\rangle$ denotes the central vertex.

The eigenproblem related to Eq. (2.33) is solved in Table 2.3. The graph Laplacian has three energy levels: the level $\varepsilon_0 = 0$, having eigenstate $|e_0\rangle$; the $(N - 2)$ -degenerate level $\varepsilon_1 = 1$, having orthonormal eigenstates $|e_1^l\rangle$, with $l = 1, \dots, N - 2$; and the level $\varepsilon_2 = N$, having eigenstate $|e_2\rangle$.

n	$ e_n\rangle$	ε_n	μ_n
0	$ e_0\rangle = \frac{1}{\sqrt{N}} \sum_{k=0}^{N-1} k\rangle$	0	1
1	$ e_1^l\rangle = \frac{1}{\sqrt{l(l+1)}} \left(\sum_{k=1}^l k\rangle - l l+1\rangle \right)$ with $l = 1, \dots, N - 2$	1	$N - 2$
2	$ e_2\rangle = \frac{1}{\sqrt{N(N-1)}} \left[(N-1) 0\rangle - \sum_{k=1}^{N-1} k\rangle \right]$	N	1

Table 2.3. Eigenvectors $|e_n\rangle$ and eigenvalues ε_n with multiplicity μ_n of the graph Laplacian in the star graph.

The perturbation involves

$$L^2 = 2I + (N^2 - N - 2) |0\rangle\langle 0| - N \sum_{k=1}^{N-1} (|k\rangle\langle 0| + |0\rangle\langle k|) + \sum_{\substack{j,k=1, \\ j \neq k}}^{N-1} |j\rangle\langle k|, \quad (2.34)$$

so the perturbed Hamiltonian (2.1) reads

$$\begin{aligned} \mathcal{H} = & (1 + 2\lambda)I + [N - 2 + \lambda(N^2 - N - 2)] |0\rangle\langle 0| \\ & - (1 + \lambda N) \sum_{k=1}^{N-1} (|k\rangle\langle 0| + |0\rangle\langle k|) + \lambda \sum_{\substack{j,k=1, \\ j \neq k}}^{N-1} |j\rangle\langle k|. \end{aligned} \quad (2.35)$$

The perturbation λL^2 thus introduces the hopping among all the outer vertices (next-nearest neighbors) and affects the hopping to and from the central vertex, i.e., the nearest-neighbor hopping, and also the on-site energies proportional to I .

For an initially localized state, there are two different time evolutions. If at $t = 0$ the walker is in the central vertex $|0\rangle$, then the time evolution is equal to the corresponding one in the complete graph of the same size. Therefore, also the resulting probability distribution, the IPR, and the coherence are equal between star and complete graphs. Instead, if at $t = 0$ the walker is localized in any of the outer vertices, then we have a different time evolution. All the outer vertices $|1 \leq i \leq N - 1\rangle$ are equivalent and differ from the central vertex $|0\rangle$, so, if we keep the central vertex as $|0\rangle$, we can always relabel the outer vertices in such a way that the starting vertex is denoted by $|1\rangle$.

The probabilities of finding the walker in the central vertex $|0\rangle$, in the starting vertex $|1\rangle$ or in any other outer vertex $|2 \leq i \leq N - 1\rangle$ at time t for a given value of λ are respectively (Fig. 2.9)

$$P_1(0, t|\lambda) = \frac{4}{N^2} \sin^2(\omega_N(\lambda)t), \quad (2.36)$$

$$P_1(1, t|\lambda) = 1 - \frac{4}{N(N-1)} \left[(N-2) \sin^2(\omega_1(\lambda)t) + \frac{N-2}{N-1} \sin^2[(\omega_N(\lambda) - \omega_1(\lambda))t] + \frac{1}{N} \sin^2(\omega_N(\lambda)t) \right], \quad (2.37)$$

$$P_1(i, t|\lambda) = \frac{4}{N(N-1)} \left[\sin^2(\omega_1(\lambda)t) + \frac{1}{N-1} \sin^2[(\omega_N(\lambda) - \omega_1(\lambda))t] - \frac{1}{N} \sin^2(\omega_N(\lambda)t) \right], \quad (2.38)$$

where the angular frequency is defined in Eq. (2.25). In particular, $P_1(0, t|\lambda)$ is periodic with period $T_N := \pi/\omega_N(\lambda)$, it is symmetric with respect to $\lambda^* = -1/N$, and $P_1(0, t|\lambda^*) = 0$, which means that the walker occupies only in the outer vertices of the star graph. Indeed, λ^* makes the hopping terms to and from the central vertex $|0\rangle$ null (see Eq. (2.35)). Instead, $P_1(1, t|\lambda)$ and $P_1(i, t|\lambda)$ are periodic if and only if the periods T_1 , T_N , and $\pi/[\omega_N(\lambda) - \omega_1(\lambda)]$ of the summands are commensurable. When this happens, then the overall probability distribution is periodic. This happens also for the particular values $\lambda = -1, -1/N, -1/(N+1)$, which make null ω_1 , ω_N , and $\omega_N - \omega_1$, respectively. Indeed, when ω_1 (ω_N) is null, the probabilities (2.36)–(2.38) only involve sine functions with ω_N (ω_1). When $\omega_N - \omega_1 = 0$, i.e., $\omega_N = \omega_1$, all the sine functions have the same angular frequency. We address in detail the periodicity of the probability distribution in Appendix 2.A.3. For $P_1(1, t|\lambda)$ and $P_1(i, t|\lambda)$ results suggest that there is no symmetry with respect to λ . Increasing the order of the graph makes the angular frequency higher, and $\lim_{N \rightarrow +\infty} P_1(1, t|\lambda) = 1$, while $\lim_{N \rightarrow +\infty} P_1(0, t|\lambda) = \lim_{N \rightarrow +\infty} P_1(i, t|\lambda) = 0$. Again, the perturbation affects the probabilities only through the angular frequency. The average probability distribution is the same as the one reported in [108], which is exactly our unperturbed CTQW.

Next we numerically evaluate the IPR (2.5) for the probability distribution in Eqs. (2.36)–(2.38); the results are shown in Fig. 2.10. The IPR oscillates between 1 and its minimum value, which grows with N , similarly to what happens in the complete graph. Indeed, for $N \rightarrow +\infty$ the IPR approaches 1 (localization), since the probability of finding the walker in the starting vertex approaches 1. The periodicity of the IPR relies upon that of the probability distribution. When the latter is periodic, the IPR periodically reaches 1, since the walker is initially localized at a vertex, and periodically returns to it. By considering $P_1(0, t|\lambda) = 1/N$, we notice that the instantaneous exactly uniform mixing is never achievable for $N > 4$ and so the IPR is never close to $1/N$, independently of λ . Instead, for $N \leq 4$ the mixing properties strongly depend on the choice of N and λ , e.g., it is achievable for $\lambda = -1/(N+1)$ and for $N = 2 \wedge \lambda = -1$. The instantaneous exactly uniform mixing is never achievable for λ^* , since $P_1(0, t|\lambda^*) = 0 \forall t$.

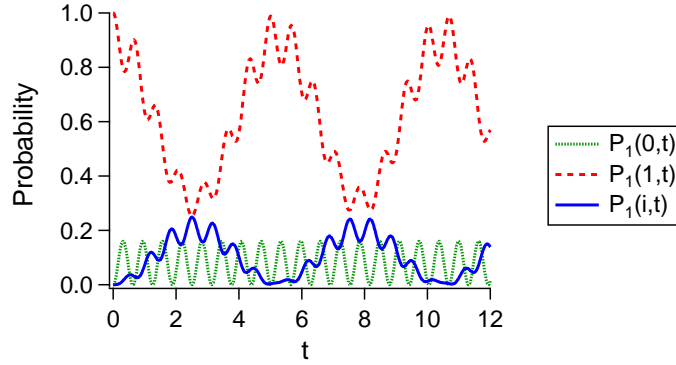


Figure 2.9. Probability of finding the walker at the central vertex $P_1(0, t|\lambda)$ (green dotted line), at the starting vertex $P_1(1, t|\lambda)$ (red dashed line) or at any other vertex $P_1(i, t|\lambda)$ (blue solid line) as a function of time in the star graph. The walker is initially localized at the vertex $|1\rangle$. Results are for $N = 5$ and $\lambda = 0.2$.

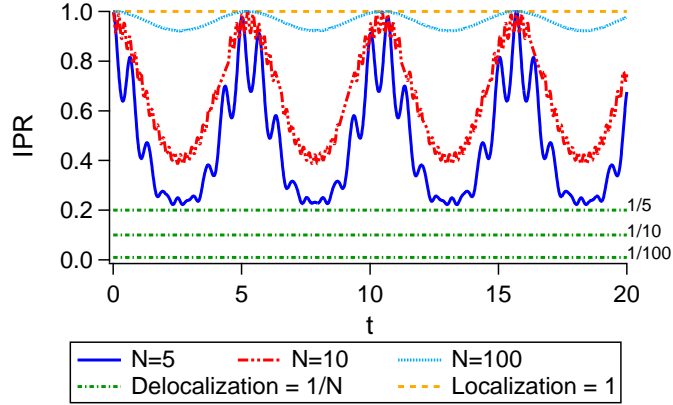


Figure 2.10. Inverse participation ratio for a walker initially localized at $|1\rangle$ on the star graph. Results suggest that for $t > 0$ there are instants of time when the IPR is close to the upper bound 1 (orange dashed line), i.e., the localization. In particular, the IPR periodically reaches 1 when the probability distribution is periodic. For $N > 4$ the IPR does not reach the value $1/N$ (green dashdotted line), i.e., the delocalization. For $N \rightarrow +\infty$ the IPR approaches 1, since the probability of finding the walker at the starting vertex approaches 1 (see Eqs. (2.36)–(2.38)). Results are for $\lambda = 0.2$.

Finally, we focus on the time dependence of the coherence of a walker initially localized in $|1\rangle$, which we derive in Appendix 2.A.3 and it is shown in Fig. 2.11. The coherence shows a complex structure of local maxima and minima. However, it is smoother and periodic for the values of λ which make the overall probability distribution periodic (see Appendix 2.A.3), e.g., $\lambda = -1, -1/N, -1/(N+1)$.

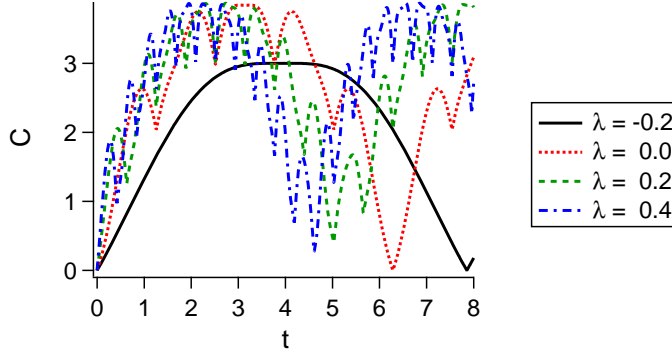


Figure 2.11. Coherence for a walker initially localized in $|1\rangle$ in the star graph with $N = 5$. The coherence is smooth and periodic for $\lambda^* = -1/N$.

2.3 Characterization

In this section we address the characterization of the CTQW Hamiltonian (2.1), i.e., the estimation of the parameter λ that quantifies the amplitude of the perturbation $\mathcal{H}_1 = L^2$. Our aim is to assess whether and to what extent we may determine the value of λ using only a snapshot of the walker dynamics, i.e., by performing measurements at a given time t . Hence, we make use of the concepts from classical and quantum estimation theories reviewed in Sec. 1.2.

We recall that the main result regarding the precision of an unbiased estimator $\hat{\lambda}$ is given by the Cramér-Rao bound

$$\sigma^2(\hat{\lambda}) \geq \frac{1}{n\mathcal{F}_c(\lambda)}, \quad (2.39)$$

where $\mathcal{F}_c(\lambda)$ is the Fisher information (FI) of the probability distribution $P(x|\lambda)$, n is the number of measurements, and λ is the parameter of interest. The above inequality sets a lower bound on the variance σ^2 of any unbiased estimator $\hat{\lambda}$, provided that the family of distribution $P(x|\lambda)$ realizes a so-called *regular statistical model*. Regular models are those with a constant support, i.e., the region in which $P(x|\lambda) \neq 0$ does not depend on the parameter λ , and with non-singular FI. If these hypotheses are not satisfied, estimators with vanishing variance may be easily found.

In a quantum scenario, the parameter must be encoded in the density matrix of the system. In turn, a *quantum statistical model* is defined as a family of quantum states $\{\rho_\lambda\}$ parametrized by the value of λ . The quantum Cramér-Rao inequality

$$\sigma^2(\hat{\lambda}) \geq \frac{1}{n\mathcal{F}_q(\lambda)}, \quad (2.40)$$

where $\mathcal{F}_q(\lambda)$ is the quantum Fisher information (QFI), establishes the ultimate lower bound of the precision in estimating a parameter λ encoded in a quantum state. Note that the quantum Cramér-Rao bound is valid for *regular quantum statistical model*, i.e., families of quantum states made of density matrices with constant rank (i.e., the rank does not depend on the parameter) and leading to non-singular QFI [77–79].

In the present work we focus on pure states subjected to the unitary evolution in Eq. (2.2), i.e., $|\psi_\lambda(t)\rangle = \mathcal{U}_\lambda(t)|\psi(0)\rangle$. For such states the QFI reads

$$\mathcal{F}_q(t, \lambda) = 4 \left[\langle \partial_\lambda \psi_\lambda(t) | \partial_\lambda \psi_\lambda(t) \rangle - |\langle \psi_\lambda(t) | \partial_\lambda \psi_\lambda(t) \rangle|^2 \right]. \quad (2.41)$$

When dealing with CTQWs on a graph, a reasonable and significant measurement is the position one. For such a measurement the FI reads

$$\mathcal{F}_c(t, \lambda) = \sum_{k=0}^{N-1} \frac{(\partial_\lambda P(k, t|\lambda))^2}{P(k, t|\lambda)}, \quad (2.42)$$

where $P(k, t|\lambda)$ is the conditional probability of finding the walker in the k -th vertex at time t when the value of the parameter is λ .

When the perturbation \mathcal{H}_1 commutes with the unperturbed Hamiltonian \mathcal{H}_0 (which is our case; see Eq. (2.1)), the unitary time evolution simplifies to

$$\mathcal{U}_\lambda(t) = e^{-it\mathcal{H}_0} e^{-it\lambda\mathcal{H}_1}. \quad (2.43)$$

Then the QFI has a simple representation in terms of the perturbation and of time. Indeed, if our probe $|\psi\rangle$ at time $t = 0$ does not depend on λ and undergoes the evolution $\mathcal{U}_\lambda(t)$, at a later time $t > 0$ we can write

$$\mathcal{F}_q(t) = 4t^2 [\langle \psi | \mathcal{H}_1^2 | \psi \rangle - \langle \psi | \mathcal{H}_1 | \psi \rangle^2] = 4t^2 \langle (\Delta \mathcal{H}_1)^2 \rangle, \quad (2.44)$$

since $|\partial_\lambda \psi_\lambda(t)\rangle = -it\mathcal{H}_1 |\psi_\lambda(t)\rangle$ when $[\mathcal{H}_0, \mathcal{H}_1] = 0$. We emphasize that the QFI does not depend on the parameter λ to be estimated. This is due to the unitary evolution and to the fact that at $t = 0$ the probe $|\psi\rangle$ does not depend on λ .

In the following, we evaluate the QFI of localized states, whose dynamics is addressed in Sec. 2.2, and we determine the states maximizing the QFI for cycle, complete, and star graph. We compare the QFI with the FI for a position measurement to assess whether it is an optimal measurement or not. Moreover, we find the simple graphs allowing the maximum QFI. Refer to Appendix 2.B for details about the analytical derivation of the results shown in the following.

2.3.1 Localized states

Cycle graph

The QFI of an initially localized state in the cycle graph is

$$\mathcal{F}_q(t) = 136t^2, \quad (2.45)$$

and it is independent of N . We numerically evaluate the FI (2.42) for the probability distribution in Eq. (2.18). The results are shown in Fig. 2.12 and suggest that the FI never reaches the QFI. Specific behaviors of the FI strongly depend on the choice of N and λ .

Complete Graph

The QFI of an initially localized state in the complete graph is

$$\mathcal{F}_q(N, t) = 4N^2(N-1)t^2. \quad (2.46)$$

The FI is

$$\mathcal{F}_c(N, t, \lambda) = \frac{4N^4(N-1)t^2 \cos^2(\omega_N(\lambda)t)}{N^2 - 4(N-1)\sin^2(\omega_N(\lambda)t)}, \quad (2.47)$$

with $\omega_N(\lambda)$ defined in Eq. (2.25). Due to the symmetry of the graph, both the QFI and the FI do not depend on the starting vertex, i.e., the estimation is completely indifferent to the choice of the initially localized state. Unlike the QFI, the FI does depend on λ and is symmetric with respect to $\lambda^* = -1/N$, as well as the probability distribution in Eqs. (2.26) and (2.27). In particular,

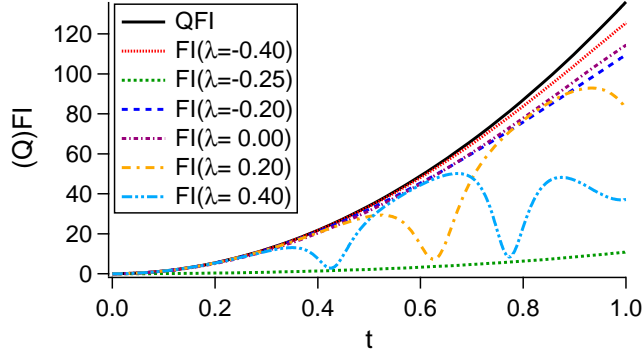


Figure 2.12. Quantum (black solid line) and classical Fisher information (colored nonsolid lines) of position measurement for an initially localized state on the cycle graph. Results are for $N = 5$.

$\mathcal{F}_c(t, \lambda^*) = \mathcal{F}_q(t)$. However, we recall that $P_0(0, t|\lambda^*) = 1$ and $P_0(i, t|\lambda^*) = 0$, i.e., the walker is in the starting vertex all the time. In this case the hypotheses leading to the Cramér-Rao bound (2.39) do not hold, since the model is not regular, and the bound may be easily surpassed. Indeed, if we perform the measurement described by the POVM $\{|0\rangle\langle 0|, \mathbb{1} - |0\rangle\langle 0|\}$, the variance of the estimator is identically zero, outperforming both classical and quantum bounds.

For $\lambda \neq \lambda^*$, the periodicity of the probabilities in Eqs. (2.26) and (2.27) results in a dependence of the FI on λ and an analogous oscillating behavior (Fig. 2.13). The FI reaches periodically its local maxima when the numerator is maximum and the denominator is minimum, and these maxima saturate the quantum Cramér-Rao bound

$$\mathcal{F}_c(t_k, \lambda) = \mathcal{F}_q(t_k, \lambda). \quad (2.48)$$

This occurs for $t_k = 2k\pi/(N + \lambda N^2)$, with $k \in \mathbb{N}$, i.e., when the walker is completely localized and we definitely find it in the starting vertex. Indeed, in the probability distribution the parameter λ is encoded only in the angular frequency, thus knowing when the walker is certainly in the starting vertex means knowing exactly its period, and thus the parameter λ . However, to perform such a measurement one needs some *a priori* knowledge of the value of the parameter. In fact, the POVM saturating the quantum Cramér-Rao bound (2.40) strongly depends on the parameter λ .

Star Graph

The time evolution of the state localized in the center of the star graph is equivalent to that of a localized state in the complete graph, as already pointed out in Sec. 2.2.3. Thus, for this state the QFI and FI are provided in Eqs. (2.46) and (2.47), respectively (see also Fig. 2.13).

Things change when we consider a walker initially localized in one of the outer vertices of the star graph. In this case the QFI is

$$\mathcal{F}_q(N, t) = 4(N^2 + N - 2)t^2. \quad (2.49)$$

We numerically evaluate the FI (2.42) for the probability distribution in Eqs. (2.36)–(2.38) and the results are shown in Fig. 2.14. Unlike the complete graph, for the star graph there is no saturation of the quantum Cramér-Rao bound. Note, however, that for $\lambda^* = -1/N$ the walker cannot reach the central site and in principle one may exploit this feature to build a nonregular model, as we discussed in the preceding section.

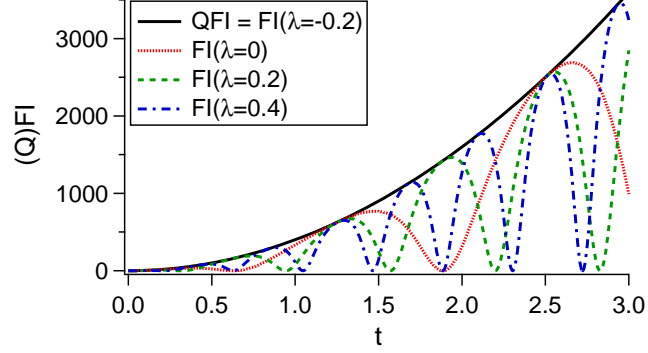


Figure 2.13. Quantum (black solid line) and classical Fisher information (colored nonsolid lines) of position measurement for an initially localized state on the complete graph. The same results are obtained for a walker initially localized at the central vertex $|0\rangle$ of the star graph of the same size. Results are for $N = 5$.

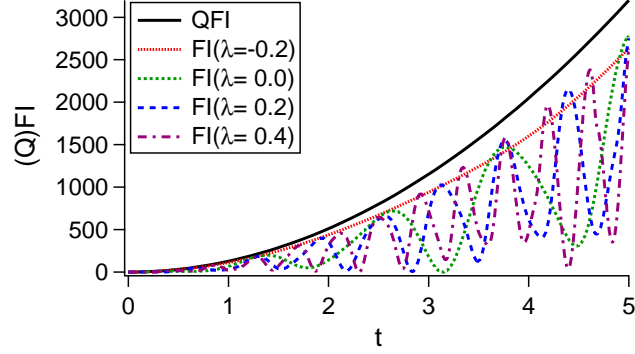


Figure 2.14. Quantum (black solid line) and classical Fisher information (colored nonsolid lines) of position measurement for a walker initially localized at an outer vertex of the star graph. Results are for $N = 5$.

2.3.2 States maximizing the QFI

In the preceding section we studied how localized states behave as quantum probes for estimating the parameter λ of the perturbation. However, we might be interested in finding the best estimate for such a parameter by searching for the state ρ_λ maximizing the QFI, hence minimizing the variance $\sigma^2(\hat{\lambda})$. For this purpose, it is worth introducing an alternative formula for QFI. When there is only one parameter to be estimated and the state is pure, the QFI reads

$$\mathcal{F}_q(\lambda, t) = \lim_{\delta\lambda \rightarrow 0} \frac{8(1 - |\langle \psi_\lambda(t) | \psi_{\lambda+\delta\lambda}(t) \rangle|)}{\delta\lambda^2}. \quad (2.50)$$

This expression involves the modulus of the scalar product

$$\langle \psi_\lambda(t) | \psi_{\lambda+\delta\lambda}(t) \rangle = \langle \psi(0) | U_{\delta\lambda}(t) | \psi(0) \rangle, \quad (2.51)$$

where

$$U_{\delta\lambda}(t) := e^{+i(\mathcal{H}_0 + \lambda\mathcal{H}_1)t} e^{-i[\mathcal{H}_0 + (\lambda + \delta\lambda)\mathcal{H}_1]t} = e^{-i\delta\lambda\mathcal{H}_1 t} \quad (2.52)$$

is a unitary operator given by the product of two unitary operators (2.2) related to the time evolutions for λ and $\lambda + \delta\lambda$ and the last equality holds since $[\mathcal{H}_0, \mathcal{H}_1] = 0$ (see Eq. (2.1)).

The QFI strongly depends on the quantum state considered. To maximize the QFI, we recall the following lemma from Parthasarathy [116].

Lemma 1. *Let W be any unitary operator in the finite dimensional complex Hilbert space \mathcal{H} with spectral resolution $\sum_{j=1}^k e^{i\theta_j} P_j$, where $e^{i\theta_1}, \dots, e^{i\theta_k}$ are the distinct eigenvalues of W with respective eigenprojections P_1, \dots, P_k . Define*

$$m(W) = \min_{\|\psi\|=1} |\langle \psi | W | \psi \rangle|^2. \quad (2.53)$$

Then the following hold.

- (a) *If there exists a unit vector $|\psi_0\rangle$ such that $\langle \psi_0 | W | \psi_0 \rangle = 0$, then $m(W) = 0$.*
- (b) *If $\langle \psi | W | \psi \rangle > 0$ for every unit vector $|\psi\rangle$, then*

$$m(W) = \min_{i \neq j} \cos^2 \left(\frac{\theta_i - \theta_j}{2} \right). \quad (2.54)$$

Furthermore, when the right-hand side is equal to $\cos^2 \left(\frac{\theta_{i_0} - \theta_{j_0}}{2} \right)$,

$$m(W) = |\langle \psi_0 | W | \psi_0 \rangle|^2 \quad (2.55)$$

where

$$|\psi_0\rangle = \frac{1}{\sqrt{2}} (|e_{i_0}\rangle + |e_{j_0}\rangle) \quad (2.56)$$

with $|e_{i_0}\rangle$ and $|e_{j_0}\rangle$ arbitrary unit vectors in the range of P_{i_0} and P_{j_0} respectively.

The idea is to exploit Lemma 1 to compute the QFI. We consider $|\psi_0\rangle$ as the initial state and we identify W with $U_{\delta\lambda}(t)$, since $\langle \psi_\lambda(t) | \psi_{\lambda+\delta\lambda}(t) \rangle = \langle \psi_0 | U_{\delta\lambda}(t) | \psi_0 \rangle$, so that

$$\mathcal{F}_q(\lambda, t) = \lim_{\delta\lambda \rightarrow 0} \frac{8 \left[1 - \sqrt{m(U_{\delta\lambda}(t))} \right]}{\delta\lambda^2}. \quad (2.57)$$

Indeed, the state $|\psi_0\rangle$ in Eq. (2.56) maximizes the QFI by minimizing the modulus of the scalar product (2.51). The unit vectors involved by $|\psi_0\rangle$ are eigenvectors of the unitary operator (2.52) and so, ultimately, of \mathcal{H}_1 . In particular, such states are those whose eigenvalues minimize Eq. (2.54). The eigenvalues of the unitary operator (2.52) are $e^{i\theta_j} = e^{-i\delta\lambda t \varepsilon_j^2}$, with $\{\varepsilon_j^2\}$ eigenvalues of $\mathcal{H}_1 = \mathcal{H}_0^2$, and $\{\varepsilon_j\}$ those of $\mathcal{H}_0 = L$. Thus, we can identify $\theta_j = -\delta\lambda t \varepsilon_j^2$. Because of this relation, we may assume $|e_{i_0}\rangle$ and $|e_{j_0}\rangle$ to be the eigenstates corresponding to the lowest- and highest-energy eigenvalue. Indeed, in the limit for $\delta\lambda t \rightarrow 0$ the cosine in Eq. (2.54) is minimized by maximizing the difference $\theta_i - \theta_j$. Then the QFI reads

$$\mathcal{F}_q(t) = t^2 (\varepsilon_{max}^2 - \varepsilon_{min}^2)^2 = t^2 \varepsilon_{max}^4. \quad (2.58)$$

Because of the choice of the state $|\psi_0\rangle$, which involves the lowest- and highest-energy eigenstates, the first equality follows from Eq. (2.44), whereas the second equality holds since $\varepsilon_{min} = 0$ for simple graphs. An eventual phase difference between the two eigenstates in Eq. (2.56) would result in the same QFI, but a different FI, as shown in Appendix 2.B.4.

General Graph

We prove that for a specific class of graphs the maximum QFI is always equal to $N^4 t^2$, provided the probe of the system is the state (2.56). Indeed, according to Lemma 1, in order to find quantum probes maximizing the QFI, we need to search for systems whose eigenvalue separation is maximum. For a graph of N vertices with no loops, the row sums and the column sums of the graph Laplacian L_N are all equal to 0, and the vector $(1, \dots, 1)$ is always an eigenvector of L with eigenvalue 0. It follows that any Laplacian spectrum contains a zero eigenvalue and to maximize the QFI we need to find graphs having the largest maximum eigenvalue.

Following Ref. [52], the Laplacian spectrum of a graph $G(V, E)$ is the set of the eigenvalues of L_N

$$S_L(G) = \{\mu_1 = 0, \mu_2, \dots, \mu_N\}, \quad (2.59)$$

where the eigenvalues μ_i are sorted in ascending order. To study the maximum eigenvalue μ_N we introduce the complementary graph \bar{G} of G . The complementary graph \bar{G} is defined on the same vertices of G and two distinct vertices are adjacent in \bar{G} if and only if they are not adjacent in G . So the adjacency matrix \bar{A} can be easily obtained from A by replacing all the off-diagonal 0's with 1's and all the 1's with 0's. Alternatively,

$$\bar{A}_N = \mathbb{J}_N - \mathbb{1}_N - A_N, \quad (2.60)$$

where \mathbb{J}_N denotes the $N \times N$ all-1 matrix and $\mathbb{1}_N$ the $N \times N$ identity matrix. A vertex in G can be at most adjacent to $N - 1$ vertices, since no loops are allowed. Then, the degree \bar{d}_j of a vertex in \bar{G} is $N - 1 - d_j$, i.e., the complement to $N - 1$ of the degree of the same vertex in G . The diagonal degree matrix is therefore

$$\bar{D}_N = (N - 1)\mathbb{1}_N - D_N. \quad (2.61)$$

In conclusion, the Laplacian matrix \bar{L}_N associated with the complementary graph \bar{G} is

$$\bar{L}_N = \bar{D}_N - \bar{A}_N = N\mathbb{1}_N - \mathbb{J}_N - L_N. \quad (2.62)$$

Lemma 2. *Any eigenvector \vec{n} of L_N is an eigenvector of \bar{L}_N . If the eigenvalue of \vec{n} for L_N is 0, then it is 0 also for \bar{L}_N . If the eigenvalue of \vec{n} for L_N is μ_i , then the eigenvalue for \bar{L}_N is $N - \mu_i$. Thus, the spectrum of L_N is given by*

$$S_{\bar{L}}(\bar{G}) = \{0, N - \mu_N, \dots, N - \mu_2\}, \quad (2.63)$$

where the eigenvalues are still sorted in ascending order.

Any L_N is positive semidefinite, i.e., $\mu_i \geq 0 \forall i$, so this holds for \bar{L}_N too. According to these remarks and to Eq. (2.63), we then observe that $\mu_N \leq N$, i.e., the largest eigenvalue is bounded from above by the number of vertices N . Moreover, the second-smallest eigenvalue μ_2 of L_N is the algebraic connectivity of G : It is greater than 0 if and only if G is a connected graph. Indeed, the algebraic multiplicity of the eigenvalue 0 is the number of connected components of the graph [117–119]. So if \bar{G} has at least two distinct components, then the second-smallest eigenvalue of \bar{L}_N is $N - \mu_N = 0$, from which $\mu_N = N$.

Lemma 3. *Given a graph G and its Laplacian spectrum $S_L(G) = \{0, \mu_2, \dots, \mu_N\}$, the largest Laplacian eigenvalue μ_N is bounded from above by $\mu_N \leq N$ and the equality is saturated only if the complementary graph \bar{G} is disconnected.*

This result in spectral graph theory has a direct impact on our estimation problem. Since our perturbation is the square of the graph Laplacian, the maximum QFI is given by Eq. (2.58) and involves the lowest and the largest eigenvalue of the Laplacian spectrum.

Lemma 4. *The simple graphs G whose complementary graph \bar{G} is disconnected are the only ones providing the maximum QFI for the estimate of the parameter λ in Eq. (2.1). For such graphs, the largest eigenvalue of the graph Laplacian is N and the lowest is 0. This results in the maximum QFI*

$$\mathcal{F}_q^{max}(N, t) = N^4 t^2. \quad (2.64)$$

This lemma allows us to predict whether or not a graph provides the maximum QFI and its value, with no need to diagonalize the graph Laplacian. Some graphs satisfying Lemma 4 are the complete, the star, the wheel, and the complete bipartite graphs. The cycle graph allows the maximum QFI only for $N \leq 4$: For $N = 2, 3$ it is just a complete graph and for $N = 4$ the complementary graph has two disconnected components; for $N > 4$ it is connected.

Cycle graph

The cycle graph satisfies Lemma 4 only for $N \leq 4$. For $N > 4$ the maximum QFI is lower than $N^4 t^2$ and it depends on N . Indeed, the energy spectrum of the cycle graph is sensitive to the parity of N , and the state maximizing the QFI at $t = 0$ is therefore

$$|\psi_0^{(\pm)}\rangle = \frac{1}{\sqrt{2}}(|e_{min}\rangle + |e_{max}^{(\pm)}\rangle), \quad (2.65)$$

where $|e_{min}\rangle$ is the ground state, while $|e_{max}^{(\pm)}\rangle$ is the eigenstate corresponding to the highest-energy level and it depends on the parity of N . For even N it is unique, whereas for odd N the highest energy level is doubly degenerate, which is the reason for the \pm sign (see Eqs. (2.14) and (2.15) and Table 2.1). The resulting QFI is

$$\mathcal{F}_q(t) = \begin{cases} 256t^2 & \text{if } N \text{ is even,} \\ 16 [1 + \cos(\frac{\pi}{N})]^4 t^2 & \text{if } N \text{ is odd.} \end{cases} \quad (2.66)$$

The QFI for odd N depends on N , and for large N it approaches the QFI for even N , which does not depend on N . Even the FI discriminates between even and odd N , because of the ambiguity in choosing the highest energy eigenstate for odd N (see Appendix 2.B.1). For even N the position measurement is optimal, i.e., $\mathcal{F}_c(t) = \mathcal{F}_q(t)$. For odd N , both eigenstates for $n = (N \pm 1)/2$ in Table 2.1 lead to $\mathcal{F}_c(t) = \mathcal{F}_q(t)$. Instead, if we choose the linear combinations of them in Eqs. (2.14) and (2.15), the FI of position measurement is no longer optimal, as shown in Fig. 2.15.

Complete graph

The complementary graph of the complete graph has N disconnected components, so it satisfies Lemma 4. A possible choice of the state maximizing the QFI (at $t = 0$) is

$$|\psi_0^l\rangle = \frac{1}{\sqrt{2}}(|e_0\rangle + |e_1^l\rangle), \quad (2.67)$$

where $|e_0\rangle$ is the ground state, while $|e_1^l\rangle$, with $l = 1, \dots, N - 1$, is the eigenstate corresponding to the highest energy level $\varepsilon_1 = N$, which is $(N - 1)$ -degenerate (see Table 2.2). Then, we are free to choose any eigenstate from the eigenspace $\{|e_1^l\rangle\}$ (or even a superposition of them) and the QFI is always given by Eq. (2.64). On the other hand, the FI does depend on the choice of $|e_1^l\rangle$.

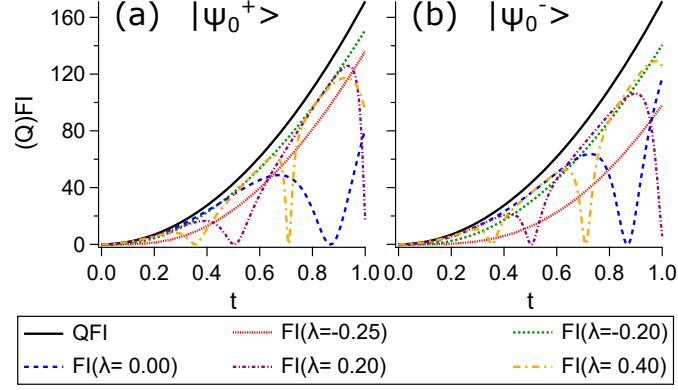


Figure 2.15. Quantum (black solid line) and classical Fisher information (colored nonsolid lines) of position measurement for the states maximizing the QFI on the cycle graph for odd N : (a) $|\psi_0^+\rangle$, where the highest-energy state is Eq. (2.14), and (b) $|\psi_0^-\rangle$, where the highest-energy state is Eq. (2.15). Indeed, for odd N the highest-energy level is doubly degenerate. While the QFI does not depend on the choice of the corresponding eigenstate, the FI does. Results are for $N = 5$.

As an example, let us consider the two states

$$|\psi_0^1\rangle = \frac{1}{\sqrt{2}}(|e_0\rangle + |e_1^1\rangle), \quad (2.68)$$

$$|\psi_0^{N-1}\rangle = \frac{1}{\sqrt{2}}(|e_0\rangle + |e_1^{N-1}\rangle). \quad (2.69)$$

These states are equivalent for the QFI (both maximize it), but they are not for the FI (see Fig. 2.16), which reads

$$\mathcal{F}_c(|\psi_0^1\rangle; N, t, \lambda) = \frac{4N^4(N+2)t^2 \sin^2(2t\omega_N(\lambda))}{(N+2)^2 - 8N \cos^2(2t\omega_N(\lambda))}, \quad (2.70)$$

$$\mathcal{F}_c(|\psi_0^{N-1}\rangle; N, t, \lambda) = \frac{4N^4(N-1)t^2 \sin^2(2t\omega_N(\lambda))}{N^2 - 4(N-1) \cos^2(2t\omega_N(\lambda))}. \quad (2.71)$$

In both cases the FI is symmetric with respect to $\lambda^* = -1/N$, and for such value it vanishes. The local maxima occur for $t_k = \pi(k+1/2)/(N+\lambda N^2)$, with $k \in \mathbb{N}$, and are

$$\mathcal{F}_c^{max}(|\psi_0^1\rangle; N, t_k, \lambda) = \frac{4N^4}{N+2} t_k^2, \quad (2.72)$$

$$\mathcal{F}_c^{max}(|\psi_0^{N-1}\rangle; N, t_k, \lambda) = 4(N-1)N^2 t_k^2. \quad (2.73)$$

For these states the FI never reaches the value of the QFI (2.64), so the position measurement on $|\psi_0^1\rangle$ is not optimal.

Star graph

The complementary graph of the star graph has two disconnected components, so it satisfies Lemma 4. The state maximizing the QFI (at $t = 0$) is

$$|\psi_0\rangle = \frac{1}{\sqrt{2}}(|e_0\rangle + |e_2\rangle), \quad (2.74)$$

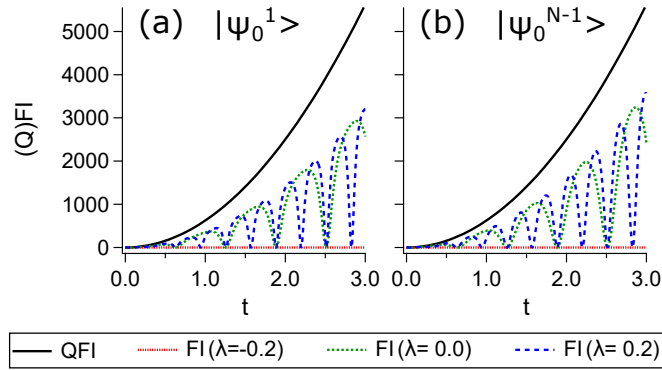


Figure 2.16. Quantum (black solid line) and classical Fisher information (colored nonsolid lines) of position measurement for two of the states maximizing the QFI on the complete graph: (a) $|\psi_0^1\rangle$ in Eq. (2.68) and (b) $|\psi_0^{N-1}\rangle$ in Eq. (2.69). Due to the degeneracy of the highest energy level, there are several states providing the same maximum QFI. While the QFI does not depend on the choice of such states, the FI does. In both cases, the FI vanishes for $\lambda^* = -1/N$. Also shown in (b) are the results for the maximum QFI state in Eq. (2.74) for the star graph of the same size. Results are for $N = 5$.

where $|e_0\rangle$ is the ground state, while $|e_2\rangle$ is the eigenstate corresponding to the highest-energy level $\varepsilon_2 = N$ (see Table 2.3). The resulting QFI is given by Eq. (2.64). Since the highest-energy level is not degenerate, there is no ambiguity in the state maximizing the QFI. For such a state the FI reads as Eq. (2.71), so also refer to Fig. 2.16(b).

2.4 Discussion and Conclusions

In this chapter, we have investigated the dynamics and the characterization of continuous-time quantum walks with Hamiltonians of the form $\mathcal{H} = L + \lambda L^2$, with L the Laplacian matrix of the underlying graph. We have considered cycle, complete, and star graphs, as they describe paradigmatic models with low and high connectivity and/or symmetry. The perturbation λL^2 to the CTQW Hamiltonian L introduces next-nearest-neighbor hopping. This strongly affects the CTQW in the cycle and in the star graph, whereas it is negligible in the complete graph, since each of its vertices is adjacent to all the others and $L^2 = NL$. Clearly $[L, \lambda L^2] = 0$, so the commutator between the unperturbed Hamiltonian and the perturbation is not indicative of how much the system is perturbed. Therefore, we consider how different is L^2 from L by assessing the Frobenius norm of the operator $\Delta = L - L^2/N$, i.e., $\|\Delta\|_F = \sqrt{\text{Tr}\{\Delta^\dagger \Delta\}}$ [120]. This turns out to be null for the complete graph, equal to $\sqrt{6N - 40 + 70/N}$ for the cycle, and to $\sqrt{N - 4 + 5/N - 2/N^2}$ for the star graph. According to this, the cycle graph is the most perturbed, and the complete the least.

Our results indicate the general quantum features of CTQWs on graphs, e.g., revivals, interference, and creation of coherence, are still present in their perturbed versions. On the other hand, interesting effects emerge, such as the appearance of symmetries in the behavior of the probability distribution and of the coherence. In the cycle graph (for $t \ll 1$), the perturbation affects the speed of the walker, while preserving the ballistic spreading. The variance is symmetric with respect to λ_0 , despite the fact that the probability distribution is not. The value λ_0 makes the next-nearest-neighbor hopping equal to the nearest-neighbor hopping. The physical interpretation of this behavior is still an open question, which deserves further investigation. In the complete graph the perturbation does not affect the dynamics, since $L^2 = NL$, so the resulting

perturbed Hamiltonian is proportional to L . In the star graph, the perturbation affects the periodicity of the system. We have determined the values of λ allowing the system to be periodic, thus to have exact revivals. In particular, the value $\lambda^* = -1/N$ makes the walker exist only in the outer vertices, provided it starts in one of them.

Characterizing the perturbed Hamiltonian amounts to estimating the parameter λ of the perturbation. We have addressed the optimal estimation of λ by means of the quantum Fisher information and using only a snapshot of the walker dynamics. The states maximizing the QFI turn out to be the equally weighted linear combination of the eigenstates corresponding to the lowest- and highest-energy levels. In addition, we have found that the simple graphs whose complementary graph is disconnected, e.g., the complete and star graphs, are the only ones providing the maximum QFI $N^4 t^2$. Moreover, we have evaluated the Fisher information of position measurements to assess whether it is optimal. We sum up the asymptotic behavior of the (Q)FI for large N in Table 2.4 and for $t \ll 1$ in Table 2.5. When the probe is a localized state, the QFI in the cycle graph is independent of the order N of the graph. In the complete graph, the local maxima of the FI equal the QFI and occur when the walker is localized in the starting vertex with probability 1; this happens periodically. However, to perform such a measurement one needs some *a priori* knowledge of the value of λ . When the probe is the maximum QFI state, the QFI in the cycle graph depends on N , and FI is optimal for even N . In general, when the highest energy level is degenerate, the QFI does not depend on the choice of the corresponding eigenstates when defining the optimal state; instead the FI does.

Besides fundamental interest, our study may find applications in designing enhanced algorithms on graphs, e.g., spatial searches, and as a necessary ingredient to study dephasing and decoherence.

	QFI			FI		
	<i>cycle</i>	<i>complete</i>	<i>star</i>	<i>cycle</i>	<i>complete</i>	<i>star</i>
<i>Localized states</i>	$O(1)$	$O(N^3)$	$O(N^2)$	$O(1)$	$O(N^3)$	$O(N^2)$
<i>Maximum QFI states</i>	$O(1)$	$O(N^4)$	$O(N^4)$	$O(1)$	$O(N^3)$	$O(N^3)$

Table 2.4. Asymptotic behavior of the quantum Fisher information and of the classical Fisher information for large order N of the cycle, complete, and star graphs, for localized and maximum QFI states.

	FI		
	<i>cycle</i>	<i>complete</i>	<i>star</i>
<i>Localized states</i>	$O(t^2)$	$O(t^2)$	$O(t^2)$
<i>Maximum QFI states</i>	$O(t^2)$ for energy eigenstates in Table 2.1 $O(t^4)$ for odd N and highest energy eigenstate (2.14) or (2.15)	$O(t^4)$	$O(t^4)$

Table 2.5. Behavior at short times t of the classical Fisher information of the cycle, complete, and star graphs, for localized and maximum QFI states. The maximum QFI state is the superposition of the ground state and the highest-energy eigenstate. The QFI is always $O(t^2)$, even at short and long times (see Eq. (2.44)), since the perturbation \mathcal{H}_1 is time independent.

Appendices

2.A Analytical derivation of the results for the dynamics

The dynamics of the system is essentially encoded in the time evolution of the density matrix. For an initially localized state $|i\rangle$, the density matrix is given by $\rho(t) = |i(t)\rangle\langle i(t)|$, whose generic element in the position basis is

$$\rho_{j,k}(t) = \langle j|\mathcal{U}_\lambda(t)|i\rangle\langle i|\mathcal{U}_\lambda^\dagger(t)|k\rangle, \quad (2.75)$$

where the time-evolution operator $\mathcal{U}_\lambda(t)$ is defined in Eq. (2.2). The probability distribution is given by the diagonal elements of the density matrix

$$P_i(j, t|\lambda) = |\langle j|i(t)\rangle|^2 = \langle j|i(t)\rangle\langle i(t)|j\rangle = \rho_{j,j}(t). \quad (2.76)$$

On the other hand, the modulus of the off-diagonal elements of the density matrix entering the definition of coherence in Eq. (2.6) can also be expressed in terms of probabilities:

$$|\rho_{j,k}(t)| = |\langle j|\mathcal{U}_\lambda(t)|i\rangle\langle k|\mathcal{U}_\lambda(t)|i\rangle| = \sqrt{P_i(j, t|\lambda)P_i(k, t|\lambda)}. \quad (2.77)$$

2.A.1 Cycle Graph

According to the time-evolution operator and to the spectral decomposition in Table 2.1, in a cycle graph an initially localized state $|j\rangle$ evolves in time as

$$|j(t)\rangle = \frac{1}{\sqrt{N}} \sum_{n=0}^{N-1} e^{-iE_n^\lambda t} e^{i\frac{2\pi}{N}jn} |e_n\rangle, \quad (2.78)$$

where $E_n^\lambda := \varepsilon_n + \lambda\varepsilon_n^2$, and $\exp\{i\frac{2\pi}{N}jn\}/\sqrt{N} = \langle e_n|j\rangle$. Then, the probability of finding the walker in the vertex k at time t is

$$P_j(k, t|\lambda) = \frac{1}{N^2} \sum_{n,m=0}^{N-1} e^{-i(E_n^\lambda - E_m^\lambda)t} e^{i\frac{2\pi}{N}(n-m)(j-k)}. \quad (2.79)$$

This expression leads to Eq. (2.18) as follows. Let p_{nm} be the summand, excluding $1/N^2$. The summation over m can be split in three different summations: one over $m = n$ (providing

$\sum_n p_{nn} = N$), one over $m > n$, and one over $m < n$. Since $p_{nm} = p_{mn}^*$, then $\sum_{m < n} p_{nm} = \sum_{m > n} p_{mn}^*$, so $\sum_{m > n} (p_{nm} + p_{mn}^*) = 2 \sum_{m > n} \text{Re}\{p_{nm}\}$, with $\text{Re}\{p_{nm}\} = \cos[\arg(p_{nm})]$.

To prove that the probability distribution is symmetric with respect to the starting vertex j , i.e., that $P_j(j+k, t|\lambda) = P_j(j-k, t|\lambda)$, we consider Eq. (2.79). The left-hand side is

$$P_j(j+k, t|\lambda) = \frac{1}{N^2} \sum_{n,m=0}^{N-1} e^{-i(E_n^\lambda - E_m^\lambda)t} e^{i(2\pi/N)(n-m)(-k)}. \quad (2.80)$$

Now, letting $l = N - n$ ($q = N - m$) be the new summation index, since $\varepsilon_{N-l} = \varepsilon_l$ ($\varepsilon_{N-q} = \varepsilon_q$), we have that

$$\begin{aligned} P_j(j+k, t|\lambda) &= \frac{1}{N^2} \sum_{l,q=1}^N e^{-i(E_l^\lambda - E_q^\lambda)t} e^{i(2\pi/N)(q-l)(-k)} \\ &= \frac{1}{N^2} \sum_{l,q=0}^{N-1} e^{-i(E_l^\lambda - E_q^\lambda)t} e^{i(2\pi/N)(l-q)[j-(j-k)]} \\ &= P_j(j-k, t|\lambda). \end{aligned} \quad (2.81)$$

The second equality holds since the summand of index $l = N$ ($q = N$) is equal to that of index $l = 0$ ($q = 0$). Indeed, according to Table 2.1, the virtual E_N^λ is equal to E_0^λ (the actual energies have index running from 0 to $N - 1$). In addition, $\exp\{i\frac{2\pi}{N}(q-l)k\}$ returns the same value if evaluated in $l = N$ ($q = N$) or $l = 0$ ($q = 0$).

Finally, we justify the expression of the variance of the position in Eq. (2.19). We assume even N , $|j = N/2\rangle$ as the initial state, and $t \ll 1$. The variance requires the expectation values of \hat{x} and \hat{x}^2 , and the vertex states are eigenstates of the position operator. The probability distribution (2.18) is symmetric about the starting vertex, thus $\langle \hat{x} \rangle = N/2$, and it involves summands of the form

$$\begin{aligned} \cos(\alpha t + \beta) &= \cos(\alpha t) \cos \beta - \sin(\alpha t) \sin \beta \\ &= \left(1 - \frac{\alpha^2}{2} t^2\right) \cos \beta - \alpha t \sin \beta + O(t^3), \end{aligned} \quad (2.82)$$

since $t \ll 1$. Hence, letting $\alpha_{nm} = E_n^\lambda - E_m^\lambda$ and $\beta_{nm}^{kj} = \frac{2\pi}{N}(n-m)(k-j)$, we can write

$$\begin{aligned} \langle \hat{x}^2(t) \rangle &\approx \frac{1}{N} \sum_{k=0}^{N-1} k^2 + \frac{2}{N^2} \sum_{\substack{n=0, \\ m>n}}^{N-1} \sum_{k=0}^{N-1} \left[k^2 \cos \beta_{nm}^{kj} - \frac{t^2}{2} k^2 \alpha_{nm}^2 \cos \beta_{nm}^{kj} - t k^2 \alpha_{nm} \sin \beta_{nm}^{kj} \right] \\ &= \frac{1}{6}(N-1)(2N-1) - \frac{1}{12}[N(N-6)+2] + 2t^2(20\lambda^2 + 8\lambda + 1) \\ &= \frac{N^2}{4} + \left[40\left(\lambda + \frac{1}{5}\right)^2 + \frac{2}{5}\right] t^2. \end{aligned} \quad (2.83)$$

Then, the variance (2.19) follows, and is symmetric with respect to $\lambda_0 = -1/5$.

2.A.2 Complete Graph

The complete graph has two energy levels (see Table 2.2), thus the unitary time-evolution operator has the spectral decomposition

$$\mathcal{U}_\lambda(t) = |e_0\rangle\langle e_0| + e^{-2i\omega_N(\lambda)t} \sum_{l=1}^{N-1} |e_1^l\rangle\langle e_1^l|, \quad (2.84)$$

with $\omega_N(\lambda)$ defined in Eq. (2.25). Hence, a localized state $|0\rangle$ evolves in time according to

$$|0(t)\rangle = \frac{1}{N} \left[1 + (N-1)e^{-i2\omega_N(\lambda)t} \right] |0\rangle + \frac{1}{N} \left(1 - e^{-i2\omega_N(\lambda)t} \right) \sum_{k=1}^{N-1} |k\rangle. \quad (2.85)$$

Then, the density matrix $\rho(t) = |0(t)\rangle\langle 0(t)|$ in the position basis is

$$\rho(t) = [1 - (N-1)A] |0\rangle\langle 0| + (A+B) \sum_{k=1}^{N-1} |0\rangle\langle k| + (A+B^*) \sum_{k=1}^{N-1} |k\rangle\langle 0| + A \sum_{j,k=1}^{N-1} |j\rangle\langle k|, \quad (2.86)$$

where

$$A = \frac{4}{N^2} \sin^2(\omega_N(\lambda)t), \quad (2.87)$$

$$B = \frac{1}{N} \left(e^{-2it\omega_N(\lambda)} - 1 \right). \quad (2.88)$$

The diagonal elements of $\rho(t)$ provide the probability distribution in Eqs. (2.26) and (2.27). Instead, the off-diagonal elements allow us to compute the coherence according to Eq. (2.6) and it reads

$$\mathcal{C}(t) = 2(N-1)|A+B| + (N-1)(N-2)|A|. \quad (2.89)$$

2.A.3 Star graph

The star graph has three energy levels (see Table 2.3), thus the unitary time-evolution operator has the spectral decomposition

$$\mathcal{U}_\lambda(t) = |e_0\rangle\langle e_0| + e^{-2it\omega_1} \sum_{l=1}^{N-2} |e_1^l\rangle\langle e_1^l| + e^{-2it\omega_N} |e_2\rangle\langle e_2|, \quad (2.90)$$

with $\omega_N(\lambda)$ defined in Eq. (2.25). Hence, a localized state $|1\rangle$, i.e., an outer vertex, evolves in time according to

$$\begin{aligned} |1(t)\rangle &= \frac{1}{N} (1 - e^{-i2\omega_N(\lambda)t}) |0\rangle + \left(\frac{1}{N} + \frac{N-2}{N-1} e^{-i2\omega_1(\lambda)t} + \frac{e^{-i2\omega_N(\lambda)t}}{N(N-1)} \right) |1\rangle \\ &+ \left(\frac{1}{N} - \frac{e^{-i2\omega_1(\lambda)t}}{N-1} + \frac{e^{-i2\omega_N(\lambda)t}}{N(N-1)} \right) \sum_{k=2}^{N-1} |k\rangle. \end{aligned} \quad (2.91)$$

Instead, if the initial state is the central vertex $|0\rangle$, we recover the time evolution of a localized state in the complete graph of the same size (see Eq. (2.85)) and thus the same results. Then the density matrix $\rho(t) = |1(t)\rangle\langle 1(t)|$ in the position basis is

$$\begin{aligned} \rho(t) &= |A|^2 |0\rangle\langle 0| + |B|^2 |1\rangle\langle 1| + |C|^2 \sum_{k=2}^{N-1} |k\rangle\langle k| + \left[|C|^2 \sum_{\substack{j,k=2, \\ k>j}}^{N-1} |j\rangle\langle k| + AB^* |0\rangle\langle 1| \right. \\ &\left. + \sum_{k=2}^{N-1} (AC^* |0\rangle\langle k| + BC^* |1\rangle\langle k|) + \text{H.c.} \right], \end{aligned} \quad (2.92)$$

where H.c. denotes the Hermitian conjugate of the off-diagonal terms only and

$$A = \frac{1}{N}(1 - e^{-i2\omega_N(\lambda)t}), \quad (2.93)$$

$$B = \frac{1}{N} + \frac{N-2}{N-1}e^{-i2\omega_1(\lambda)t} + \frac{e^{-i2\omega_N(\lambda)t}}{N(N-1)}, \quad (2.94)$$

$$C = \frac{1}{N} - \frac{e^{-i2\omega_1(\lambda)t}}{N-1} + \frac{e^{-i2\omega_N(\lambda)t}}{N(N-1)} \quad (2.95)$$

are the coefficients of $|1(t)\rangle$ in the position basis (see Eq. (2.91)). The diagonal elements of $\rho(t)$ provide the probability distribution in Eqs. (2.36)–(2.38). Instead, the off-diagonal elements allow us to compute the coherence according to Eq. (2.6). Given the counting of the different matrix elements, since $|\rho_{j,k}(t)| = |\rho_{k,j}(t)|$, the coherence reads

$$\mathcal{C}(t) = 2|AB^*| + 2(N-2)(|AC^*| + |BC^*|) + (N-2)(N-3)|C|^2. \quad (2.96)$$

The issue of the periodicity of the probability distribution is still pending. Ultimately, the overall probability distribution is periodic if and only if the periods of the sine functions involved by the probabilities (2.36)–(2.38) are commensurable. Since such sine functions are squared, the periods are:

$$T_1(\lambda) := \frac{\pi}{\omega_1(\lambda)} = \frac{2\pi}{1+\lambda}, \quad (2.97)$$

$$T_N(\lambda) := \frac{\pi}{\omega_N(\lambda)} = \frac{2\pi}{N+\lambda N^2}, \quad (2.98)$$

$$T_{N,1}(\lambda) := \frac{\pi}{\omega_N(\lambda) - \omega_1(\lambda)} = \frac{2\pi}{(N-1)[1+\lambda(N+1)]}. \quad (2.99)$$

Two nonzero real numbers are commensurable if their ratio is a rational number. The idea is therefore to express both $T_1(\lambda)$ and $T_{N,1}(\lambda)$ as multiple integers of $T_N(\lambda)$. From the ratio $T_1(\lambda)/T_N(\lambda)$ we get

$$T_1(\lambda) = \frac{N(1+\lambda N)}{1+\lambda}T_N(\lambda) =: p_N^\lambda T_N(\lambda), \quad (2.100)$$

with $\lambda \neq -1 \wedge \lambda \neq -1/N$, and from $T_{N,1}(\lambda)/T_N(\lambda)$

$$T_{N,1}(\lambda) = \frac{N(1+\lambda N)}{(N-1)[1+\lambda(N+1)]}T_N(\lambda) =: q_N^\lambda T_N(\lambda), \quad (2.101)$$

with $\lambda \neq -1/N \wedge \lambda \neq -1/(N+1)$. Then, we need to find the value of λ such that $p_N^\lambda, q_N^\lambda \in \mathbb{N}$ at the same time. Combining the definition of p_N^λ and q_N^λ in Eqs. (2.100) and (2.101), we find that they are related to λ and N by

$$\lambda = \frac{p_N^\lambda - q_N^\lambda(N-1)}{q_N^\lambda(N^2-1) - p_N^\lambda}. \quad (2.102)$$

Note that Eq. (2.102) is to be understood together with Eqs. (2.100) and (2.101). As an example, for $p_N^\lambda = q_N^\lambda$ we get $\lambda = (2-N)/(N^2-2)$ from Eq. (2.102). However, the period is unique, so we cannot choose any $p_N^\lambda = q_N^\lambda$. Indeed, for such a value of λ we get $p_N^\lambda = q_N^\lambda = 2$ from Eqs. (2.100) and (2.101). In the end, by considering the least common multiple of the latter two integers, the total period of the probability distribution is

$$T = \text{lcm}(p_N^\lambda, q_N^\lambda)T_N(\lambda). \quad (2.103)$$

The above ratios (2.100) and (2.101) between the different periods are properly defined unless $\lambda = -1, -1/N, -1/(N+1)$. Nevertheless, for such values of λ the overall probability distribution is actually periodic. If we let $p, q \in \mathbb{Z}$, we recover them from Eq. (2.102) for $q = 0, q = -p$, and $p = 0$, respectively. These values of λ make ω_1, ω_N , and $\omega_N - \omega_1$ vanish, respectively. When $\omega_1 = 0$ ($\omega_N = 0$), the probabilities only involve sine functions with ω_N (ω_1). When $\omega_N = \omega_1$, all the sine functions have the same angular frequency.

2.B Fisher Information and Quantum Fisher Information for localized states and states maximizing the QFI

In this appendix we prove the analytical results about the quantum Fisher information in Eq. (2.41) and the Fisher information in Eq. (2.42) in the different graphs. We provide the FI for a local position measurement whose POVM is given by $\{|0\rangle\langle 0|, |1\rangle\langle 1|, \dots, |N-1\rangle\langle N-1|\}$, i.e., by the projectors on the vertex states. Lemma 1 (from Parthasarathy) leads to the QFI in Eq. (2.58), because the state maximizing the QFI involves the ground state and the highest energy eigenstate. The highest-energy level might be degenerate, but choosing any eigenstate of such level results in the same QFI. Instead, the FI does depend on such a choice.

2.B.1 Cycle graph

Localized state The QFI in Eq. (2.44) requires the expectation values of L^2 (2.16) and of

$$L^4 = 70I + \sum_{k=0}^{N-1} (|k-4\rangle\langle k| - 8|k-3\rangle\langle k| + 28|k-2\rangle\langle k| - 56|k-1\rangle\langle k| + \text{H.c.}), \quad (2.104)$$

on the initial state $|j\rangle$. These are $\langle L^2 \rangle = 6$ and $\langle L^4 \rangle = 70$, from which Eq. (2.45) follows.

States maximizing the QFI In the cycle graph the ground state is unique, whereas the degeneracy of the highest-energy level depends on the parity of N (see Table 2.1). We define $E_\lambda := \varepsilon_{max} + \lambda \varepsilon_{max}^2$, where ε_{max} is the highest-energy eigenvalue of L (see Eqs. (2.10) and (2.12) for even and odd N , respectively).

For even N , according to Eq. (2.65) the state maximizing the QFI is

$$|\psi_0(t)\rangle = \frac{1}{\sqrt{2N}} \sum_{k=0}^{N-1} [1 + (-1)^k e^{-iE_\lambda t}] |k\rangle, \quad (2.105)$$

and the maximum QFI (2.66) follows from Eq. (2.58). Then, the probability distribution associated with a position measurement is

$$P_M(k, t|\lambda) = \frac{1}{N} [1 + (-1)^k \cos(E_\lambda t)]. \quad (2.106)$$

Hence, observing that the dependence on the vertex is encoded only into an alternating sign, the

FI is

$$\begin{aligned}
 \mathcal{F}_c(N, t, \lambda) &= \sum_{k=0}^{N/2-1} \left[\frac{(\partial_\lambda P_M(2k, t|\lambda))^2}{P_M(2k, t|\lambda)} + \frac{(\partial_\lambda P_M(2k+1, t|\lambda))^2}{P_M(2k+1, t|\lambda)} \right] \\
 &= \frac{\varepsilon_{max}^4 t^2 \sin^2(E_\lambda t)}{N^2} \sum_{k=0}^{N/2-1} \left[\frac{N}{1 + \cos(E_\lambda t)} + \frac{N}{1 - \cos(E_\lambda t)} \right] \\
 &= \frac{\varepsilon_{max}^4 t^2 \sin^2(E_\lambda t)}{N^2} \frac{N}{2} \frac{2N}{\sin^2(E_\lambda t)} = \varepsilon_{max}^4 t^2 = \mathcal{F}_q(t). \tag{2.107}
 \end{aligned}$$

That is to say, the position measurement for the state maximizing the QFI in a cycle graph having an even number of vertices is optimal, since the corresponding FI equals the QFI.

For odd N , the situation is trickier: The state maximizing the QFI is not unique, because of the degeneracy of the highest-energy level. We may consider the two corresponding eigenstates according to Table 2.1, which lead to the states maximizing the QFI,

$$|\varphi_0^\pm(t)\rangle = \frac{1}{\sqrt{2N}} \sum_{k=0}^{N-1} [1 + (-1)^k e^{\pm i\theta_k} e^{-iE_\lambda t}] |k\rangle, \tag{2.108}$$

where $\theta_k = \pi k/N$. On the other hand, we may also consider the linear combinations of such eigenstates (see Eqs. (2.14) and (2.15)), which lead to the states maximizing the QFI,

$$|\psi_0^+(t)\rangle = \frac{1}{\sqrt{2N}} \sum_{k=0}^{N-1} [1 + \sqrt{2}(-1)^k \cos \theta_k e^{-iE_\lambda t}] |k\rangle, \tag{2.109}$$

$$|\psi_0^-(t)\rangle = \frac{1}{\sqrt{2N}} \sum_{k=0}^{N-1} [1 + \sqrt{2}(-1)^k \sin \theta_k e^{-iE_\lambda t}] |k\rangle. \tag{2.110}$$

Under the assumption of odd N , and according to the results

$$\sum_{k=0}^{N-1} \cos^2 \theta_k = \sum_{k=0}^{N-1} \sin^2 \theta_k = \frac{N}{2}, \tag{2.111}$$

$$\sum_{k=0}^{N-1} (-1)^k e^{\pm i\theta_k} = \frac{1 + (-1)^N}{1 + e^{\pm i\frac{\pi}{N}}} \stackrel{\text{odd } N}{=} 0, \tag{2.112}$$

the maximum QFI (2.66) follows from Eq. (2.58) and does not depend on the choice of these states. Instead, we prove that the FI does depend on them. Again, there is an alternating sign which depends on the vertex. In the following, we will split the sum over even and odd indices, and for odd N it reads

$$\sum_{k=0}^{N-1} a_k = \sum_{k=0}^{(N-1)/2} a_{2k} + \sum_{k=0}^{(N-1)/2-1} a_{2k+1}. \tag{2.113}$$

We first consider the states $|\varphi_0^\pm(t)\rangle$ in Eq. (2.108). The probability distribution associated with a position measurement is

$$P_M^\pm(k, t|\lambda) = \frac{1}{N} [1 + (-1)^k \cos(E_\lambda t \mp \theta_k)]. \tag{2.114}$$

Hence the FI is

$$\begin{aligned}
 \mathcal{F}_c^\pm(|\varphi_0^\pm\rangle; N, t, \lambda) &= \frac{\varepsilon_{max}^4 t^2}{N} \left[\sum_{k=0}^{(N-1)/2} \frac{\sin^2(E_\lambda t \mp \theta_{2k})}{1 + \cos(E_\lambda t \mp \theta_{2k})} + \sum_{k=0}^{(N-1)/2-1} \frac{\sin^2(E_\lambda t \mp \theta_{2k+1})}{1 - \cos(E_\lambda t \mp \theta_{2k+1})} \right] \\
 &= \frac{\varepsilon_{max}^4 t^2}{N} \left[\sum_{k=0}^{(N-1)/2} (1 - \cos(E_\lambda t \mp \theta_{2k})) + \sum_{k=0}^{(N-1)/2-1} (1 + \cos(E_\lambda t \mp \theta_{2k+1})) \right] \\
 &= \frac{\varepsilon_{max}^4 t^2}{N} \left[\frac{N-1}{2} + 1 + \frac{N-1}{2} - 1 + 1 \right] \\
 &= \varepsilon_{max}^4 t^2 = \mathcal{F}_q(t). \tag{2.115}
 \end{aligned}$$

Indeed, for odd N ,

$$\sum_{k=0}^{(N-1)/2} \cos(\theta_{2k} + \phi) - \sum_{k=0}^{(N-1)/2-1} \cos(\theta_{2k+1} + \phi) = \sum_{k=0}^{N-1} (-1)^k \cos(\theta_k + \phi) = 0. \tag{2.116}$$

Now we focus on the state $|\psi_0^+(t)\rangle$ in Eq. (2.109). The probability distribution associated with a position measurement is

$$P_M^+(k, t|\lambda) = \frac{1}{2N} \left[1 + 2\sqrt{2}(-1)^k \cos \theta_k \cos(E_\lambda t) + 2 \cos^2 \theta_k \right]. \tag{2.117}$$

Hence the FI is

$$\begin{aligned}
 \mathcal{F}_c^+(|\psi_0^+\rangle; N, t, \lambda) &= \frac{4\varepsilon_{max}^4 t^2 \sin^2(E_\lambda t)}{N} \left[\sum_{k=0}^{(N-1)/2} \frac{\cos^2 \theta_{2k}}{1 + 2\sqrt{2} \cos \theta_{2k} \cos(E_\lambda t) + 2 \cos^2 \theta_{2k}} \right. \\
 &\quad \left. + \sum_{k=0}^{(N-1)/2-1} \frac{\cos^2 \theta_{2k+1}}{1 - 2\sqrt{2} \cos \theta_{2k+1} \cos(E_\lambda t) + 2 \cos^2 \theta_{2k+1}} \right]. \tag{2.118}
 \end{aligned}$$

Analogously for $|\psi_0^-(t)\rangle$ in Eq. (2.110), we find

$$\begin{aligned}
 \mathcal{F}_c^-(|\psi_0^-\rangle; N, t, \lambda) &= \frac{4\varepsilon_{max}^4 t^2 \sin^2(E_\lambda t)}{N} \left[\sum_{k=0}^{(N-1)/2} \frac{\sin^2 \theta_{2k}}{1 + 2\sqrt{2} \sin \theta_{2k} \cos(E_\lambda t) + 2 \sin^2 \theta_{2k}} \right. \\
 &\quad \left. + \sum_{k=0}^{(N-1)/2-1} \frac{\sin^2 \theta_{2k+1}}{1 - 2\sqrt{2} \sin \theta_{2k+1} \cos(E_\lambda t) + 2 \sin^2 \theta_{2k+1}} \right]. \tag{2.119}
 \end{aligned}$$

Numerical results suggest that $\mathcal{F}_c^\pm(|\psi_0^\pm\rangle; N, t, \lambda) < \mathcal{F}_q(t)$. Notice that

$$\mathcal{F}_c^\pm(|\psi_0^\pm\rangle; N, t, \lambda = -1/\varepsilon_{max}) = 0 \quad \forall t. \tag{2.120}$$

Indeed, for such a value of λ we have that $E_\lambda = 0$.

2.B.2 Complete graph

Localized state The QFI in Eq. (2.44) requires the expectation values of L^2 and of L^4 on the initial state $|0\rangle$. Because of Eqs. (2.21) and (2.22), we only need $\langle L \rangle = N - 1$, from which Eq. (2.46) follows.

States maximizing the QFI The complete graph has two energy levels: The ground state is unique, but the highest energy level is $N - 1$ degenerate (see Table 2.2). The QFI does not depend on the choice of the eigenstate of the highest energy level, but the FI does. As an example, we consider two different states maximizing the QFI $|\psi_0^1\rangle$ and $|\psi_0^{N-1}\rangle$, i.e., the states in Eq. (2.67) for $l = 1$ and $l = N - 1$, respectively.

The first state is

$$|\psi_1^0(t)\rangle = \frac{1}{\sqrt{2}} \left[|e_0\rangle + \frac{1}{\sqrt{2}} e^{-2it\omega_N(\lambda)} (|0\rangle - |1\rangle) \right]. \quad (2.121)$$

The probability distribution associated with a position measurement is

$$P_M^0(0, t|\lambda) = \frac{1}{4} + \frac{1}{2N} + \frac{\cos(2t\omega_N(\lambda))}{\sqrt{2N}}, \quad (2.122)$$

$$P_M^0(1, t|\lambda) = \frac{1}{4} + \frac{1}{2N} - \frac{\cos(2t\omega_N(\lambda))}{\sqrt{2N}}, \quad (2.123)$$

$$P_M^0(k, t|\lambda) = \frac{1}{2N}, \quad (2.124)$$

with $2 \leq k \leq N - 1$. Then, since the $N - 2$ contributions from the vertices $2 \leq k \leq N - 1$ are null and since $\partial_\lambda(P_M^0(k, t|\lambda)) = 0$, only the probabilities associated with the vertices $|0\rangle$ and $|1\rangle$ contribute to the FI (2.42), which results in Eq. (2.70).

Similarly, the second state is

$$|\psi_0^{N-1}(t)\rangle = \frac{1}{\sqrt{2}} \left\{ |e_0\rangle + \frac{1}{\sqrt{N^2 - N}} e^{-2it\omega_N(\lambda)} [|0\rangle + \dots + |N - 2\rangle - (N - 1)|N - 1\rangle] \right\}. \quad (2.125)$$

The probability distribution associated with a position measurement is

$$P_M^{N-1}(k, t|\lambda) = \frac{1}{2(N - 1)} + \frac{1}{N\sqrt{N - 1}} \cos(2t\omega_N(\lambda)), \quad (2.126)$$

with $0 \leq k \leq N - 2$, and

$$P_M^{N-1}(N - 1, t|\lambda) = \frac{1}{2} - \frac{\sqrt{N - 1}}{N} \cos(2t\omega_N(\lambda)). \quad (2.127)$$

Then, having $N - 1$ equal contributions from the vertices $0 \leq k \leq N - 2$ and a particular one from $N - 1$, the FI (2.42) results in Eq. (2.71).

2.B.3 Star graph

Localized state Considering the central vertex $|0\rangle$ as the initial state provides the same results observed in the complete graph of the same size. Thus, we consider as the initial state $|1\rangle$, i.e., one of the outer vertices. The QFI in Eq. (2.44) requires the expectation values of L^2 (2.34) and of

$$\begin{aligned} L^4 = & (N^2 + N + 2)I - N^3 \sum_{k=1}^{N-1} (|k\rangle\langle 0| + |0\rangle\langle k|) + (N - 2)(N^3 + N^2 + N + 1) |0\rangle\langle 0| \\ & + (N^2 + N + 1) \sum_{\substack{j,k=1, \\ j \neq k}}^{N-1} |j\rangle\langle k| \end{aligned} \quad (2.128)$$

on the initial state $|1\rangle$. These are $\langle L^2 \rangle = 2$ and $\langle L^4 \rangle = N^2 + N + 2$, from which Eq. (2.49) follows.

States maximizing the QFI In the star graph the state maximizing the QFI, according to Eq. (2.74), is

$$|\psi_0(t)\rangle = \frac{1}{\sqrt{2}} \left(|e_0\rangle + e^{-2it\omega_N(\lambda)} |e_2\rangle \right), \quad (2.129)$$

since both the ground and the highest-energy levels are not degenerate (see Table 2.3). Then the probability distribution associated with a position measurement is

$$P_M(0, t|\lambda) = \frac{1}{2} + \frac{\sqrt{N-1}}{N} \cos(2t\omega_N(\lambda)), \quad (2.130)$$

$$P_M(k, t|\lambda) = \frac{1}{2(N-1)} - \frac{1}{N\sqrt{N-1}} \cos(2t\omega_N(\lambda)), \quad (2.131)$$

with $1 \leq k \leq N-1$. Then, the FI follows from Eq. (2.42).

2.B.4 Maximum QFI states: the role of the phase factor in the superposition of energy eigenstates

So far we have studied the states maximizing the QFI without bothering to consider a different linear combination of the ground state and the highest energy state. According to Lemma 1 from Parthasarathy, the two eigenstates defining the state in Eq. (2.56) are equally weighted. However, we may suppose that the second one has a phase factor, i.e.,

$$|\psi_0\rangle = \frac{1}{\sqrt{2}} (|e_0\rangle + e^{i\phi} |e_1\rangle). \quad (2.132)$$

In this section, we study how the phase ϕ affects the FI and QFI.

The states $|e_0\rangle$ and $|e_1\rangle$ denote the eigenstates of minimum and maximum energy eigenvalues, i.e., ε_{min} and ε_{max} respectively, and we know that for simple graphs $|e_0\rangle = (1, \dots, 1)/\sqrt{N}$ and $\varepsilon_{min} = 0$. Moreover, since the Laplacian matrix is real and symmetric, we can always deal with real eigenstates. Because of Eq. (2.44), we already know that the QFI is (2.58) and therefore it is independent of a phase shift. On the other hand, the FI reads

$$\mathcal{F}_c(t, \lambda) = 2t^2 \varepsilon_{max}^4 \sin^2(E_\lambda t - \phi) \sum_{i=0}^{N-1} \frac{\langle i|e_1\rangle^2}{N\langle i|e_1\rangle^2 + 2\sqrt{N}\langle i|e_1\rangle \cos(E_\lambda t - \phi) + 1}, \quad (2.133)$$

where $E_\lambda := \varepsilon_{max} + \lambda \varepsilon_{max}^2$, and $\langle i|e_1\rangle \in \mathbb{R}$, since the vectors involved are real. Hence, the phase is encoded as a phase shift in all the sine and cosine functions. However, this does not result in a global time shift, because the quadratic term in t is not affected by ϕ .

Chapter 3

Continuous-time quantum walks on planar lattices and the role of the magnetic field

In this chapter we address the dynamics of continuous-time quantum walks (CTQW) on planar lattice graphs (regular tessellations of the Euclidean plane). We analytically derive the Hamiltonian of the system and numerically simulate the time evolution of an initially localized walker. We find that the CTQW of the free walker is not universally characterized by the ballistic spreading, which is proved only on hypercubes and in 1D. We impute this to the distinction between Bravais and non-Bravais lattices and to the different amount of coherence generated by the evolution. Then we insert a perpendicular uniform magnetic field and compare two different approaches: (i) introducing the Peierls phase-factors; (ii) spatially discretizing the Hamiltonian of the corresponding system in the continuum. The larger the field is, the more localized the walker stays. The approach (ii) also provides a variance of the position characterized by pseudo-oscillations, a reminiscence of the harmonic oscillator behind the Hamiltonian in the continuum.

3.1 Introduction

Quantum walks (QWs) describe the motion of a quantum particle in a discrete space, e.g., a graph or a lattice. QWs can be either *discrete* (DTQW) [2-4, 121] or *continuous* (CTQW) [5, 6] in time. In the former case, the evolution operator of the system is given by the product of two unitary operators – a “coin flip” operator and a conditional shift operator – and it is applied only in discrete time steps, while in the latter case, the evolution operator involves the Hamiltonian of the system, it can be applied at any time, and no coin is involved. QWs show a *ballistic* spreading, faster than their classical analogs, characterized by a *diffusive* spreading. This is usually observed on a line, but it has been also proved for DTQWs in a higher number of spatial dimensions (the particle moves by one unit in every dimension), revealing the universal feature of a quadratic gain over the classical random walk [122].

The interest in considering general graphs [99], different topologies, and in increasing the number of spatial dimensions of the lattice stems from the variety of applications and potential use of the QWs. In this regard we mention the use of QWs in search algorithms on graphene [123, 124] and crystal [125] lattices, the universal quantum computation by means of a simple QW on a sparse graph [26], implementing quantum gates by means of DTQWs using graphene armchair and zigzag nanoribbons [126], and modeling phenomena of quantum transport on graphene structures [127]. Experimentally, two-dimensional (2D) DTQWs have been implemented for a

neutral atom in an array of optical microtraps or an optical lattice [128] and for photons by using an optical fiber network [129, 130]. On the other hand, 2D CTQWs have been implemented by using the external geometry of photonic waveguide arrays, e.g., for a square lattice (showing a ballistic spreading) [18] and for a hexagonal graph mapped into a photonic chip (demonstrating quantum fast hitting) [19].

In the present chapter, we study CTQWs on planar lattice graphs, i.e., those forming a regular tessellation of the Euclidean plane, and we examine the spreading dynamics of the walker by means of the variance of the space coordinates and the maps of probability distribution. The choice of these geometries allows us to go beyond the CTQW on a line, introducing some degree of arbitrariness while avoiding the complexity of higher dimensional lattices. An analogous problem, the CTQW on root lattice A_n (triangular lattice for $n = 2$) and honeycomb one, has been investigated by using the spectral distribution method in Ref. [131], and DTQWs on the honeycomb and triangular lattices have been proved to have, as continuum limit, the Dirac equation [132]. The prototypical CTQW on a graph is defined from the graph Laplacian, but, in principle, any Hamiltonian (or, generally, any Hermitian operator) which respects the topology of the graph defines a CTQW [11, 12]. Indeed, the graph Laplacian plays the role of the free particle energy, but, in addition to this kinetic term, the Hamiltonian may also include noise [94, 133], potentials, or interaction terms [46, 134].

Recently, DTQWs on square lattices under artificial magnetic fields have been considered [135]. An artificial or synthetic magnetic field can be simulated as follows [136]: Instead of using charged particles in an actual magnetic field, one typically uses neutral particles upon which the effects of a fictitious magnetic field are imposed, e.g., Raman-laser-induced Berry phases [137]. Another approach to realize DTQWs in synthetic gauge fields is to use integrated photonic circuits [138]. It has been shown recently that 2D DTQWs can simulate the coupling of a Dirac fermion to a constant uniform magnetic field [139].

To the best of our knowledge, 2D CTQWs in the presence of a magnetic field have not been yet investigated. We address the problem in two ways: (i) by introducing the Peierls phase-factors, according to which the tunneling matrix element of the free particle becomes complex [135], and (ii) by spatially discretizing the original Hamiltonian in the continuum by means of finite difference formulas, which is the way lattice quantum magnetometry has been introduced [140]. Whereas the Peierls model is fundamentally based on the graph Laplacian, the spatial discretization of the Hamiltonian requires also the discrete analog of the first-order differential operator, since the linear momentum is now present even at the first order, due to the cross terms with the vector potential. In turn, the spatial discretization of differential operators for nonsquare lattices is nontrivial.

3.2 CTQW on planar lattice graphs

3.2.1 Planar lattice graph

In graph theory, a graph G is said to be *planar* if it can be drawn in the plane in such a way that pairs of edges intersect only at vertices, if at all. Such a drawing is a *planar embedding* of G [51, 141]. A *lattice graph* is a graph possessing a drawing whose embedding in a Euclidean space \mathbb{R}^n forms a *regular tiling* [142–144]. It is a simple graph with a distance measurement (called metric) of a geometric object, it is a regular graph, and each edge has the same weight or represents the same distance in Euclidean space as in other spaces [145]. A *tiling* of regular polygons (in two dimensions), polyhedra (in three dimensions), or polytopes (in n dimensions) is called a *tessellation*. In other words, we may say that a tessellation is *regular* if it has regular faces and a regular vertex figure at each vertex. There are exactly three regular tessellations composed of regular polygons symmetrically tiling the plane: equilateral triangles, squares and regular hexagons

(Fig. 3.1) [146–148]. Tessellations can be specified using a *Schläfli symbol*, which is a symbol of the form $\{p, q, r, \dots\}$ used to describe regular polygons, polyhedra, and their higher dimensional counterparts. The symbol $\{p, q\}$ denotes a tessellation of regular p -gons, q surrounding each vertex [146, 149]. In view of these preliminary definitions, we call *planar lattice graph* (PLG) a graph possessing a drawing whose embedding in a Euclidean plane forms a regular tiling, i.e., a regular tessellation. This leads only to triangular, square, and honeycomb lattice graphs.

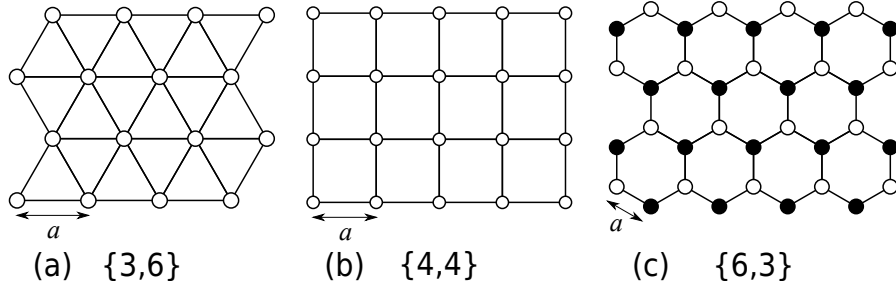


Figure 3.1. The three regular tessellations of the Euclidean plane: (a) equilateral triangles, (b) squares, and (c) regular hexagons. Below each tessellation, the corresponding Schläfli symbol is reported. These tessellations lead, respectively, to triangular, square, and honeycomb lattice graph. Equivalent vertices are represented with same circles and a denotes the lattice parameter.

In a Bravais lattice, both the arrangement and orientation of the array of vertices must appear the same from every vertex in the lattice. Unlike in the triangular and square lattice graph, which are clearly Bravais lattices and all their vertices are equivalent, in the honeycomb one vertices are not all equivalent. Structural relations are identical, but not orientational relations, so the vertices of a honeycomb do not form a Bravais lattice [150].

We introduce here below the notation adopted in the following. When considering a lattice, a generic vertex (site) V is identified by a couple of discrete indices $(j_V, k_V) \in \mathbb{Z}^2$. We denote the lattice parameter by a , the coordinates of the vertex V by (x_V, y_V) , and a generic scalar function of the position by $f(x_V, y_V)$. In the following, since the explicit use of discrete indices or coordinates might be misleading and confusing (see Appendix 3.B.2 for details), we will refer to a generic vertex V and its nearest neighbors (NNs) as shown in Table 3.1, and we simplify the notation according to $f_V := f(x_V, y_V)$. Moreover, the honeycomb lattice graph is characterized by two classes of non-equivalent vertices, $\{\circ, \bullet\}$ (see Fig. 3.1(c)). Thus, for this PLG, we define the variable $\odot \in \{\circ, \bullet\}$, we denote by $\bar{\odot}$ its complement in the same set, i.e., $\bar{\circ} = \bullet$ and $\bar{\bullet} = \circ$, and we define

$$\text{sgn}(\odot) = \begin{cases} +1 & \text{if } \odot = \circ, \\ -1 & \text{if } \odot = \bullet. \end{cases} \quad (3.1)$$

3.2.2 The CTQW Hamiltonian on PLGs

We first consider the CTQW of the free particle, whose Hamiltonian merely consists of the kinetic term

$$T = -JL, \quad (3.2)$$

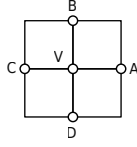
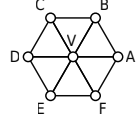
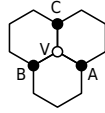
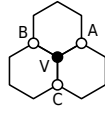
PLG	NNs of $V = (x_V, y_V)$
<p><i>Square</i></p> 	$\deg(V) = 4$ $A = (x_V + a, y_V)$ $B = (x_V, y_V + a)$ $C = (x_V - a, y_V)$ $D = (x_V, y_V - a)$
<p><i>Triangular</i></p> 	$\deg(V) = 6$ $A = (x_V + a, y_V)$ $B = (x_V + a/2, y_V + \sqrt{3}a/2)$ $C = (x_V - a/2, y_V + \sqrt{3}a/2)$ $D = (x_V - a, y_V)$ $E = (x_V - a/2, y_V - \sqrt{3}a/2)$ $F = (x_V + a/2, y_V - \sqrt{3}a/2)$
<p><i>Honeycomb, (V, \circ)</i></p> 	$\deg(V, \circ) = 3$ $(A, \bullet) = (x_V + \sqrt{3}a/2, y_V - a/2)$ $(B, \bullet) = (x_V - \sqrt{3}a/2, y_V - a/2)$ $(C, \bullet) = (x_V, y_V + a)$
<p><i>Honeycomb, (V, \bullet)</i></p> 	$\deg(V, \bullet) = 3$ $(A, \circ) = (x_V + \sqrt{3}a/2, y_V + a/2)$ $(B, \circ) = (x_V - \sqrt{3}a/2, y_V + a/2)$ $(C, \circ) = (x_V, y_V - a)$

Table 3.1. NNs of a vertex V in square, triangular, and honeycomb lattice graphs. The two classes of nonequivalent vertices in a honeycomb lattice graph are denoted as $\{\circ, \bullet\}$. The number of NNs is given by the degree of the vertex.

where $J \in \mathbb{R}^+$ is the hopping amplitude and we define the graph Laplacian¹ as

$$L = A - D, \quad (3.3)$$

in close connection to the Laplace operator ∇^2 . To find the generator of CTQWs on PLGs we have therefore to spatially discretize the kinetic energy term ($\hbar = 1$)

$$T = -\frac{1}{2m}\nabla^2 \quad (3.4)$$

according to the different PLGs. In doing so, we follow the same idea underlying the heuristic proof of the origin of the graph Laplacian in Sec. 1.1.2, i.e., Taylor expanding a scalar function f evaluated in the NNs about the given vertex and combining the resulting expansions in such a way that the discrete version of the Laplacian $\nabla^2 f = (\partial_x^2 + \partial_y^2)f$ is found in terms of finite differences. The hopping amplitude J will collect the factor $1/2m$ and all the geometrical factors resulting from the spatial discretization. For further details, please refer to Appendix 3.A.

We anticipate that in each PLG the discrete Laplacian turns out to be of the form

$$\nabla^2 f_V \sim \sum_{W \in NN(V)} f_W - \deg(V) f_V, \quad (3.5)$$

with $NN(V)$ the set of NNs of V , consistent with Eq. (3.3). The reason why we compute the Laplacian by means of Taylor expansion, even though it is analogous to the graph Laplacian, whose definition is much more manageable, is that this approach allows us to actually take into account the underlying geometry of the PLG. Indeed the graph Laplacian is a ready-made operator and there is no computation telling us how the hopping amplitude of the resulting CTQW Hamiltonian changes in the different PLGs. Instead, using Taylor expansion is a constructive way to determine the Laplacian, and the resulting Hamiltonian has a different hopping amplitude depending on the graph. This is a valuable feature, because by changing the degree of a vertex we expect the hopping amplitude to change accordingly.

Square lattice graph

A vertex V has four NNs, namely A , B , C , and D (see Table 3.1). We evaluate the following Taylor expansions about V up to the second order:

$$f_A \approx f_V + a\partial_x f_V + \frac{a^2}{2}\partial_x^2 f_V, \quad (3.6)$$

$$f_B \approx f_V + a\partial_y f_V + \frac{a^2}{2}\partial_y^2 f_V, \quad (3.7)$$

$$f_C \approx f_V - a\partial_x f_V + \frac{a^2}{2}\partial_x^2 f_V, \quad (3.8)$$

$$f_D \approx f_V - a\partial_y f_V + \frac{a^2}{2}\partial_y^2 f_V. \quad (3.9)$$

Now we consider a linear combination of the expressions above, understood as equalities:

$$\begin{aligned} \alpha f_A + \beta f_B + \gamma f_C + \delta f_D &= (\alpha + \beta + \gamma + \delta) f_V + a(\alpha - \gamma)\partial_x f_V + a(\beta - \delta)\partial_y f_V \\ &+ \frac{a^2}{2}(\alpha + \gamma)\partial_x^2 f_V + \frac{a^2}{2}(\beta + \delta)\partial_y^2 f_V. \end{aligned} \quad (3.10)$$

¹The proper mathematical definition of the Laplacian matrix is $L = D - A$. See also Sec. 1.1.2.

If we set $\alpha = \beta = \gamma = \delta = 1$, we get

$$\nabla^2 f_V = \frac{1}{a^2} (f_A + f_B + f_C + f_D - 4f_V). \quad (3.11)$$

The resulting finite-difference formula is the same used in numerical analysis [151]. According to this graph Laplacian, the Hamiltonian reads then as follows:

$$\hat{\mathcal{H}} = -J_S \sum_V (|A\rangle\langle V| + |B\rangle\langle V| + |C\rangle\langle V| + |D\rangle\langle V| - 4|V\rangle\langle V|), \quad (3.12)$$

where the hopping amplitude is

$$J_S := \frac{\hbar^2}{2ma^2}. \quad (3.13)$$

Triangular lattice graph

A vertex V has six NNs, namely A, B, C, D, E , and F (see Table 3.1). We evaluate the following Taylor expansions about V up to the second order:

$$f_A \approx f_V + a\partial_x f_V + \frac{a^2}{2}\partial_x^2 f_V, \quad (3.14)$$

$$f_B \approx f_V + \frac{a}{2}\partial_x f_V + \frac{\sqrt{3}a}{2}\partial_y f_V + \frac{a^2}{8}\partial_x^2 f_V + \frac{3a^2}{8}\partial_y^2 f_V, \quad (3.15)$$

$$f_C \approx f_V - \frac{a}{2}\partial_x f_V + \frac{\sqrt{3}a}{2}\partial_y f_V + \frac{a^2}{8}\partial_x^2 f_V + \frac{3a^2}{8}\partial_y^2 f_V, \quad (3.16)$$

$$f_D \approx f_V - a\partial_x f_V + \frac{a^2}{2}\partial_x^2 f_V, \quad (3.17)$$

$$f_E \approx f_V - \frac{a}{2}\partial_x f_V - \frac{\sqrt{3}a}{2}\partial_y f_V + \frac{a^2}{8}\partial_x^2 f_V + \frac{3a^2}{8}\partial_y^2 f_V, \quad (3.18)$$

$$f_F \approx f_V + \frac{a}{2}\partial_x f_V - \frac{\sqrt{3}a}{2}\partial_y f_V + \frac{a^2}{8}\partial_x^2 f_V + \frac{3a^2}{8}\partial_y^2 f_V. \quad (3.19)$$

Now we consider a linear combination of the expressions above, understood as equalities:

$$\begin{aligned} \alpha f_A + \beta f_B + \gamma f_C + \delta f_D + \varepsilon f_E + \phi f_F &= (\alpha + \beta + \gamma + \delta + \varepsilon + \phi) f_V \\ &+ \frac{a}{2} (2\alpha + \beta - \gamma - 2\delta - \varepsilon + \phi) \partial_x f_V + \frac{\sqrt{3}a}{2} (\beta + \gamma - \varepsilon - \phi) \partial_y f_V \\ &+ \frac{a^2}{8} (4\alpha + \beta + \gamma + 4\delta + \varepsilon + \phi) \partial_x^2 f_V + \frac{3a^2}{8} (\beta + \gamma + \varepsilon + \phi) \partial_y^2 f_V. \end{aligned} \quad (3.20)$$

If we set $\alpha = \beta = \gamma = \delta = \varepsilon = \phi = 1$, we get

$$\nabla^2 f_V = \frac{2}{3a^2} (f_A + f_B + f_C + f_D + f_E + f_F - 6f_V), \quad (3.21)$$

which has the same structure of the Laplacian of Eq. (3.11) and is consistent with those reported in Refs. [152, 153]. In particular, in Ref. [152], it is also shown that, while the 2D Laplacian is usually represented as a sum of 1D second derivatives in two orthogonal directions $\nabla^2 = \partial_x^2 + \partial_y^2$, it may more generally be represented as a summation of 1D second derivatives in any $n \geq 2$ symmetrically distributed directions (Fig. 3.2)

$$\nabla^2 = \frac{2}{n} \sum_{i=1}^n \partial_{x_i}^2, \quad (3.22)$$

which, for $n = 3$ and replacing each $\partial_{x_i}^2$ with its discrete form (see Appendix 3.A.3), is consistent with Eq. (3.21). In this case, the axes x_1, x_2, x_3 are represented by the unit vectors in \mathbb{R}^2 :

$$\mathbf{x}_1 = \begin{pmatrix} 1 \\ 0 \end{pmatrix}, \quad \mathbf{x}_2 = \begin{pmatrix} -\frac{1}{2} \\ \frac{\sqrt{3}}{2} \end{pmatrix}, \quad \mathbf{x}_3 = \begin{pmatrix} -\frac{1}{2} \\ -\frac{\sqrt{3}}{2} \end{pmatrix}. \quad (3.23)$$

According to this graph Laplacian, the Hamiltonian reads then as follows:

$$\hat{\mathcal{H}} = -J_T \sum_V (|A\rangle\langle V| + |B\rangle\langle V| + |C\rangle\langle V| + |D\rangle\langle V| + |E\rangle\langle V| + |F\rangle\langle V| - 6|V\rangle\langle V|), \quad (3.24)$$

where the hopping amplitude is

$$J_T := \frac{\hbar^2}{3ma^2} = \frac{2}{3}J_S. \quad (3.25)$$

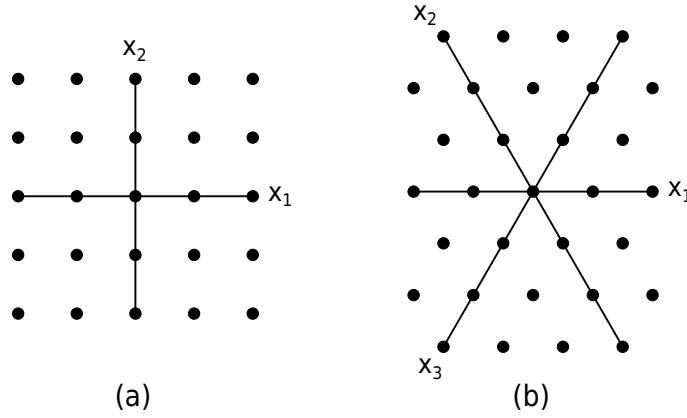


Figure 3.2. n symmetrically distributed directions in a (a) square ($n = 2$) and (b) triangular ($n = 3$) lattice graph.

Honeycomb lattice graph

A vertex (V, \odot) , with $\odot \in \{\circ, \bullet\}$, has three NNs, namely $(A, \bar{\odot})$, $(B, \bar{\odot})$, and $(C, \bar{\odot})$ (see Table 3.1). We evaluate the following Taylor expansions about (V, \odot) up to the second order:

$$f_{(A, \bar{\odot})} \approx f_{(V, \odot)} + \frac{\sqrt{3}a}{2} \partial_x f_{(V, \odot)} - \text{sgn}(\odot) \frac{a}{2} \partial_y f_{(V, \odot)} + \frac{3a^2}{8} \partial_x^2 f_{(V, \odot)} + \frac{a^2}{8} \partial_y^2 f_{(V, \odot)}, \quad (3.26)$$

$$f_{(B, \bar{\odot})} \approx f_{(V, \odot)} - \frac{\sqrt{3}a}{2} \partial_x f_{(V, \odot)} - \text{sgn}(\odot) \frac{a}{2} \partial_y f_{(V, \odot)} + \frac{3a^2}{8} \partial_x^2 f_{(V, \odot)} + \frac{a^2}{8} \partial_y^2 f_{(V, \odot)}, \quad (3.27)$$

$$f_{(C, \bar{\odot})} \approx f_{(V, \odot)} + \text{sgn}(\odot) a \partial_y f_{(V, \odot)} + \frac{a^2}{2} \partial_y^2 f_{(V, \odot)}. \quad (3.28)$$

Now we consider a linear combination of the expressions above, understood as equalities:

$$\begin{aligned} \alpha f_{(A, \bar{\odot})} + \beta f_{(B, \bar{\odot})} + \gamma f_{(C, \bar{\odot})} &= (\alpha + \beta + \gamma) f_{(V, \odot)} + \frac{\sqrt{3}a}{2} (\alpha - \beta) \partial_x f_{(V, \odot)} \\ &\quad - \text{sgn}(\odot) \frac{a}{2} (\alpha + \beta - 2\gamma) \partial_y f_{(V, \odot)} \\ &\quad + \frac{3a^2}{8} (\alpha + \beta) \partial_x^2 f_{(V, \odot)} + \frac{a^2}{8} (\alpha + \beta + 4\gamma) \partial_y^2 f_{(V, \odot)}. \end{aligned} \quad (3.29)$$

If we set $\alpha = \beta = \gamma = 1$, we get

$$\nabla^2 f_{(V,\odot)} = \frac{4}{3a^2} (f_{(A,\bar{\odot})} + f_{(B,\bar{\odot})} + f_{(C,\bar{\odot})} - 3f_{(V,\odot)}), \quad (3.30)$$

which has the same structure of the Laplacian of Eq. (3.11). Notice also that, because the honeycomb lattice a non-Bravais lattice, we cannot obtain the Laplacian from Eq. (3.22). According to this graph Laplacian, the Hamiltonian reads then as follows:

$$\hat{\mathcal{H}} = -J_H \sum_{\odot \in \{\circ, \bullet\}} \sum_{(V,\odot)} (|A, \bar{\odot}\rangle\langle V, \odot| + |B, \bar{\odot}\rangle\langle V, \odot| + |C, \bar{\odot}\rangle\langle V, \odot| - 3|V, \odot\rangle\langle V, \odot|), \quad (3.31)$$

where the hopping amplitude is

$$J_H := \frac{2\hbar^2}{3ma^2} = \frac{4}{3}J_S. \quad (3.32)$$

3.2.3 Numerical simulation

Parameter setting

Units. For the computational implementation we set $a = \hbar = 1$, where a is the lattice parameter and \hbar is the reduced Planck's constant. According to this choice, the dimensions and the units of the fundamental quantities are examined in Appendix 3.C. Please notice that all the results shown in the following concern dimensionless quantities.

Time evolution. In the *Schrödinger picture*, the time evolution of the state of a quantum system is ruled by the unitary *time-evolution operator*

$$\hat{\mathcal{U}}(t, t_0) = e^{-i\hat{\mathcal{H}}(t-t_0)}, \quad (3.33)$$

where t_0 and t denote the initial and final times, respectively. Because of the previous units, the mass is left as the only dimensional quantity and it is controlled through the hopping amplitude J , as shown, e.g., in Eq. (3.13). Such parameter enters the Hamiltonian as a global multiplicative factor; thus, if we focus on the time-evolution operator in Eq. (3.33), we can appreciate its role as a time-scaling factor in $iJ \sum_V [\dots](t - t_0)$: greater J , lighter m , and faster the time evolution all correlate, whereas lower J , heavier m , and slower time evolution correlate. The quantum system, therefore, has a characteristic time given by $\tau = 1/J$. We set $J_S = 1$ and J_T and J_H follow according to Eqs. (3.25) and (3.32), respectively. This is equivalent to fixing the mass of the walker and comparing its CTQW on the different PLGs. Because of the aforementioned role of the hopping amplitude, in order to have a proper comparison of the results, these will be expressed as a function of the dimensionless time Jt (where J takes the proper value in the different PLGs).

Lattice size. Unlike the square lattice graph, for which we can define the size as $N_x \times N_y$, where N_x (N_y) is the number of vertices along the x (y) direction, for the triangular and honeycomb ones the definition of the size is not straightforward: The “directions” to be considered might be polylines (see Appendix 3.B.2). We refer to N_j (N_k) as the number of vertices along the j (k) polyline, which plays the role of the x (y) direction, and the resulting size of the graph is therefore $N_j \times N_k = \dim(\mathcal{H})$, where \mathcal{H} denotes the Hilbert space of the system. We consider a *finite* $(2n + 1) \times (2m + 1)$ PLG (see Appendix 3.B.3), with $n, m \in \mathbb{N}$, since it has a properly defined center in $(n + 1, m + 1)$, of coordinates (x_c, y_c) (in the following, we partially restore the two-indices notation for labeling sites; see Sec. 3.2.1). We set $N_j = N_k = 41$ for the triangular

lattice graph, $N_j = N_k = 31$ for the square one, and $N_j = 31$, $N_k = 21$ for the honeycomb one. The size chosen for these graphs allows us to make the system evolve for a long enough time, at a reasonable computational cost, to observe interesting effects before the wave function reaches the boundaries. The choice of setting $N_k < N_j$ for the honeycomb lattice graph is due to the following reason: Two adjacent vertices (j, k) and $(j + 1, k)$ differ by $\sqrt{3}a/2$ along the x direction, whereas (j, k) and $(j, k + 1)$ by a or $2a$ along the y direction (see Appendix 3.B.2, Fig. 3.23(c)). A honeycomb lattice graph with $N_j = N_k$ would be strongly unbalanced and the wave function would reach the j boundary much earlier than the k one.

Quantities of interest. We study the time evolution of an initial state $|\psi(0)\rangle$ localized in the central vertex (x_c, y_c) of the PLG (hence it is an eigenstate of \hat{x} and \hat{y}). We look at the probability distribution of the walker and at the variance of the space coordinates as a function of time. We therefore introduce the *probability density* $\rho_{j,k}(t) = |\psi_{j,k}(t)|^2$ of finding the walker in the site (j, k) at the time t . Maps of the probability density are to be understood according to Appendix 3.B.1, and axis ticks according to Appendix 3.B.2 (the indexing of vertices runs along polylines). The variance of the space coordinates is computed after recovering the spatial coordinates (x_j, y_k) of vertices (see Appendix 3.B.2) according to $\sigma_x^2 = \langle \hat{x}^2 \rangle - \langle \hat{x} \rangle^2$, where $\langle \hat{x} \rangle = \sum_{j,k=1}^{N_j, N_k} \rho_{j,k} x_{j,k}$, since, in general, the x coordinate of a vertex depends on both the indices (e.g., in the honeycomb and triangular lattice graphs), and analogously for σ_y^2 .

Results

The first study concerns the CTQW of a free particle on the different PLGs. For such a CTQW, we expect a ballistic spreading of the wave function, i.e., $\sigma^2(Jt) \propto (Jt)^2$. Therefore, we analyze the resulting variance of the space coordinates (Fig. 3.3) according to the fitting curve²

$$f(Jt) = A(Jt)^p. \quad (3.34)$$

CTQWs on a square or triangular lattice graph show the same ballistic behavior for both the spatial coordinates, i.e., $\sigma_x^2(Jt) = \sigma_y^2(Jt) \propto (Jt)^2$. On the other hand, for the CTQW on a honeycomb lattice graph, we observe $\sigma_x^2(Jt) = \sigma_y^2(Jt) \propto (Jt)^p$, with $1 < p < 2$, i.e., a behavior which is neither ballistic ($p = 2$) nor diffusive ($p = 1$), but *sub-ballistic*. It is important to note that this numerical result puts limits to the universal ballistic spreading for both 1D and 2D QWs, as instead suggested in Ref. [18]. The reason is believed to reside in the fact that, unlike the triangular and square lattice graphs, which are Bravais lattices, the honeycomb lattice graph is a non-Bravais lattice. Whereas in the former ones we can always go further along the same direction, in the latter one when we move one step from a vertex to an adjacent one, we change class of vertex and the NNs of the final vertex are arranged and oriented differently from those of the initial one (see Sec. 3.2.1). This difference turns out to slow down the spreading of the quantum walker. We also notice that $\sigma_H^2(Jt) \leq \sigma_S^2(Jt) \leq \sigma_T^2(Jt)$, i.e., the largest variance is obtained in the triangular lattice graph, while the lowest one in the honeycomb lattice graph. This behavior can be related to the different degrees of a vertex in each PLG: 6 in the triangular, 4 in the square, and only 3 in the honeycomb lattice graph.

A further clue that CTQWs behave differently on Bravais and non-Bravais lattice is provided by the CTQW on another 2D non-Bravais lattice: the *truncated square tiling* (or *truncated quadrille* [154]), whose Schläfli symbol is $t\{4,4\}$ (legend of Fig. 3.3). It is a *semiregular* or *Archimedean* tessellation, all of whose tiles are regular polygons, with one square and two octagonal tiles about

²No offset is introduced since the walker is initially localized in a single vertex, thus, as we checked, $\sigma_x^2(0) = \sigma_y^2(0) = 0$.

each vertex, and the tiling pattern around each vertex being the same [148]. Weakening the definition of lattice graph in order to include also semiregular tilings, in the following we will refer to this non-Bravais lattice as the truncated square lattice graph. In such graph, a generic vertex has $\deg(V) = 3$, as in the honeycomb lattice graph, but unlike the latter, here there are four classes of nonequivalent vertices $\{\circ, \bullet, \odot, \ominus\}$. The CTQW Hamiltonian matrix $\mathcal{H} = -JL$ has been here defined according to Eq. (3.3). Indeed, since for a given vertex the hopping directions are not symmetrically distributed, defining the Laplacian by means of finite-difference formulas from Taylor expansion is ill defined, since it provides different hopping terms depending on the direction. Even in this case, we observe $\sigma_x^2(Jt) = \sigma_y^2(Jt) \propto (Jt)^p$, with $1 < p < 2$, i.e., a sub-ballistic spreading.

A proper measure of quantum coherence is provided by the l_1 norm of coherence [113, 155]

$$C_{l_1}(\rho) = \sum_{m \neq n} |\rho_{mn}| = \sum_{m,n} |\rho_{mn}| - 1, \quad (3.35)$$

i.e., the sum of the absolute values of the off-diagonal elements of the density matrix. According to this definition, after writing the density matrix in the vertex states basis, we observe that the PLGs causing more coherence are those in which the CTQW is properly ballistic, and *vice versa* CTQWs on the non-Bravais PLGs are characterized by a lower coherence and a sub-ballistic spreading (Fig. 3.4). This is in agreement with the idea that the ballistic spreading is due to interference phenomena.

Maps of the time-evolving probability density are shown in Fig. 3.5. In each case, the spread path is characterized by the symmetry of the underlying lattice.

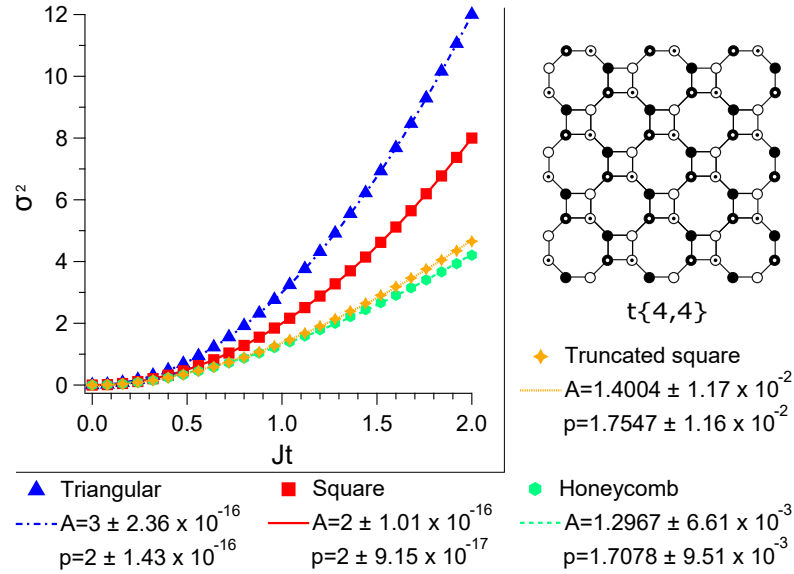


Figure 3.3. Variance of the space coordinates obtained in a CTQW of a free particle on a square (red squares), triangular (blue triangles), honeycomb (green hexagons), and truncated square (yellow four-pointed star) lattice graph. The latter, shown in the legend, consists of squares and octagons and it is characterized by four classes of nonequivalent vertices $\{\circ, \bullet, \odot, \ominus\}$. The variance of the two spatial coordinates is equal, $\sigma_x^2(Jt) = \sigma_y^2(Jt) = \sigma^2(Jt)$. Lines denote the fitting curves in Eq. (3.34).

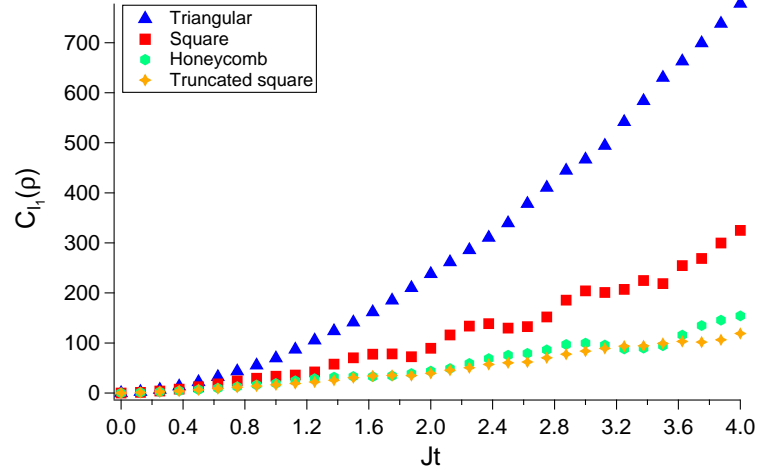


Figure 3.4. Quantum coherence of a CTQW of a free particle on square (red squares), triangular (blue triangles), honeycomb (green hexagons), and truncated square (yellow four-pointed star) lattice graphs. In this computation, the same lattice size has been adopted for all the PLGs, in order to have Hilbert spaces of the same dimension and so a proper comparison.

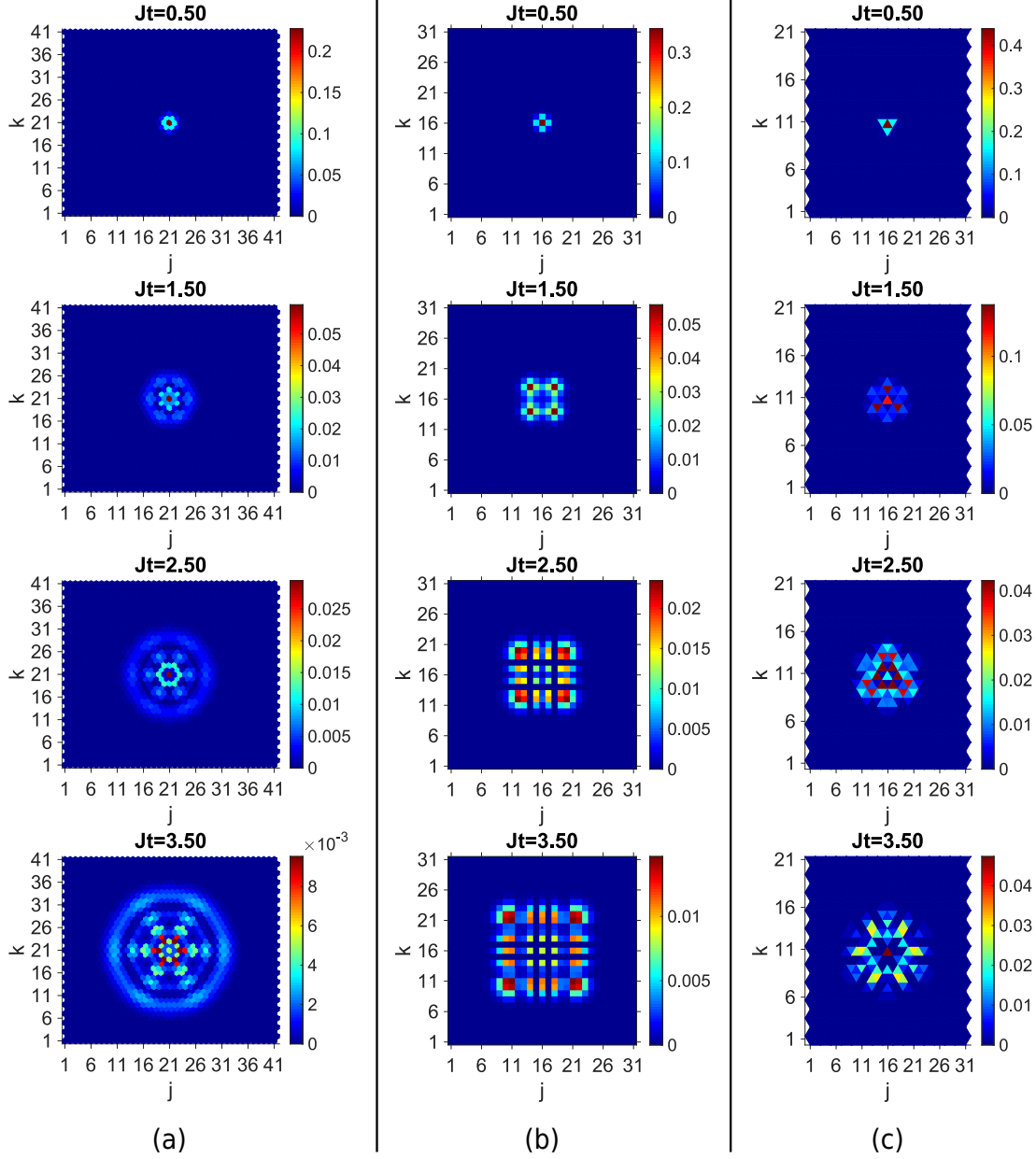


Figure 3.5. Maps of the time evolution of the probability density according to the CTQW of a free particle on a (a) 41×41 triangular, (b) 31×31 square, and 31×21 (c) honeycomb lattice graph.

3.3 A charged quantum walker in a magnetic field

3.3.1 The Hamiltonian of the system: The issue of the spatial discretization

The Hamiltonian of a particle of mass m and charge q in a plane in the presence of a electromagnetic field is obtained on the basis of the Hamiltonian of the free particle through the minimal substitution $\hat{\mathbf{p}} \rightarrow \hat{\mathbf{p}} - q\mathbf{A}$ and by inserting the electric potential, namely

$$\hat{\mathcal{H}} = \frac{1}{2m} (\hat{\mathbf{p}} - q\mathbf{A})^2 + q\phi, \quad (3.36)$$

where ϕ and \mathbf{A} are, respectively, the scalar and vector potential of the electric field $\mathbf{E} = -\nabla\phi - \partial_t\mathbf{A}$ and magnetic field $\mathbf{B} = \nabla \times \mathbf{A}$. In order to study a charged particle in the presence of the perpendicular magnetic field only, we set $\phi = 0$ and choose a time-independent vector potential $\mathbf{A} = A^x(x, y)\hat{\mathbf{i}} + A^y(x, y)\hat{\mathbf{j}}$. The Hamiltonian is then

$$\hat{\mathcal{H}} = \frac{1}{2m} \hat{\mathbf{p}}^2 - \frac{q}{2m} (\hat{\mathbf{p}} \cdot \mathbf{A} + \mathbf{A} \cdot \hat{\mathbf{p}}) + \frac{q^2}{2m} \mathbf{A}^2, \quad (3.37)$$

where $\hat{\mathbf{p}} \cdot \mathbf{A}$ acts on the wave function as $\hat{\mathbf{p}} \cdot (\mathbf{A}\psi(\mathbf{r}))$.

In the light of the strict connection between the generator of the evolution of the CTQW and the Hamiltonian (see Sec. 1.1.2), the straightforward approach to get a CTQW Hamiltonian is to spatially discretize the Hamiltonian of the corresponding system in the continuum. Several works addressed the presence of potentials [156], defects, or disorder [157] which depend on the vertices and interactions between the walkers when in the same vertex or in NNs [15]. However, this spatial dependence has been usually considered for 1D systems or graphs, the latter intended as mathematical objects for algorithmic purposes [158]. When inserting the magnetic field, the vector potential has an actual spatial dependence we cannot prescind from the spatial coordinates of vertices. Moreover, unlike the aforementioned cases, the Hamiltonian in Eq. (3.37) includes a cross term $\sim (\mathbf{A} \cdot \hat{\mathbf{p}} + \hat{\mathbf{p}} \cdot \mathbf{A})$, the orbital paramagnetic term, which couples the field to the particle's orbital motion, so that the linear momentum is present both at first and second orders. This means that not only the Laplacian, but also the first-order differential operator is required. We expect the Laplacian to behave like the graph one, for which we already have a general definition in Eq. (3.3), but we expect also the first-order differential operator, for which we do not have an analogous general definition, to be sensitive to the geometry of the lattice and to return not only non-negative results for NNs, as instead the kinetic term (the graph Laplacian) does ($L_{jk} = 1$ if $j \neq k$ and connected). Here lies the crux of the present work and its peculiarity, i.e., the hard task of spatially discretizing Eq. (3.37) – and so the differential operators – in a 2D space according to the different geometries characterizing the PLGs. Indeed, to the best of our knowledge, such issue has not been addressed for CTQWs yet. However, there are works considering DTQWs under artificial magnetic fields on square lattices involving Peierls phase-factors [135, 138], and this is a first hint to treat our CTQW in the presence of a magnetic field without explicitly involving the spatial discretization of differential operators. On the other hand, we are also interested in finding a way to spatially discretize the Hamiltonian in Eq. (3.37) according to the different geometries of the PLGs (Fig. 3.1).

In the free-particle Hamiltonian we know the hopping must be equiprobable along the allowed directions, i.e., the walker must have the same jumping rate forward or backward, along a direction or another (see Sec. 1.1.2). Such requirement is usually satisfied computing $\nabla^2\psi_V$ in a given vertex V by means of *central* finite difference formulas,³ which involve all the NNs of V .

³The use of *backward* or *forward* finite difference formulas, instead, would produce a bias in the hopping of the walker, a non-Hermitian Hamiltonian, and so the system would not describe a CTQW.

Moreover, this ensures the hermiticity of the Hamiltonian (as regards the terms in $\hat{\mathbf{p}}$). The latter, we recall, is the ultimate condition for having a CTQW, since any Hermitian operator abiding the topology of the graph can describe a CTQW. Let us consider the 1D case for the free particle: The central difference formula to compute the $\nabla^2\psi(x_n)$, with $x_n = n \in \mathbb{Z}$, involves the vertex x_n itself and its NNs $x_{n\pm 1}$. Considering the hopping terms, the central difference formula allows the walker to jump from x_n to $x_{n\pm 1}$, with the same jumping rate (see Eq. (1.22)). Since it holds $\forall n$, this Hamiltonian matrix is symmetric (hermiticity for a real-valued matrix), meaning that the hopping term from x_n to $x_{n\pm 1}$ is the same as the one from $x_{n\pm 1}$ to x_n . This reasoning also applies to a complex-valued Hamiltonian matrix and hermiticity, where the hopping terms between two NNs are each the Hermitian conjugate of the other.

We assume a hopping to NNs which takes into account the contribution of the magnetic field. We therefore explore the two approaches: (i) the introduction of the Peierls phase-factors (Sec. 3.4), according to which the tunneling matrix element of the free particle becomes complex, accompanied by the Peierls phase due to the vector potential; and (ii) the spatial discretization of the Hamiltonian of Eq. (3.37) in terms of finite-difference formulas (Sec. 3.5). In the first case, the assumption on the hopping to NNs is fulfilled for free, since the model is based on the CTQW Hamiltonian of the free particle (ultimately on the graph Laplacian); in the second case, the differential operators must be discretized according to the NNs of a given vertex by means of “central difference”-like formulas.

3.3.2 Numerical simulation: Parameter setting

In addition to what stated in Sec. 3.2.3, we set the following:

Units. For the computational implementation we set the electric charge $q = 1$ (see Appendix 3.C for units and dimensions). Please notice that all the results shown in the following concern dimensionless quantities.

Gauge and magnetic field. A uniform magnetic field $\mathbf{B} = B\hat{\mathbf{k}}$ is introduced by means of the vector potential (symmetric gauge) $\mathbf{A} = \frac{B}{2}(-(y - y_c), (x - x_c), 0)$. In this gauge, as known, the Hamiltonian in Eq. (3.37) turns out to be the Hamiltonian of a 1D harmonic oscillator, whose degenerate energy levels are the so-called *Landau levels* [159] and which is characterized by the *cyclotron frequency* $\omega_0 = qB/m$, which depends on the magnetic field. This choice of gauge breaks translational symmetry in both the x and the y directions, but it does preserve rotational symmetry about the center (x_c, y_c) of the PLG. This means that the angular momentum together with the Landau level are good quantum numbers [160] to label states. The angular momentum is classically defined as $\mathbf{L} = \mathbf{r} \times \mathbf{p}$, but since our charged particle lies in the xy plane, the angular momentum is $\mathbf{L} = L_z\hat{\mathbf{k}}$ and the corresponding operator is

$$\hat{L}_z = (\hat{x}\hat{p}_y - \hat{y}\hat{p}_x). \quad (3.38)$$

Since the symmetric gauge belongs to the Coulomb gauge, where $\nabla \cdot \mathbf{A} = 0$ so $[\hat{\mathbf{p}}, \hat{\mathbf{A}}] = 0$, it can be proved that $[\hat{\mathcal{H}}, \hat{L}_z] = 0$, i.e., $\hat{\mathcal{H}}$ and \hat{L}_z represent a complete set of compatible observables. The states belonging to the lowest Landau level, i.e., the ground state, are characterized by a ring-shaped probability density. So, if we allow the PLG to better follow the rotational symmetry of the Hamiltonian, we expect more circular structures in the probability density of the walker. In particular, we expect the triangular lattice graph, because of its six NNs per vertex, to provide the best discrete approximation of a circle among the PLGs; instead, because of the only three NNs per vertex, we expect the honeycomb lattice graph to provide the worst one. Moreover, due to structure of nonequivalent vertices of the latter, symmetries may struggle to emerge. It is

important to keep in mind this premise about the rotational symmetry and the harmonic oscillator because it will be of help in the interpretation of the results in the following.

The *magnetic length* is the fundamental characteristic length scale for any quantum phenomena in the presence of a magnetic field [160] and it imposes an upper bound to the interval of fields investigated. Indeed, it is defined as

$$l_B := \sqrt{\frac{\hbar}{qB}} = B^{-\frac{1}{2}}, \quad (3.39)$$

where the last equality holds because of our units ($\hbar = q = a = 1$), so, since for $B > 1$ the magnetic length becomes smaller than the lattice constant a , we consider $B \in [0,1]$.

3.4 CTQW under magnetic field: The Peierls model

3.4.1 The Peierls phase-factors

The motion of a charged particle in a magnetic field is accompanied by a geometric phase, the Aharonov-Bohm phase [161]. On a lattice, these phases are introduced in the form of the so-called *Peierls phases* that a particle picks up when hopping in the lattice. Such phases allow us to rewrite the tight-binding Hamiltonian of a charged particle in a magnetic field as the tight-binding Hamiltonian of a free particle where tunneling matrix elements are complex and hopping in the lattice is accompanied by the Peierls phase [162, 163]. The spectrum of the Hamiltonian so obtained is the famous Hofstadter butterfly [164]. According to Feynman, the Hamiltonian having such Peierls phase-factors can be traced, in some limits, to the well-known Hamiltonian in Eq. (3.36) [165, 166].

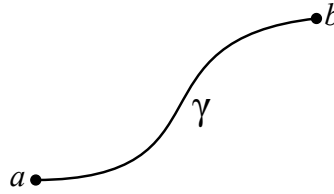


Figure 3.6. The probability amplitude to go from a to b along the path γ , in the presence of a vector potential \mathbf{A} , is proportional to $\exp\left[\frac{iq}{\hbar} \int_a^b \mathbf{A} \cdot d\mathbf{s}\right]$.

Proof. Feynman's argument develops as follows. An external magnetic field is described by a vector potential. The probability amplitude that a particle goes from one place to another, along a certain path when there is a field present (Fig. 3.6), is

$$\langle b|a\rangle_{\text{in } \mathbf{A}} = \langle b|a\rangle_{A=0} \cdot \exp\left[\frac{iq}{\hbar} \int_a^b \mathbf{A} \cdot d\mathbf{s}\right]; \quad (3.40)$$

i.e., it is the same as that of the particle going along the same path when there is no field, multiplied by a phase factor which depends on the line integral of the vector potential.

Feynman considers then a simple example in which instead of having a continuous situation there is a line of atoms along the x axis with the spacing a , an electron has a probability amplitude $-K$ to jump from one atom to another when there is no field, and there is a vector potential in

the x direction $A_x(x, t)$. The rate of change of the probability amplitude $C(x)$ to find the electron at the atom “ n ” located at x is given by the following equation:

$$i\hbar\partial_t C(x) = E_0 C(x) - K e^{-iaf(x+a/2)} C(x+a) - K e^{+iaf(x-a/2)} C(x-a), \quad (3.41)$$

where E_0 is the energy of the electron if located at x , $f(x) := (q/\hbar)A_x$, and $-KC(x \pm a)$ is the probability amplitude for the electron to have jumped backward or forward, respectively, one step from atom “ $n \pm 1$ ”, located at $x \pm a$. If A_x is not changing appreciably in one atomic spacing, the integral can be written as just the value of A_x at the midpoint times the spacing a , resulting in a phase factor $\exp\{\pm ia f(x \pm a/2)\}$. The sign of the phase shift reflects the direction of the hopping: backward (–) or forward (+).

If the function $C(x)$ is smooth enough (long wavelength limit), and if we let the atoms get closer together ($a \rightarrow 0$), Eq. (3.41) will approach the behavior of an electron in free space. So the next step is to Taylor expand the right-hand side of Eq. (3.41) ($C(x)$, $f(x)$, and the exponentials) in powers of a , to collect the terms up to $O(a^2)$ and to recast all into

$$i\hbar\partial_t C(x) = (E_0 - 2K)C(x) - Ka^2 [\partial_x - if(x)]^2 C(x). \quad (3.42)$$

The solutions for zero magnetic field represent a particle with an effective mass m_{eff} given by

$$Ka^2 = \frac{\hbar^2}{2m_{\text{eff}}}. \quad (3.43)$$

After setting $E_0 = 2K$ and restoring $f(x) = (q/\hbar)A_x$, we can easily check that Eq. (3.42) is the same as the first part of Eq. (3.36). Hence, the proposition of Eq. (3.40) that the vector potential changes all the probability amplitudes by the exponential factor is the same as the rule that the momentum operator $-i\hbar\nabla$ gets replaced by

$$-i\hbar\nabla - q\mathbf{A}, \quad (3.44)$$

as we see in the Schrödinger equation of Eq. (3.36). \square

Since resorting to Peierls phase-factors is equivalent to the minimal substitution in the Hamiltonian, they can be used to study the CTQW in the presence of a magnetic field, with no need of discrete differential operators but the graph Laplacian. In other words, we may simply correct the free-particle Hamiltonian according to the Peierls substitution [167], i.e., by making the tunneling matrix element complex:

$$J \longrightarrow J \exp \left[\frac{iq}{\hbar} \int_{\mathbf{r}_a}^{\mathbf{r}_b} \mathbf{A} \cdot d\mathbf{r} \right], \quad (3.45)$$

where J is the NN hopping amplitude and the integral is evaluated along the edge connecting \mathbf{r}_a and \mathbf{r}_b , i.e., the initial and final positions (vertices) of the particle, respectively. However, the Peierls phase-factors are equivalent to the minimal substitution in the continuum limit. This means that the quadratic term in \mathbf{A} is recovered only in such limit, and so it is not present in this Hamiltonian. Indeed, such term would affect the diagonal elements, the on-site energies, but in this model they are left as the degree of the vertex (or set equal to zero, being the lattice graph regular – $\deg(V) = \text{const}$ – and so providing an irrelevant global phase to the wave function).

The Peierls phase-factor in Eq. (3.45) involves a line integral which does depend on the chosen path (Fig. 3.6), and it is calculated as follows:

$$\begin{aligned} \int_{\gamma} \mathbf{A}(\mathbf{r}) \cdot d\mathbf{r} &= \int_a^b \mathbf{A}(\mathbf{r}(t)) \cdot \mathbf{r}'(t) dt \\ &= \int_a^b [A^x(\mathbf{r}(t))x'(t) + A^y(\mathbf{r}(t))y'(t)] dt, \end{aligned} \quad (3.46)$$

where $\mathbf{r}(t) : [a, b] \rightarrow \gamma$ is a bijective parametrization of the curve γ such that $\mathbf{r}_a := \mathbf{r}(a)$ and $\mathbf{r}_b := \mathbf{r}(b)$ give the endpoints of γ . In particular, $\mathbf{r}(t) = x(t)\hat{\mathbf{i}} + y(t)\hat{\mathbf{j}}$ and $\mathbf{r}'(t) = \frac{d\mathbf{r}}{dt}$. Such line integral has to be evaluated along the edges of the PLG, i.e., pieces of straight lines that we parametrize as follows:

$$\begin{cases} x(t) = x_0 + t(x_1 - x_0) \\ y(t) = y_0 + t(y_1 - y_0) \end{cases}, \quad t \in [0, 1], \quad (3.47)$$

from which $x' = x_1 - x_0$ and $y' = y_1 - y_0$ are constants. Then the integral is approximated according to the *trapezoidal rule* [168, 169]:

$$\int_0^1 \mathbf{A}(\mathbf{r}(t)) \cdot \mathbf{r}'(t) dt \approx \frac{1}{2} [(x_1 - x_0)(A^x(\mathbf{r}_0) + A^x(\mathbf{r}_1)) + (y_1 - y_0)(A^y(\mathbf{r}_0) + A^y(\mathbf{r}_1))], \quad (3.48)$$

where $\mathbf{r}_0 = (x_0, y_0)$ and $\mathbf{r}_1 = (x_1, y_1)$ are the coordinates of the initial and final vertex, respectively. Moreover, if the vector potential components depend linearly on the x and y coordinates, e.g., in the Landau and in the symmetric gauge (providing a uniform magnetic field $\mathbf{B} = B\hat{\mathbf{k}}$), Eq. (3.48) is exact and it holds as equality. Indeed, let $f(x) = mx + q$, then

$$\int_a^b f(x) dx = \frac{b-a}{2}(ma + mb + 2q) = \frac{b-a}{2}(f(a) + f(b)). \quad (3.49)$$

3.4.2 The CTQW Hamiltonian

Square lattice graph

With reference to Table 3.1, the Hamiltonian describing the CTQW according to the Peierls model is

$$\begin{aligned} \hat{\mathcal{H}} = & -J_S \sum_V \left[\exp\left\{\frac{iqu}{2\hbar}(A_V^x + A_A^x)\right\} |A\rangle\langle V| \right. \\ & + \exp\left\{\frac{iqu}{2\hbar}(A_V^y + A_B^y)\right\} |B\rangle\langle V| \\ & + \exp\left\{-\frac{iqu}{2\hbar}(A_V^x + A_C^x)\right\} |C\rangle\langle V| \\ & \left. + \exp\left\{-\frac{iqu}{2\hbar}(A_V^y + A_D^y)\right\} |D\rangle\langle V| - 4|V\rangle\langle V| \right], \quad (3.50) \end{aligned}$$

where J_S is defined in Eq. (3.13).

Triangular lattice graph

With reference to Table 3.1, the Hamiltonian describing the CTQW according to the Peierls model is

$$\begin{aligned}
 \hat{\mathcal{H}} = & -J_T \sum_V \left[\exp\left\{\frac{iqua}{2\hbar}(A_V^x + A_A^x)\right\} |A\rangle\langle V| \right. \\
 & + \exp\left\{\frac{iqua}{4\hbar} \left[A_V^x + A_B^x + \sqrt{3}(A_V^y + A_B^y)\right]\right\} |B\rangle\langle V| \\
 & + \exp\left\{-\frac{iqua}{4\hbar} \left[A_V^x + A_C^x - \sqrt{3}(A_V^y + A_C^y)\right]\right\} |C\rangle\langle V| \\
 & + \exp\left\{-\frac{iqua}{2\hbar}(A_V^x + A_D^x)\right\} |D\rangle\langle V| \\
 & + \exp\left\{-\frac{iqua}{4\hbar} \left[A_V^x + A_E^x + \sqrt{3}(A_V^y + A_E^y)\right]\right\} |E\rangle\langle V| \\
 & + \exp\left\{\frac{iqua}{4\hbar} \left[A_V^x + A_F^x - \sqrt{3}(A_V^y + A_F^y)\right]\right\} |F\rangle\langle V| \\
 & \left. - 6 |V\rangle\langle V| \right], \tag{3.51}
 \end{aligned}$$

where J_T is defined in Eq. (3.25).

Honeycomb lattice graph

With reference to Table 3.1, the Hamiltonian describing the CTQW according to the Peierls model is

$$\begin{aligned}
 \hat{\mathcal{H}} = & -J_H \sum_{\odot \in \{\circ, \bullet\}} \sum_{(V, \odot)} \left[e^{i\theta_{AV}} |A, \odot\rangle\langle V, \odot| + e^{i\theta_{BV}} |B, \odot\rangle\langle V, \odot| + e^{i\theta_{CV}} |C, \odot\rangle\langle V, \odot| \right. \\
 & \left. - 3 |V, \odot\rangle\langle V, \odot| \right], \tag{3.52}
 \end{aligned}$$

where J_H is defined in Eq. (3.32), and we have defined:

$$\theta_{AV} := \frac{qa}{4\hbar} \left[\sqrt{3} \left(A_{(V, \odot)}^x + A_{(A, \odot)}^x \right) - \text{sgn}(\odot) \left(A_{(V, \odot)}^y + A_{(A, \odot)}^y \right) \right], \tag{3.53}$$

$$\theta_{BV} := -\frac{qa}{4\hbar} \left[\sqrt{3} \left(A_{(V, \odot)}^x + A_{(B, \odot)}^x \right) + \text{sgn}(\odot) \left(A_{(V, \odot)}^y + A_{(B, \odot)}^y \right) \right], \tag{3.54}$$

$$\theta_{CV} := \text{sgn}(\odot) \frac{qa}{2\hbar} \left(A_{(V, \odot)}^y + A_{(C, \odot)}^y \right). \tag{3.55}$$

3.4.3 Numerical simulation: results

The behavior of the variance of the space coordinates is shown in Fig. 3.7, and it is the same for both the x and y coordinates, i.e., $\sigma_x^2(Jt) = \sigma_y^2(Jt)$. We observe that, as the modulus of the magnetic field increases, the curve of the variance of the space coordinates deviates from that of the free particle, decreasing.

Maps of the time evolution of the probability density are shown in Figs. 3.8–3.10 and are characterized by a trade-off between the circular symmetry due to the gauge and the symmetry of the underlying lattice. In general, we observe a distribution of probability which initially spreads over the lattice, and then the maxima come back toward the initial vertex and eventually move

away from it. However, during the time evolution, the tails of the wave function continue to get away from the center of the lattice graph. Indeed, in the Peierls model, being its Hamiltonian based on the graph Laplacian, there is no term confining or limiting the spreading of the walker, since the quadratic term in \mathbf{A} is not explicitly present but only recovered, in the continuum limit, from the Peierls phase-factors of the hopping terms.

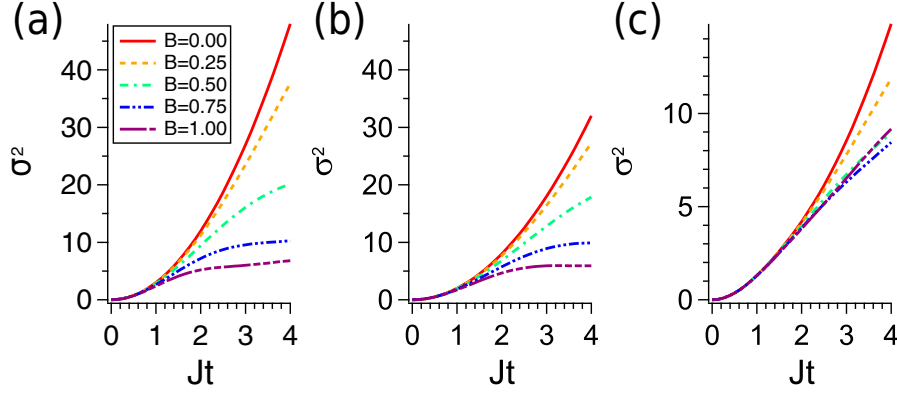


Figure 3.7. Variance of the space coordinates obtained in a CTQW of a charged particle in the (a) triangular, (b) square, and (c) honeycomb lattice graphs for increasing values of the modulus B of the perpendicular uniform magnetic field. As the latter increases, the variance deviates from the curve of the free particle. The variance of the two spatial coordinates is equal, $\sigma_x^2(t) = \sigma_y^2(t)$. The stronger magnetic fields correlate with smaller variances. The CTQW Hamiltonian is obtained from the Peierls model.

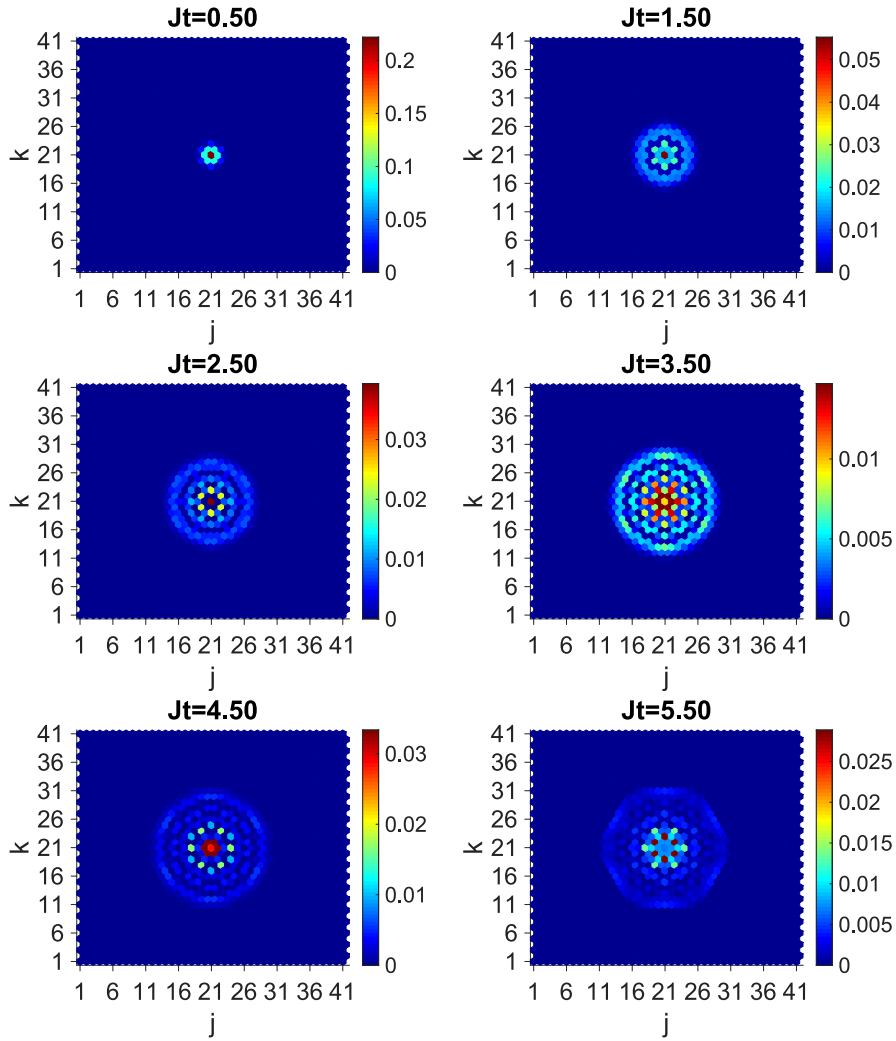


Figure 3.8. Map of the time evolution of the probability density according to the CTQW of a charged particle on a triangular lattice graph in the presence of a perpendicular uniform magnetic field ($B = 0.6$). The CTQW Hamiltonian is obtained from the Peierls model.

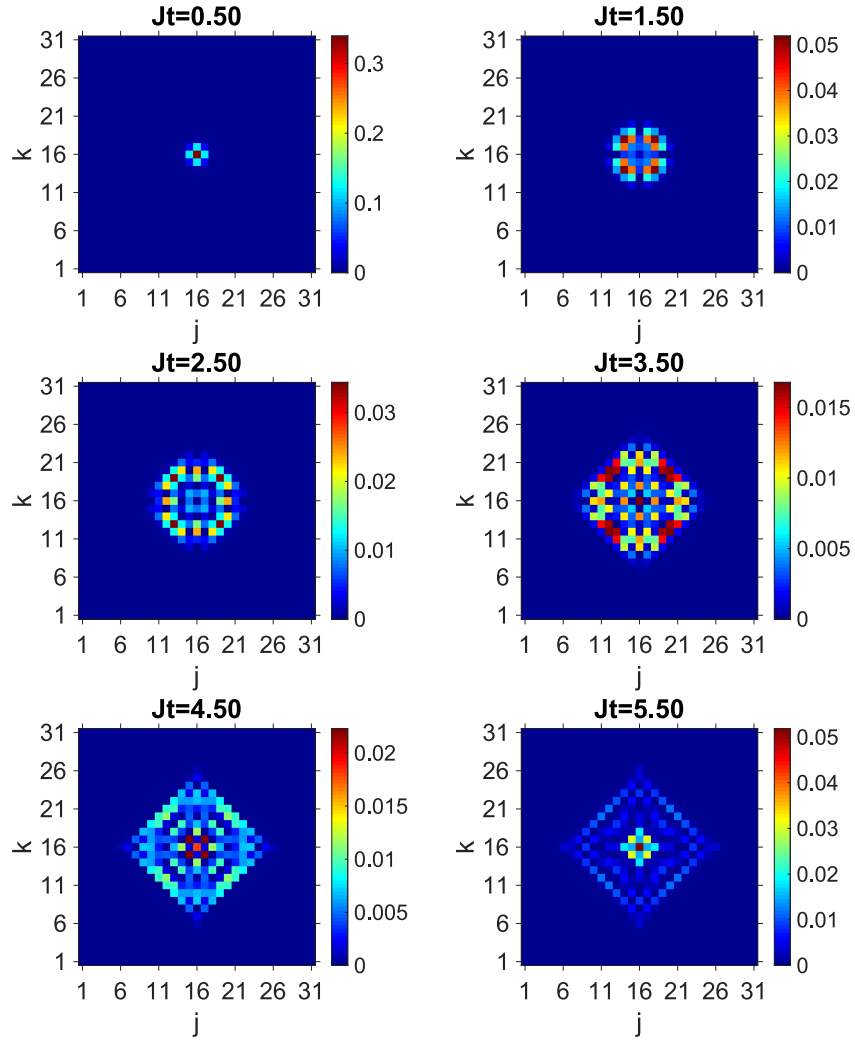


Figure 3.9. Map of the time evolution of the probability density according to the CTQW of a charged particle on a square lattice graph in the presence of a perpendicular uniform magnetic field ($B = 0.6$). The CTQW Hamiltonian is obtained from the Peierls model.

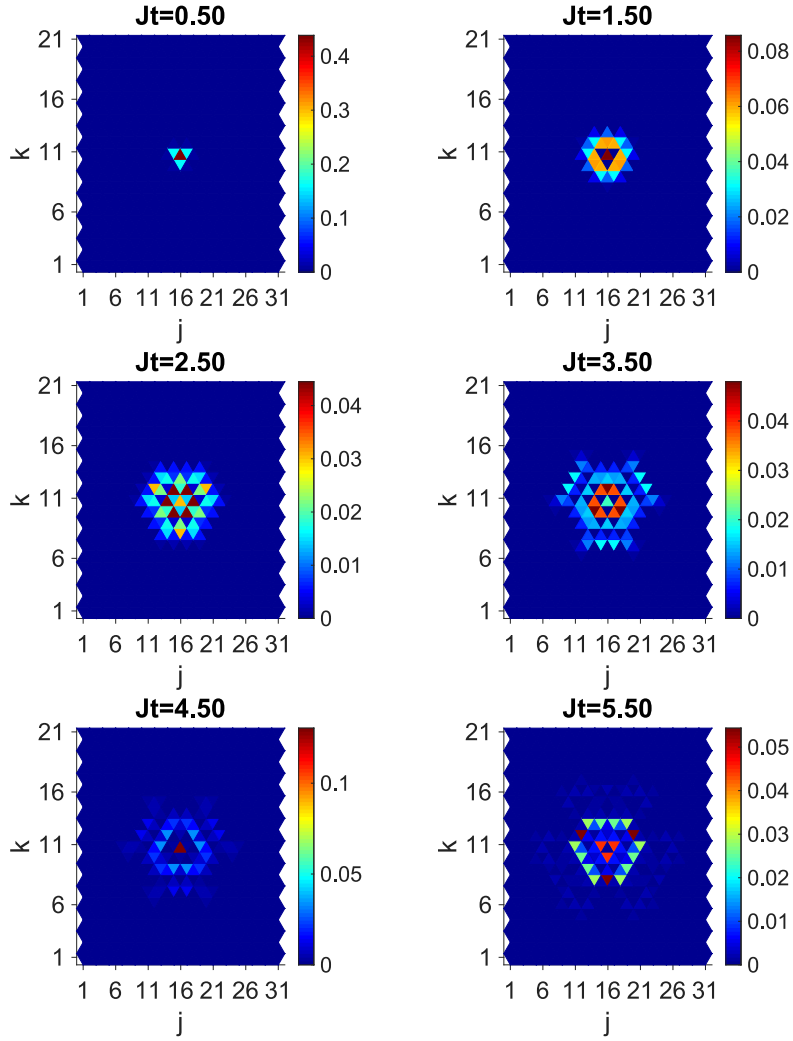


Figure 3.10. Map of the time evolution of the probability density according to the CTQW of a charged particle on a honeycomb lattice graph in the presence of a perpendicular uniform magnetic field ($B = 0.6$). The CTQW Hamiltonian is obtained from the Peierls model.

3.5 CTQW under magnetic field: the spatial discretization of the Hamiltonian

3.5.1 Finite-difference formulas with Taylor expansion

Here we show how far we can go in using the Taylor expansion in order to get finite-difference formulas for differential operators, as usually done for a square lattice. The same approach has been already used in Sec. 3.2.2 to obtain the Laplacian in the different PLGs, so all we are left to do is to determine the discrete version of the first partial derivatives of a scalar function f . The idea is, again, to Taylor expand f evaluated in the NN vertices about the given one V and combining the resulting expansions to obtain $\partial_x f_V$ and $\partial_y f_V$ in terms of finite differences. We point out that after combining such Taylor expansions we have then to solve a system of linear equations specific for each term we are interested in: The corresponding coefficient of the linear combination will be set to 1, whereas all the others to 0. In particular, such systems consist of five equations (one condition on the coefficient of f_V , two on the first partial derivatives, and two on the second partial derivatives forming the Laplacian) in $\deg(V)$ unknowns.

Square lattice graph

To find the first partial derivatives of f , we recall the linear combination in Eq. (3.10) and we impose the following systems of equations:

$$\left\{ \begin{array}{l} \alpha + \beta + \gamma + \delta \\ a(\alpha - \gamma) \\ a(\beta - \delta) \\ \frac{a^2}{2}(\alpha + \gamma) \\ \frac{a^2}{2}(\beta + \delta) \end{array} \right. \begin{array}{l} \text{(i) } \partial_x f_V \\ = 0 \\ = 1 \\ = 0 \\ = 0 \\ = 0 \end{array} \quad \text{and} \quad \begin{array}{l} \text{(ii) } \partial_y f_V \\ = 0 \\ = 0 \\ = 1 \\ = 0 \\ = 0. \end{array} \quad (3.56)$$

- (i) $\partial_x f_V$ is obtained from the solution of a system of five equations in four unknowns: If we consider only the last four equations, the resulting system of four equations is definite; i.e., it admits the unique solution $(\alpha, \beta, \gamma, \delta) = (\frac{1}{2a}, 0, -\frac{1}{2a}, 0)$, which also satisfies the first equation. This leads to

$$\partial_x f_V = \frac{1}{2a} (f_A - f_C). \quad (3.57)$$

- (ii) $\partial_y f_V$ is obtained from the solution of a system of five equations in four unknowns: If we consider only the last four equations, the resulting system of four equations is definite and admits the unique solution $(\alpha, \beta, \gamma, \delta) = (0, \frac{1}{2a}, 0, -\frac{1}{2a})$, which also satisfies the first equation. This leads to

$$\partial_y f_V = \frac{1}{2a} (f_B - f_D). \quad (3.58)$$

This approach, on a square lattice graph, provides the finite-difference formulas both for the first partial derivatives, Eqs. (3.57) and (3.58), and for the Laplacian, Eq. (3.11), and these are consistent with those used in numerical analysis [151]. A point we want to stress is that the systems of equations returning the first partial derivatives are characterized by a coefficient matrix whose rank is the same as that of the augmented matrix and equal to the number of unknowns. This is the reason why we can state that solutions are unique.

Triangular lattice graph

To find the first partial derivatives of f , we recall the linear combination in Eq. (3.20). The resulting systems consist of five equations in six unknowns, and hence we can not have a (unique) solution. Even if we increase the order of the Taylor expansion (in order to have systems of more equations than unknowns), the rank of the coefficient matrix turns out to be less than the number of unknowns. So, there is no way of finding a unique solution, if any. This approach, on a triangular lattice graph, can only provide the finite-difference formula of the Laplacian, Eq. (3.21).

Honeycomb lattice graph

To find the first partial derivatives of f we recall the linear combination in Eq. (3.29). The resulting systems consist of five equations in three unknowns. The rank of the coefficient matrix is equal to the number of unknowns, the rank of the augmented matrix of the system for $\partial_x f_{(V,\odot)}$ is equal to the rank of the coefficient matrix, but the rank of the augmented matrix of the system for $\partial_y f_{(V,\odot)}$ is greater than the rank of the coefficient matrix. This approach, on a honeycomb lattice graph, does not provide finite-difference formulas of both first partial derivatives (only $\partial_x f_{(V,\odot)}$ is returned), whereas it does for the Laplacian, Eq. (3.30).

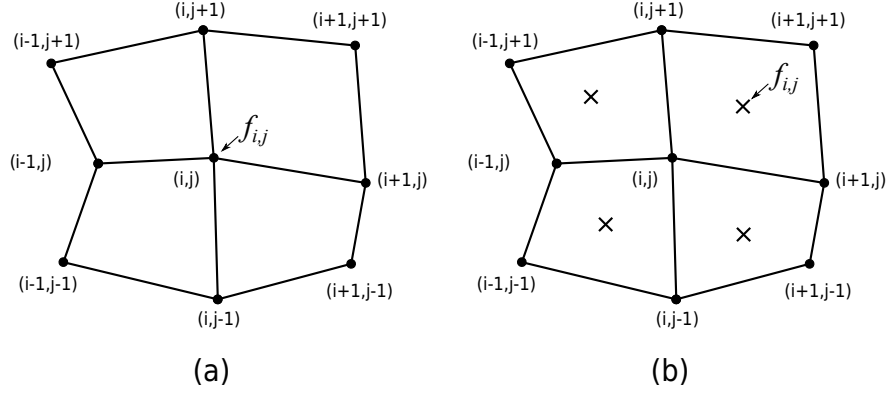
3.5.2 Conservative finite-difference methods

Numerically solving problems has shown that the best results are usually obtained by using discrete models that reproduce fundamental properties of the original continuum model of the underlying physical problem, such as conservation, symmetries of the solution, etc. The development of the discrete algorithms that capture all the important characteristics of the physical problem becomes more difficult with the increasing complexity of the latter (number of involved physical processes, shape of the physical domain, etc.). Hence, there is need to have a discretization method that is sufficiently general to be applied to a wide range of physical systems. In Ref. [170], it is shown how to construct, by using the *support-operators method* [171, 172], high-quality finite-difference schemes such that the resulting discrete difference operators mimic the crucial properties of the continuum differential operators, e.g., symmetry, conservation, stability, and the integral identities between the gradient, curl, and divergence. Moreover, many of the standard finite difference methods, e.g., the finite-volume methods, are special cases of the support-operators method. Unlike the former ones, the latter one can be used to construct finite-difference schemes on grids of arbitrary structure and, because invariant operators are used, the method can be easily used in any coordinate system. However, there are some points of such method differing from our constraints and purposes (see Sec. 3.3.1), so that it can not directly apply to the present work:

- (i) There are two main types of scalar functions of a discrete argument depending on the discretization adopted: *nodal discretization*, where the values of the function correspond to the nodes, or *cell-valued* (or *cell-centered*) *discretization*, where the value of a function does not correspond to a specific point in the cell but corresponds to the cell as a whole geometrical object (Fig. 3.11). It is shown in Ref. [170] that if we choose the nodal discretization for the scalar function (since we know the wave function on the nodes of the graph), then the difference analog, e.g., of the derivative ∂_x , which is the discrete operator D_x , acts as follows:

$$D_x : HN \longrightarrow HC, \quad (3.59)$$

where HN and HC denote the spaces of discrete scalar functions according to nodal and cell-valued discretization, respectively. In other words, if we know the scalar function f on the nodes of the graph, then its first partial derivatives are assigned to the cell used for the discretization as a whole, but we want them to be assigned to a node.

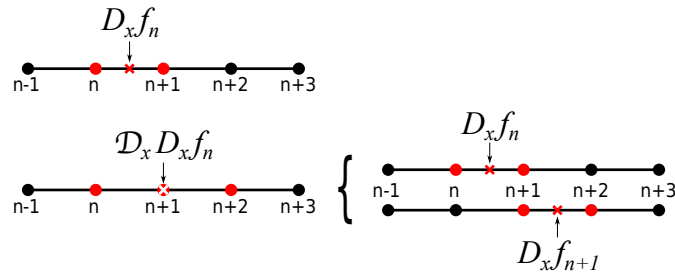

 Figure 3.11. (a) Nodal and (b) cell-valued discretizations of a scalar function f in 2D.

- (ii) This method involves quadrangular cells, because related to 2D logically rectangular grids (very suitable for algorithmic implementation), and it is inspired to the *forward* difference method. In our case, then, we can not remap our PLGs into rectangular grids, because otherwise the resulting discrete operators would not involve all and only the NNs of a given node.
- (iii) The Laplacian is rightly seen as the divergence of the gradient, but in terms of finite differences this means that the Laplacian is computed as difference of differences, so involving further nodes. A first cell is needed to compute the gradient of a scalar function $f \in HN$, then computing the divergence of ∇f requires the differences of the components of the latter, so the adjacent cells are involved (Fig. 3.12). Therefore, in order to approximate the second derivative, we must construct another difference analog for the first derivative

$$\mathcal{D}_x : HC \longrightarrow HN, \quad (3.60)$$

so that the discrete analog of the second derivative is

$$\mathcal{D}_x \mathcal{D}_x : HN \longrightarrow HN. \quad (3.61)$$


 Figure 3.12. 1D example of the different nodes involved in the computation of the discrete analog of the gradient and the Laplacian of a discrete scalar function $f \in HN$. The discrete operator $D : HN \rightarrow HC$, whereas $\mathcal{D} : HC \rightarrow HN$, so that the Laplacian $\nabla^2 = \nabla \cdot \nabla$ reads $\mathcal{D} \cdot \mathcal{D} : HN \rightarrow HN$.

Despite these issues, this method provides an effective tool to compute the first partial derivatives. Green's formulas [173], which are the key to determine the discrete version $D = (D_x, D_y)$ of the differential operator $\nabla = (\partial_x, \partial_y)$, descend from the proof of the Green's theorem in a plane (Appendix 3.A.1) and read as follows:

$$\partial_x f = \lim_{S \rightarrow 0} \frac{\oint_{\partial S} f \, dy}{S}, \quad (3.62)$$

$$\partial_y f = - \lim_{S \rightarrow 0} \frac{\oint_{\partial S} f \, dx}{S}, \quad (3.63)$$

where S is some area and ∂S is its boundary (Fig. 3.13(a)).

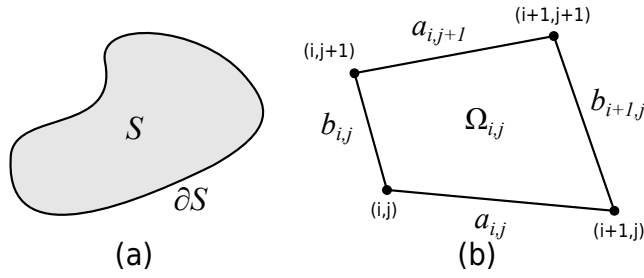


Figure 3.13. Continuous and discrete version of the region needed to compute the first partial derivatives of a scalar function f according to Green's formulas, Eqs. (3.62)–(3.63). (a) A region S in \mathbb{R}^2 with boundary ∂S (line); (b) a cell grid $\Omega_{i,j}$ whose boundary is the union $a_{i,j} \cup b_{i+1,j} \cup a_{i,j+1} \cup b_{i,j}$.

In a discrete case, the role of S is played by the grid cell $\Omega_{i,j}$ and therefore the boundary ∂S is the union of sides $a_{i,j}$, $b_{i+1,j}$, $a_{i,j+1}$, and $b_{i,j}$ (Fig. 3.13(b)). For approximation of the contour integral in the right-hand side of Eqs. (3.62) and (3.63), we divide the contour integral into four integrals each over the corresponding side of quadrangle $\Omega_{i,j}$ and for the approximate evaluation of each integral we use the trapezoidal rule. According to this, as a result, we get the following expression for the difference analog of the derivative $\partial_x f$:

$$(D_x f)_{i,j} = \frac{1}{\Omega_{i,j}} \left[\frac{f_{i+1,j} + f_{i,j}}{2} (y_{i+1,j} - y_{i,j}) + \frac{f_{i+1,j+1} + f_{i+1,j}}{2} (y_{i+1,j+1} - y_{i+1,j}) \right. \\ \left. + \frac{f_{i,j+1} + f_{i+1,j+1}}{2} (y_{i,j+1} - y_{i+1,j+1}) + \frac{f_{i,j} + f_{i,j+1}}{2} (y_{i,j} - y_{i,j+1}) \right], \quad (3.64)$$

where $y_{i,j}$ denotes the y coordinate of the node (i, j) and $\Omega_{i,j}$ is also the area of the grid cell. Notice that this area is the area of the region bounded by the contour of integration. In the same way, the difference analog of the derivative $\partial_y f$ can be found.

In the present work we analogously apply the Green's formulas to our purposes, i.e., by defining a suitable closed path crossing the nodes of interest (Fig. 3.14) and then performing a discrete evaluation of the contour integral according to the trapezoidal rule. Indeed, as previously said, the first partial derivatives of a scalar function $f \in HN$ are cell-valued, and hence the need to design our approach in such a way that all the NNs of a node are involved, so that the result can be reasonably intended as node valued. In the following, for sake of simplicity, we will denote by ∂_x , ∂_y , and ∇^2 also their discrete version, and with Ω the area of the region bounded by the closed curve γ . Notice that for a PLG such area is constant, $\Omega_{i,j} = \Omega \forall (i, j) \in \mathbb{Z}^2$.

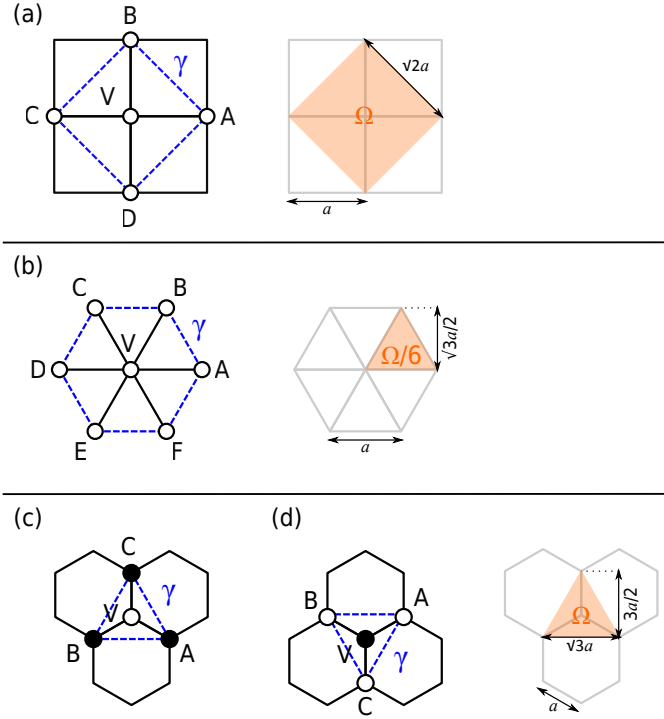


Figure 3.14. NNs of a vertex V and closed path γ (blue dashed line) involved in the computation of the discrete analogs of $\partial_x f_V$ and $\partial_y f_V$ in the different PLGs. The geometry of the region of area Ω (orange shade) bounded by the curve γ is also reported. (a) Square ($\Omega = 2a^2$), (b) triangular ($\Omega = \frac{3\sqrt{3}}{2}a^2$), and (c)–(d) honeycomb ($\Omega = \frac{3\sqrt{3}}{4}a^2$) lattice graph, with lattice parameter a .

Square lattice graph

A vertex V has four NNs, i.e., A , B , C , and D (see Fig. 3.14(a) and Table 3.1). We denote by γ the closed path crossing such adjacent vertices and bounding a region of area $\Omega = 2a^2$. According to Green's formulas, the discrete analogs of the first partial derivatives read

$$\partial_x f_V = \frac{1}{2a}(f_A - f_C), \quad (3.65)$$

$$\partial_y f_V = \frac{1}{2a}(f_B - f_D), \quad (3.66)$$

since

$$\oint_{\gamma} f \, dy \approx a(f_A - f_C), \quad (3.67)$$

$$\oint_{\gamma} f \, dx \approx -a(f_B - f_D). \quad (3.68)$$

The finite-difference formulas so computed are the same used in numerical analysis [151] and already seen in Eqs. (3.57) and (3.58).

Triangular lattice graph

A vertex V has six NNs, i.e., $A, B, C, D, E,$ and F (see Fig. 3.14(b) and Table 3.1). We denote by γ the closed path crossing such adjacent vertices and bounding a region of area $\Omega = \frac{3\sqrt{3}}{2}a^2$. According to Green's formulas, the discrete analogs of the first partial derivatives read

$$\partial_x f_V = \frac{1}{6a}(2f_A + f_B - f_C - 2f_D - f_E + f_F), \quad (3.69)$$

$$\partial_y f_V = \frac{1}{2\sqrt{3}a}(f_B + f_C - f_E - f_F), \quad (3.70)$$

since

$$\oint_{\gamma} f \, dy \approx \frac{\sqrt{3}}{4}a(2f_A + f_B - f_C - 2f_D - f_E + f_F), \quad (3.71)$$

$$\oint_{\gamma} f \, dx \approx -\frac{3}{4}a(f_B + f_C - f_E - f_F). \quad (3.72)$$

Honeycomb lattice graph

A vertex V has three NNs, i.e., $A, B,$ and C (see Fig. 3.14(c) and (d) and Table 3.1). We denote by γ the closed path crossing such adjacent vertices and bounding a region of area $\Omega = \frac{3\sqrt{3}}{4}a^2$. According to Green's formulas, the discrete analogs of the first partial derivatives read

$$\partial_x f_{(V,\odot)} = \frac{1}{\sqrt{3}a}(f_{(A,\odot)} - f_{(B,\odot)}), \quad (3.73)$$

$$\partial_y f_{(V,\odot)} = \frac{\text{sgn}(\odot)}{3a}(2f_{(C,\odot)} - f_{(A,\odot)} - f_{(B,\odot)}), \quad (3.74)$$

since

$$\oint_{\gamma} f \, dy \approx \frac{3}{4}a(f_{(A,\odot)} - f_{(B,\odot)}), \quad (3.75)$$

$$\oint_{\gamma} f \, dx \approx -\text{sgn}(\odot)\frac{\sqrt{3}}{4}a(2f_{(C,\odot)} - f_{(A,\odot)} - f_{(B,\odot)}). \quad (3.76)$$

3.5.3 The CTQW Hamiltonian

Whereas the Peierls phase-factors are a suitable solution to our problem, the issue about the spatial discretization of the Hamiltonian satisfying our assumptions is still open, in particular in the triangular and honeycomb lattice graph. If the finite difference formulas from Taylor expansion are well-behaved only in the square lattices and ill-defined in the other PLGs, then this approach returns, for all the PLGs, a discrete Laplacian which is analogous to the graph one. The discrete first partial derivatives, instead, are provided by the discretization of the Green's formulas. Following the latter approach, the discrete Laplacian is given by the divergence of the gradient, i.e., as a finite difference of finite differences, thus involving next NNs of a given vertex. This point is at odds with our assumption of hopping only to NNs (Sec. 3.3.1), because the kinetic term of the free particle would be accountable for the hopping up to next NNs, whereas the orbital paramagnetic term for the hopping only to NNs. In view of these results, we therefore suggest a hybrid method which combines the above-mentioned results: The discrete first partial derivatives are provided by conservative finite-difference methods (Sec. 3.5.2), whereas the Laplacian by finite difference formulas from Taylor expansion (Sec. 3.5.1). According to this approach, we spatially

discretize Eq. (3.37) in order to obtain the Hamiltonian describing the CTQW of a charged particle on the different PLGs in the presence of a perpendicular magnetic field. As we are going to see below, what we obtain is reminiscent of the Peierls model (Sec. 3.4). Indeed, the hopping terms can be regarded as the first-order Taylor expansion of the Peierls phase-factors but now the diagonal elements of the Hamiltonian matrix, i.e., the on-site terms, also include the quadratic term in \mathbf{A} .

Square lattice graph

With reference to Table 3.1, according to the Laplacian in Eq. (3.11) and the first partial derivatives in Eqs. (3.65) and (3.66), the resulting CTQW Hamiltonian reads

$$\begin{aligned} \hat{\mathcal{H}} = -J_S \sum_V \bigg\{ & \left[1 + i \frac{qa}{2\hbar} (A_V^x + A_A^x) \right] |A\rangle\langle V| \\ & + \left[1 + i \frac{qa}{2\hbar} (A_V^y + A_B^y) \right] |B\rangle\langle V| \\ & + \left[1 - i \frac{qa}{2\hbar} (A_V^x + A_C^x) \right] |C\rangle\langle V| \\ & + \left[1 - i \frac{qa}{2\hbar} (A_V^y + A_D^y) \right] |D\rangle\langle V| \\ & - \left[4 + \frac{q^2 a^2}{\hbar^2} (A_V^x{}^2 + A_V^y{}^2) \right] |V\rangle\langle V| \bigg\}, \end{aligned} \quad (3.77)$$

where J_S is defined in Eq. (3.13).

Triangular lattice graph

With reference to Table 3.1, according to the Laplacian in Eq. (3.21) and the first partial derivatives in Eqs. (3.69) and (3.70), the resulting CTQW Hamiltonian reads

$$\begin{aligned} \hat{\mathcal{H}} = -J_T \sum_V \bigg\{ & \left[1 + i \frac{qa}{2\hbar} (A_V^x + A_A^x) \right] |A\rangle\langle V| \\ & + \left[1 + i \frac{qa}{4\hbar} (A_V^x + A_B^x + \sqrt{3}(A_V^y + A_B^y)) \right] |B\rangle\langle V| \\ & + \left[1 - i \frac{qa}{4\hbar} (A_V^x + A_C^x - \sqrt{3}(A_V^y + A_C^y)) \right] |C\rangle\langle V| \\ & + \left[1 - i \frac{qa}{2\hbar} (A_V^x + A_D^x) \right] |D\rangle\langle V| \\ & + \left[1 - i \frac{qa}{4\hbar} (A_V^x + A_E^x + \sqrt{3}(A_V^y + A_E^y)) \right] |E\rangle\langle V| \\ & + \left[1 + i \frac{qa}{4\hbar} (A_V^x + A_F^x - \sqrt{3}(A_V^y + A_F^y)) \right] |F\rangle\langle V| \\ & - \left[6 + \frac{3q^2 a^2}{2\hbar^2} (A_V^x{}^2 + A_V^y{}^2) \right] |V\rangle\langle V| \bigg\}, \end{aligned} \quad (3.78)$$

where J_T is defined in Eq. (3.25).

Honeycomb lattice graph

With reference to Table 3.1, according to the Laplacian in Eq. (3.30) and the first partial derivatives in Eqs. (3.73) and (3.74), the resulting CTQW Hamiltonian reads

$$\hat{\mathcal{H}} = -J_H \sum_{\odot \in \{\circ, \bullet\}} \sum_{(V, \odot)} \left[h_{AV} |A, \odot\rangle \langle V, \odot| + h_{BV} |B, \odot\rangle \langle V, \odot| + h_{CV} |C, \odot\rangle \langle V, \odot| + h_{VV} |V, \odot\rangle \langle V, \odot| \right], \quad (3.79)$$

where J_H is defined in Eq. (3.32), and we have defined

$$h_{AV} := 1 + i \frac{qa}{4\hbar} \left[\sqrt{3} \left(A_{(V, \odot)}^x + A_{(A, \odot)}^x \right) - \text{sgn}(\odot) \left(A_{(V, \odot)}^y + A_{(A, \odot)}^y \right) \right], \quad (3.80)$$

$$h_{BV} := 1 - i \frac{qa}{4\hbar} \left[\sqrt{3} \left(A_{(V, \odot)}^x + A_{(B, \odot)}^x \right) + \text{sgn}(\odot) \left(A_{(V, \odot)}^y + A_{(B, \odot)}^y \right) \right], \quad (3.81)$$

$$h_{CV} := 1 + \text{sgn}(\odot) i \frac{qa}{2\hbar} \left(A_{(V, \odot)}^y + A_{(C, \odot)}^y \right), \quad (3.82)$$

$$h_{VV} := - \left[3 + \frac{3q^2 a^2}{4\hbar^2} \left(A_{(V, \odot)}^{x^2} + A_{(V, \odot)}^{y^2} \right) \right]. \quad (3.83)$$

3.5.4 Numerical simulation: results

The behavior of the variance of the space coordinates is shown in Fig. 3.15, and it is the same for both the x and y coordinate, i.e., $\sigma_x^2(Jt) = \sigma_y^2(Jt)$. We observe that, as the modulus of the magnetic field increases, the curve of the variance of the space coordinates deviates from that of the free particle, it shows a maximum which lowers, and an oscillation having increasing frequency. This is more evident in the square and triangular lattice graph than in the honeycomb one.

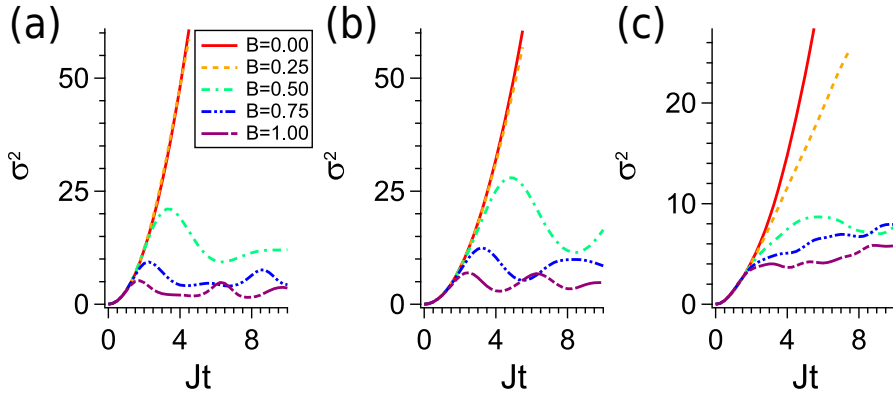


Figure 3.15. Variance of the space coordinates obtained in a CTQW of a charged particle in the (a) triangular, (b) square, and (c) honeycomb lattice graph for increasing values of the modulus B of the perpendicular uniform magnetic field. As the latter increases, the variance deviates from the curve of the free particle. Stronger magnetic fields correlate with smaller variance and higher frequency *pseudo*-oscillations. The variance of the two spatial coordinates is equal, $\sigma_x^2(t) = \sigma_y^2(t)$. The CTQW Hamiltonian is obtained from the spatial discretization of Eq. (3.37).

Maps of the time evolution of the probability density are shown in Figs. 3.16–3.18. We observe that CTQWs on PLGs are characterized by an oscillating (spiral) probability density which arises from the trade-off among the symmetry of the lattice, the rotational symmetry of the Hamiltonian

in the continuum and the harmonic oscillator behind the latter. Moreover the probability density, in time, seems to rotate, mimicking the effects of the Lorentz force (this is particularly evident on the square lattice graph, Fig. 3.17).

Clues of the harmonic oscillator behind the Hamiltonian in the continuum are revealed by the maps of the time evolution of the probability density, alternating phases of expansion and contraction, and by the variance of the space coordinates, alternating local maxima and minima, which become more frequent for increasing magnetic field (reminiscent of the cyclotron frequency). However, the observed behavior is not exactly oscillating and periodic because of the spatial discretization. Even in the Peirls model we observe something similar, e.g., the probability distribution has an expansion and then a contraction, but this model is based on the Hamiltonian of the free particle, and indeed the tails of the wave function continue to move away. Instead, when spatially discretizing Eq. (3.37), the quadratic term in \mathbf{A} – absent in the Peirls model – is here explicitly present. In the symmetric gauge such a term reads as

$$\frac{q^2}{2m} \mathbf{A}^2 = \frac{q^2 B^2}{8m} [(x - x_c)^2 + (y - y_c)^2] , \quad (3.84)$$

i.e., it is a 2D harmonic potential. The role of this term is clearer in Fig. 3.19, where we report the variance of the space coordinate for a CTQW on a square lattice according to different models: the original Peierls model (Sec. 3.4); i.e., the presence of the magnetic field is encoded in the Peierls phase-factors describing the hopping terms. Then we correct such a model by including in the Hamiltonian the on-site energies due to Eq. (3.84) and the spatial discretization of the Hamiltonian of the corresponding system in the continuum (Sec. 3.5). In the end, we consider the CTQW of a particle in a harmonic potential equivalent to Eq. (3.84).

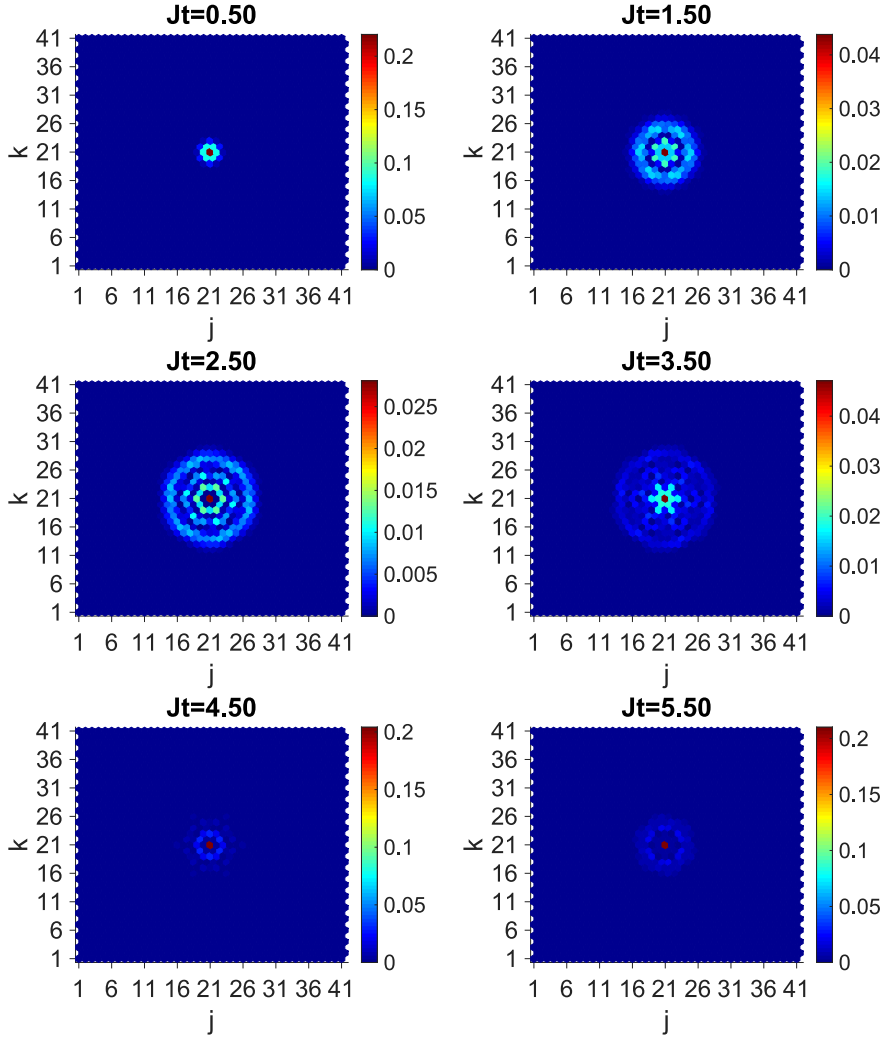


Figure 3.16. Map of the time evolution of the probability density according to the CTQW of a charged particle on a triangular lattice graph in the presence of a perpendicular uniform magnetic field ($B = 0.6$). The CTQW Hamiltonian is obtained from the spatial discretization of Eq. (3.37).

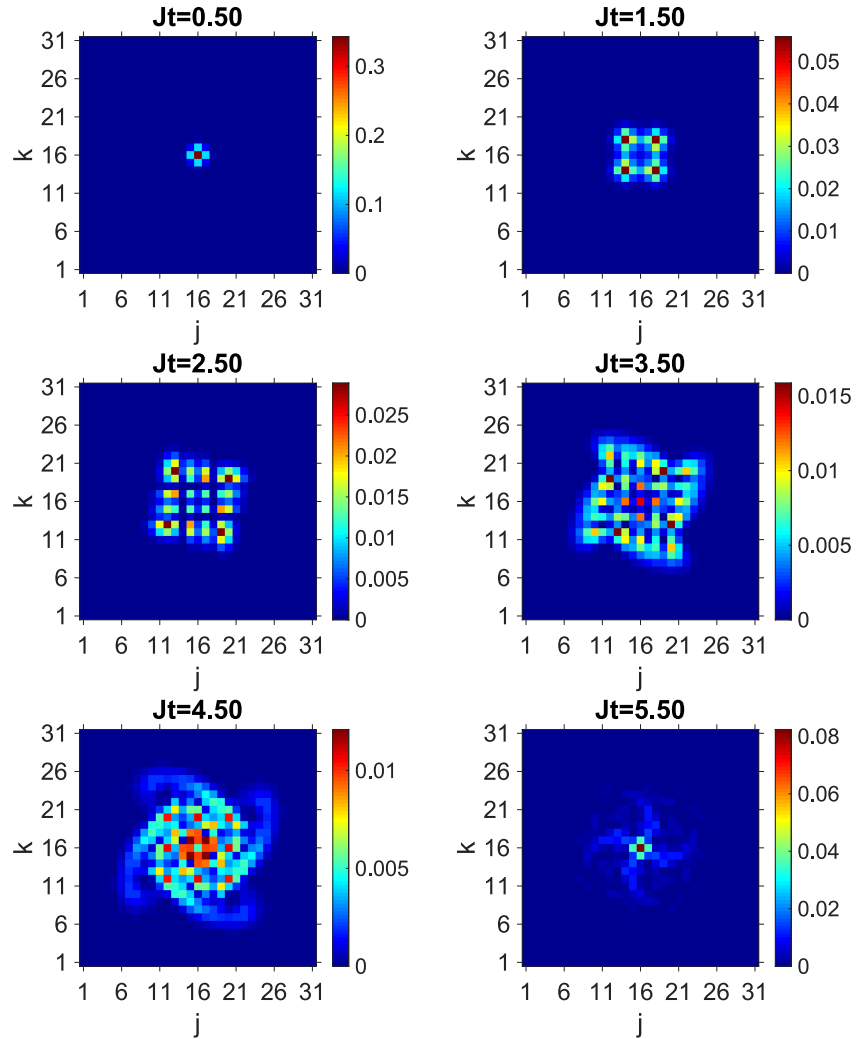


Figure 3.17. Map of the time evolution of the probability density according to the CTQW of a charged particle on a square lattice graph in the presence of a perpendicular uniform magnetic field ($B = 0.6$). The CTQW Hamiltonian is obtained from the spatial discretization of Eq. (3.37).

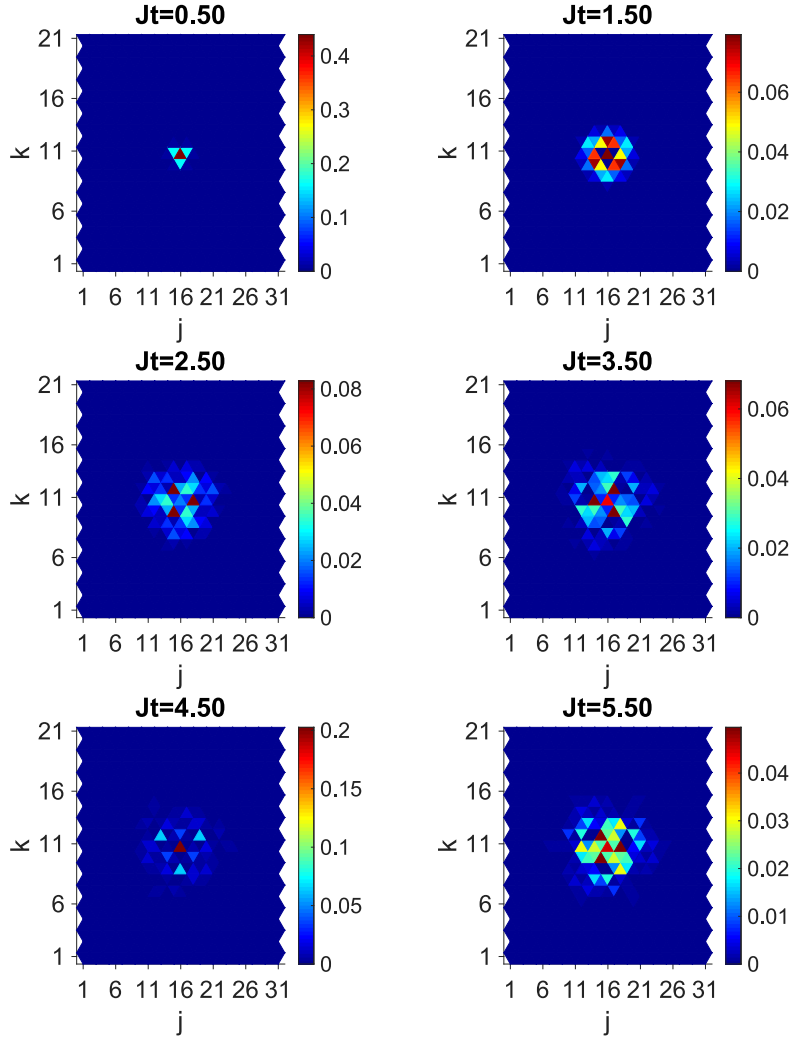


Figure 3.18. Map of the time evolution of the probability density according to the CTQW of a charged particle on a honeycomb lattice graph in the presence of a perpendicular uniform magnetic field ($B = 0.6$). The CTQW Hamiltonian is obtained from the spatial discretization of Eq. (3.37).

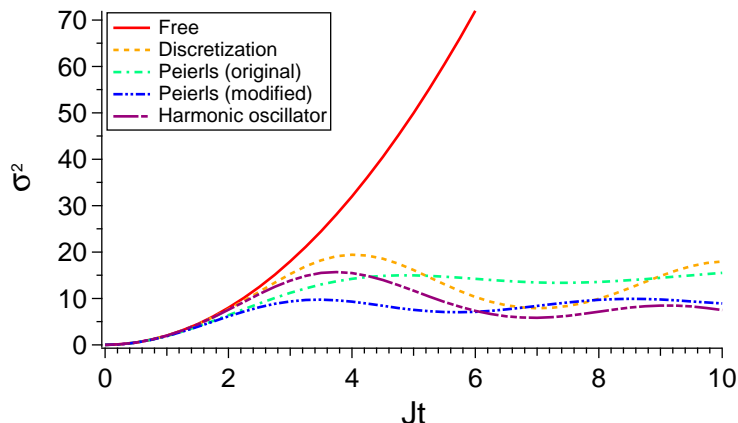


Figure 3.19. Comparison of the variance of the space coordinates obtained in a CTQW of a charged particle on a square lattice graph in the presence of a perpendicular uniform magnetic field ($B = 0.6$) according to different models: “Peirls (original),” the model according to which the presence of the magnetic field is encoded in the Peierls phase-factors describing the hopping terms; “Peirls (modified),” a correction to the Peirls model by including in the Hamiltonian the on-site energies due to the quadratic term $q^2 \mathbf{A}^2 / 2m$; “Discretization,” the spatial discretization of the Hamiltonian of the corresponding system in the continuum; and “Harmonic oscillator,” the CTQW of a particle in a harmonic potential equivalent to the quadratic term $q^2 \mathbf{A}^2 / 2m$ (\mathbf{A} in the symmetric gauge). The curve of the free particle is reported as reference. The variance of the two spatial coordinates is equal, $\sigma_x^2(Jt) = \sigma_y^2(Jt)$.

3.6 Conclusions

In the present chapter, we have studied the continuous-time quantum walks (CTQWs) of a charged particle in the presence of a perpendicular uniform magnetic field on planar lattice graphs (PLGs), i.e., graphs possessing a drawing whose embedding in a Euclidean plane forms a regular tessellation (triangular, square, and honeycomb lattice graphs). Because of the strict connection between the generator of the evolution of the CTQW and the Hamiltonian, the straightforward approach to get a CTQW Hamiltonian has been to spatially discretize the Hamiltonian of the corresponding system in the continuum. Then we have numerically simulated the CTQWs in order to study the time evolution of the probability density and variance of the spatial coordinates of a walker initially localized in the center of the PLG.

CTQW of the free particle. As a reference, we have first considered the CTQW of the free particle, whose Hamiltonian only consists of the kinetic term. In the vertex states basis, we have spatially discretized the Laplacian by means of finite difference formulas derived from Taylor expansion. The reason for this, even though the discrete Laplacian so obtained has turned out to be analogous to the graph Laplacian, is that this approach allows us to actually take into account the underlying geometry of the PLG. Indeed, by changing the degree of a vertex we expect the hopping amplitude to change accordingly: While for the graph Laplacian, because of its definition in terms of adjacency and diagonal degree matrices, there is no computation telling us how the hopping amplitude changes in the different PLGs, using Taylor expansion is a constructive way to determine the discrete Laplacian and the resulting hopping amplitude depends on the PLG. From the numerical simulations of the CTQWs of the free particle, the first result is that the variance of the two spatial coordinates is equal, $\sigma_x^2(t) = \sigma_y^2(t) =: \sigma^2(t)$, and it can be related to

the degree of the generic vertex in the different PLGs: $\sigma_H^2(t) \leq \sigma_S^2(t) \leq \sigma_T^2(t)$ and in the honeycomb lattice graph $\deg(V) = 3$, in the square lattice graph $\deg(V) = 4$, and in the triangular lattice graph $\deg(V) = 6$. An analogous behavior has been observed for the quantum coherence. The second, but more relevant result is that there exist limits to the envisaged universal ballistic spreading for both 1D and 2D QWs: On the square and triangular lattice graphs (Bravais lattices, thus characterized by discrete translation invariance), we have observed a variance of the space coordinates $\sigma^2(t) \propto t^2$ (*ballistic* spreading), whereas on the honeycomb lattice graph (non-Bravais lattice) $\sigma^2(t) \propto t^p$, with $1 < p < 2$ (*sub-ballistic* spreading, because neither ballistic, $p = 2$, nor diffusive, $p = 1$). The hypothesis that the underlying reason is to be found in the presence or not of discrete translation invariance is further corroborated by the fact that we have observed an analogous *sub-ballistic* spreading on another 2D non-Bravais lattice, the truncated square tiling, which consists of octagons and squares. After all, the *ballistic* spreading has been usually proved for QWs on a line or on a n -D hypercube and in the latter the walker moves one unit in each dimension, and thus it clearly reproduces the results on the line, because it is as if the QW is taking place on n orthogonal lines (dimensions).

CTQW under magnetic field. Then we have turned on the perpendicular uniform magnetic field, considering the vector potential in the symmetric gauge. In such gauge, the Hamiltonian in the continuum is known to be the Hamiltonian of a 1D harmonic oscillator, having degenerate energy levels (the so-called *Landau levels*) and cyclotron frequency $\omega_0 = qB/m$. This choice of gauge breaks translational symmetry in both the x and the y directions, but it does preserve rotational symmetry, i.e., $[\hat{\mathcal{H}}, \hat{L}_z] = 0$. Under the assumption of a hopping to nearest neighbors (NN), we have addressed the definition of the CTQW Hamiltonian in the presence of a magnetic field in two ways:

- (i) Peierls model, i.e., the tunneling matrix elements of the free-particle Hamiltonian are now accompanied by complex Peierls phase-factors due to the vector potential. To our knowledge, this is the way the discrete-time QWs under artificial magnetic field have been studied.
- (ii) Spatial discretization of the Hamiltonian of a spinless charged particle in the presence of a magnetic field. Since the linear momentum is present both at the first and second orders, we have faced the non-trivial issue of determining the finite difference formulas approximating the first partial derivatives (from Green's formulas) and the Laplacian (from Taylor expansion, already obtained for the free particle) in the different PLGs.

Again, the first result is that $\sigma_x^2(t) = \sigma_y^2(t) =: \sigma^2(t)$. In both cases we have observed that the variance of the space coordinates lowers as the modulus B of the magnetic field increases and, as expected, we have found more circular structures in the probability density of the walker when allowing the PLG to better follow the rotational symmetry of the Hamiltonian: The triangular lattice graph, $\deg(V) = 6$, provides the best discrete approximation of a circle among the PLGs, while the honeycomb lattice graph, $\deg(V) = 3$, provides the worst one. In particular, the maps of the time evolution of the probability density are characterized by a trade-off between the circular symmetry due to the gauge and the symmetry of the underlying lattice. Apart from these qualitatively common features, as soon as we let the CTQW evolve longer, the difference between the two methods shows up and the quadratic term in the vector potential $q^2 \mathbf{A}^2/2m$ plays a crucial role in it. In the Peierls model, the walker initially spreads over the lattice; then the maxima of probability density come back toward the initial vertex and eventually move away from it (as revealed also by the variance). However, during the time evolution, the tails of the wave function continue to get away from the center of the lattice graph: Being this CTQW Hamiltonian based on the graph Laplacian, there is no term confining or limiting the spreading of the walker, since

the equations of the curves STU and SVU respectively. We then write

$$\begin{aligned}
 \iint_R \partial_y P dx dy &= \int_a^b dx \int_{y_1(x)}^{y_2(x)} dy \partial_y P \\
 &= \int_a^b dx [P(x, y)]_{y=y_1(x)}^{y=y_2(x)} \\
 &= \int_a^b [P(x, y_2(x)) - P(x, y_1(x))] dx \\
 &= - \oint_C P dx,
 \end{aligned}$$

where the last equality follows from $\int_a^b P(x, y_2(x)) dx = - \int_b^a P(x, y_2(x)) dx$. If we now let $x = x_1(y)$ and $x = x_2(y)$ be the equations of the curves TSV and TUV respectively, we can similarly show that

$$\begin{aligned}
 \iint_R \partial_x Q dx dy &= \int_c^d dy \int_{x_1(y)}^{x_2(y)} dx \partial_x Q \\
 &= \int_c^d dy [Q(x, y)]_{x=x_1(y)}^{x=x_2(y)} \\
 &= \int_c^d [Q(x_2(y), y) - Q(x_1(y), y)] dy \\
 &= \oint_C Q dy,
 \end{aligned}$$

where the last equality follows from $-\int_c^d Q(x_1(y), y) dy = \int_d^c Q(x_1(y), y) dy$. Subtracting these two results gives Green's theorem in a plane. \square

3.A.2 Spatial discretization

Let us consider a particle in a plane: The spatial discretization is accomplished by reducing the Euclidean plane into a square lattice of lattice parameter a . Sites of the lattice correspond to positions $(x_j, y_k) = (ja, ka)$, where $j, k \in \mathbb{Z}$, and so each site can be labeled by the couple of indices (j, k) . The Hilbert space of such discretized system can be obtained as

$$\mathcal{H} = \mathcal{H}_x \otimes \mathcal{H}_y, \quad (3.86)$$

with $\dim(\mathcal{H}) = \dim(\mathcal{H}_x) \times \dim(\mathcal{H}_y)$, i.e., as a tensor product of two Hilbert subspaces – \mathcal{H}_x and \mathcal{H}_y – describing the states of the particle within 1D orthogonal lattices. The basis of each Hilbert subspace is provided, e.g., by the complete set of eigenstates of the position within the corresponding 1D lattice: $\{|j\rangle\}_{j=1, \dots, \dim(\mathcal{H}_x)}$ for \mathcal{H}_x and $\{|k\rangle\}_{k=1, \dots, \dim(\mathcal{H}_y)}$ for \mathcal{H}_y . Then, the basis of the resulting Hilbert space \mathcal{H} is

$$\{|j, k\rangle = |j\rangle \otimes |k\rangle\}_{j, k}, \quad (3.87)$$

according to which we outline in Table 3.2 the discrete version of the basic relations involving a generic abstract state and position eigenstates in the position space.

	Continuum		Lattice
Position eigenstate	$ x, y\rangle$	\longrightarrow	$ j, k\rangle$
Wave function	$\langle x, y \psi\rangle = \psi(x, y)$	\longrightarrow	$\langle j, k \psi\rangle = \psi_{j,k}$
Orthonormality	$\langle x', y' x, y\rangle = \delta(x' - x)\delta(y' - y)$	\longrightarrow	$\langle j', k' j, k\rangle = \delta_{j',j}\delta_{k',k}$
Completeness relation	$\int_{-\infty}^{+\infty} \int_{-\infty}^{+\infty} x, y\rangle\langle x, y dx dy = 1$	\longrightarrow	$\sum_{(j,k) \in \mathbb{Z}^2} j, k\rangle\langle j, k = 1$
Expansion of a state	$ \psi\rangle = \int_{-\infty}^{+\infty} \int_{-\infty}^{+\infty} \psi(x, y) x, y\rangle dx dy$	\longrightarrow	$ \psi\rangle = \sum_{(j,k) \in \mathbb{Z}^2} \psi_{j,k} j, k\rangle$

Table 3.2. Discrete version of the basic relations involving a generic abstract state $|\psi\rangle$ and position eigenstates in the position space. The lattice is assumed to be infinite and to have lattice parameter a , so the discrete positions are $(x_j, y_k) = (ja, ka) \rightarrow (j, k) \in \mathbb{Z}^2$. Notice that the discrete version of the Dirac δ is the Kronecker δ .

3.A.3 Discrete differential operators

The next step is the discretization of the differential operators (first partial derivatives and Laplacian⁴) by means of finite difference formulas [151]. If we consider a function $f(x)$ defined on a 1D lattice, whose sites are $x_j = ja$, and assume the lattice parameter a to be small enough, then we can evaluate the following Taylor expansions up to the second order:

$$f(x_j \pm a) \approx f(x_j) \pm f'(x_j)a + \frac{1}{2}f''(x_j)a^2. \quad (3.88)$$

Letting $f_j := f(x_j)$, we have the following:

- (i) The difference of such quantities provides the first derivative of f in the site j

$$f'_j \approx \frac{f_{j+1} - f_{j-1}}{2a}; \quad (3.89)$$

- (ii) the sum of such quantities provides the second derivative of f in the site j

$$f''_j \approx \frac{f_{j+1} + f_{j-1} - 2f_j}{a^2}. \quad (3.90)$$

Notice that the discrete differential operator ∂_x acts on a product of functions $f(x)g(x)$ as on $(fg)(x)$, i.e.,

$$\frac{d(fg)_j}{dx} = \frac{1}{2a} [(fg)_{j+1} - (fg)_{j-1}] = \frac{1}{2a} (f_{j+1}g_{j+1} - f_{j-1}g_{j-1}), \quad (3.91)$$

since $(fg)(x) = f(x)g(x)$.

⁴The first partial derivatives are not involved by the Hamiltonian of a free particle but they are when inserting the magnetic field.

Proof. This can be easily proved by considering the Taylor expansion of the product of such functions

$$(fg)(x \pm a) \approx (fg)(x) \pm (fg)'(x)a + \frac{1}{2}(fg)''(x)a^2, \quad (3.92)$$

from which, as before,

$$(fg)'(x) \approx \frac{1}{2a} [(fg)(x+a) - (fg)(x-a)]. \quad (3.93)$$

□

Then, in 2D, the discrete versions of the gradient and the Laplacian are obtained by evaluating the partial derivatives according to Eqs. (3.89) and (3.90):

$$\nabla f_{j,k} = \frac{1}{2a} [(f_{j+1,k} - f_{j-1,k}) \hat{\mathbf{i}} + (f_{j,k+1} - f_{j,k-1}) \hat{\mathbf{j}}] \quad (3.94)$$

and

$$\nabla^2 f_{j,k} = \frac{1}{a^2} (f_{j+1,k} + f_{j-1,k} + f_{j,k+1} + f_{j,k-1} - 4f_{j,k}), \quad (3.95)$$

where $f_{j,k} := f(x_j, y_k)$ and $\hat{\mathbf{i}}, \hat{\mathbf{j}}$ denote the unit vectors of the x, y axis, respectively.

3.A.4 Linear momentum operator

The linear momentum operator in the position space reads as follows:

$$\hat{\mathbf{p}} = -i\hbar\nabla. \quad (3.96)$$

For sake of simplicity, we consider a 1D space. If we recall the study of the linear momentum as the generator of infinitesimal translations [175], the action of \hat{p} on a state $|\psi\rangle = \int dx' \psi(x')|x'\rangle$, where $\psi(x') = \langle x'|\psi\rangle$, gives

$$\hat{p}|\psi\rangle = \int dx' |x'\rangle (-i\hbar\partial_{x'}\psi(x')), \quad (3.97)$$

or equivalently

$$\langle x'|\hat{p}|\psi\rangle = -i\hbar\partial_{x'}\psi(x'), \quad (3.98)$$

from which, for the matrix element \hat{p} in the x representation, we obtain

$$\langle x'|\hat{p}|x''\rangle = -i\hbar\partial_{x'}\delta(x' - x''). \quad (3.99)$$

By repeatedly applying Eq. (3.98), we also have

$$\langle x'|\hat{p}^n|\psi\rangle = (-i\hbar)^n \partial_{x'}^n \psi(x'). \quad (3.100)$$

Now we adapt this result to a discrete 1D space (see also Table 3.2). The state $|\psi\rangle$ is expanded on the site states basis $\{|j\rangle\}_j$, the equivalent of position states, as $|\psi\rangle = \sum_j \psi_j |j\rangle$, where $\psi_j = \langle j|\psi\rangle$. Then, by reading ∇ as the *discrete* differential operator acting on the wave function according to Eq. (3.89), we have that

$$\langle j|\hat{p}|\psi\rangle = \frac{-i\hbar}{2a} (\psi_{j+1} - \psi_{j-1}) = \frac{-i\hbar}{2a} (\langle j+1| - \langle j-1|)|\psi\rangle, \quad (3.101)$$

and so

$$\begin{aligned}
 \hat{p}|\psi\rangle &= \frac{-i\hbar}{2a} \sum_j |j\rangle (\psi_{j+1} - \psi_{j-1}) \\
 &= \frac{-i\hbar}{2a} \sum_j \psi_j (|j-1\rangle - |j+1\rangle) \\
 &= \left[\frac{-i\hbar}{2a} \sum_j (|j-1\rangle\langle j| - |j+1\rangle\langle j|) \right] |\psi\rangle, \tag{3.102}
 \end{aligned}$$

where the second equality follows from rescaling the dummy index of summation, with the latter being infinite. Analogously, by reading ∇^2 as the *discrete* Laplacian acting on the wave function according to Eq. (3.90), we have that

$$\begin{aligned}
 \hat{p}^2|\psi\rangle &= \frac{(-i\hbar)^2}{a^2} \sum_j |j\rangle (\psi_{j+1} + \psi_{j-1} - 2\psi_j) \\
 &= \frac{(-i\hbar)^2}{a^2} \sum_j \psi_j (|j-1\rangle + |j+1\rangle - 2|j\rangle) \\
 &= \left[-\frac{\hbar^2}{a^2} \sum_j (|j-1\rangle\langle j| + |j+1\rangle\langle j| - 2|j\rangle\langle j|) \right] |\psi\rangle. \tag{3.103}
 \end{aligned}$$

The point we want to stress is that, as well as in the continuum, differential operators act on the wave functions, not on the kets. Indices of bras and kets are then accordingly rescaled after the differential operators acted on the wave function.

3.A.5 Derivation of the discrete Hamiltonian: details

As seen in Sec. 3.A.4, the way to obtain the Hamiltonian in terms of projectors all in the form $|W\rangle\langle V|$, where V denotes an initial vertex and W denotes one of its NNs, comes through the rescaling of the indices of summation. Another way, more suitable when dealing with PLGs, is to exploit the Hermiticity of the Hamiltonian, so that $\mathcal{H}_{WV} = \langle W|\hat{\mathcal{H}}|V\rangle = \langle V|\hat{\mathcal{H}}|W\rangle^* = (\mathcal{H}_{VW})^*$. This allows us to write the Hamiltonian in terms of projectors in the form $|W\rangle\langle V|$ knowing the matrix element describing the opposite hopping \mathcal{H}_{VW} . Below, we show further details in the derivation of the CTQW Hamiltonian from the spatial discretization of Eq. (3.37) (the free-particle Hamiltonian is recovered for $B = 0$). Notice that the term $\hat{\mathbf{p}} \cdot \mathbf{A}\psi_V = -i\hbar [\partial_x(A^x f_V) + \partial_y(A^y f_V)]$ is to be computed in the spirit of Eq. (3.91). The outline to obtain the CTQW Hamiltonian is as follows:

- (i) We expand the generic state $|\psi\rangle$ on the vertex states basis $\{|V\rangle\}$ as

$$|\psi\rangle = \sum_V \psi_V |V\rangle, \tag{3.104}$$

where $\psi_V = \langle V|\psi\rangle$ is the wave function and the index of summation runs over all the vertices in the graph (infinite, in principle);

- (ii) the differential operators act on ψ_V ;
- (iii) we exploit the Hermiticity of the Hamiltonian in order to write it in terms of projectors in the form $|W\rangle\langle V|$, where V is the starting vertex and W the final one.

Square lattice graph

With reference to Eqs. (3.11), (3.13), (3.65), and (3.66) and to Table 3.1, the CTQW Hamiltonian acts on a state $|\psi\rangle$ as follows:

$$\begin{aligned}
 \hat{\mathcal{H}}|\psi\rangle &= -\frac{\hbar^2}{2ma^2} \sum_V \left\{ (\psi_A + \psi_B + \psi_C + \psi_D - 4\psi_V) - i\frac{qa}{2\hbar} [(A_V^x + A_A^x)\psi_A - (A_V^x + A_C^x)\psi_C] \right. \\
 &\quad \left. - i\frac{qa}{2\hbar} [(A_V^y + A_B^y)\psi_B - (A_V^y + A_D^y)\psi_D] - \frac{q^2a^2}{\hbar^2} (A_V^{x^2} + A_V^{y^2})\psi_V \right\} |V\rangle \\
 &= -J_S \sum_V \left\{ \left[1 - i\frac{qa}{2\hbar} (A_V^x + A_A^x)\right] |V\rangle\langle A| + \left[1 - i\frac{qa}{2\hbar} (A_V^y + A_B^y)\right] |V\rangle\langle B| \right. \\
 &\quad + \left[1 + i\frac{qa}{2\hbar} (A_V^x + A_C^x)\right] |V\rangle\langle C| + \left[1 + i\frac{qa}{2\hbar} (A_V^y + A_D^y)\right] |V\rangle\langle D| \\
 &\quad \left. - \left[4 + \frac{q^2a^2}{\hbar^2} (A_V^{x^2} + A_V^{y^2})\right] |V\rangle\langle V| \right\} |\psi\rangle \\
 &= \sum_V (\mathcal{H}_{VA} |V\rangle\langle A| + \mathcal{H}_{VB} |V\rangle\langle B| + \mathcal{H}_{VC} |V\rangle\langle C| + \mathcal{H}_{VD} |V\rangle\langle D| + \mathcal{H}_{VV} |V\rangle\langle V|) |\psi\rangle.
 \end{aligned} \tag{3.105}$$

Exploiting $\mathcal{H}^\dagger = \mathcal{H}$, Eq. (3.105) can be recast into Eq. (3.77).

Triangular lattice graph

With reference to Eqs. (3.21), (3.25), (3.69), and (3.70) and to Table 3.1, the CTQW Hamiltonian acts on a state $|\psi\rangle$ as follows:

$$\begin{aligned}
 \hat{\mathcal{H}}|\psi\rangle &= -\frac{\hbar^2}{3ma^2} \sum_V \left\{ (\psi_A + \psi_B + \psi_C + \psi_D + \psi_E + \psi_F - 6\psi_V) - i\frac{qa}{4\hbar} [2(A_V^x + A_A^x)\psi_A \right. \\
 &\quad + (A_V^x + A_B^x)\psi_B - (A_V^x + A_C^x)\psi_C - 2(A_V^x + A_D^x)\psi_D - (A_V^x + A_E^x)\psi_E + (A_V^x + A_F^x)\psi_F] \\
 &\quad - i\frac{\sqrt{3}qa}{4\hbar} [(A_V^y + A_B^y)\psi_B + (A_V^y + A_C^y)\psi_C - (A_V^y + A_E^y)\psi_E - (A_V^y + A_F^y)\psi_F] \\
 &\quad \left. - \frac{3q^2a^2}{2\hbar^2} (A_V^{x^2} + A_V^{y^2})\psi_V \right\} |V\rangle \\
 &= -J_T \sum_V \left\{ \left[1 - i\frac{qa}{2\hbar} (A_V^x + A_A^x)\right] |V\rangle\langle A| + \left[1 - i\frac{qa}{4\hbar} (A_V^x + A_B^x + \sqrt{3}(A_V^y + A_B^y))\right] |V\rangle\langle B| \right. \\
 &\quad + \left[1 + i\frac{qa}{4\hbar} (A_V^x + A_C^x - \sqrt{3}(A_V^y + A_C^y))\right] |V\rangle\langle C| + \left[1 + i\frac{qa}{2\hbar} (A_V^x + A_D^x)\right] |V\rangle\langle D| \\
 &\quad + \left[1 + i\frac{qa}{4\hbar} (A_V^x + A_E^x + \sqrt{3}(A_V^y + A_E^y))\right] |V\rangle\langle E| \\
 &\quad + \left[1 - i\frac{qa}{4\hbar} (A_V^x + A_F^x - \sqrt{3}(A_V^y + A_F^y))\right] |V\rangle\langle F| \\
 &\quad \left. - \left[6 + \frac{3q^2a^2}{2\hbar^2} (A_V^{x^2} + A_V^{y^2})\right] |V\rangle\langle V| \right\} |\psi\rangle \\
 &= \sum_V (\mathcal{H}_{VA} |V\rangle\langle A| + \mathcal{H}_{VB} |V\rangle\langle B| + \mathcal{H}_{VC} |V\rangle\langle C| + \mathcal{H}_{VD} |V\rangle\langle D| + \mathcal{H}_{VE} |V\rangle\langle E| \\
 &\quad + \mathcal{H}_{VF} |V\rangle\langle F| + \mathcal{H}_{VV} |V\rangle\langle V|) |\psi\rangle.
 \end{aligned} \tag{3.106}$$

Exploiting $\mathcal{H}^\dagger = \mathcal{H}$, Eq. (3.106) can be recast into Eq. (3.78).

Honeycomb lattice graph

With reference to Eqs. (3.30), (3.32), (3.73), and (3.74) and to Table 3.1, the CTQW Hamiltonian acts on a state

$$|\psi\rangle = \sum_{\odot \in \{\circ, \bullet\}} \sum_{(V, \odot)} \psi_{(V, \odot)} |V, \odot\rangle, \quad \text{where } \psi_{(V, \odot)} = \langle V, \odot | \psi \rangle, \quad (3.107)$$

as follows:

$$\begin{aligned} \hat{\mathcal{H}} |\psi\rangle &= -\frac{2\hbar^2}{3ma^2} \sum_{\odot \in \{\circ, \bullet\}} \sum_{(V, \odot)} \left\{ (\psi_{(A, \bar{\odot})} + \psi_{(B, \bar{\odot})} + \psi_{(C, \bar{\odot})} - 3\psi_{(V, \odot)}) \right. \\ &\quad - i\frac{\sqrt{3}qa}{4\hbar} \left[(A_{(V, \odot)}^x + A_{(A, \bar{\odot})}^x) \psi_{(A, \bar{\odot})} - (A_{(V, \odot)}^x + A_{(B, \bar{\odot})}^x) \psi_{(B, \bar{\odot})} \right] \\ &\quad - \text{sgn}(\odot) i\frac{qa}{4\hbar} \left[2(A_{(V, \odot)}^y + A_{(C, \bar{\odot})}^y) \psi_{(C, \bar{\odot})} - (A_{(V, \odot)}^y + A_{(A, \bar{\odot})}^y) \psi_{(A, \bar{\odot})} \right. \\ &\quad \left. - (A_{(V, \odot)}^y + A_{(B, \bar{\odot})}^y) \psi_{(B, \bar{\odot})} \right] - \frac{3q^2a^2}{4\hbar^2} (A_{(V, \odot)}^{x2} + A_{(V, \odot)}^{y2}) \psi_{(V, \odot)} \left. \right\} |V, \odot\rangle \\ &= -J_H \sum_{\odot \in \{\circ, \bullet\}} \sum_{(V, \odot)} \\ &\quad \left\{ \left[1 - i\frac{qa}{4\hbar} \left(\sqrt{3} (A_{(V, \odot)}^x + A_{(A, \bar{\odot})}^x) - \text{sgn}(\odot) (A_{(V, \odot)}^y + A_{(A, \bar{\odot})}^y) \right) \right] |V, \odot\rangle \langle A, \bar{\odot}| \right. \\ &\quad + \left[1 + i\frac{qa}{4\hbar} \left(\sqrt{3} (A_{(V, \odot)}^x + A_{(B, \bar{\odot})}^x) + \text{sgn}(\odot) (A_{(V, \odot)}^y + A_{(B, \bar{\odot})}^y) \right) \right] |V, \odot\rangle \langle B, \bar{\odot}| \\ &\quad + \left[1 - \text{sgn}(\odot) i\frac{qa}{2\hbar} (A_{(V, \odot)}^y + A_{(C, \bar{\odot})}^y) \right] |V, \odot\rangle \langle C, \bar{\odot}| \\ &\quad \left. - \left[3 + \frac{3q^2a^2}{4\hbar^2} (A_{(V, \odot)}^{x2} + A_{(V, \odot)}^{y2}) \right] |V, \odot\rangle \langle V, \odot| \right\} |\psi\rangle \\ &= \sum_{\odot \in \{\circ, \bullet\}} \sum_{(V, \odot)} (\mathcal{H}_{VA} |V, \odot\rangle \langle A, \bar{\odot}| + \mathcal{H}_{VB} |V, \odot\rangle \langle B, \bar{\odot}| + \mathcal{H}_{VC} |V, \odot\rangle \langle C, \bar{\odot}| \\ &\quad + \mathcal{H}_{VV} |V, \odot\rangle \langle V, \odot|) |\psi\rangle. \end{aligned} \quad (3.108)$$

Exploiting $\mathcal{H}^\dagger = \mathcal{H}$, Eq. (3.108) can be recast into Eq. (3.79), since $\mathcal{H}_{WV} = -J_H h_{WV}$.

3.B Computational details

3.B.1 Plotting the maps

Here we report how we plot the maps representing the time evolution of the probability density (population of the vertices). The idea is to assign to each vertex a patch colored according to the corresponding value of the population. The patch must have a shape reproducing the degree of the vertex, so that the adjacent patches really represent its NNs. The *dual* of $\{p, q\}$ is the tessellation whose edges are the perpendicular bisectors of the edges of $\{p, q\}$ (Fig. 3.21). Thus the dual of $\{p, q\}$ is $\{q, p\}$, and *vice versa*; the vertices of either are the centers of the faces of the other [146]. Adopting the dual of the tessellation of interest provides patches exactly meeting our needs. So, the proper way of representing and interpreting the maps of the populations of the vertices is shown in Fig. 3.22. Be aware that a map made of hexagonal patches refers to triangular lattice graph, whereas a map made of triangular patches refers to honeycomb lattice graph, because one

is the dual of the other; instead, a map made of square patches refers to square lattice graph, since the dual of $\{4, 4\}$ is an equal $\{4, 4\}$.

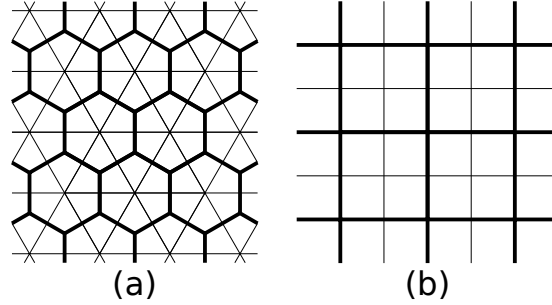


Figure 3.21. Duals of the regular tessellations of the Euclidean plane: (a) $\{6,3\} \xleftrightarrow{dual} \{3,6\}$, (b) $\{4,4\} \xleftrightarrow{dual} \{4,4\}$. See also Fig. 3.1.

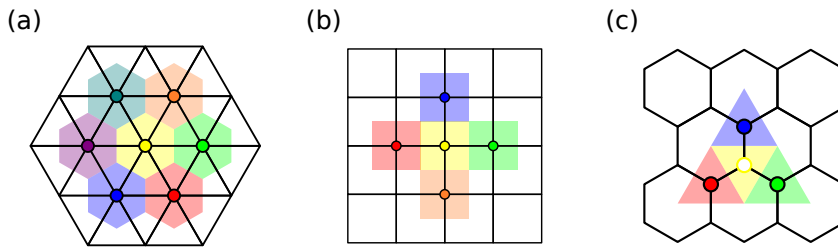


Figure 3.22. The expedient adopted to represent the maps of the populations of the vertices for the (a) triangular, (b) square, and (c) honeycomb lattice graphs: The value of the population in a vertex (colored circle) of the lattice graph is assigned to the corresponding patch of its dual lattice. In doing so, the degree of the vertex is recovered.

3.B.2 Indexing and coordinates of vertices

Indexing

When numerically dealing with PLGs (in particular the nonsquare ones), the first issue is how to label each vertex of the graph with a couple of indices (j, k) , with $j = 1, \dots, N_j$ and $k = 1, \dots, N_k$ (the lattice graph is finite). We adopt the indexing shown in Fig. 3.23. While for the square lattice graph the x and y directions provide the natural framework in which defining the couple of indices (j, k) , for the non-square PLGs we have to define *polylines* of vertices referring to the same x index, denoted as j , or to the same y index, denoted as k . So, we denote by N_j and N_k the total number of vertices along the j and k polylines, respectively. Notice, when implementing the system, that the NNs of a vertex may be differently labeled depending on the location of such vertex.

Triangular. In a triangular lattice graph, according to our indexing (Fig. 3.23(a)), we have to distinguish between *even* ($k \bmod 2 = 0$) and *odd* ($k \bmod 2 = 1$) y indices, k . Consider, e.g., the

vertex $V = (j, k) = (2, 1)$: If we move one step along the unit vector $(1/2, \sqrt{3}/2)$ we reach the vertex $(2, 2) = (j, k + 1)$, but if we do the same starting from $V' = (j', k') = (2, 2)$ we reach the vertex $(3, 3) = (j' + 1, k' + 1)$, not $(2, 3) = (j', k' + 1)$.

Square. In a square lattice graph (Fig. 3.23(b)) the coordinates of a vertex are integer multiples of the lattice parameter $a = 1$, so they provide the indices $(x_j, y_k) = (j, k)$.

Honeycomb. In a honeycomb lattice graph there are two classes of nonequivalent vertices $\{\circ, \bullet\}$. According to our indexing (Fig. 3.23(c)), a vertex $V = (j, k)$ belongs to either class according to the following rule:

$$V = \begin{cases} (V, \circ) & \text{if } (j + k) \bmod 2 = 0, \\ (V, \bullet) & \text{if } (j + k) \bmod 2 = 1. \end{cases} \quad (3.109)$$

Truncated square. In a truncated square lattice graph there are four classes of nonequivalent vertices $\{\circ, \bullet, \odot, \ominus\}$. According to our indexing (Fig. 3.23(d)), a vertex $V = (j, k)$ belongs to one of the different classes according to the following rule:

$$V = \begin{cases} (V, \odot) & \text{if } (k \bmod 2 = 1 \wedge j \bmod 4 = 1) \vee (k \bmod 2 = 0 \wedge j \bmod 4 = 3), \\ (V, \bullet) & \text{if } (k \bmod 2 = 1 \wedge j \bmod 4 = 2) \vee (k \bmod 2 = 0 \wedge j \bmod 4 = 0), \\ (V, \circ) & \text{if } (k \bmod 2 = 1 \wedge j \bmod 4 = 3) \vee (k \bmod 2 = 0 \wedge j \bmod 4 = 1), \\ (V, \ominus) & \text{if } (k \bmod 2 = 1 \wedge j \bmod 4 = 0) \vee (k \bmod 2 = 0 \wedge j \bmod 4 = 2). \end{cases} \quad (3.110)$$

Notice that being this lattice graph symmetric under rotation of $\pi/2$, we may adopt the same indexing along the y axis as well as along the x axis. However, this would generate a virtual logically rectangular grid where we should discard the vertices not corresponding to the actual ones: E.g., we might pick up a virtual vertex inside the octagon which actually does not exist. Adopting an indexing analogous to that of the honeycomb ensures that any couple of indices (j, k) is associated to an actual vertex.

In conclusion, after labeling each vertex with a couple of indices (j, k) (which also label the vertex state $|j, k\rangle$), from the computational point of view it is worth indexing vertices with a single index l . This is accomplished, for instance, as follows:

$$(j, k) \longrightarrow l = N_k(j - 1) + k, \quad (3.111)$$

where N_k denotes the number of vertices along the k polyline, which plays the role of the y axis.

Coordinates

Here we show how to restore the coordinates (x_V, y_V) of a vertex V given its indices $(j_V, k_V) \in [1, N_j] \times [1, N_k]$ (lattice parameter $a = 1$).

Triangular. In a triangular lattice graph, the coordinate y_V is an integer multiple of $\sqrt{3}/2$, whereas the coordinate x_V is integer or half-integer depending on the parity of the index k_V :

- 1: $x_V = j_V + [1 - \text{mod}(k_V, 2)]/2$;
- 2: $y_V = \sqrt{3} \times k_V/2$;

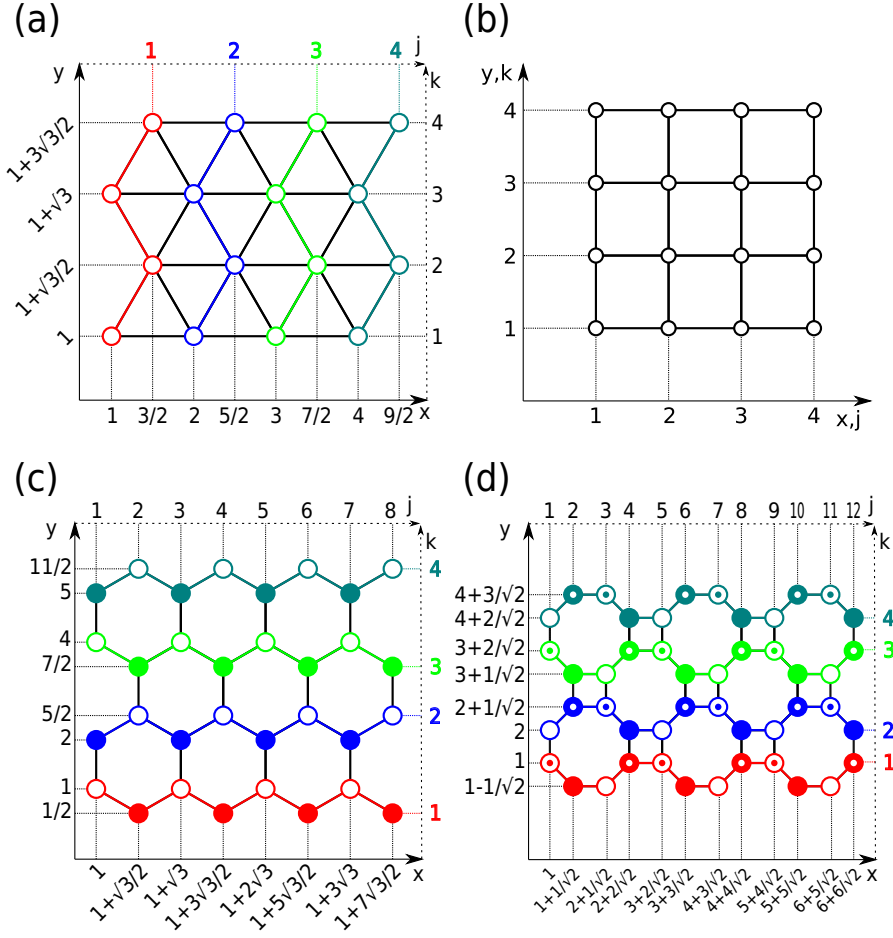


Figure 3.23. Labeling of vertices with a couple of indices (j, k) and corresponding (x, y) coordinates for the (a) triangular, (b) square, (c) honeycomb, and (d) truncated square lattice graphs. Lattice parameter $a = 1$.

Square. In a square lattice graph, the coordinates x_V and y_V of a vertex coincide with the indices j_V and k_V , respectively:

- 1: $x_V = j_V$;
- 2: $y_V = k_V$;

Honeycomb. In a honeycomb lattice graph, the coordinate x_V of a vertex is an integer multiple of $\sqrt{3}/2$, whereas the coordinate y_V , with respect to the index k_V , requires a correction depending on the parity of both the indices (j_V, k_V) and a shift by $\Delta = \Delta(k_V)$:

- 1: $x_V = \sqrt{3} \times j_V/2$;
- 2: $\Delta = \text{floor}[(k_V - 1)/2]$;
- 3: $y_V = k_V + \Delta + [1 - \text{mod}(j_V, 2)] \times [1/2 - \text{mod}(k_V, 2)]$;

where the expression $[1 - \text{mod}(j_V, 2)] \times [1/2 - \text{mod}(k_V, 2)]$ adjusts the value $k_V + \Delta$ by 0 or $\pm 1/2$ according to the parity of the indices.

Truncated square. In a truncated square lattice graph, along the x and y axes the coordinate increases by 1 or $1/\sqrt{2}$. Because of the indexing analogous to the honeycomb lattice graph, the coordinate $x_V = x_V(j_V)$, whereas the coordinate y_V , with respect to the index k_V , requires a correction depending on the parity of both the indices (j_V, k_V) and a shift by $\Delta = \Delta(k_V)$:

- 1: $x_V = \text{floor}[(j_V + 1)/2] + \text{floor}(j_V/2)/\sqrt{2}$;
- 2: $\Delta = \sqrt{2} \times \text{floor}[(k_V - 1)/2]$;
- 3: $y_V = k_V + \Delta + \sqrt{2}[1/2 - \text{mod}(k_V, 2)] \times [\text{mod}(j_V, 2) \neq \text{mod}(j_V, 4)]$;

where the expression $\text{mod}(j_V, 2) \neq \text{mod}(j_V, 4)$ is to be understood as the (logical) value 1 if true and 0 if false.

3.B.3 Boundary conditions

When dealing with the magnetic field, since the hopping terms depend on the vector potential evaluated in both the initial and final vertices, boundary conditions may raise some issues. In Fig. 3.24, the components A^x and A^y of the vector potential (symmetric gauge) computed in the different PLGs are reported and they show a discontinuity at the boundaries. Since the hopping terms in the Hamiltonian may involve both the components, e.g., in the triangular (see Eqs. (3.51) and (3.78)) and honeycomb (see Eqs. (3.52) and (3.79)) lattice graph, periodic boundary conditions are not appropriate. On the other hand, in the square lattice graph the hopping occurs along the orthogonal directions x and y and it respectively only involves A^x and A^y (see Eqs. (3.50) and (3.77)). Thus, in this case, periodic boundary condition can be assumed.

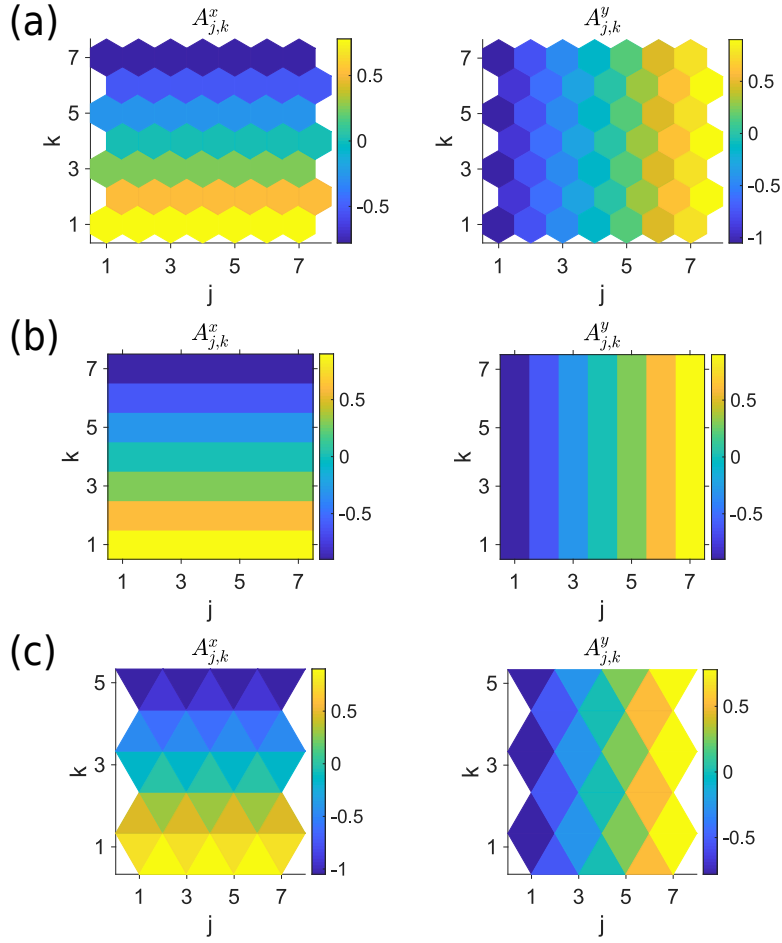


Figure 3.24. The components A^x and A^y of the vector potential (symmetric gauge, $B = 0.6$) computed in (a) 7×7 triangular, (b) 7×7 square, and (c) 7×5 honeycomb lattice graphs. The vector potential is centered in $(4,4)$ in the triangular and square lattice graph and in $(4,3)$ in the honeycomb one. Such components show a discontinuity at the boundaries. So, since the hopping terms in the Hamiltonian may involve both the components, periodic boundary conditions are not appropriate. However, since in the square lattice graph the hopping along the $x(y)$ direction only involves $A^{x(y)}$, periodic boundary conditions can be assumed.

3.C Units

The CTQW Hamiltonian of the system has some characteristic parameters, such as the electric charge q , the mass m of the particle, and the lattice parameter a . In order to perform numerical simulations, we have to declare them. We consider it appropriate to design a computation whose character is as general as possible. To this end, we set the lattice parameter, the reduced Planck's constant and the elementary electric charge equal to 1, i.e., $a = \hbar = e = 1$, and so these quantities are dimensionless in the resulting system of units, which we refer to as *QW units*. The physical quantities we treat in the present work derive from the fundamental ones (in the SI): mass (M), length (L), time (T), and electric current (I). Setting $a = \hbar = e = 1$ means that:

- (i) length is measured in units of a (lattice parameter);

- (ii) angular momentum (its modulus $|\mathbf{L}|$) is measured in units of \hbar (reduced Planck's constant);
and
- (iii) electric charge q is measured in units of e (elementary electric charge).

Let X be a physical quantity. Then, its dimensions read as follows:

$$\begin{aligned}
 [X] &= \overbrace{M^\alpha L^\beta T^\gamma I^\delta}^{\text{SI base quantities}} \\
 &= \underbrace{M^A L^B [|\mathbf{L}|]^C [q]^D}_{\text{QW base quantities}} = M^{A+C} L^{B+2C} T^{-C+D} I^D,
 \end{aligned} \tag{3.112}$$

since $[|\mathbf{L}|] = ML^2T^{-1}$ and $[q] = IT$. This means that

$$\begin{cases} \alpha = A + C, \\ \beta = B + 2C, \\ \gamma = -C + D, \\ \delta = D, \end{cases} \Rightarrow \begin{cases} A = \alpha + \gamma - \delta, \\ B = \beta + 2\gamma - 2\delta, \\ C = -\gamma + \delta, \\ D = \delta, \end{cases} \tag{3.113}$$

from which

$$[X] = M^{\alpha+\gamma-\delta} L^{\beta+2\gamma-2\delta} [|\mathbf{L}|]^{-\gamma+\delta} [q]^\delta. \tag{3.114}$$

Then, we have

$$[X] |_{QW} = M^{\alpha+\gamma-\delta}, \tag{3.115}$$

since $a|_{QW} = \hbar|_{QW} = e|_{QW} = 1$, and so the relation between QW units and the SI ones is:

$$X|_{QW} = x|_{QW} k g^{\alpha+\gamma-\delta} = x k g^\alpha m^\beta s^\gamma A^\delta, \tag{3.116}$$

where $x = x|_{QW} a^{\beta+2\gamma-2\delta} \hbar^{-\gamma+\delta} e^\delta$. In the present work the relevant quantities are:

- (i) space coordinates, for which $\alpha = \gamma = \delta = 0, \beta = 1$;
- (ii) time, for which $\alpha = \beta = \delta = 0, \gamma = 1$;
- (iii) modulus of magnetic field, for which $\alpha = 1, \beta = 0, \gamma = -2, \delta = -1$;
- (iv) hopping amplitude (see, e.g., Eq. (3.13)), for which $\alpha = 1, \beta = 2, \gamma = -2, \delta = 0$.

The definition of this system of units is consistent with the SI. In particular, if we consider the four fundamental quantities – length, time, mass and electric current – length is redefined accordingly to $a = 1$, whereas time and electric current are refined accordingly to $\hbar = e = 1$. In this way, the dimensions of all the physical quantities are expressed in terms of mass (hence J), which becomes the only characteristic physical quantity of the system (see Table 3.3).

Base quantity	Dimensions		
	SI	SI \rightarrow QW	QW
Mass	M	M	M
Length	L	L	
Angular momentum	ML^2T^{-1}	$[\mathbf{L}]$	
Electric charge	IT	$[q]$	

Derived quantity	Dimensions		
	SI	SI \rightarrow QW	QW
Time	T	$ML^2 [\mathbf{L}]^{-1}$	M
Magnetic field	$MT^{-2}I^{-1}$	$L^{-2} [\mathbf{L}] [q]^{-1}$	
Hopping amplitude	ML^2T^{-2}	$M^{-1}L^{-2} [\mathbf{L}]^2$	M^{-1}

Table 3.3. Dimensional analysis of the QW base quantities and the derived quantities in different systems of units: in the International System of Units (SI), after redefining the base quantities (SI \rightarrow QW), and in the QW system of units (QW), for which $a = \hbar = e = 1$.

Part III

Adagio.

Quantum estimation

Chapter 4

Lattice quantum magnetometry

In this chapter we put forward the idea of lattice quantum magnetometry, i.e., quantum sensing of magnetic fields by a charged (spinless) particle placed on a finite two-dimensional lattice. In particular, we focus on the detection of a locally static transverse magnetic field, either homogeneous or inhomogeneous, by performing ground-state measurements. The system turns out to be of interest as a quantum magnetometer, since it provides non-negligible quantum Fisher information (QFI) in a large range of configurations. Moreover, the QFI shows some relevant peaks, determined by the spectral properties of the Hamiltonian, suggesting that certain values of the magnetic fields may be estimated better than others, depending on the value of other tunable parameters. We also assess the performance of coarse-grained position measurement, showing that it may be employed to realize nearly optimal estimation strategies.

4.1 Introduction

A quantum probe is a physical system, usually a microscopic one, prepared in a quantum superposition. As a result, the system may become very sensitive to changes occurring in its environment and, in particular, to fluctuations affecting one or more parameters of interest. Quantum sensing [55, 176] is thus the art of exploiting the inherent fragility of quantum systems in order to design quantum protocols of metrological interest. Usually, a quantum probe also offers the advantage of being small compared to its environment and, in turn, non-invasive and only weakly disturbing. In recent years, quantum probes have been proved useful in several branches of metrology, ranging from quantum thermometry [177–180] to magnetometry [181–186], also including characterization of complex systems [187–198].

In this chapter, we address a specific instance of the quantum probing technique, which we term *lattice quantum magnetometry*. It consists in employing a charged spinless particle, confined on a finite two-dimensional square lattice (see Fig. 4.1), in order to detect and estimate the value of a transverse magnetic field, either homogeneous or inhomogeneous. Our scheme finds its root in the study of continuous-time quantum walks (CTQWs) [5, 6] and their noisy versions [33, 93, 94, 133] on two-dimensional systems [18, 199–201], but it does not exploit the dynamical properties of the quantum walker, being based on performing measurement on the ground state of the system. Indeed, a charged quantum walker may be used as a quantum magnetometer *even when it is not walking* since, as we will see, the ground-state quantum Fisher information (QFI) is non-negligible in a large range of configurations. In addition, the QFI has a non-trivial behavior (with peaks) as a function of the field itself, suggesting that certain values of the magnetic field may be estimated better than the others. Those values may be in turn tuned by varying other parameters, e.g., the field gradient, making the overall scheme tunable and robust. Moreover, focusing on a finite discrete system allows us to avoid the infinite degeneracy of the continuous

case ground state for a homogeneous magnetic field (the so-called *lowest Landau level*).

We also investigate whether measuring the position distribution on the ground state provides information about the external field. Our results indicate that this is indeed the case, and that position measurements, also when coarse grained, may be employed to realize nearly optimal magnetometry. In turn, as a possible implementation of our scheme we might think of the quantum walk of a charged particle in an ion trap lattice [202] or of an excitation in a ferromagnetic film [203].

As already mentioned above, in order to assess and compare different estimation schemes, we employ the QFI as figure of merit. This is a proper choice, since we address situations where some *a priori* information about the field is available, and a local estimation approach is thus appropriate to optimize the detection scheme. We evaluate the QFI through the ground-state fidelity and link it to the physical properties of the system. In particular, we observe a relationship between the structure of the Hamiltonian spectrum and the QFI obtained from a ground-state measurement, thus linking precision to the spectral properties of the probe. We also introduce a possible strategy to optimize this estimation process by using a space-dependent magnetic field.

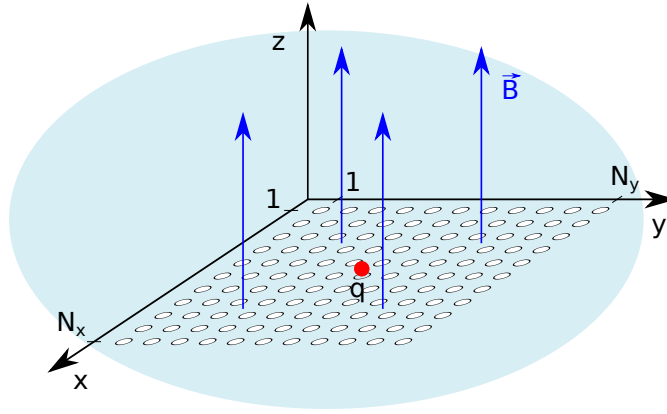


Figure 4.1. Schematic diagram of the probing technique discussed in this work. A charged spinless particle confined on a finite two-dimensional square lattice is placed in a region subject to a locally transverse magnetic field. The presence of the magnetic field alters the eigenvectors and the spectra of the Hamiltonian, such that information about the value of the field may be retrieved by performing measurement on the particle in its ground state. We derive the ultimate achievable precision and also assess the performance of coarse-grained position measurement, showing that it may be employed to realize nearly optimal estimation strategies.

4.2 The probing system

The quantum probe consists of a charged spinless particle on a finite two-dimensional (2D) square lattice in the presence of a locally transverse magnetic field. The lattice lays on the xy plane and the magnetic field in the neighboring region is parallel to the z axis. The finiteness of the system is implemented by preventing the particle from hopping beyond the boundaries (see Fig. 4.2). We set $\hbar = q = d = 1$, where \hbar is the reduced Planck constant, q the electric charge, and d the lattice constant. The lattice has size $N_x \times N_y$, where we denote, respectively, with N_x and N_y the total number of sites in the x and y directions. We set $N_x = N_y = 31$, since a $(2n+1) \times (2n+1)$ lattice has a properly defined center in $(n+1, n+1)$ (i.e., having n sites before and after itself along the two orthogonal directions).

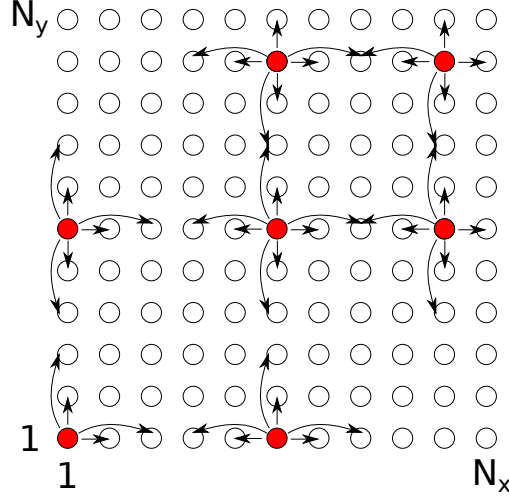


Figure 4.2. The finiteness of the system, i.e., of the $N_x \times N_y$ square lattice, is encoded in the allowed hopping paths, i.e., in the fact that the particle cannot jump beyond the boundaries. In this work we consider the hopping up to next-nearest neighbors. Here are some relevant cases: in the middle of the lattice the hopping is allowed up to next-nearest neighbors in both the directions; at the boundaries the hopping beyond the ends is forbidden; in the second last site along either or both of the directions the hopping to nearest neighbors is preserved, while some paths towards next-nearest neighbors are forbidden.

In the following we first discuss the details of the magnetic field and then the Hamiltonian of this system. In particular, we briefly describe the configurations we are going to consider, with emphasis on the constraints arising out of the particular shape chosen for the inhomogeneous magnetic field. A homogeneous magnetic field orthogonal to the xy plane

$$\mathbf{B} = B_0 \hat{\mathbf{k}} \quad (4.1)$$

can be obtained by choosing the symmetric gauge with the vector potential defined as

$$\mathbf{A} = \frac{B_0}{2} (-(y - y_0), (x - x_0), 0), \quad (4.2)$$

where the magnetic field magnitude B_0 is constant, and (x_0, y_0) are the coordinates of the lattice center.

We are also interested in the study of space-dependent magnetic fields. In particular, we will consider a magnetic field profile constant along one axis (e.g., y) and varying along the other, such that it reaches its maximum value in the middle of the lattice – sites of coordinates (x_0, y) –, as shown in Fig. 4.3. So, in order to get the desired magnetic field, we introduce a function

$$f(x) = \beta - \alpha|x - x_0|, \quad (4.3)$$

where $\alpha, \beta \in \mathbb{R}^+$, which leads to the following generalized expression for the vector potential:

$$\mathbf{A} = \frac{f(x)}{2} (-(y - y_0), (x - x_0), 0). \quad (4.4)$$

According to this definition, the analytical expression of the magnetic field reads

$$\mathbf{B} = (B_0 - m_x|x - x_0|)\hat{\mathbf{k}}, \quad (4.5)$$

where $m_x = 3\alpha/2$ is the gradient and $B_0 = \beta$ is the maximum value of the magnitude of the magnetic field assumed on the sites of coordinates (x_0, y) , i.e., in the middle of the lattice. Notice that, having chosen a $(2n + 1) \times (2n + 1)$ lattice, the magnitude of the magnetic field at the boundaries of the lattice (along x) is the same. It should be emphasized that such a magnetic field profile is fully characterized by the two parameters B_0 and m_x , the homogeneous magnetic field being just a special case for $m_x = 0$.

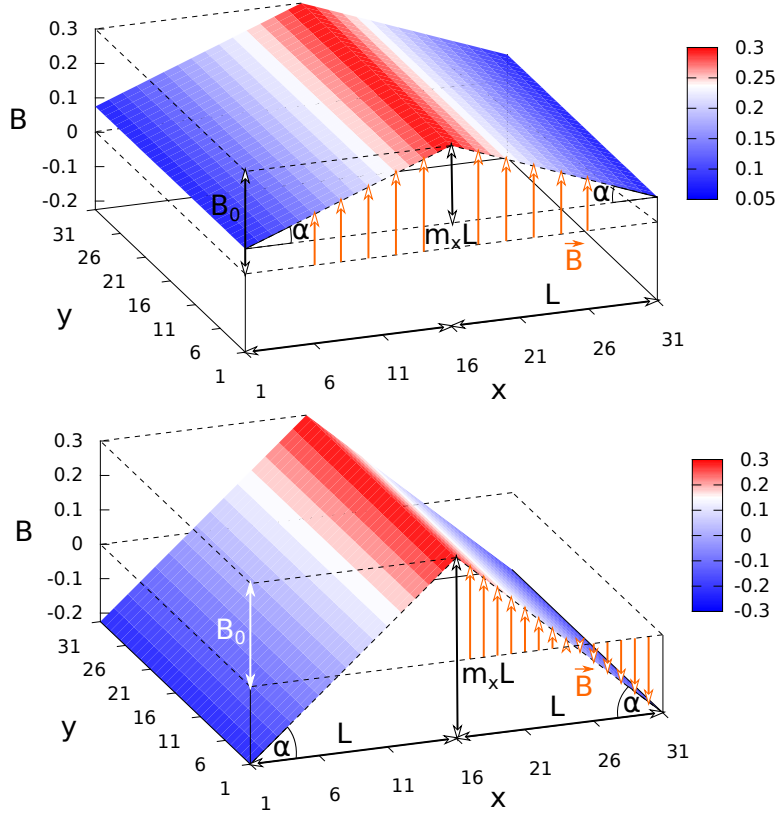


Figure 4.3. (Top panel) Spatial dependence of the inhomogeneous magnetic field ($B_0 = 0.3$, $m_x = 0.015$) described in Eq. (4.5). It reaches its maximum value B_0 in the middle of the lattice, i.e., in the sites of coordinates (x_0, y) . By moving away from it, it decreases linearly (slope $\pm m_x$, with $m_x = \tan(\alpha)$) along the x direction, while it is constant along the y one. (Bottom panel) The couple of parameters ($B_0 = 0.3$, $m_x = 0.035$) must be chosen in a way that the reversal of \mathbf{B} , occurring when Eq. (4.7) holds, is avoided.

The spatial dependence of the inhomogeneous magnetic field and the *magnetic length* play a crucial role in defining the interval of fields investigated. The upper limit is given by the magnetic length l_B , which is the fundamental characteristic length scale for any quantum phenomena in the presence of a magnetic field [160], and which is defined as follows:

$$l_B := \sqrt{\frac{\hbar}{qB}}. \quad (4.6)$$

According to our units ($\hbar = q = d = 1$) the magnetic length reads $l_B = B^{-1/2}$. For $B > 1$ the magnetic length becomes smaller than the lattice constant d , hence we consider only $B_0 < 1$. The

lower limit, instead, is due to the need of avoiding the reversal of the magnetic field (see bottom panel of Fig. 4.3), which occurs when

$$B_0 < m_x L, \quad (4.7)$$

where $L := \max_x(|x - x_0|) = 15$, in our system. In conclusion, we consider $B_0 \in [m_x L, 1]$.

The Hamiltonian describing a charged spinless particle in an electromagnetic field reads [204]

$$\mathcal{H} = \frac{1}{2m} (\mathbf{p} - q\mathbf{A})^2 + q\phi, \quad (4.8)$$

where q is the charge and m the mass of the particle, ϕ and \mathbf{A} are the scalar and vector potential respectively. The former is set to zero in this work since we are interested in having the magnetic field only. These potentials are defined by the following relations:

$$\mathbf{E} = -\nabla\phi - \frac{\partial\mathbf{A}}{\partial t}, \quad (4.9)$$

$$\mathbf{B} = \nabla \times \mathbf{A}, \quad (4.10)$$

where \mathbf{E} and \mathbf{B} are the electric and magnetic field, respectively. In order to have a magnetic field parallel to the z axis, one can choose the vector potential $\mathbf{A} = (A_x(x, y), A_y(x, y), 0)$.

The Hamiltonian describing such a system on a lattice is obtained by introducing a space discretization of Eq. (4.8), i.e., by discretizing the xy plane into a square lattice. Since we are considering a lattice, we have to express derivatives with finite difference and this, in turn, corresponds to discretizing the space. We adopt a five-point finite difference formula [151] to express derivatives and, according to this choice, we are able to write down the analytical expression of the resulting Hamiltonian:

$$\begin{aligned} \mathcal{H} = -J \sum_{j,k=1}^{N_x, N_y} & \left\{ \left[-5 - \left(A_{j,k}^x{}^2 + A_{j,k}^y{}^2 \right) \right] |j, k\rangle\langle j, k| \right. \\ & - \frac{1}{12} \left[1 + i \left(A_{j-2,k}^x + A_{j,k}^x \right) \right] |j, k\rangle\langle j-2, k| \\ & + \frac{2}{3} \left[2 + i \left(A_{j-1,k}^x + A_{j,k}^x \right) \right] |j, k\rangle\langle j-1, k| \\ & + \frac{2}{3} \left[2 - i \left(A_{j+1,k}^x + A_{j,k}^x \right) \right] |j, k\rangle\langle j+1, k| \\ & - \frac{1}{12} \left[1 - i \left(A_{j+2,k}^x + A_{j,k}^x \right) \right] |j, k\rangle\langle j+2, k| \\ & - \frac{1}{12} \left[1 + i \left(A_{j,k-2}^y + A_{j,k}^y \right) \right] |j, k\rangle\langle j, k-2| \\ & + \frac{2}{3} \left[2 + i \left(A_{j,k-1}^y + A_{j,k}^y \right) \right] |j, k\rangle\langle j, k-1| \\ & + \frac{2}{3} \left[2 - i \left(A_{j,k+1}^y + A_{j,k}^y \right) \right] |j, k\rangle\langle j, k+1| \\ & \left. - \frac{1}{12} \left[1 - i \left(A_{j,k+2}^y + A_{j,k}^y \right) \right] |j, k\rangle\langle j, k+2| \right\}, \quad (4.11) \end{aligned}$$

where $|j, k\rangle$ (with $j = 1, \dots, N_x$ and $k = 1, \dots, N_y$) denotes a position eigenvector, i.e., a state describing the particle localized on the site of coordinates (jd, kd) . Analogously, the components of the vector potential have to be intended as $A_{j,k}^{x(y)} = A^{x(y)}(jd, kd)$. The parameter J is a constant and, after restoring the fundamental constants and parameters, it reads $J = \hbar^2/(2md^2)$. We set $m = 1/2$ and thus $J = 1$.

The expression of \mathcal{H} in Eq. (4.11) fits the usual interpretation of the Hamiltonian describing a CTQW [205] and it is consistent with the one given in Ref. [206]. In this case it would describe the CTQW of a charged spinless particle on a finite 2D square lattice. The hopping of the walker is described by projectors onto different position eigenvectors. For example $|j, k\rangle\langle j-1, k|$ is the tunneling from site $(j-1, k)$ to site (j, k) , and the associated tunneling amplitude depends on the vector potential. Moreover, the on-site energy (associated to projectors onto the same state) depends quadratically on the magnitude of the vector potential.¹

4.3 The estimation procedure

In this section we make use of the concepts from classical and quantum estimation theory, reviewed in Sec. 1.2, on the estimation of a parameter λ , which in our case is the magnitude B_0 of the (in)homogeneous magnetic field. Let us consider the family ρ_λ of the possible states of our probe, labeled by the parameter λ to be estimated. The main goal is to infer the value of λ by measuring some observable quantity over ρ_λ . The variance of an unbiased estimator has a classical lower bound, the Cramèr-Rao inequality, but the ultimate lower bound is posed by quantum mechanics, the quantum Cramèr-Rao inequality:

$$\text{Var}(\lambda) \geq \frac{1}{MF(\lambda)} \geq \frac{1}{MH(\lambda)}, \quad (4.12)$$

where M is the number of measurements, $F(\lambda)$ is the Fisher information (FI)

$$F(\lambda) = \int dx p(x|\lambda) [\partial_\lambda \ln p(x|\lambda)]^2, \quad (4.13)$$

with $p(x|\lambda)$ the conditional probability of obtaining the outcome x when the value of the parameter is λ , and $H(\lambda)$ is the quantum Fisher information (QFI).² We recall that the FI of any quantum

¹The method adopted in Chapter 3 to define the Hamiltonian of the system in a discrete space is different from the one adopted in this Chapter. Such a difference reflects the difference of purposes. Purpose of Chapter 3 is to provide a suitable way to include a magnetic field in CTQWs. The assumption of hopping only to nearest neighbors (NNs) allows us i) to assess the effects of the magnetic field at the lowest order and ii) to have a model which can be easily generalized to non-square lattices. Therefore, we have used finite-difference formulas (FDFs) based on the NNs to approximate derivatives. Purpose of this Chapter, instead, is to estimate the magnetic field performing ground-state measurement on a charged quantum particle in a finite 2D square lattice. This lattice is a suitable grid for considering five-point stencils to approximate derivatives of a scalar function. Using five points means involving NNs and next-NNs of the point at which we want to evaluate the derivative. For simplicity, we focus on the 1D case but analogous results apply to partial derivatives in 2D. Upon denoting by h the spacing between points in the grid, first- and second-order derivatives of a scalar function $f(x)$ are approximated as

$$\begin{aligned} \frac{df_n}{dx} &\approx \frac{1}{12h} (f_{n-2} - 8f_{n-1} + 8f_{n+1} - f_{n+2}) + O(h^4), \\ \frac{d^2f_n}{dx^2} &\approx \frac{1}{12h^2} (-f_{n-2} + 16f_{n-1} - 30f_n + 16f_{n+1} - f_{n+2}) + O(h^4). \end{aligned}$$

The five-point FDFs return an error of order $O(h^4)$, which is more accurate than the error returned by three-point FDFs, $O(h^2)$. Using the five-point FDFs, the information on the magnetic field is encoded not only in the NN hopping but also in the next-NN hopping (see Eq. (4.11)). Therefore, performing ground-state measurement on a system whose Hamiltonian is based on five-point FDFs provides more information on the magnetic field than an analogous system whose Hamiltonian is based on three-point FDFs.

²In this chapter, unlike the others, we use a different notation for the FI and the QFI for sake of clarity. Indeed, in Eq. (4.18) we introduce the FI for a coarse-grained position measurement (subscript g), and the usual notation $\mathcal{F}_g, \mathcal{F}_c$, together with $\mathcal{F}_{c,g}$ would not be as clear as using the notation with different letters for FI and QFI.

measurement is bounded by the QFI

$$F(\lambda) \leq H(\lambda) := \text{Tr}[\rho_\lambda L_\lambda^2], \quad (4.14)$$

with L_λ the symmetric logarithmic derivative (SLD). When the condition $F(\lambda) = H(\lambda)$ holds, the measurement is said to be optimal. An optimal (projective) measure is given by the spectral measure of the SLD which, however, may not be easy to implement practically.

In this work we deal with pure states and we are interested in estimating a single parameter. This leads to the following simple expression for the QFI:

$$H(\lambda) = \lim_{\delta\lambda \rightarrow 0} \frac{8(1 - |\langle \psi_\lambda | \psi_{\lambda+\delta\lambda} \rangle|)}{(\delta\lambda)^2}. \quad (4.15)$$

For a given λ , a large value of the QFI implies that the quantum states $|\psi_\lambda\rangle$ and $|\psi_{\lambda+\delta\lambda}\rangle$ are statistically more distinguishable than the same pair of states for a value λ corresponding to smaller QFI. This confirms the intuitive picture where optimal estimability (diverging QFI) is reached when quantum states are sent far apart upon infinitesimal variations of the parameter.

Besides the SLD, the natural choice for an observable providing information about the field is the position. We consider the two observables X and Y such that

$$X|j, k\rangle = jd|j, k\rangle \quad \text{and} \quad Y|j, k\rangle = kd|j, k\rangle, \quad (4.16)$$

where d is the lattice constant and $\{|j, k\rangle\}$ is the orthonormal basis of the position eigenvectors. We measure the compatible pair of observables (X, Y) and, in order to assess the performance, we evaluate the ratio

$$R(\lambda) = \frac{F(\lambda)}{H(\lambda)} \in [0, 1] \quad (4.17)$$

between the position FI F and the QFI H , respectively given in Eq. (4.13) and Eq. (4.15), in the light of Eq. (4.14). This ratio tells us how much the FI of a given measurement is close to the QFI, which is achieved when $R = 1$. We perform a ground-state measurement, then the probabilities entering Eq. (4.13) are straightforwardly given by the square modulus of the projections of the ground state onto the position eigenvectors. The Hamiltonian in Eq. (4.11) is already written in the basis of position eigenvectors, thus the components of the ground state are actually the projections we need.

In addition, we investigate the performance of coarse-grained position measurement, i.e., whether position measurement is robust when the resolution of the measurement does not permit us to measure the probability associated with a single site of the lattice. To this purpose, we define square grains of size $g \times g$, where $g = 1, 3, 5, 10$ denotes the number of sites forming the side of the cluster (see Fig. 4.4). We keep as reference H and compute F at different g by rewriting Eq. (4.13) in terms of grain probabilities rather than site probabilities. This may be done as follows: let us denote a generic site as $s := (j, k)$ and a grain, i.e., a cluster of sites, of size $g \times g$ as G_g . Notice that these clusters are disjoint ($G_g \cap G'_g = \emptyset$). Then we compute the FI as

$$F_g(\lambda) = \sum_{G_g} P(G_g|\lambda) \left[\partial_\lambda \ln P(G_g|\lambda) \right]^2, \quad (4.18)$$

where

$$P(G_g|\lambda) = \sum_{s \in G_g} p(s|\lambda) \quad (4.19)$$

is the grain probability and $p(s|\lambda)$ is the site probability, i.e., the conditional probability of finding the walker in the site s when the parameter takes the value λ . Clearly, for $g = 1$ grain probability corresponds to site probability.

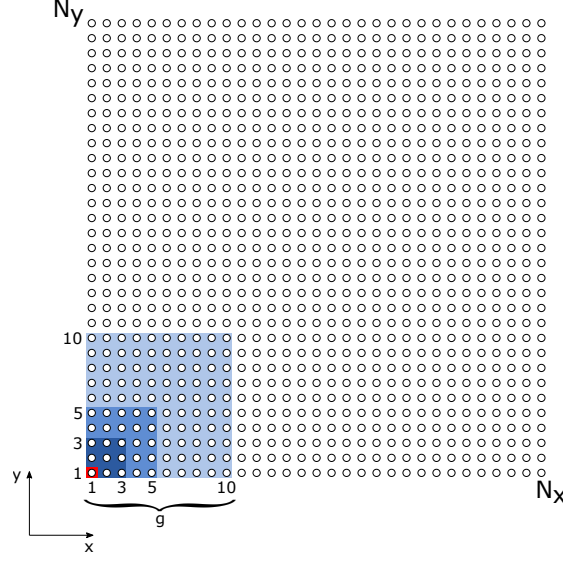


Figure 4.4. A coarse-grained position within the $N_x \times N_y = 31 \times 31$ square lattice is defined as a $(g \times g)$ -sized cluster of sites, where $g = 1, 3, 5, 10$.

4.4 Ground-state quantum magnetometry

In this section we focus on ground-state measurements in order to assess the behavior of this system as a quantum magnetometer, i.e., as a probe to estimate the magnitude of the magnetic field acting on it. To this aim we compute the QFI via Eq. (4.15): the parameter λ to be estimated is the magnetic field magnitude B_0 , whereas $|\psi_\lambda\rangle$ and $|\psi_{\lambda+\delta\lambda}\rangle$ are the system ground states corresponding to magnetic field magnitudes B_0 and $B_0 + \delta B > B_0$, respectively.

4.4.1 Homogeneous magnetic field

To understand whether our system is of potential use as a quantum magnetometer, we first consider a static homogeneous magnetic field ($m_x = 0$). We compute the QFI for different values of B_0 , and the position FI to assess its performance and to study which values of the parameter, if any, can be better estimated (see top panel of Fig. 4.5).

The first observation is that the QFI (solid black line H) is non-vanishing in the whole magnetic field interval considered, showing that estimation of the field may be indeed obtained from ground-state measurement. Then, we notice that even if the position FI (dashed colored lines F) is smaller than the QFI, it has the same order of magnitude. In particular, it decreases for increasing the grain size g , but it still preserves a structure analogous to that of the QFI. The behavior of the FI is more clearly depicted in bottom panel of Fig. 4.5, where we see that the ratio $R = F/H$ moderately decreases as the grain size increases. Yet, for $g = 1$, F overlaps very well to the curve of H , as proved by the fact that the ratio R is close to 1 in the whole interval of B_0 considered. In order to compare the results of Fig. 4.5 to those of the corresponding continuous infinite case (no lattice), it is worth evaluating the QFI of the ground state of Eq. (4.8) (for $\phi = 0$ and symmetric gauge). Assuming zero angular momentum, the wave function of the ground state for the case of a homogeneous magnetic field B is ($q = \hbar = 1$)

$$\psi_c(x, y) = \sqrt{\frac{B}{2\pi}} e^{-\frac{B}{4}(x^2 + y^2)}, \quad (4.20)$$

and according to Eq. (4.15) $H_c(B) = B^{-2}$, which is exactly the behavior observed in the top panel of Fig. 4.5 for large values of B_0 . Therefore, the first remarkable effect due to the finite discretization is the appearance of a maximum instead of a divergence for vanishing B_0 . Notice also that $H(0) > 0$.

In Fig. 4.6 we illustrate the behavior of the QFI: it is dependent on the magnetic field and the region of high QFI suggests that some values can be estimated more efficiently than the others. Indeed, as it can be seen from Eq. (4.15), high values of QFI denote that a slight change in the parameter of interest greatly affects the ground state, in a way that $|\langle \psi_{\lambda+\delta\lambda} | \psi_\lambda \rangle| < 1$. The same interval of B_0 characterized by a high QFI is also where the system partial energy spectrum, i.e., the lowest Hamiltonian eigenvalues, shows the more complex dependence on B_0 . In other words, the discretization is making the energy spectrum at low B_0 more structured and, in turn, much more sensitive to small changes in the value of B_0 . On the contrary, for large B_0 we approach a situation of *quasi*-degeneracy of continuous states and the system becomes overall less sensitive.

4.4.2 Inhomogeneous magnetic field

The interesting features shown by the QFI for a static homogeneous magnetic field ($m_x = 0$) are further investigated here by considering a static inhomogeneous magnetic field ($m_x > 0$). In this case, as we notice in top panel of Fig. 4.7, the QFI (solid black line H) is still non-null within the whole interval of magnetic field considered. The position FI does not follow the behavior of the QFI for low B_0 but it does it in correspondence with the peak of the QFI. Also in this case we show the ratio $R = F/H$ in the bottom panel of Fig. 4.7.

As it may be seen looking at Fig. 4.8, the QFI peak occurs for the value of B_0 such that the lowest energy eigenvalues present an avoided crossing phenomenon, such that the behavior of the QFI may be interpreted in terms of the structure of a two-level effective system. Indeed, in systems with parameter-dependent Hamiltonians, small perturbations may induce relevant changes in the ground state of the system, and this behavior is emphasized in the presence of level anticrossing. Summarizing from [184], we have that for a two-level system with (generic) Hamiltonian of the form

$$\mathcal{H}_2 = \omega_0 \sigma_0 - \Delta(\lambda) \sigma_3 + \gamma(\lambda) \sigma_1, \quad (4.21)$$

where σ_k (with $k = 0, \dots, 3$) denote the Pauli matrices, the QFI $H(\lambda)$ may be written as

$$H(\lambda) = 16 \left(\frac{\Delta}{h_+ - h_-} \right)^4 [\partial_\lambda (\gamma/\Delta)]^2, \quad (4.22)$$

where h_\pm are the eigenvalues of \mathcal{H}_2 .

In Fig. 4.9 we plot the QFI as a function of B_0 for different values of the gradient m_x . These results clearly show that for any value of the parameter B_0 to be estimated, there is a gradient value m_x which maximizes the QFI. Therefore estimability performances can be enhanced by a proper choice of m_x . In other words, the system may actually be employed as a quantum magnetometer, since it allows us to estimate the magnetic field magnitude B_0 starting from a ground-state measurement, which can be optimized by choosing the optimal gradient m_x . We stress again that the estimation of B_0 and the prior knowledge of m_x are enough to fully describe the magnetic field shape. We notice here that the complementary problem of gradient magnetometry has been recently addressed [207] with atomic ensembles, showing that achieving the precision bounds requires the knowledge of the homogeneous part of the field. The correlation between the QFI maxima and the structures of the energy spectrum can be exploited by considering the possibility of obtaining information about the energy spectrum starting from the QFI, or *vice versa* by investigating the energy spectrum in order to gain information about the quantum estimation properties of the system.

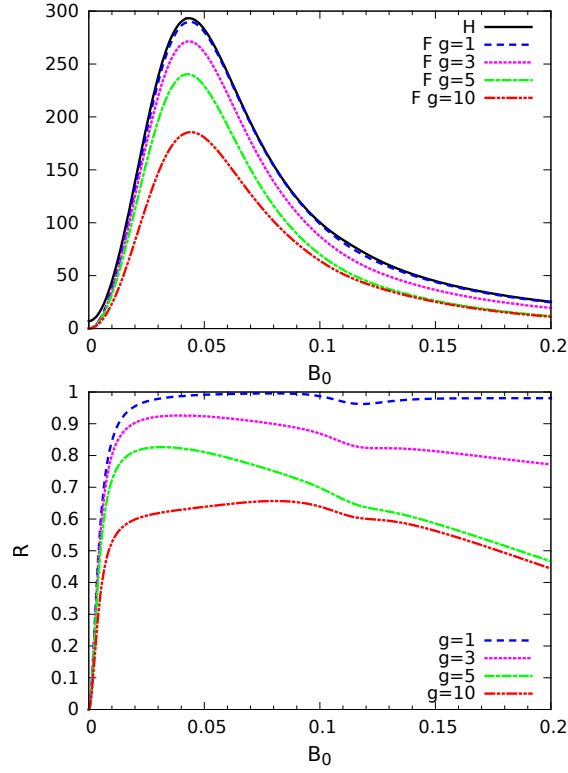


Figure 4.5. Quantum Fisher information H , position Fisher information F (at different grain size g) (top panel) and their ratio $R = F/H$ (bottom panel) as a function of the magnitude B_0 of the static homogeneous magnetic field ($m_x = 0$). Notice that in the top panel $H(0) > 0$, whereas $F(0) = 0 \forall g$.

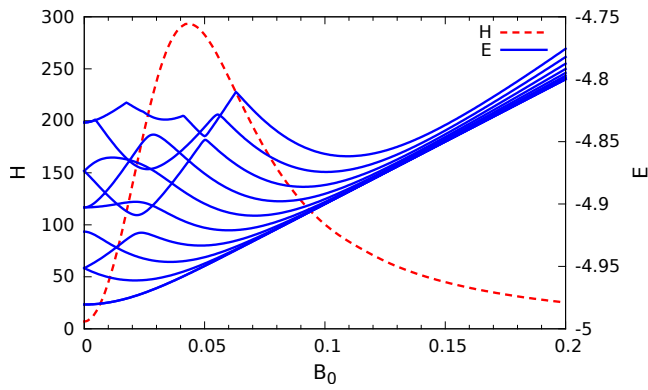


Figure 4.6. Quantum Fisher information H (dashed red line) and lower-energy spectrum (solid blue line) as a function of the magnitude B_0 of the static homogeneous magnetic field ($m_x = 0$).

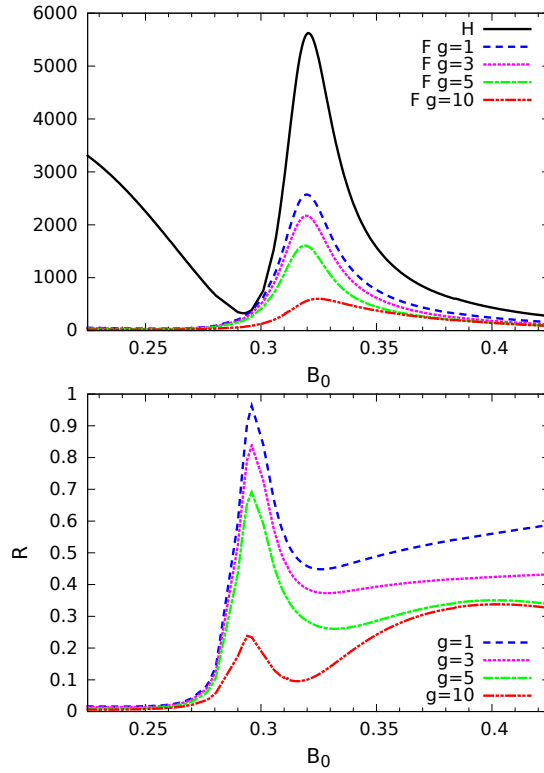


Figure 4.7. Quantum Fisher information H , position Fisher information F (at different grain size g) (top panel) and their ratio $R = F/H$ (bottom panel) as a function of the magnitude B_0 (value in the lattice center) of the static inhomogeneous magnetic field ($m_x = 0.015$).

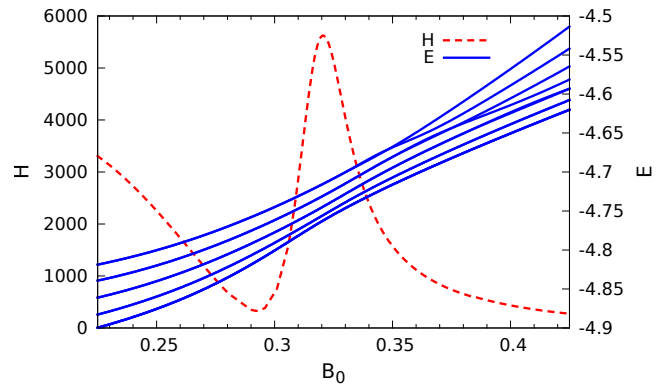


Figure 4.8. Quantum Fisher information H (dashed red line) and lower-energy spectrum (solid blue line) as a function of the magnitude B_0 (value in the lattice center) of the static inhomogeneous magnetic field ($m_x = 0.015$).

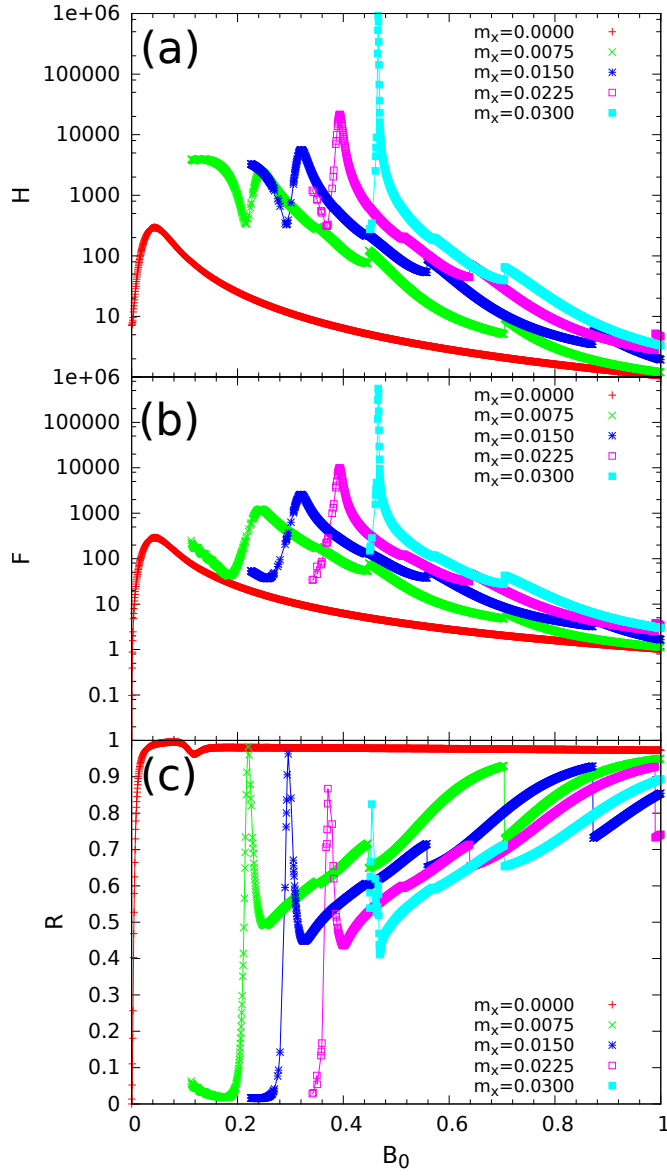


Figure 4.9. (a) Quantum Fisher information H , (b) position Fisher information F at grain size $g = 1$ and (c) their ratio $R = F/H$ at varying magnitude B_0 (value in the lattice center) of the static inhomogeneous magnetic field for different values of the gradient m_x .

4.5 Conclusions

In this chapter, we have studied a charged spinless particle on a finite 2D square lattice in the presence of a locally transverse magnetic field. The Hamiltonian has been derived from a spatial discretization of the Hamiltonian of the corresponding system in a plane, and the time-independent Schrödinger equation has been solved exactly by numerical diagonalization for a lattice size 31×31 . Our focus has been on the potential use of the quantum features of this system as quantum magnetometer. In particular, we have analyzed its performance in the estimation of a transverse magnetic field, either homogeneous or inhomogeneous, by performing measurements on the system's ground state.

Our results show that the system is of interest from the metrological standpoint: the ground state QFI for the magnetic field is non-negligible in a large range of configurations. We have first seen this behavior for the case of a homogeneous magnetic field, and then for a space-dependent magnetic field. In particular, we have found that the QFI shows peaks at specific values of the magnetic field and of its gradient, making it possible to optimize the estimation strategy by properly tuning the value of the latter. To gain insight into the origin of the QFI peaks, we analyzed the structure of the Hamiltonian spectra, and found that the relation between the QFI peaks and the values of magnetic field at which they occur may be understood in terms of avoided crossing phenomena between the two lowest Hamiltonian eigenvalues.

We have also studied the performance of position measurements. In the case of ground-state measurements the corresponding FI provides a quite good approximation to the QFI, showing an analogous peak structure. In particular, for a homogeneous magnetic field the FI overlaps very well the QFI. For an inhomogeneous magnetic field the FI reproduces the behavior of QFI at least in the neighborhood of QFI peak. Concerning robustness, we found that if one is not able to perform measurements at site resolution, but one has access to coarse-grained measurement only at level of clusters of sites, the FI decreases as the grain size increases. On the other hand, the FI has the same order of magnitude of the QFI and preserves a peak structure analogous to QFI, proving the robustness of this kind of measurement.

In conclusion, our results show that effective quantum sensing of magnetic fields is possible using a charged spinless particle on a finite two-dimensional lattice. In particular, ultimate bounds to precision may be approached by position measurement on the ground state of the system, which is also robust against coarse-graining, i.e., reduction of resolution.

Appendices

4.A The role of the lattice size

In this appendix we investigate the role of the lattice size in determining the position and the height of the peak of the QFI in the case of a static homogeneous magnetic field ($m_x = 0$), as shown in Fig. 4.10. In the top panel we observe that as the size of the lattice increases, the peak gets sharper and higher and it occurs at lower values of the magnetic field. In fact, this result approaches the limit of an infinite lattice, which in turn, for an infinitesimal lattice parameter, should recover the continuum. For the latter we know that the QFI is $H_c(B) = B^{-2}$, i.e., it shows a divergence in $B = 0$. In the bottom panel it is shown the dependence of the position and the height of the peak of the QFI on $N = 2n + 1$, which defines the lattice size as $N \times N$. In particular, we observe that, in our range of lattice sizes, the position of the peak scales as $\sim N^{-1.905}$, while its height as $\sim N^{3.923}$. This result provides a better insight into the behavior of the QFI shown in the top panel. In particular, it tells us that in the limit of $N \rightarrow \infty$ the position of the peak is zero and its height diverges, as expected for the infinite continuous case.

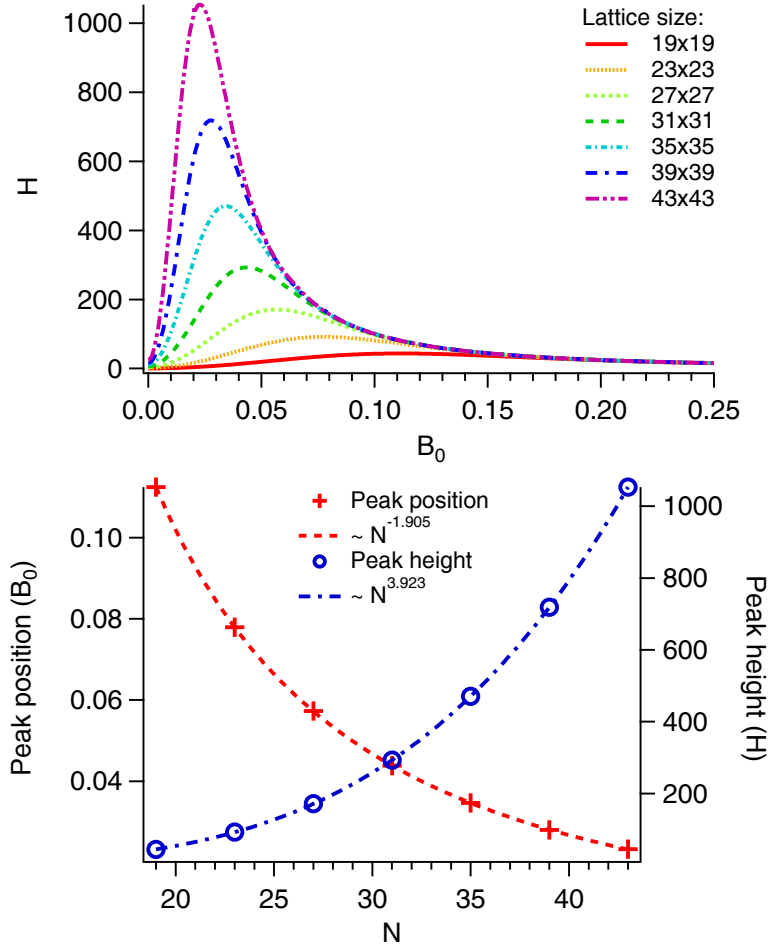


Figure 4.10. Study of the peaks of the quantum Fisher information for different lattice sizes $N \times N$, where $N = 2n + 1$, in the case of a static homogeneous magnetic field ($m_x = 0$). (Top panel) QFI H as a function of the magnitude B_0 of the static homogeneous magnetic field for different lattice sizes. (Bottom panel) Position and height of the peak of the QFI as a function of the lattice size. Increasing the lattice size makes the peak sharper and higher and makes it occur at lower values of B_0 . This approaches the result expected in the limit of an infinite lattice.

Chapter 5

Role of topology in determining the precision of a finite thermometer

Temperature fluctuations of a finite system follow the Landau bound $\delta T^2 = T^2 / C(T)$ where $C(T)$ is the heat capacity of the system. In turn, the same bound sets a limit to the precision of temperature estimation when the system itself is used as a thermometer. In this chapter, we employ graph theory and the concept of Fisher information to assess the role of topology on the thermometric performance of a given system. We find that low connectivity is a resource to build precise thermometers working at low temperatures, whereas highly connected systems are suitable for higher temperatures. Upon modeling the thermometer as a set of vertices for the quantum walk of an excitation, we compare the precision achievable by position measurement to the optimal one, which itself corresponds to energy measurement.

5.1 Introduction

Thermometry is based on the zeroth law of thermodynamics. A probing object (the thermometer) is put in contact with the system under investigation and when they achieve thermal equilibrium the temperature of both is determined by performing a measurement on the thermometer. Good thermometers are those with a heat capacity much smaller than the object under study, such that the thermal equilibrium is reached at a temperature very close to the original temperature of the object. This straightforward line of reasoning leads to consider *small* thermometers, possibly subject to the laws of quantum mechanics [208]. Additionally, since the heat capacity itself depends on temperature, one is led to investigate whether the heat capacity of a thermometer may be tailored for a specific range of temperatures [209].

The topic has become of interest in the last two decades, due to the development of controlled quantum systems at the classical-quantum boundary [210–227], which makes it relevant to have a precise determination of temperature for quantum systems [228–234], and to understand the ultimate bounds to precision in the estimation of temperature [178, 235–245]. At the same time, precise manipulation of quantum systems makes it possible to design and realize quantum thermometers, i.e., thermometers where temperature is precisely estimated looking at tiny changes in genuine quantum features such as entanglement or coherence [246–249].

As a matter of fact, temperature is not an observable in a strict sense, i.e., it is not possible to build a self-adjoint operator corresponding to temperature. Besides, temperature represents a macroscopic manifestation of random energy exchanges between particles and, as such, does fluctuate for a system at thermal equilibrium. In fact, this has made the concept of temperature fluctuations controversial [250–258]. In order to retain the operational definition of temperature,

one should conclude that although temperature itself does not fluctuate, any temperature estimate is going to fluctuate, since it is based on the measurement of one or more proper observables of the systems, e.g., energy or population.

In this framework, upon considering temperature as a function of the exact and fluctuating values of the other state parameters, Landau and Lifshitz derived a relation for the temperature fluctuations of a finite system [259, 260]. This is given by $\delta T^2 = T^2/C$ where $C = C(T)$ is the (temperature-dependent) heat capacity of the system and appears as a fundamental bound to the precision of any temperature estimation. The same problem may be addressed by leveraging tools from quantum parameter estimation and the Landau bound may be shown to be equivalent to the so-called Cramér-Rao bound to precision, built by evaluating the quantum Fisher information (QFI) of equilibrium states [179]. In turn, the link between the QFI and the heat capacity have been established in different frameworks, such as in quantum phase transition and in systems with vanishing gap [179, 261–264].

In this work, we exploit the above connection to address the role of topology in determining the precision of a finite thermometer. In particular, upon modeling a finite thermometer as a set of connected subunits, we employ graph theory, together with QFI, to assess the role of topology on the thermometric performance of the system. We confirm that measuring the energy of the system is the best way to estimate temperature, and also find that systems with low connectivity are suitable to build precise thermometers working at low temperatures, whereas highly connected systems are suitable for higher temperatures. We also compare the optimal precision with that achievable by measuring the position of thermal excitations. Our results indicate that quantum probes are especially useful at low temperatures and that systems with low connectivity provide more precise thermometers. At high temperatures, precision degrades as $O(T^4)$ with highly connected systems providing at least a better proportionality constant. Reference models are physical systems in which the connectivity plays a relevant role, e.g., quantum dots arranged in lattices [265] and qubits in quantum annealers [266, 267]. Evidence suggests that a system of qubits in D-Wave quantum annealers quickly thermalizes with the cold environment [268] and that a pause midway through the annealing process increases the probability of successfully finding the ground state of the problem Hamiltonian, and this has been related to the thermalization of the system [269].

5.2 Equilibrium Thermometry

5.2.1 Estimation Theory

In the quantum realm observables are described by self-adjoint operators. However, if the quantity of interest we want to estimate, λ , is not an observable (such as the temperature), then we can not directly measure it. For this reason, one needs the tools provided by quantum estimation theory to find the best optimal probing strategy (see Sec. 1.2). Given an experimental set of outcomes of size μ , $\{\vec{x}\} \in \mathcal{M}^{\oplus \mu}$, which depends on some parameter λ , we can infer the value of the parameter through an estimator function $\hat{\lambda}(\vec{x})$. The variance of an unbiased estimator, i.e., its precision, is lower bounded as follows

$$\text{Var}(\hat{\lambda}) \geq \frac{1}{\mu \mathcal{F}_c(\lambda)} \geq \frac{1}{\mu \mathcal{F}_q(\lambda)}. \quad (5.1)$$

The first inequality is known as the (classical) Cramér-Rao inequality, and the second one is the quantum Cramér-Rao inequality, which sets the ultimate lower bound on the variance of $\hat{\lambda}$. Throughout the section we will consider a discrete set of outcomes \mathcal{M} with cardinality $N_{\mathcal{M}}$. The

Fisher information (FI) is defined as

$$\mathcal{F}_c(\lambda) = \sum_{m=1}^{N_{\mathcal{M}}} \frac{(\partial_\lambda p(x_m|\lambda))^2}{p(x_m|\lambda)}, \quad (5.2)$$

where $p(x_m|\lambda)$ is the probability distribution of the outcomes, and the quantum Fisher information (QFI) is defined as

$$\mathcal{F}_c(\lambda) \leq \mathcal{F}_q(\lambda) = \text{Tr}[\rho_\lambda L_\lambda^2], \quad (5.3)$$

where L_λ is the symmetric logarithmic derivative. The QFI sets the minimum attainable error among the sets of all probing schemes in the estimation problem of λ .

5.2.2 Quantum Fisher Information

In this work we focus on a finite-size quantum system living in a N -dimensional Hilbert space and described by a Hamiltonian operator $\hat{H} = \sum_k E_k |e_k\rangle\langle e_k|$, with $k = 0, \dots, N-1$. The idea is to use a finite system as a probe to estimate the temperature T of an external environment. We thus consider the customary thermodynamic situation occurring in thermalization processes, when a system is in contact with a thermal bath at temperature T and, after some time, it eventually reaches an equilibrium state at the same temperature T of the bath. The final equilibrium state of the probing system is thus given by the Gibbs state

$$\rho_T = \frac{1}{Z} e^{-\hat{H}/T} = \sum_n \sum_{\alpha=1}^{g_n} \frac{e^{-E_n/T}}{Z} |e_{n,\alpha}\rangle\langle e_{n,\alpha}|. \quad (5.4)$$

We set the Boltzmann constant $k_B = 1$. In the last equality we make explicit the possible degeneracy of the energy levels: n labels the distinct energy levels and g_n is the corresponding degeneracy. In terms of the latter, the partition function Z can be written as

$$Z = \sum_{k=0}^{N-1} e^{-E_k/T} = \sum_n g_n e^{-E_n/T}. \quad (5.5)$$

Since the state (5.4) is diagonal in the energy eigenbasis, and since the latter does not depend on the parameter T , the statistical model reduces to a classical-like estimation problem, where the optimal POVM is realized exactly by $\{|e_{n,\alpha}\rangle\langle e_{n,\alpha}|\}$.¹ Moreover, the QFI is easily obtained and turns out to be proportional to the variance of the Hamiltonian operator \hat{H} ,

$$\mathcal{F}_q(T) = \frac{1}{T^4} \left(\langle \hat{H}^2 \rangle - \langle \hat{H} \rangle^2 \right), \quad (5.6)$$

where the expectation values of \hat{H}^p for a Gibbs state are given as

$$\langle \hat{H}^p \rangle = \sum_n g_n \frac{e^{-E_n/T}}{Z} E_n^p. \quad (5.7)$$

¹The optimal measurement, for which the FI equals the QFI, is the projective measurement of energy (PME). A PME on a quantum system is a quantum measurement determined by the Hamiltonian of the system. In this chapter we will consider the Hamiltonian $H = L$ (Laplacian matrix). This is a mathematically suitable way to model the topology of a given system without explicitly modeling all the potentials and the constraints required to have such topology. PME protocols exist when the Hamiltonian is given in advance [270]. Whenever the Hamiltonian is fully known, a PME can be performed, e.g., by means of the quantum Metropolis sampling [271]. Instead, unknown Hamiltonians can be identified by quantum tomography, but the time cost to achieve a given accuracy increases exponentially with the size of the quantum system. To work this out, a PME protocol, which exploits a modified version of quantum phase estimation and does not use quantum tomography, has been proposed [272].

5.2.3 Fisher Information for a position measurement

Our system lives in a N -dimensional space, and we assume the position space to be finite and discrete. When a system is confined to discrete positions, a position measurement is a suitable and standard measurement. In this section we study how informative the position measurement is for estimating the temperature. The POVM is given by $\{|j\rangle\langle j|\}$, where $j = 0, \dots, N - 1$ labels the discrete positions. The probability of observing the system in the j th position given the temperature T is

$$p(j|T) = \text{Tr}[\rho_T |j\rangle\langle j|] = \sum_{k=0}^{N-1} \frac{e^{-E_k/T}}{Z} |\langle j|e_k\rangle|^2. \quad (5.8)$$

Therefore, the FI for the position measurement is

$$\mathcal{F}_c(T) = \sum_{j=0}^{N-1} \frac{(\partial_T p(j|T))^2}{p(j|T)}, \quad (5.9)$$

which can be rewritten (see Appendix 5.B) in a form similar to that of the QFI,

$$\mathcal{F}_c(T) = \frac{1}{T^4} \left(\sum_{j=0}^{N-1} \frac{\langle \hat{H} \rho_T \rangle_j^2}{p(j|T)} - \langle \hat{H} \rangle^2 \right), \quad (5.10)$$

where

$$\langle \hat{H} \rho_T \rangle_j = \sum_{k=0}^{N-1} \frac{e^{-E_k/T} E_k}{Z} |\langle j|e_k\rangle|^2 \quad (5.11)$$

is the expectation value of $\hat{H} \rho_T$ on the position eigenstate $|j\rangle$.

5.3 Network Thermometry

We focus on the estimation of temperature using quantum probes which may be regarded as set of connected subunits, i.e., described by connected simple graphs (undirected and not multigraph). A graph is a pair $G = (V, E)$ where V denotes the nonempty set of vertices and E the set of undirected edges, which tell which vertices are connected. The set of vertices is the finite set of discrete positions the quantum system can take. The set of edges accounts for all and only the possible paths the system can follow to reach two given vertices. The number of vertices $|V| = N$ determines the order of the graph, and the number of the edges is $|E| = M$. All this information determines the topology of the graph and is encoded in the Laplacian matrix² $L = D - A$. A graph G is said to be k -regular if all its vertices have the same degree k . The Laplacian matrix for an undirected graph is positive semidefinite, and symmetric, and the smallest Laplacian eigenvalue is 0, which, for connected graphs, has degeneracy $g_0 = 1$. Instead, the second-smallest Laplacian eigenvalue is also known as algebraic connectivity [118, 273, 274]: smaller values represent less connected graphs.

A continuous-time quantum walk (CTQW) is the motion of a quantum particle with kinetic energy when confined to discrete positions, e.g., the vertices of a graph, and the CTQW Hamiltonian is $H = \gamma L$. Hence, a quantum walker has intrinsically the topology of the graph, and so it is a promising candidate to be the probe for estimating the temperature of an external environment

²See also Sec. 1.1.2.

with respect to the topology of the network. We have already set $k_B = 1$, and in the following we also set $\gamma = 1$, which is the hopping amplitude of the walk and accounts for the energy scale of the system. Therefore, energy and temperature are hereafter dimensionless. Notice that, in this way, the energy eigenvalues E_n are the Laplacian eigenvalues and the scale of temperature should be intended as referred to the energy scale specific of the system considered, i.e., to γ .

5.3.1 Low-temperature regime

First, we analyze the regime of low temperatures T . Therefore, we assume that the system is mostly in the ground state and can access only the first excitation energy E_1 , $E_n \gg T$ for $n > 1$. For this reason, the partition function is

$$Z = 1 + g_1 e^{-E_1/T}. \quad (5.12)$$

Since the ground state energy is null, the mean value of the energy is $\langle \hat{H} \rangle = g_1 E_1 e^{-E_1/T} Z^{-1}$, and it follows that the QFI in the low temperature regime can be approximated as

$$\mathcal{F}_q^{low}(x) \simeq \frac{f_{g_1}(x)}{E_1^2}, \quad (5.13)$$

where $x = E_1/T$ and the function $f_{g_1}(x)$ is defined as

$$f_{g_1}(x) = \frac{g_1 x^4 e^{-x}}{(1 + g_1 e^{-x})^2}. \quad (5.14)$$

The value $x_{max} > 0$ at which the latter exhibits the maximum is the solution of the following transcendental equation

$$e^{x_{max}} = g_1 \frac{x_{max} + 4}{x_{max} - 4}, \quad (5.15)$$

obtained from $df_{g_1}(x)/dx = 0$. Solutions of this equation can be obtained graphically, as shown in Fig. 5.1. The x_{max} depends only on the degeneracy g_1 and numerical results show that $x_{max}(g_1)$ is a sublinear function, i.e., it increases less than linearly with g_1 .

The FI in the low-temperature regime can be approximated as

$$\mathcal{F}_c^{low}(T) \simeq \frac{E_1^2 e^{-2E_1/T}}{Z T^4} \left(\sum_{j=0}^{N-1} \frac{\eta_j^2}{\frac{1}{N} + e^{-E_1/T} \eta_j} - \frac{g_1^2}{Z} \right), \quad (5.16)$$

since $p(j|T) \simeq \frac{1}{Z} (\frac{1}{N} + \exp\{-E_1/T\} \eta_j)$ and $\langle \hat{H} \rho_T \rangle_j \simeq \frac{1}{Z} \exp\{-E_1/T\} E_1 \eta_j$, where $\eta_j = \sum_{\alpha=1}^{g_1} |\langle j | e_{1,\alpha} \rangle|^2$.

5.3.2 High-temperature regime

We move now to the opposite regime, high temperature, in which we assume that $T \gg E_k$ for all k . The single-walker probe is no longer valid in the high-temperature regime, where many excitations, not only one, come into play. Yet it can be used for small thermometers with bounded spectrum and large energy gap $E_1 - E_0$, so that we may expect few excitations, and the single-walker model can still approximate the real system. In this regime, the density matrix, in the energy eigenbasis, can be approximated by the maximally mixed state³ $\rho_T \simeq I_N/N$, where I_N is

³The results presented in this section rely on the assumption of ρ_T maximally mixed state. This follows from the Gibbs state (5.4) where we have assumed $\exp[-E_n/T] \approx 1$, because of the high-temperature regime. If we consider the

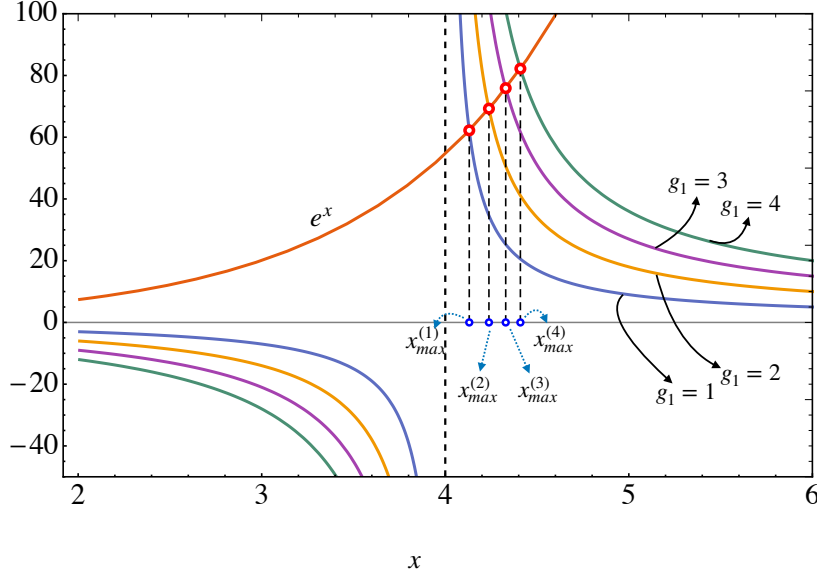


Figure 5.1. Graphical solution $x_{max}^{(g_1)}$ of the transcendental equation (5.15) for different values of g_1 .

the $N \times N$ identity matrix. Accordingly, the QFI becomes

$$\begin{aligned} \mathcal{F}_q^{high}(T) &\simeq \frac{1}{T^4} \left[\frac{1}{N} \sum_{k=0}^{N-1} E_k^2 - \frac{1}{N^2} \left(\sum_{k=0}^{N-1} E_k \right)^2 \right] \\ &= \frac{1}{NT^4} \left[\sum_{k=0}^{N-1} d_k^2 + 2M \left(1 - \frac{2M}{N} \right) \right]. \end{aligned} \quad (5.17)$$

Refer to Appendix 5.A for details on the sum of the energy eigenvalues and that of their square. Thus, in the limit of high temperatures, the QFI tends to zero as $O(T^{-4})$ and proportionally to a topology-dependent factor.

The sum of the squared degree can be bounded as

$$\frac{4M^2}{N} \leq \sum_{k=0}^{N-1} d_k^2 \leq M \left(\frac{2M}{N-1} + N - 2 \right), \quad (5.18)$$

where the upper bound is proved in [275] and the lower bound follows from the Cauchy-Schwartz inequality for the inner product of two N -dimensional vectors, $(1, \dots, 1)$ and (d_0, \dots, d_{N-1}) , using

next term of the Taylor polynomial, $\exp[-E_n/T] \approx 1 - E_n/T$, then the partition function is $Z \approx N - 2M/T$, since $\text{Tr}[H] = \text{Tr}[L] = 2M$ with M the number of edges of the graph. The Gibbs state is

$$\rho_T \approx \frac{I_N - H/T}{N - 2M/T} \approx \frac{I_N}{N} + \frac{2M - NH}{N^2 T},$$

and for both the approximations $\text{Tr}[\rho_T] = 1$. We observe that ρ_T is the maximally mixed state with a correction of order $O(T^{-1})$, which does depend on the temperature. The QFI (5.6) and the FI for the position measurement (5.10) involve expectation values computed in ρ_T and probability distributions arising from ρ_T . Hence, if we include the term of order $O(T^{-1})$ in ρ_T , then the results of the QFI (5.17) and FI (5.20) presented in this section can be read as the leading terms of the approximation in the high temperature regime, where we have neglected terms of order $O(T^{-5})$.

$\sum_{k=0}^{N-1} d_k = 2M$. Hence, we can bound $\mathcal{F}_q^{high}(T)$ as

$$\frac{2M}{NT^4} \leq \mathcal{F}_q^{high}(T) \leq \frac{M}{T^4} \left[1 - \frac{2M(N-2)}{N^2(N-1)} \right]. \quad (5.19)$$

The upper bound in (5.18) is saturated by the complete graph, while the lower bound is saturated, e.g., by the cycle graph and the complete bipartite graph whose partite sets have both cardinality $N/2$: hence, these bounds are actually achievable, and, accordingly, the bounds (5.19) on the QFI are saturated by the above mentioned graphs (see Sec. 5.4 for details). For high temperatures the optimal thermometer is the complete graph, which, among the simple graphs, has the maximum number of edges M . Notice also that the complete graph has the maximum energy gap, since $E_1 - E_0 = N$. Thus, unlike the low-temperature regime, in the high-temperature regime the graphs which perform better are those with high connectivity, in the sense of those with a high number of edges M .

Recalling that in the high-temperature regime $\rho_T \simeq I_N/N$, we can approximate the FI as

$$\begin{aligned} \mathcal{F}_c^{high}(T) &\simeq \frac{1}{N^2 T^4} \left[N \sum_{j=0}^{N-1} \left(\sum_{k=0}^{N-1} E_k |\langle j|e_k\rangle|^2 \right)^2 - 4M^2 \right] \\ &= \frac{1}{N^2 T^4} \left(N \sum_{j=0}^{N-1} d_j^2 - 4M^2 \right), \end{aligned} \quad (5.20)$$

where the second equality follows from

$$\sum_{k=0}^{N-1} E_k |\langle j|e_k\rangle|^2 = \sum_{k=0}^{N-1} \langle j|L|e_k\rangle \langle e_k|j\rangle = \langle j|L|j\rangle = d_j. \quad (5.21)$$

Therefore, the asymptotic value of the ratio $\mathcal{F}_c(T)/\mathcal{F}_q(T)$ is

$$\lim_{T \rightarrow +\infty} \frac{\mathcal{F}_c(T)}{\mathcal{F}_q(T)} = \frac{N \sum_{k=0}^{N-1} d_k^2 - 4M^2}{N \left[\sum_{k=0}^{N-1} d_k^2 + 2M \left(1 - \frac{2M}{N} \right) \right]} = \frac{1}{1 + \lambda_{N,M}}, \quad (5.22)$$

where we have introduced the quantity

$$\lambda_{N,M} = \frac{2M}{\sum_{k=0}^{N-1} d_k^2 - \frac{4M^2}{N}} \quad (5.23)$$

to capture the (asymptotic) discrepancy between the FI and the QFI in terms of the topology features of the graphs: small $\lambda_{N,M}$ means a ratio close to 1, $\mathcal{F}_c(T) \simeq \mathcal{F}_q(T)$; large $\lambda_{N,M}$ means a ratio close to 0, $\mathcal{F}_c(T) \ll \mathcal{F}_q(T)$.

5.3.3 Fisher Information for circulant graphs

In this section we prove that the FI for position measurement is identically null in the case of circulant graphs, e.g., the complete graph and the cycle graph. A circulant graph is defined as the regular graph whose adjacency matrix is circulant, and accordingly so is the Laplacian matrix [276–278]. A circulant matrix is a special Toeplitz matrix where every row of the matrix is a right cyclic shift of the row above it. The eigenproblem for circulant matrices is solved [114], and the Laplacian eigenstates of circulant graphs are

$$|e_k\rangle = \frac{1}{\sqrt{N}} \sum_{j=0}^{N-1} \omega^{kj} |j\rangle, \quad (5.24)$$

with $\omega = \exp\{2\pi i/N\}$ and $0 \leq k \leq N-1$. This means that $|\langle j|e_k\rangle|^2 = 1/N \forall k$ and consequently

$$p(j|T) = \frac{1}{N}, \quad (5.25)$$

while

$$\langle \hat{H} \rho_T \rangle_j = \frac{1}{N} \langle \hat{H} \rangle. \quad (5.26)$$

From Eq. (5.10) we clearly see that $\mathcal{F}_c(T) = 0$. We conclude that for circulant graphs the position measurement does not carry any information on the temperature T .

Actually, the result is more general: the FI for a position measurement is null not only for circulant graphs, but for all the graphs such that $|\langle j|e_k\rangle|^2 = t_j$ does not depend on k . Indeed, in this case we have $p(j|T) = t_j$ and $\langle \hat{H} \rho_T \rangle_j = t_j \langle \hat{H} \rangle$, from which we see that (5.10) is identically 0, since $\sum_{j=0}^{N-1} t_j = 1$.

5.4 Results

In this section, we address the study for some remarkable connected simple graphs and some lattice graphs by means of the previously found general results. To avoid repetitions, we recall that the ground state energy $E_0 = 0$ is not degenerate for connected simple graphs, $g_0 = 1$, and the corresponding eigenstate is

$$|e_0\rangle = \frac{1}{\sqrt{N}} \sum_{k=0}^{N-1} |k\rangle. \quad (5.27)$$

Results of QFI and FI for position measurement for graphs (see Fig. 5.2) are shown in Fig. 5.3 and 5.4, for lattices (see Fig. 5.5) in Fig. 5.6, and results of the ratio of FI and QFI for both graphs and lattices are summarized in Fig. 5.7. The analytical results suitable for a comparison are reported in Table 5.1.

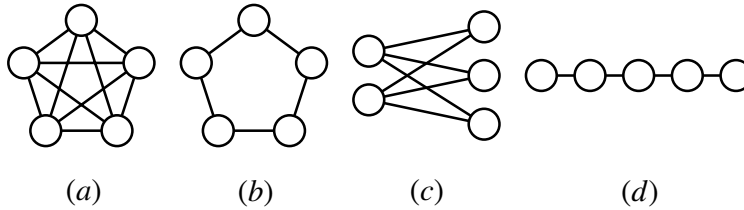


Figure 5.2. Graphs considered in the present work (example for $N = 5$ vertices): (a) Complete graph K_5 , (b) cycle graph C_5 , (c) complete bipartite graph $K_{2,3}$, and (d) path graph P_5 .

5.4.1 Complete graph

A complete graph is a simple graph whose vertices are pairwise adjacent, i.e., each pair of distinct vertices is connected by a unique edge (see Fig. 5.2(a)). The complete graph with N vertices is denoted K_N , is $(N-1)$ -regular, and has $M = N(N-1)/2$ edges. Its energy spectrum consists of two energy levels: the ground state and the second level $E_1 = N$ with degeneracy $g_1 = N-1$. The graph is circulant, thus the eigenvectors are given by (5.24) and the FI for a position measurement is identically null.

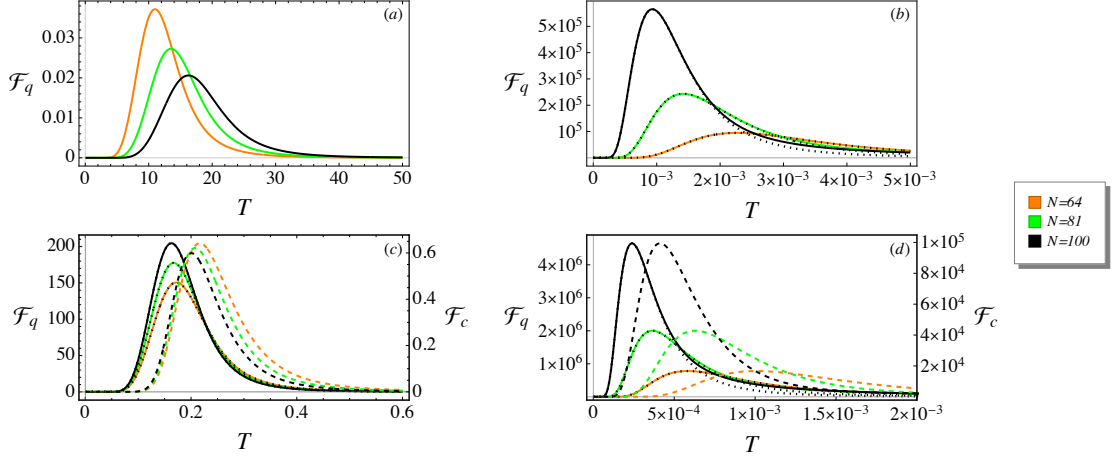


Figure 5.3. QFI and FI for position measurement for different graphs of order N : (a) complete graph, (b) cycle graph, (c) star graph, and (d) path graph. Solid colored line: QFI \mathcal{F}_q . Dotted black line: QFI at low temperature \mathcal{F}_q^{low} (5.13) (not reported for the complete graph since it coincides with Eq. (5.28)). Dashed colored line: FI for position measurement \mathcal{F}_c . The FI for complete graph and cycle graph (circulant graphs) is null, and therefore is not shown. Because of the different ranges, values of QFI are referred to the left y -axis, and values of FI are referred to the right y -axis.

In this case, the approximation for the low-temperature regime is actually exact and holds at all the temperatures, because the system has precisely two distinct energy levels. Hence, the QFI reads as

$$\mathcal{F}_q(T) = \frac{N^2(N-1)e^{-N/T}}{T^4[1+(N-1)e^{-N/T}]^2}. \quad (5.28)$$

The algebraic connectivity $E_1 = N$ and the degeneracy $g_1 = N - 1$ grow with the order N of the graph. In Fig. 5.3(a) we observe that maxima of QFI occur at higher temperatures as N increases. According to Eq. (5.15) and Fig. 5.1, we expect the maximum of QFI to occur at increasing values of $x_{max} = E_1/T_{max}$ as $g_1(N)$ increases. Hence, this means that T_{max} increases less than linearly with N . For this reason the complete graph is not a good thermometer for low T . On the other hand, the complete graph saturates the upper bound in (5.18), since $M = N(N-1)/2$. It follows that in the high-temperature regime the complete graph is the optimal thermometer and, accordingly, the QFI is $\mathcal{F}_q^{high}(T) = (N-1)/T^4$.

5.4.2 Cycle graph

A cycle graph with $N \geq 3$ vertices (or N -cycle) is a simple graph whose vertices $\{v_j\}_{j=1,\dots,N}$ can be (re)labeled such that its edges are $v_1v_2, v_2v_3, \dots, v_{N-1}v_N$, and v_Nv_1 (see Fig. 5.2(b)). In other words, we may think of it as a one-dimensional lattice with N sites and periodic boundary conditions. The cycle graph with N vertices is denoted C_N , is 2-regular, and has $M = N$ edges. Its energy spectrum is $E_k = 2[1 - \cos(2\pi k/N)]$, with $k = 0, \dots, N-1$. The lowest energy level is not degenerate, while the degeneracy of the highest energy level depends on the parity of N : no degeneracy for even N , $g_{N/2} = 1$, but double degeneracy for odd N , $g_{(N+1)/2} = 2$. The remaining energy levels have degeneracy 2. The cycle graph is circulant, thus the eigenvectors are (5.24), the same of those of the complete graph, and the FI for a position measurement is identically null.

The algebraic connectivity $E_1 = 2[1 - \cos(2\pi/N)]$ decreases as N increases, while $g_1 = 2$ is constant. According to Eq. (5.15) and Fig. 5.1, we expect the maximum of QFI to occur at the constant value of $x_{max} = E_1/T_{max}$ independently of N , because g_1 is constant. Since E_1 decreases as N increases, then T_{max} must also decrease to ensure x_{max} constant. Indeed, the maxima of QFI occur at lower temperatures as N increases, as shown in Fig. 5.3(b). It follows that the larger N the better the cycle graph behaves as a low-temperature probe. Instead, the cycle graph saturates the lower bound in (5.18), since $M = N$, and so the QFI at high temperatures is $\mathcal{F}_q^{high}(T) = 2/T^4$.

5.4.3 Complete Bipartite Graph

A graph G is bipartite if the set of vertices $V(G)$ is the union of two disjoint independent sets V_1 and V_2 , called partite sets of G , such that every edge of G joins a vertex of V_1 and a vertex of V_2 . A complete bipartite graph is a simple bipartite graph such that two vertices are adjacent if and only if they are in different partite sets, i.e., if every vertex of V_1 is adjacent to every vertex of V_2 (see Fig. 5.2(c)). The complete bipartite graph having partite sets with $|V_1| = N_1$ and $|V_2| = N_2$ vertices is denoted K_{N_1, N_2} , has $M = N_1 N_2$ edges, and the total number of vertices is $N = N_1 + N_2$. Without loss of generality we assume $N_1 \leq N_2$. The energy spectrum is given by $E_1 = N_1$, $E_2 = N_2$, and $E_3 = N_1 + N_2$, with degeneracy $g_0 = 1$, $g_1 = N_2 - 1$, $g_2 = N_1 - 1$, and $g_3 = 1$, respectively. The corresponding eigenvectors are

$$\begin{aligned} |e_1^n\rangle &= \frac{1}{\sqrt{n(n+1)}} \left(\sum_{k=N_1}^{N_1-1+n} |k\rangle - n |N_1 + n\rangle \right), \\ |e_2^m\rangle &= \frac{1}{\sqrt{m(m+1)}} \left(\sum_{k=0}^{m-1} |k\rangle - m |m\rangle \right), \\ |e_3\rangle &= \frac{1}{\sqrt{N}} \left(\sqrt{\frac{N_2}{N_1}} \sum_{k=0}^{N_1-1} |k\rangle - \sqrt{\frac{N_1}{N_2}} \sum_{k=N_1}^{N-1} |k\rangle \right), \end{aligned} \quad (5.29)$$

where $n = 1, \dots, N_2 - 1$ and $m = 1, \dots, N_1 - 1$. Note that for $N_1 = N_2 = N/2$ the complete bipartite graph is circulant [279] and the spectrum reduces to $E_0, E_1 = N/2$, and $E_2 = N$, with degeneracy, respectively, $g_0 = 1$, $g_1 = N - 2$, and $g_2 = 1$. Instead, for $N_1 = 1$ and $N_2 = N - 1$ we obtain the star graph S_N , whose spectrum reduces to $E_0, E_1 = 1$, and $E_2 = N$, with degeneracy, respectively, $g_0 = 1$, $g_1 = N - 2$, and $g_2 = 1$.

Regarding the low-temperature regime, the algebraic connectivity is $E_1 = N_1$ while $g_1 = N_2 - 1$. The complete bipartite graph is completely defined only by the total number of vertices N , so we discuss where the maximum of the QFI occur according to Eq. (5.15) and Fig. 5.1 first for a given value N_1 , and then for a given value of $N = N_1 + N_2$.

For N_1 fixed, we expect the maximum of QFI to occur at increasing values of $x_{max} = E_1/T_{max}$ as N increases, because N_2 and thus g_1 increase. Since E_1 is constant, then T_{max} must decrease to ensure that x_{max} increases. Indeed, for a given N_1 , the maxima of QFI occur at lower temperatures as N increases, as shown in Fig. 5.4(a). In particular, this is also the case of the star graph S_N , because it is $K_{1, N-1}$, even if such behavior is less evident in Fig. 5.3(c).

For N fixed, we expect the maximum of QFI to occur at decreasing values of $x_{max} = E_1/T_{max}$ as N_1 increases, because N_2 and thus g_1 decrease. Since E_1 increases as N_1 increases, then T_{max} must increase more than N_1 to ensure that x_{max} decreases. Indeed, for a given N , the maxima of QFI occur at higher temperatures as N_1 increases, as shown in Fig. 5.4(b). This means that, at fixed N , we can tune the temperature at which the QFI is maximum just by varying the number of vertices in the two partite sets. From Fig. 5.4(b) we observe that the highest maximum of QFI is provided by the star graph S_N , whose algebraic connectivity $E_1 = 1$ is constant and minimum,

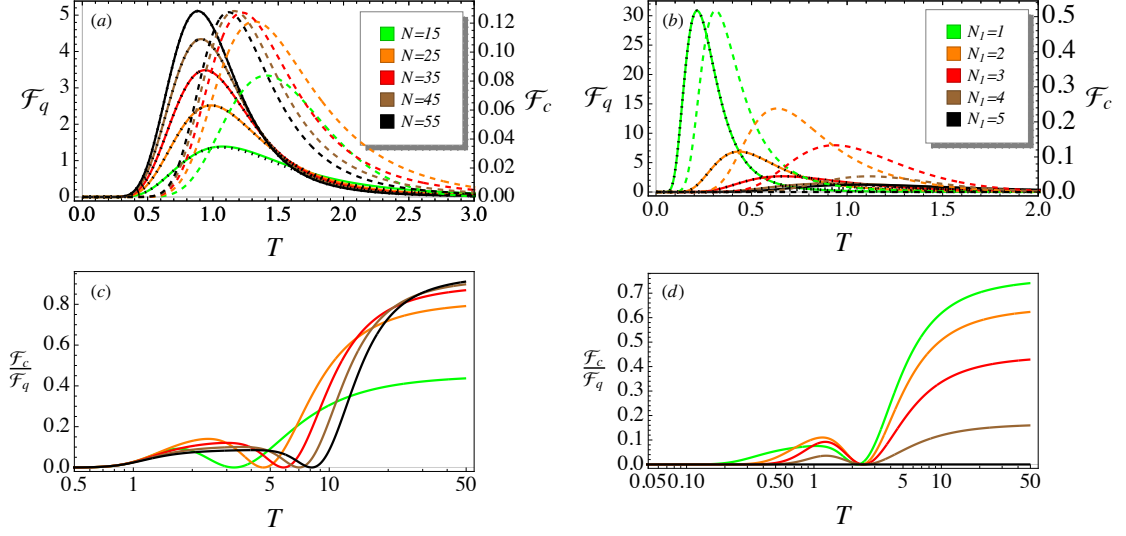


Figure 5.4. Results of the estimation problem of the temperature for the complete bipartite graph K_{N_1, N_2} of order $N = N_1 + N_2$. Left-column plots: results for different N at fixed $N_1 = 5$. Right-column plots: results for different N_1 at fixed $N = 10$. Values of $N_1 > N/2$ are not considered because of the symmetry of the graph when exchanging the two partite sets and so N_1 and N_2 . For $N_1 = N_2 = N/2$ the FI is identically null because the corresponding complete bipartite graph is circulant. Top-row plots: QFI \mathcal{F}_q (solid colored line), QFI at low temperature \mathcal{F}_q^{low} (5.13) (dotted black line), and FI for position measurement \mathcal{F}_c (dashed colored line). Because of the different ranges, values of QFI are referred to the left y -axis, and values of FI are referred to the right y -axis. Bottom-row plots: ratio $\mathcal{F}_c/\mathcal{F}_q$.

while the lowest maximum of QFI is provided by $K_{N/2, N/2}$, i.e., for $N_1 = N_2$, whose algebraic connectivity $E_1 = N/2$ is the largest among all the complete bipartite graphs.

In the high-temperature regime, since $\sum_k d_k^2 = N_1 N_2 (N_1 + N_2)$ and $M = N_1 N_2$, the QFI is

$$\mathcal{F}_q^{high}(T) = \frac{N_1 N_2 [(N_1 - N_2)^2 + 2(N_1 + N_2)]}{T^4 (N_1 + N_2)^2}. \quad (5.30)$$

Notice that for $N_1 = N_2 = N/2$, the complete bipartite graph is $N/2$ -regular, and saturates the lower bound in (5.18), since $M = N^2/4$, and so the QFI at high temperatures is $\mathcal{F}_q^{high}(T) = N/(2T^4)$.

The asymptotic behavior of the ratio $\mathcal{F}_c(T)/\mathcal{F}_q(T)$ at high temperature (5.22) is characterized by $\lambda_{N_1+N_2, N_1 N_2} = 2(N_1 + N_2)/(N_2 - N_1)^2$. Depending on the number of vertices in the two subsets, results differ. When $N_1 = N_2$, the difference $N_2 - N_1$ is null, the complete bipartite graph is circulant and so the FI is identically null, for any T . Instead, the difference $N_2 - N_1$ is maximum for the star graph S_N . This results in $\lambda_{N, N} = 2N/(N - 2)^2$: hence, $\lambda_{N, N} \rightarrow 0$ for large N and, accordingly, the FI approaches the QFI in the limit of high temperatures. Actually, since for the star graph $\sum_k d_k^2 = N(N - 1)$, the QFI in the high-temperature regime has the same asymptotic behavior of the complete graph, i.e., $\mathcal{F}_q^{high} = (N - 1)/T^4 + O(1/(NT^4))$.

In this section we have approximated the QFI for the complete bipartite graph under the assumptions of low or high temperature. The exact analytical expression of the QFI is reported in Appendix 5.D.

5.4.4 Path graph

A path graph with N vertices is a simple graph whose vertices $\{v_j\}_{j=1,\dots,N}$ can be (re)labeled such that its edges are $v_1v_2, v_2v_3, \dots, v_{N-1}v_N$ (see Fig. 5.2(d)). In other words, we may think of it as a one-dimensional lattice with N sites and open boundary conditions. The path graph with N vertices is denoted P_N , and has $M = N - 1$ edges. Its nondegenerate energy spectrum is $E_k = 2[1 - \cos(\pi k/N)]$, with $k = 0, \dots, N - 1$, and the corresponding eigenvectors are

$$|e_k\rangle = \sum_{j=0}^{N-1} \cos\left(\frac{\pi k}{2N}(2j-1)\right) |j\rangle. \quad (5.31)$$

The energy spectrum is similar to that of the cycle, and this is reflected in its thermometric behavior. Indeed, the algebraic connectivity $E_1 = 2[1 - \cos(\pi/N)]$ decreases as N increases, while $g_1 = 1$ is constant. Hence, as for the cycle graph, the maximum of the QFI occurs at lower temperature as N increases, as shown in Fig. 5.3(d). Further, the similarity extends also in the high-temperature regime, where, due to $\sum_k d_k^2 = 2(2N - 3)$ and $M = N - 1$, we have that $\mathcal{F}_q^{\text{high}}(T) = 2/T^4 + O(1/(N^2T^4))$, which is asymptotically equivalent to that of the cycle.

Nevertheless, there is a difference between the cycle and the path, and this is due to the different boundary conditions of the two graphs. In the first, the periodic boundary conditions ensure that the cycle graph is a circulant graph, and consequently the FI for the position measurement is null. Instead, in the second, the open boundary conditions lead to a non-null FI for the position measurement. The asymptotic behavior of the ratio $\mathcal{F}_c(T)/\mathcal{F}_q(T)$ at high temperature (5.22) is characterized by $\lambda_{N,N-1} = N(N-1)/(N-2)$, which is monotonically increasing with the order of the graph. Thus, in the limit of high temperature the FI is very small compared to QFI.

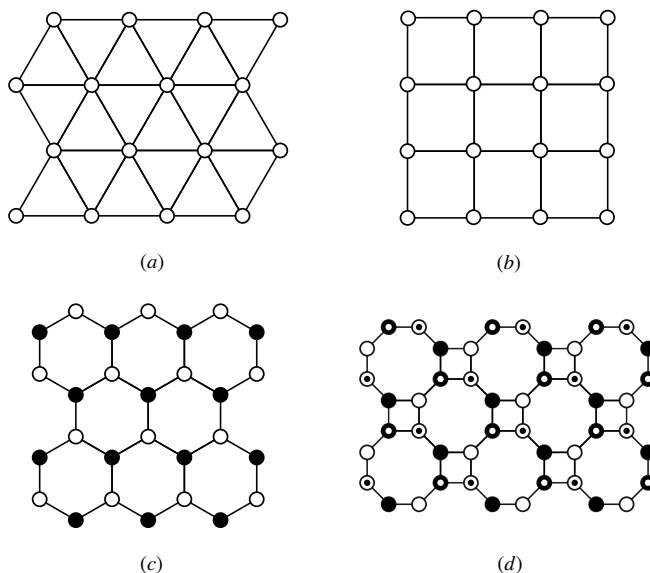


Figure 5.5. Two-dimensional lattices considered in the present work: (a) triangular, (b) square, (c) honeycomb, and (d) truncated square lattice. Equivalent vertices are equally represented.

5.4.5 Lattices

In this section we address the thermometry on some two-dimensional lattices. There are three regular tessellations composed of regular polygons symmetrically tiling the Euclidean plane: equilateral triangles, squares, and regular hexagons (Figs. 5.5(a)-(c)). In addition to these we also consider the truncated square lattice in Fig. 5.5(d). Triangular and square lattices are Bravais lattices, while honeycomb and truncated square lattices are not. This difference is reflected in the spreading of CTQWs, which is ballistic on Bravais lattices and subballistic on non-Bravais lattices [280]. A generic vertex in the triangular lattice has degree 6, in the square lattice has degree 4, and both in the honeycomb and in the truncated square lattice has degree 3. We consider the lattices either with open boundary conditions (OBCs) or with periodic boundary conditions (PBCs). Notice that the lattices with PBCs are regular, while the lattices with OBCs are not, because the vertices at the boundaries have a lower degree than the vertices within the lattice.

Numerical results of QFI and FI for the lattices with OBCs are shown in Fig. 5.6. We observe that the maximum of the QFI gets sharper and higher, and shifts to lower temperatures as the size of the lattice, i.e., the number of vertices, increases. A similar behavior occurs as the degree of the vertex of the lattice decreases: the maximum of the QFI for honeycomb and truncated square lattices is sharper and higher, and at lower temperature than the peak of the QFI for the triangular lattice. The predicted behavior of the QFI at low temperature (5.13) is a good approximation for honeycomb and truncated square lattices, because it fits the maximum of the QFI, its height and position. For the square it is fairly good approximation, but for the triangular lattices it fits only the QFI at the temperatures closer to zero. The FI of position measurement is a couple of orders of magnitude lower than the QFI (see the ratio $\mathcal{F}_c(T)/\mathcal{F}_q(T)$ in Fig. 5.7), and its maximum is at higher temperature than the maximum of the QFI.

For lattices with PBCs the behavior of the QFI is qualitatively the same as regards the goodness of the lower-temperature approximation (5.13) and the dependence of the QFI on the size of the lattice and the degree of the vertices. However, the maxima of QFI for lattices with PBCs are lower and occur at higher temperature than the maxima of QFI for lattices with OBCs. Remarkably, the FI for these lattices with PBCs is identically null.

Some analytical results can be obtained for the square lattice, both with OBCs and with PBCs. Indeed, the $m \times n$ square lattice with OBCs is actually a grid graph and is the Cartesian product of two path graphs, $G_{m,n} = P_m \square P_n$ [281]. Instead, the $m \times n$ square lattice with PBCs is actually the torus grid graph and is the Cartesian product of two cycle graphs, $T_{m,n} = C_m \square C_n$ [282]. For the Cartesian product $G_1 \square G_2$ of two graphs G_1 and G_2 we can easily obtain the QFI and FI as follows (proof in Appendix 5.C):

$$\mathcal{F}_q(G_1 \square G_2 | T) = \mathcal{F}_q(G_1 | T) + \mathcal{F}_q(G_2 | T), \quad (5.32)$$

$$\mathcal{F}_c(G_1 \square G_2 | T) = \mathcal{F}_c(G_1 | T) + \mathcal{F}_c(G_2 | T). \quad (5.33)$$

Thus, since the FI of position measurement for the cycle graph is identically null, this result analytically proves the null FI for the square lattice with PBCs.

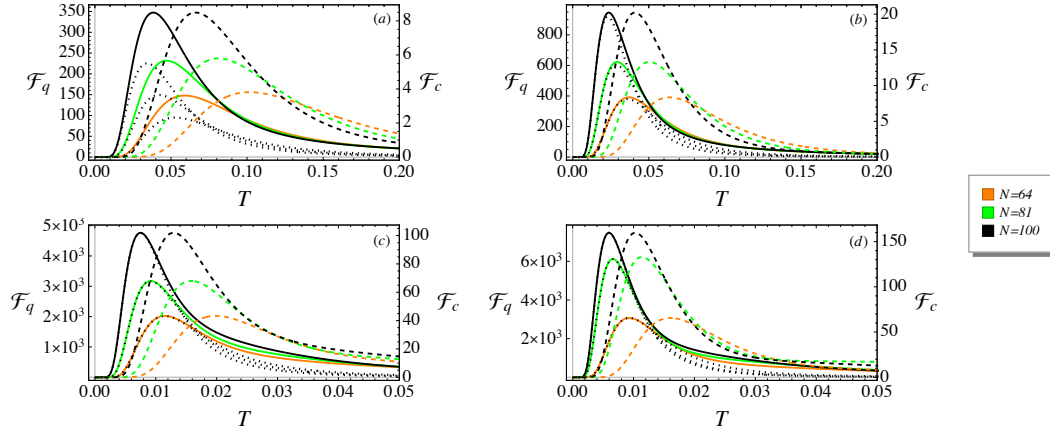


Figure 5.6. QFI and FI for position measurement for different $\sqrt{N} \times \sqrt{N}$ lattices with open boundary conditions (OBC): (a) Triangular lattice, (b) square lattice, (c) honeycomb lattice, and (d) truncated square lattice. Solid colored line: QFI \mathcal{F}_q . Dotted black line: QFI at low temperature \mathcal{F}_q^{low} (5.13). Dashed colored line: FI for position measurement \mathcal{F}_c . Because of the different ranges, values of QFI are referred to the left y -axis, and values of FI are referred to the right y -axis.

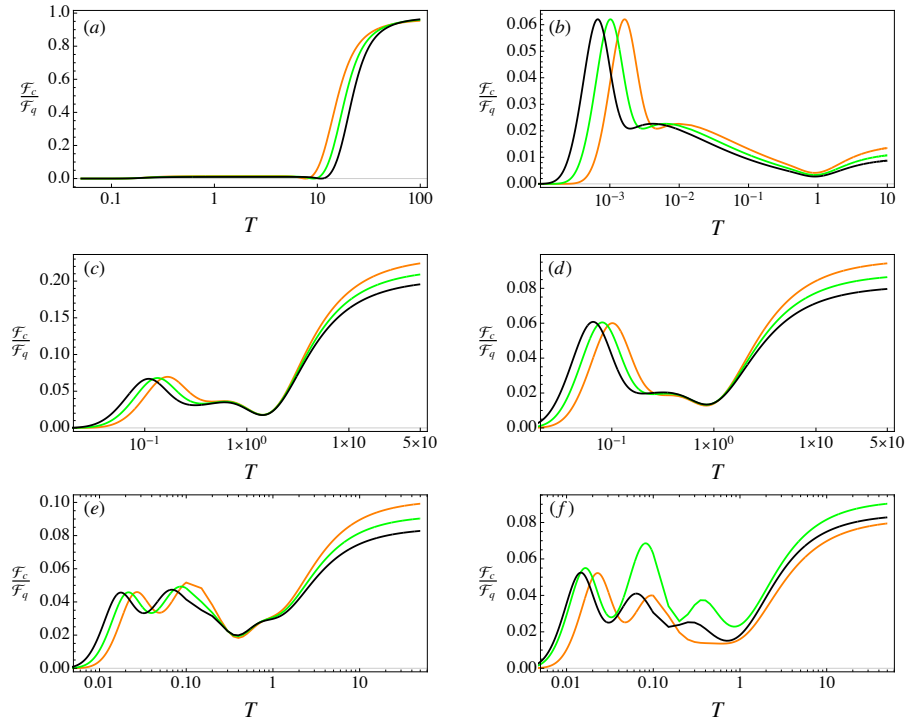


Figure 5.7. Ratio $\mathcal{F}_c/\mathcal{F}_q$ of FI and QFI for the graphs of order N and the $\sqrt{N} \times \sqrt{N}$ lattices providing non-null FI. (a) Star graph, (b) path graph, (c) triangular lattice (OBCs), (d) square lattice (OBCs), (e) honeycomb lattice (OBCs), and (f) truncated square (OBCs). Note the logarithmic scale of the temperature axis.

Graph	Low-temperature	High-temperature		
	$T^4 \mathcal{F}_q^{low}$	$T^4 \mathcal{F}_q^{high}$	$T^4 \mathcal{F}_c^{high}$	$\mathcal{F}_c^{high} / \mathcal{F}_q^{high}$
K_N	$\frac{N^2(N-1) \exp(-N/T)}{[1+(N-1) \exp(-N/T)]^2}$	$N-1$	0	0
C_N	$\frac{32 \exp[-4 \sin^2(\pi/N)/T] \sin^4(\pi/N)}{(1+2 \exp[-4 \sin^2(\pi/N)/T])^2}$	2	0	0
K_{N_1, N_2}	$\frac{\exp(-N_1/T) N_1^2 (N_2-1)}{[1+(N_2-1) \exp(-N_1/T)]^2}$	$\frac{(N^2-\Delta^2)(\Delta^2+2N)}{4N^2}$	$\frac{(N^2-\Delta^2)\Delta^2}{4N^2}$	$\frac{1}{1+2N/\Delta^2}$
S_N	$\frac{(N-2) \exp(-1/T)}{[1+(N-2) \exp(-1/T)]^2}$	$\frac{(N-1)[N(N-2)+4]}{N^2}$	$\frac{(N-1)(N-2)^2}{N^2}$	$\frac{(N-2)^2}{N(N-2)+4}$
P_N	$\frac{16 \exp[-4 \sin^2(\pi/2N)/T] \sin^4(\pi/2N)}{(1+\exp[-4 \sin^2(\pi/2N)/T])^2}$	$\frac{2(N^2-2)}{N^2}$	$\frac{2(N-2)}{N^2}$	$\frac{N-2}{N^2-2}$
$G_{\sqrt{N}, \sqrt{N}}$	$\frac{32 \exp[-4 \sin^2(\pi/2\sqrt{N})/T] \sin^4(\pi/2\sqrt{N})}{(1+2 \exp[-4 \sin^2(\pi/2\sqrt{N})/T])^2}$	$\frac{4(N-2)}{N}$	$\frac{4(\sqrt{N}-2)}{N}$	$\frac{\sqrt{N}-2}{N-2}$
$T_{\sqrt{N}, \sqrt{N}}$	$\frac{64 \exp[-4 \sin^2(\pi/\sqrt{N})/T] \sin^4(\pi/\sqrt{N})}{(1+4 \exp[-4 \sin^2(\pi/\sqrt{N})/T])^2}$	4	0	0

Table 5.1. QFI \mathcal{F}_q^{low} (5.13) in the low-temperature regime and QFI \mathcal{F}_q^{high} (5.17), FI \mathcal{F}_c^{high} (5.20), and their ratio in the high-temperature regime for the graphs considered in the present work: complete graph K_N , cycle graph C_N , complete bipartite K_{N_1, N_2} , star graph S_N , and path graph P_N . Analytical results are also available for the $\sqrt{N} \times \sqrt{N}$ square lattice with OBCs (grid graph $G_{\sqrt{N}, \sqrt{N}}$) and with PBCs (torus grid graph $T_{\sqrt{N}, \sqrt{N}}$), since the grid graph and torus grid graph are the Cartesian product of two path graphs and two cycle graphs respectively (see Appendix 5.C). To have a fair comparison in terms of the total number of vertices N , we report the result for $\sqrt{N} \times \sqrt{N}$ square lattices, and for the complete bipartite graph K_{N_1, N_2} we write results as a function of $N = N_1 + N_2$ and $\Delta = N_2 - N_1$ ($N_2 \geq N_1$ as assumed in this work), except for the QFI in the low-temperature regime. The FI \mathcal{F}_c^{low} in the low-temperature regime is not reported, because an expression suitable for a comparison is not available (see Eq. (5.16)). Both QFI and FI in the high-temperature regime depend on the temperature as T^{-4} , thus we report their values multiplied by T^4 to focus on the factor which depends on the topology of the graph. The same criterion is adopted for the QFI in the low-temperature regime for consistency. Numerical results show that graphs with low degree, e.g., C_N and P_N , exhibit the highest maxima of the QFI at low temperatures. Conversely, at high temperatures and at fixed N , the maximum QFI is obtained with the complete and the star graph, whose QFI scales linearly with the order N . Indeed, in the limit of $N \rightarrow \infty$, the QFI of P_N approaches that of C_N , as well as the QFI of $G_{\sqrt{N}, \sqrt{N}}$ approaches that of $T_{\sqrt{N}, \sqrt{N}}$.

5.5 Role of coherence

Temperature is a classical parameter, i.e., any change in the temperature modifies the eigenvalues of the Gibbs state but not the eigenvectors, which coincide with the eigenvectors of the Hamiltonian at any temperature. As a consequence, one may wonder whether quantumness is playing any role in our analysis, which also does not rely upon quantum effects as entanglement. Despite the above arguments, the quantum nature of the systems under investigation indeed plays a role in determining topological effects in thermometry. In fact, thermal states (5.4) are diagonal in the Hamiltonian basis, but show quantum coherence in the position basis, which itself is the reference *classical basis* when looking at topological effects in graphs. In turn, as we will see in the following, the peak of the QFI occurs in the interval of temperatures over which the coherence starts to decrease.

In order to quantitatively assess the role of coherence, let us consider the l_1 norm of coherence [113]

$$\mathcal{C}(\rho) = \sum_{\substack{j,k=0, \\ j \neq k}}^{N-1} |\rho_{j,k}| \quad (5.34)$$

as a measure of quantum coherence of a state ρ . For convenience, we normalize this measure to its maximum value $\mathcal{C}(\rho_N) = N - 1$, thus defining $C(\rho) := \mathcal{C}(\rho)/(N - 1)$. At $T = 0$, the system is at thermal equilibrium in its ground state and since the Hamiltonian of the system is the Laplacian of a simple graph, the ground state is the maximally coherent state $|\psi_N\rangle = \sum_{j=1}^N |j\rangle/\sqrt{N}$. The normalized coherence is thus equal to one.

As far as the temperature is very low, the ground state is robust, the coherence remains close to one, and the QFI is small, i.e., the robustness of the ground state prevents the system to effectively monitor any change in temperature. On the other hand, when temperature increases, thermal effects becomes more relevant, coherence decreases, and the QFI increases. In other words, it is the fragility of quantum coherence which makes the system a good sensor for temperature (a common feature in the field of *quantum probing*). For higher temperatures, the Gibbs state approaches a *flat* mixture, almost independent of temperature, and both the coherence and the QFI vanish. In order to illustrate the argument, let us consider the case of complete graphs, for which we have analytic expressions for the QFI, see Eq. (5.28), and for the normalized coherence

$$C(\rho_T) = \frac{|1 - e^{-N/T}|}{1 + (N - 1)e^{-N/T}}. \quad (5.35)$$

As it is apparent from Fig. 5.8, where we show the two quantities, the peak of QFI indeed occurs in the interval of temperatures over which the coherence is reduced by a factor $1/e$ (we have numerically observed analogous behavior also for the other graphs). Upon comparison of Eq. (5.28) with Eq. (5.35) we may also write

$$\frac{T^4 \mathcal{F}_q(T)}{N - 1} = [1 - C(\rho_T)] [1 + (N - 1)C(\rho_T)]. \quad (5.36)$$

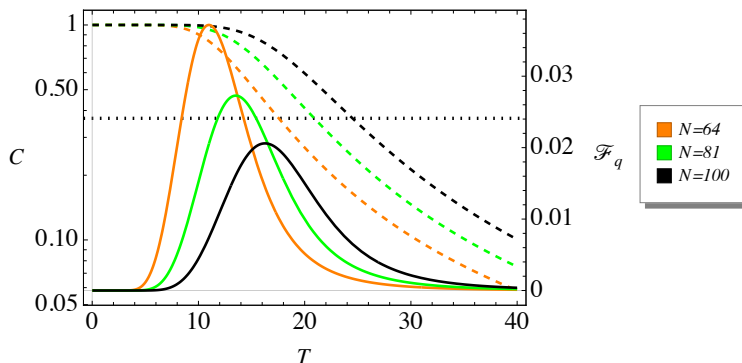


Figure 5.8. QFI \mathcal{F}_q (solid line) and normalized coherence C (dashed line) of a Gibbs state ρ_T as a function of T for a complete graph of order N . The black horizontal dotted line represents the constant value $1/e$.

5.6 Conclusions

We have addressed the role of topology in determining the precision of thermometers. The key idea is to use a finite system as a probe for estimating the temperature T of an external environment. The probe is regarded as a connected set of subunits and may be ultimately modeled as a quantum walker moving continuously in time on a graph. In particular, we have considered equilibrium thermometry, and evaluated the quantum Fisher information of Gibbs states. Since the Hamiltonian of a quantum walker corresponds to the Laplacian matrix of the graph, the topology is inherently taken into account. We have considered some paradigmatic graphs and two-dimensional lattices, evaluated the Fisher information (FI) for a position measurement and compared it with the quantum Fisher information (QFI, energy measurement), providing analytical and numerical results. In particular, we have focused on the low- and the high-temperature regimes, which we have investigated by means of analytic approximations which allow us to have a better understanding of the behavior of the system.

We have proved, by numerical and analytical means, that the maximum of the QFI and the corresponding optimal temperature depend on the two topological parameters of the graph: the algebraic connectivity and the degeneracy of the first energy level. In our system, the algebraic connectivity also represents the energy gap between the first excited energy level and the ground state, and the smaller is the algebraic connectivity, the higher is the maximum of the QFI. These results are supported by a number of examples. In particular, graphs and lattices whose vertices have low degree, e.g., path and cycle graphs, as well as honeycomb and truncated square lattices, show the highest maxima of QFI. We also notice that the maximum of the QFI and the corresponding optimal T decrease as N increase in the complete graph, while in all the other cases we have the opposite behavior.

At intermediate temperatures, the analytical approximation we have at low temperatures is no longer valid, as shown by the discrepancy between the dotted lines (analytical approximation) and the solid lines (exact results) in Figs. 5.3–5.4, and 5.6. However, the low-temperature approximation captures quite well the maximum of the QFI, after which the QFI decreases, tending to zero, as the temperature increases. This behavior is confirmed by the exact analytical expressions of the QFI we have for the complete graph, Eq. (5.28), and the complete bipartite graph (see Appendix 5.D), and we also have numerical evidence of it for the other graphs and lattices. Hence, no relevant structures of the QFI are expected at intermediate temperatures.

At high temperatures the QFI is of order $O(T^{-4})$, with a proportionality constant which depends on the topology of the graph. In this regime, the maximum QFI is attained by the complete graph, which is the simple graph that, at given number of vertices, has the highest number of edges. A remarkable thermometer is also obtained considering the complete bipartite graph. Despite its low QFI (if compared with the cycle and path graphs) it is possible to tune the position of the maximum of QFI just by varying the number of vertices in the two partite sets of the graph keeping fixed their sum.

Finally, we have discussed the role of coherence (in the position basis) in determining the precision. Our results provides some general indications on the role of topology in using quantum probes for thermometry, and provide new insights in the thermometry of finite-size quantum systems at equilibrium, at least for the class of systems where the Hamiltonian is in the form of a Laplacian matrix. In particular, our results suggest that quantum probes are particularly efficient in the low-temperatures regime, where the QFI reaches its maximum. They also pave the way to investigate the role of topology in out-of-equilibrium thermometry.

Appendices

5.A Sum of the Laplacian eigenvalues and sum of their square

First, we focus on the sum of the Laplacian eigenvalues E_k

$$\sum_{k=0}^{N-1} E_k = \text{Tr}[L] = \text{Tr}[D] = \sum_{k=0}^{N-1} d_k = 2M, \quad (5.37)$$

where the last equality was first proved by Euler and it is known as the degree sum formula or the handshaking lemma [283, 284]. Next, we write the sum of the E_k^2 as

$$\sum_{k=0}^{N-1} E_k^2 = \text{Tr}[L^2] = \text{Tr}[D^2] - \text{Tr}[AD] - \text{Tr}[DA] + \text{Tr}[A^2]. \quad (5.38)$$

Using the definition of degree and adjacency matrices,⁴ we see that

$$(DA)_{k,j} = \begin{cases} 0 & \text{if } k = j, \\ d_k A_{k,j} & \text{otherwise,} \end{cases} \quad (5.39)$$

$$(AD)_{k,j} = \begin{cases} 0 & \text{if } k = j, \\ A_{k,j} d_j & \text{otherwise,} \end{cases} \quad (5.40)$$

$$(A^2)_{k,j} = \sum_{m=0}^{N-1} A_{k,m} A_{m,j}, \quad (5.41)$$

and clearly $\text{Tr}[DA] = \text{Tr}[AD] = 0$, whereas

$$\text{Tr}[A^2] = \sum_{k=0}^{N-1} (A^2)_{k,k} = \sum_{k=0}^{N-1} \sum_{m=0}^{N-1} A_{k,m} A_{m,k} = \sum_{k=0}^{N-1} \sum_{m=0}^{N-1} A_{k,m} = \sum_{k=0}^{N-1} d_k = 2M, \quad (5.42)$$

⁴The degree matrix D is diagonal with elements $D_{jj} = \text{deg}(j) =: d_j$, the degree of vertex j , while the adjacency matrix A has elements $A_{jk} = 1$ if the vertices j and k are connected by an edge or $A_{jk} = 0$ otherwise.

since the adjacency matrix is symmetric, $A_{k,m} = A_{m,k}$, and for simple graphs $A_{k,m} \in \{0,1\}$, thus $A_{k,m}^2 = A_{k,m}$. We also notice that this result is somehow related to the well-known fact that $(A^2)_{k,j}$ is the number of walks of length 2 connecting the vertexes k and j . Eventually we obtain

$$\sum_{k=0}^{N-1} E_k^2 = \sum_{k=0}^{N-1} d_k^2 + 2M. \quad (5.43)$$

5.B Fisher Information for a position measurement

Let us consider the position measurement, whose POVM is given by $\{|j\rangle\langle j|\}$. Given an equilibrium state ρ_T at temperature T , the probability distribution of the outcomes is given by the Born rule

$$p(j|T) = \text{Tr}[\rho_T |j\rangle\langle j|] = \sum_{k=0}^{N-1} \frac{e^{-E_k/T}}{Z} |\langle j|e_k\rangle|^2, \quad (5.44)$$

and the FI by definition is (5.9). From classical thermodynamics we recall that

$$\partial_T Z = \frac{Z\langle \hat{H} \rangle}{T^2}, \quad (5.45)$$

and the first derivative of the probability distribution is

$$\begin{aligned} \partial_T p(j|T) &= \sum_{k=0}^{N-1} \partial_T \left(\frac{e^{-E_k/T}}{Z} \right) |\langle j|e_k\rangle|^2 \\ &= \frac{1}{T^2} \sum_{k=0}^{N-1} e^{-E_k/T} \left(\frac{E_k - \langle \hat{H} \rangle}{Z} \right) |\langle j|e_k\rangle|^2 \\ &= \frac{1}{T^2} \left(\langle \hat{H} \rho_T \rangle_j - \langle \hat{H} \rangle p(j|T) \right), \end{aligned} \quad (5.46)$$

where $\langle \hat{H} \rho_T \rangle_j$ is given in Eq. (5.11). From this result, the FI simplifies as

$$\begin{aligned} \mathcal{F}_c(T) &= \frac{1}{T^4} \sum_{j=0}^{N-1} \frac{1}{p(j|T)} \left(\langle \hat{H} \rho_T \rangle_j^2 + \langle \hat{H} \rangle^2 p(j|T)^2 - 2 \langle \hat{H} \rho_T \rangle_j \langle \hat{H} \rangle p(j|T) \right) \\ &= \frac{1}{T^4} \sum_{j=0}^{N-1} \frac{\langle \hat{H} \rho_T \rangle_j^2}{p(j|T)} + \frac{1}{T^4} \langle \hat{H} \rangle^2 \sum_{j=0}^{N-1} p(j|T) - \frac{2}{T^4} \langle \hat{H} \rangle \sum_{j=0}^{N-1} \langle \hat{H} \rho_T \rangle_j. \end{aligned} \quad (5.47)$$

Since $\sum_{j=0}^{N-1} |\langle j|e_k\rangle|^2 = 1$, we observe that

$$\sum_{j=0}^{N-1} \langle \hat{H} \rho_T \rangle_j = \sum_{k=0}^{N-1} \frac{e^{-E_k/T} E_k}{Z} \sum_{j=0}^{N-1} |\langle j|e_k\rangle|^2 = \langle \hat{H} \rangle, \quad (5.48)$$

from which the FI for a position measurement (5.10) follows.

5.C QFI and FI for the Cartesian product of two graphs

5.C.1 Cartesian product of two graphs

The Cartesian product $G_1 \square G_2$ of two graphs G_1 and G_2 is a graph with vertex set $V(G_1) \times V(G_2)$. Therefore, a generic vertex of $G_1 \square G_2$ is denoted by $(j, k) \in V(G_1) \times V(G_2)$ and the adjacency of vertices is determined as follows: two vertices (j, k) and (j', k') are adjacent if either $(j = j' \text{ and } k \sim k')$ or $(j \sim j' \text{ and } k = k')$, where the \sim symbol indicates the adjacency relation between two vertices. If G_1 and G_2 are graphs on N_1 and N_2 vertices, respectively, then the Laplacian matrix of $G_1 \square G_2$ is

$$L(G_1 \square G_2) = L(G_1) \otimes I_{N_2} + I_{N_1} \otimes L(G_2), \quad (5.49)$$

where I_N denotes the $N \times N$ identity matrix. If $(E_1^{(1)}, \dots, E_{N_1}^{(1)})$ and $(E_1^{(2)}, \dots, E_{N_2}^{(2)})$ are the Laplacian spectra of G_1 and G_2 , respectively, then the eigenvalues of $L(G_1 \square G_2)$ are

$$E_m^{(1)} + E_n^{(2)}, \quad (5.50)$$

with $1 \leq m \leq N_1$ and $1 \leq n \leq N_2$. Moreover, if $|e_m^{(1)}\rangle$ is the eigenstate of $L(G_1)$ corresponding to $E_m^{(1)}$, and $|e_n^{(2)}\rangle$ the eigenstate of $L(G_2)$ corresponding to $E_n^{(2)}$, then

$$|e_m^{(1)}\rangle \otimes |e_n^{(2)}\rangle \quad (5.51)$$

is the eigenstate of $L(G_1 \square G_2)$ corresponding to $E_m^{(1)} + E_n^{(2)}$ [285].

5.C.2 Quantum Fisher Information

The Laplacian matrix $L(G)$ is the Hamiltonian of a CTQW on the graph $G_1 \square G_2$. According to the energy eigenvalues (5.50), the partition function is

$$Z(G_1 \square G_2) = Z(G_1)Z(G_2), \quad (5.52)$$

where $Z(G_1)$ is the partition function for a CTQW on the graph G_1 , and $Z(G_2)$ is the partition function for a CTQW on the graph G_2 . It follows that the expectation value of the energy is

$$\langle \hat{H}(G_1 \square G_2) \rangle = \langle \hat{H}(G_1) \rangle + \langle \hat{H}(G_2) \rangle. \quad (5.53)$$

Moreover

$$\langle \hat{H}^2(G_1 \square G_2) \rangle = \langle \hat{H}^2(G_1) \rangle + \langle \hat{H}^2(G_2) \rangle + 2\langle \hat{H}(G_1) \rangle \langle \hat{H}(G_2) \rangle, \quad (5.54)$$

and so the QFI (5.32) follows by definition (5.6).

5.C.3 Fisher Information for position measurement

A generic vertex of $G_1 \square G_2$ is $(j, k) \in V(G_1) \times V(G_2)$, meaning that $j \in V(G_1)$ and $k \in V(G_2)$. Accordingly, a position eigenstate in $G_1 \square G_2$ is $|j\rangle \otimes |k\rangle$. According to Eqs. (5.50)–(5.52), the Gibbs state is

$$\rho_T(G_1 \square G_2) = \rho_T(G_1) \otimes \rho_T(G_2). \quad (5.55)$$

The probability of finding the walker in (j, k) at a given temperature T is

$$\begin{aligned} p(j, k|T) &= \text{Tr} [\rho_T(G_1 \square G_2) |j\rangle\langle j| \otimes |k\rangle\langle k|] \\ &= \sum_m \frac{e^{-E_m^{(1)}/T}}{Z(G_1)} |\langle j|e_m^{(1)}\rangle|^2 \sum_n \frac{e^{-E_n^{(2)}/T}}{Z(G_2)} |\langle k|e_n^{(2)}\rangle|^2 \\ &= p_1(j|T)p_2(k|T), \end{aligned} \quad (5.56)$$

where $p_1(j|T)$ is the probability of finding the walker in the vertex j of G_1 , and, analogously, $p_2(k|T)$ is the probability of finding the walker in the vertex k of G_2 . Notice that $\sum_j p_1(j|T) = \sum_k p_2(k|T) = 1$. Since

$$\partial_T p(j, k|T) = [\partial_T p_1(j|T)] p_2(k|T) + p_1(j|T) \partial_T p_2(k|T), \quad (5.57)$$

we find that the FI (5.10) is

$$\begin{aligned} \mathcal{F}_c(G_1 \square G_2|T) &= \sum_j \frac{(\partial_T p_1(j|T))^2}{p_1(j|T)} \sum_k p_2(k|T) + \sum_k \frac{(\partial_T p_2(k|T))^2}{p_2(k|T)} \sum_j p_1(j|T) \\ &\quad + 2 \sum_j \partial_T p_1(j|T) \sum_k \partial_T p_2(k|T), \end{aligned} \quad (5.58)$$

from which Eq. (5.33) follows, since $\sum_j \partial_T p_1(j|T) = \partial_T \sum_j p_1(j, T) = 0$ and analogously $\sum_k \partial_T p_2(k|T) = 0$.

5.C.4 Grid graph and torus grid graph

In this section we offer some details to assess the QFI and the FI for the grid graph and torus grid graph in Table 5.1. In particular, we report the number of edges M and the sum of the degrees squared $\sum_k d_k^2$ required to compute the QFI (5.17) and the FI (5.20) in the high-temperature regime, as well as the energy level E_1 and its degeneracy g_1 required to compute the QFI (5.13) in the low-temperature regime.

The grid graph $G_{N,N} = P_N \square P_N$ is the Cartesian product of two path graphs P_N , and represents a $N \times N$ square lattice with OBCs. The total number of vertices is N^2 , while the number of edges is $M = 2N(N - 1)$. There are four vertices with degree 2 (the corners), $(N - 2)$ vertices with degree 3 on each side of square lattice, and the remaining $N^2 - 4 - 4(N - 2) = (N - 2)^2$ vertices have degree 4. Hence $\sum_k d_k^2 = 4(4N^2 - 7N + 2)$. The path graph P_N has nondegenerate energies $E_0 = 0$ and $E_1 = 2[1 - \cos(\pi/N)]$. The grid graph has exactly the same E_1 but with degeneracy $g_1 = 2$, since, according to Eq. (5.50), it results from the two possible combinations of E_0 and E_1 of the two P_N .

The torus grid graph $T_{N,N} = C_N \square C_N$ is the Cartesian product of two cycle graphs C_N , and represents a $N \times N$ square lattice with PBC. The total number of vertices is N^2 , while the number of edges is $M = 2N^2$. It is 4-regular, hence $\sum_k d_k^2 = 16N^2$. The cycle graph C_N has nondegenerate energy $E_0 = 0$ and 2-degenerate energy $E_1 = 2[1 - \cos(2\pi/N)]$. The torus grid graph has exactly the same E_1 but with degeneracy $g_1 = 4$, since, according to Eq. (5.50), it results from the four possible combinations of E_0 and E_1 of the two C_N .

5.D Exact QFI for the complete bipartite graph

The energy spectrum of the complete bipartite graph K_{N_1, N_2} consists of only four energy levels (see Sec. 5.4.3). This allows us to obtain the QFI at all the temperatures from Eq. (5.6)

$$\begin{aligned} \mathcal{F}_q(T) &= \frac{e^{-2(N_1+N_2)/T}}{Z^2 T^4} \left\{ N_1^2 e^{N_1/T} \left[(N_1 - 1) + e^{2N_2/T} (N_2 - 1) \right] \right. \\ &\quad + N_2^2 e^{N_2/T} \left[e^{2N_1/T} (N_1 - 1) + (N_2 - 1) \right] \\ &\quad + e^{(N_1+N_2)/T} \left[N_1^3 (N_2 - 1) - N_2^2 (N_2 - 2) \right. \\ &\quad \left. \left. + N_1 N_2^2 (N_2 + 1) - N_1^2 (2N_2^2 - N_2 - 2) \right] \right\}, \end{aligned} \quad (5.59)$$

where $Z = 1 + (N_2 - 1)e^{-N_1/T} + (N_1 - 1)e^{-N_2/T} + e^{-(N_1 + N_2)/T}$. For the star graph S_N , which is the complete bipartite graph $K_{1, N-1}$, the spectrum reduces to three energy levels, and the resulting QFI is

$$\mathcal{F}_q(T) = \frac{e^{-(N+1)/T} [e^{N/T}(N-2) + (N-2)(N-1)^2 + e^{1/T}N^2]}{T^4 [1 + (N-2)e^{-1/T} + e^{-N/T}]^2}. \quad (5.60)$$

Part IV

Presto.

Modeling of transport phenomena

Chapter 6

Transport efficiency of continuous-time quantum walks on graphs

As known, a continuous-time quantum walk describes the propagation of a quantum particle (or an excitation) evolving continuously in time on a graph. As such, it provides a natural framework for modeling transport processes, e.g., in light-harvesting systems. In particular, the transport properties strongly depend on the initial state and on the specific features of the graph under investigation. In this chapter, we address the role of graph topology, and investigate the transport properties of graphs with different regularity, symmetry, and connectivity. We neglect disorder and decoherence, and assume a single trap vertex accountable for the loss processes. In particular, for each graph, we analytically determine the subspace of states having maximum transport efficiency. Our results provide a set of benchmarks for environment-assisted quantum transport, and suggest that connectivity is a poor indicator for transport efficiency. Indeed, we observe some specific correlations between transport efficiency and connectivity for certain graphs, but in general they are uncorrelated.

6.1 Introduction

Modeling quantum transport processes by means of continuous-time quantum walks (CTQWs) is indeed a well-established practice and an appropriate mathematical framework. Quantum transport has been investigated with this approach on restricted geometries [286], semi-regular spidernet graphs [287], Sierpinski fractals [288], and on large-scale sparse regular networks [289]. CTQWs have been used to model transport of nonclassical light in coupled waveguides [290], coherent exciton transport on hierarchical systems [291], small-world networks [292], Apollonian networks [293], and on an extended star graph [294], coherent transport on complex networks [41], and exciton transfer with trapping [295, 296]. It is worth noting that CTQWs do not necessarily perform better than their classical counterparts, since the transport properties strongly depend on the graph, the initial state, and on the propagation direction under investigation [297]. A measure of the efficiency of quantum and classical transport on graphs by means of density of states has been proposed in [298].

Biological systems are known to show quantum effects [299, 300] and efficient transport processes. Hence the great interest in studying also CTQWs to model, e.g., exciton transport on dendrimers [301], photosynthetic energy transfer [43], environment-assisted quantum transport [302], dephasing-assisted transport on quantum networks and biomolecules [44], excitation

transfer in light-harvesting systems [303, 304] and its limits [305]. There also studies concerning disorder-assisted quantum transport on hypercubes and binary trees [306], because the latter can model dendrimer-like structure for artificial light-harvesting systems [307, 308].

A full characterization of the transport properties on different structures is therefore desired. Formally speaking, the CTQW Hamiltonian modeling transport processes shows similarities with the CTQW Hamiltonian adopted to study the spatial search. Both of them consist of the sum, with proper coefficients, of the Laplacian matrix, accountable for the motion of the walker on the graph, and the projector onto one or more specific vertices. This projector is the trapping Hamiltonian in transport problems and the oracle Hamiltonian in spatial search problems. Regularity, global symmetry, and connectivity of the graph have proved to be unnecessary for fast spatial search [12, 309, 310] by invoking certain graphs, e.g., complete bipartite graphs, strongly regular graphs, joined complete graphs, and a simplex of complete graphs, as counterexamples of these false beliefs. In this work, we address the transport by CTQW on the above mentioned graphs, which are different in terms of regularity, symmetry, and connectivity, and we assess the transport efficiency for initial states localized at a vertex and for an initial superposition of two vertices. Our focus is on the role of connectivity, if any. Indeed, regularity and global symmetry are not required for efficient transport, because removing some edges in the complete graph and the hypercube, which are regular and highly symmetric graphs, has been shown to improve the transport efficiency [311].

6.2 Dimensionality reduction method

A graph is a pair $G = (V, E)$, where V denotes the non-empty set of vertices and E the set of edges. In most CTQW problems, the quantity of interest is the probability amplitude at a certain vertex of the graph. The graph encoding the problem to solve often contains symmetries which allow us to simplify the problem, since the evolution of the system actually occurs in a subspace of the complete N -dimensional Hilbert space \mathcal{H} spanned by the vertices of the graph, $\mathcal{H} = \text{span}(\{|v\rangle \mid v \in V\})$. We can determine the minimal subspace which contains the vertex of interest and is invariant under the unitary time evolution via the dimensionality reduction method for CTQW, proposed by Novo *et al.* [311], which we briefly review in this section for completeness. Such subspace, also known as a Krylov subspace [106], contains the vertex of interest and all powers of the Hamiltonian applied to it. The relevance and the power of this method is that the graph encoding a given problem can be mapped onto an equivalent weighted graph, whose order is lower than the order of the original graph and whose vertices are the basis states of the invariant subspace. The corresponding reduced Hamiltonian still fully describes the dynamics relevant to the considered problem.

The unitary evolution can be expressed as

$$|\psi(t)\rangle = e^{-iHt} |\psi_0\rangle = \sum_{k=0}^{\infty} \frac{(-it)^k}{k!} H^k |\psi_0\rangle, \quad (6.1)$$

so $|\psi(t)\rangle$ is contained in the subspace $\mathcal{I}(H, |\psi_0\rangle) = \text{span}(\{H^k |\psi_0\rangle \mid k \in \mathbb{N}_0\})$. This subspace of \mathcal{H} is invariant under the action of the Hamiltonian and thus also of the unitary evolution. Naturally, $\dim \mathcal{I}(H, |\psi_0\rangle) \leq \dim \mathcal{H} = N$, but if the Hamiltonian is highly symmetrical, only a small number of powers of $H^k |\psi_0\rangle$ are linearly independent, so the dimension of $\mathcal{I}(H, |\psi_0\rangle)$ can be much smaller than N .

Let P be the projector onto $\mathcal{I}(H, |\psi_0\rangle)$. Then

$$U(t) |\psi_0\rangle = PU(t)P |\psi_0\rangle = \sum_{k=0}^{\infty} \frac{(-it)^k}{k!} (PHP)^k |\psi_0\rangle = e^{-iPHPt} |\psi_0\rangle = e^{-iH_{\text{red}}t} |\psi_0\rangle, \quad (6.2)$$

where $H_{\text{red}} = PHP$ is the reduced Hamiltonian, and we used the fact that $P^2 = P$ (projector), $P|\psi_0\rangle = |\psi_0\rangle$, and $PU(t)|\psi_0\rangle = U(t)|\psi_0\rangle$.

For any state $|\phi\rangle \in \mathcal{H}$, which we consider the solution of the CTQW problem, we have

$$\langle\phi|U(t)|\psi_0\rangle = \langle\phi|PPU(t)P|\psi_0\rangle = \langle\phi|Pe^{-iH_{\text{red}}t}|\psi_0\rangle = \langle\phi_{\text{red}}|e^{-iH_{\text{red}}t}|\psi_0\rangle, \quad (6.3)$$

where, the reduced state, $|\phi_{\text{red}}\rangle = P|\phi\rangle$. Reasoning analogously with the projector P' onto the subspace $\mathcal{I}(H, |\phi\rangle)$ we obtain

$$\langle\phi|U(t)|\psi_0\rangle = \langle\phi|e^{-iH'_{\text{red}}t}|\psi_{0\text{red}}\rangle, \quad (6.4)$$

with $H'_{\text{red}} = P'HP'$ and $|\psi_{0\text{red}}\rangle = P'|\psi_0\rangle$.

An orthonormal basis of $\mathcal{I}(H, |\phi\rangle)$, denoted by $\{|e_1\rangle, \dots, |e_m\rangle\}$, can be obtained iteratively as follows: the first basis state is $|e_1\rangle = |\phi\rangle$, then the successive ones are obtained by applying H on the current basis state and orthonormalizing with respect to the previous basis states. The procedure stops when we find the minimum m such that $H|e_m\rangle \in \text{span}(\{|e_1\rangle, \dots, |e_m\rangle\})$. The reduced Hamiltonian, i.e., H written in the basis of the invariant subspace, has a tridiagonal form, so the original problem is mapped onto an equivalent problem governed by a tight-binding Hamiltonian of a line with m sites.

6.3 Quantum transport

The CTQW on a graph $G(V, E)$ of N vertices provides a useful framework to model, e.g., the dynamics of a particle or a quasi-particle (excitation) in a network. The quantum walker moves under the Hamiltonian

$$H = \gamma L = \gamma \sum_{i \in V} \text{deg}(i) |i\rangle\langle i| - \gamma \sum_{(i,j) \in E} (|i\rangle\langle j| + |j\rangle\langle i|), \quad (6.5)$$

where $L = D - A$ is the graph Laplacian.¹ The Hamiltonian (6.5) can be read as a tight-binding Hamiltonian with uniform nearest-neighbor couplings $\gamma \in \mathbb{R}^+$ and on-site energies $\gamma \text{deg}(i)$. In the following we set the units such that $\gamma = \hbar = 1$, so hereafter time and energy will be dimensionless.

However, in general, an excitation does not stay forever in the system in which it was created. In biological light-harvesting systems, the excitation gets absorbed at the reaction center, where it is transformed into chemical energy. In such scenario, the total probability of finding the excitation within the network is not conserved. We assume a graph in which the walker can only vanish at one vertex $w \in V$, known as *trap vertex* or *trap*. The component of the walker's wave function at the trap vertex is absorbed by the latter at a trapping rate $\kappa \in \mathbb{R}^+$ [41]. Then, to phenomenologically model such loss processes we have to change the Hamiltonian (6.5), so we introduce the trapping Hamiltonian

$$H_{\text{trap}} = -i\kappa |w\rangle\langle w|, \quad (6.6)$$

which is anti-Hermitian. This leads to the desired non-unitary dynamics described by the total Hamiltonian

$$H = L - i\kappa |w\rangle\langle w|. \quad (6.7)$$

¹See also Sec. 1.1.2.

This Hamiltonian has the same structure as the Hamiltonian for the spatial search of a marked vertex w [31], i.e., it is the sum of the Laplacian matrix and the projector onto $|w\rangle$, with proper coefficients. For spatial search, the projector onto $|w\rangle$ plays the role of the oracle Hamiltonian and the search Hamiltonian is Hermitian. For quantum transport, the projector onto $|w\rangle$, because of the pure imaginary constant, plays the role of the trapping Hamiltonian (6.6) and the transport Hamiltonian (6.7) is not Hermitian.

A relevant measure for a quantum transport process is the transport efficiency [302], which can be defined as the integrated probability of trapping at the vertex w

$$\eta = 2\kappa \int_0^{+\infty} \langle w | \rho(t) | w \rangle dt = 1 - \text{Tr} \left[\lim_{t \rightarrow +\infty} \rho(t) \right], \quad (6.8)$$

where $2\kappa \langle w | \rho(t) | w \rangle dt$ is the probability that the walker is successfully absorbed at the trap within the time interval $[t, t + dt]$ and $\rho(t) = |\psi(t)\rangle\langle\psi(t)|$ is the density matrix of the walker. The second equality of Eq. (6.8) is due to the following reason. The surviving total probability of finding the walker within the graph at time t is $\langle\psi(t)|\psi(t)\rangle = \text{Tr}[\rho(t)]$ and it is ≤ 1 because of the loss processes at the trap vertex. Since the transport efficiency is the integrated probability of trapping in the limit of infinite time, we can also assess the transport efficiency as the complement to 1 of the probability of surviving within the graph, which is the complementary event.

In this scenario there is no disorder in the couplings or site energies of the Hamiltonian nor decoherence during the transport. In this ideal regime computing the transport efficiency amounts to finding the overlap of the initial state with the subspace $\Lambda(H, |w\rangle)$ spanned by the eigenstates of the Hamiltonian $|\lambda_k\rangle$ having a non-zero overlap with the trap $|w\rangle$, as proved by Caruso *et al.* [304]. Indeed, the dynamics is such that the component of the initial state within the space Λ is absorbed by the trap, whereas the component outside this subspace, i.e., in $\bar{\Lambda} = \mathcal{H} \setminus \Lambda$, remains in the graph (see Fig. 6.1). Let us expand the initial state on the basis of the eigenstates of the Hamiltonian

$$|\psi_0\rangle = \sum_{k=1}^m \langle\lambda_k|\psi_0\rangle |\lambda_k\rangle + \sum_{k=m+1}^N \langle\lambda_k|\psi_0\rangle |\lambda_k\rangle = |\psi_\Lambda\rangle + |\psi_{\bar{\Lambda}}\rangle, \quad (6.9)$$

where we assume the eigenstates form an orthonormal basis² and are ordered in such a way that $\Lambda = \text{span}(\{|\lambda_k\rangle \mid 1 \leq k \leq m\})$ and $\bar{\Lambda} = \text{span}(\{|\lambda_k\rangle \mid m+1 \leq k \leq N\})$. Then, the components in Λ are not affected by the open-dynamics which acts at the trap vertex w . The remaining components evolve in the subspace $\bar{\Lambda}$ defined by having a finite overlap with the trap and are therefore absorbed at the trap. In the limit of $t \rightarrow +\infty$ the net result is the following: the total survival probability of finding the walker in the graph is $\langle\psi_{\bar{\Lambda}}|\psi_{\bar{\Lambda}}\rangle \leq 1$, i.e., it is due to the part of the initial state expansion in $\bar{\Lambda}$; instead, the part of the initial state expansion in Λ is fully absorbed at the trap, and so $\eta = \langle\psi_\Lambda|\psi_\Lambda\rangle = \sum_{k=1}^m |\langle\lambda_k|\psi_0\rangle|^2$. A further consequence of this is that if the system is initially prepared in a state $|\psi_0\rangle \in \bar{\Lambda}$, then the walker will stay forever in the graph without reaching the trap ($\eta = 0$); if the system is initially prepared in a state $|\psi_0\rangle \in \Lambda$, then the walker will be completely absorbed by the trap ($\eta = 1$).

If on the one hand this analytical technique allows one to compute the transport efficiency without solving dynamical equations, on the other hand diagonalizing the Hamiltonian still might be a hard task. The dimensionality reduction method in Sec. 6.2 allows one to avoid diagonalizing the Hamiltonian, since it can be proved that $\Lambda(H, |w\rangle) = \mathcal{I}(H, |w\rangle)$ (see Appendix 6.A). Hence, we compute the transport efficiency as

$$\eta = \sum_{k=1}^m |\langle e_k | \psi_0 \rangle|^2, \quad (6.10)$$

²In case of degenerate energy levels we consider the eigenstates after orthonormalization.

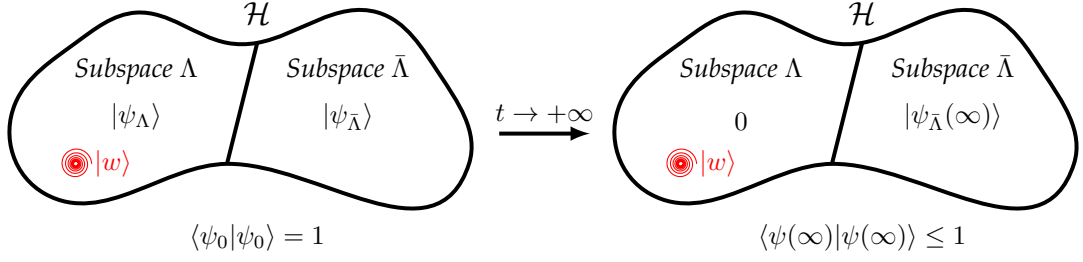


Figure 6.1. The quantum walker is in the initial state $|\psi_0\rangle$ (6.9) and has components in $\Lambda(H, |w\rangle)$, the subspace spanned by the eigenstates of the Hamiltonian having a non-zero overlap with the trap $|w\rangle$, and in $\bar{\Lambda} = \mathcal{H} \setminus \Lambda$, the complement of Λ in the complete Hilbert space \mathcal{H} . In the limit of $t \rightarrow +\infty$, the dynamics is such that the component having non-zero overlap with the trap is fully absorbed by the trap, i.e., $|\psi_{\bar{\Lambda}}(\infty)\rangle = 0$, whereas the component in $\bar{\Lambda}$ survives. The dynamics is not unitary and the total survival probability of finding the walker within the graph is not conserved, i.e., $\langle\psi(\infty)|\psi(\infty)\rangle \leq 1$.

i.e., as the overlap of the initial state $|\psi_0\rangle$ with the subspace $\mathcal{I}(H, |w\rangle) = \text{span}(\{|e_k\rangle \mid 1 \leq k \leq m\})$.

We consider as the initial state either a state localized at a vertex, $|\psi_0\rangle = |v\rangle$, or a superposition of two vertices, $|\psi_0\rangle = (|v_1\rangle + e^{i\theta} |v_2\rangle)/\sqrt{2}$. The localized initial state is a paradigmatic choice to take into account the fact that an excitation is usually created locally in a system. We also considered a superposition to investigate possible effects of coherence. The transport efficiency for the superposition of two vertices

$$\eta_s = \frac{1}{2} \sum_{k=1}^m |\langle e_k | v_1 \rangle + e^{i\theta} \langle e_k | v_2 \rangle|^2 \quad (6.11)$$

can be easily assessed, in some cases, when knowing the transport efficiency η_1 and η_2 for an initial state localized at v_1 and v_2 , respectively. If $|v_1\rangle$ and $|v_2\rangle$ have the same overlap with the basis states, i.e., $\langle e_k | v_1 \rangle = \langle e_k | v_2 \rangle$ for $1 \leq k \leq m$, then $\eta_1 = \eta_2 = \eta$ and we have

$$\eta_s(\theta) = \frac{1}{2} |1 + e^{i\theta}|^2 \eta = (1 + \cos \theta) \eta, \quad (6.12)$$

so $0 \leq \eta_s(\theta) \leq 2\eta$. Instead, if $|v_1\rangle$ and $|v_2\rangle$ have nonzero overlap with different basis states, i.e., $\langle e_k | v_1 \rangle \neq 0$ for $1 \leq k \leq m_1$ and $\langle e_k | v_2 \rangle \neq 0$ for $m_1 + 1 \leq k \leq m_2$, with $m_2 \leq m$, then we have

$$\eta_s = \frac{1}{2} (\eta_1 + \eta_2), \quad (6.13)$$

and it does not depend on θ .

In the following sections we study quantum transport on different graphs which are relevant in terms of symmetry, regularity, and connectivity. For each graph, we determine the basis of the subspace in which the system evolves, the reduced Hamiltonian (6.7), and the transport efficiency (6.10) for an initial state localized at a vertex or a superposition of two vertices which is not covered by Eq. (6.12). To analytically deal with a graph, we will group together the vertices which evolve identically by symmetry [12, 309, 310, 312]. We mean that such vertices behave identically under the action of the Hamiltonian, in the sense that they are equivalent upon relabeling of vertices, as well as, e.g., all the vertices in a complete graph are equivalent. This does not mean that the time evolution $|v_1(t)\rangle$ of an initial state localized at a vertex v_1 is exactly equal to the time evolution $|v_2(t)\rangle$ of another initial state localized at $v_2 \neq v_1$, but it means that these two time

evolutions are the same upon exchanging the labels of the two vertices. Note that the Hamiltonian (6.7) acts on a generic vertex as the Laplacian, except for the trap vertex, which thus forms a subset of one element, itself. The equal superpositions of the vertices in each subset form an orthonormal basis for a subspace of the Hilbert space and the Hamiltonian written in such basis still fully describes the evolution of the system. However, we point out that such basis spans a subspace which, in general, is not the subspace $\mathcal{I}(H, |w\rangle)$ we need to compute the transport efficiency. Nevertheless, this grouping of vertices provides a useful framework to analytically deal with the system, and for this reason we will introduce it. Clearly, identically evolving vertices have the same transport properties. However, vertices which are not equivalent for the Hamiltonian can provide the same transport efficiency. For this reason, in the following we will stress when this is the case.

6.3.1 Complete bipartite graph

The complete bipartite graph (CBG) $G(V_1, V_2, E)$ is a highly symmetrical structure which, in general, is not regular. The CBG has two sets of vertices, V_1 and V_2 , such that each vertex of V_1 is only connected to all the vertices of V_2 and vice versa. The set of CBGs is usually denoted as K_{N_1, N_2} , where the orders of the two partitions $N_1 = |V_1|$ and $N_2 = |V_2|$ are such that $N_1 + N_2 = N$, with N the total number of vertices. The CBG is non regular as long as $N_1 \neq N_2$ (see $K_{4,3}$ in Fig. 6.2), and the star graph is a particular case of CBG with $N_1 = N - 1$ and $N_2 = 1$. Without loss of generality, we assume the trap vertex $w \in V_1$.

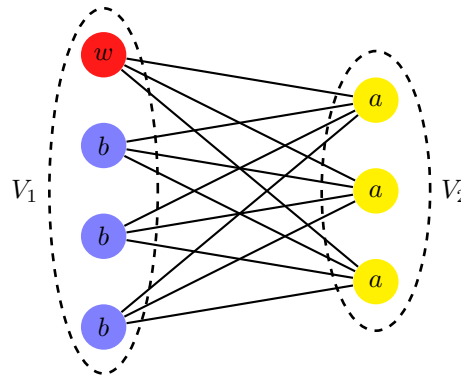


Figure 6.2. Complete bipartite graph $K_{4,3}$. The trap vertex $w \in V_1$ is colored red. Identically evolving vertices have same transport properties and are identically colored and labeled.

The system evolves in a 3-dimensional subspace (see Appendix 6.B.1) spanned by the orthonormal basis states

$$|e_1\rangle = |w\rangle, \quad |e_2\rangle = \frac{1}{\sqrt{N_2}} \sum_{i \in V_2} |i\rangle, \quad |e_3\rangle = \frac{1}{\sqrt{N_1 - 1}} \sum_{\substack{i \in V_1 \\ i \neq w}} |i\rangle. \quad (6.14)$$

This is also the basis we would obtain by grouping together the identically evolving vertices in the subsets $V_a = V_2$ and $V_b = V_1 \setminus \{w\}$ (see Fig. 6.2) [12]. In this subspace the reduced Hamiltonian

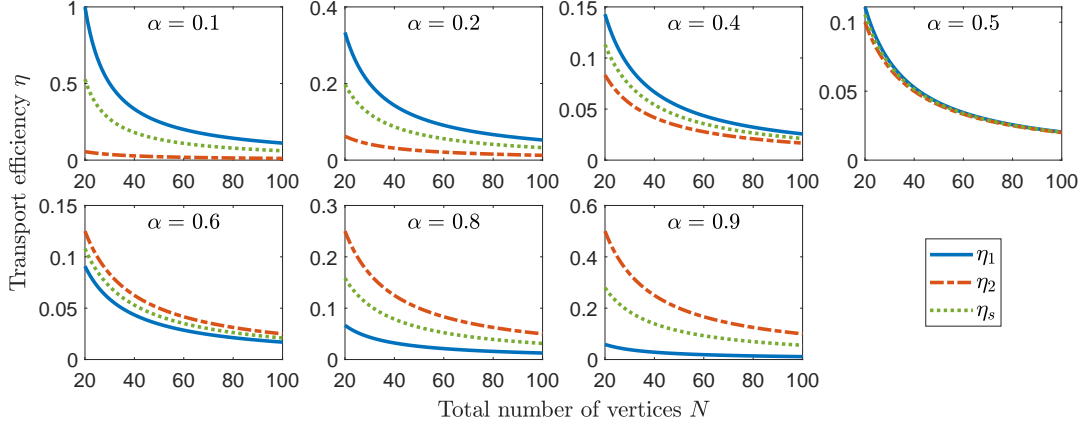


Figure 6.3. Transport efficiency η as a function of the order N of the complete bipartite graph for different values of $\alpha = N_1/N$, with $N_1 = |V_1|$, and different initial states. Transport efficiencies $\eta_{1(2)}$ (6.16) when the initial state is localized at a vertex in $V_{1(2)}$, and η_s (6.18) when the initial state is the superposition of two vertices, one in V_1 and the other in V_2 . The trap vertex $w \in V_1$.

is

$$H = \begin{pmatrix} (1-\alpha)N - i\kappa & -\sqrt{(1-\alpha)N} & 0 \\ -\sqrt{(1-\alpha)N} & \alpha N & -\sqrt{(1-\alpha)(\alpha N - 1)N} \\ 0 & -\sqrt{(1-\alpha)(\alpha N - 1)N} & (1-\alpha)N \end{pmatrix}, \quad (6.15)$$

where $\alpha = N_1/N \in \mathbb{Q}^+$, $N_2 = (1-\alpha)N$, since $N_1 + N_2 = N$. Notice that for G to be a CBG, α must satisfy the condition $1/N \leq \alpha \leq 1 - 1/N$.

If the initial state is localized at a vertex $v \neq w$, then the transport efficiency is

$$\eta = \begin{cases} \frac{1}{\alpha N - 1} & \text{if } v \in V_1, \\ \frac{1}{(1-\alpha)N} & \text{if } v \in V_2, \end{cases} \quad (6.16)$$

and we observe that

$$\eta_1 < \eta_2 \Leftrightarrow 2\alpha > 1 + \frac{1}{N}, \quad (6.17)$$

where $\eta_{1(2)} := \eta(v \in V_{1(2)})$. Instead, if the initial state is a superposition of two vertices each of which belongs to a different partition, i.e., $v_1 \in V_1 \setminus \{w\}$ and $v_2 \in V_2$, then the transport efficiency

$$\eta_s = \frac{N-1}{2N(\alpha N - 1)(1-\alpha)} \quad (6.18)$$

follows from Eq. (6.13), so clearly $\eta_{2(1)} \leq \eta_s \leq \eta_{1(2)}$, where the alternative depends on the condition (6.17). The transport efficiency depends on the parameters of the graph, N and α , as well as on the initial state (see Fig. 6.3). Whether we consider an initial localized state or a superposition of two localized states, the asymptotic behavior is $\eta = O(1/N)$ if both N_1 and N_2 are sufficiently large.

6.3.2 Strongly regular graph

A strongly regular graph (SRG) with parameters (N, k, λ, μ) is a graph with N vertices, not complete or edgeless, where each vertex is adjacent to k vertices, for each pair of adjacent vertices there are λ vertices adjacent to both, and for each pair of nonadjacent vertices there are μ vertices adjacent to both [52, 313]. If we consider the red vertex w in Fig. 6.4, this means that there are k yellow adjacent vertices, and $N - k - 1$ blue vertices, all at distance 2. SRGs have a local symmetry, but most have no global symmetry [309]. The four parameters (N, k, λ, μ) are not independent, and for some parameters there are no SRGs. One necessary but not sufficient condition is that the parameters satisfy

$$k(k - \lambda - 1) = (N - k - 1)\mu, \quad (6.19)$$

which can be proved by counting in two ways the vertices at distance 0, 1, and 2 from a given vertex. Let us focus on the red vertex in Fig. 6.4 and count the pairs of yellow and blue vertices adjacent to it. On the left-hand side of Eq. (6.19), the red vertex has k neighbors, the yellow ones. Each yellow vertex has k neighbors, one of which is the red one and λ of which are other yellow vertices, so it is adjacent to $k - \lambda - 1$ blue vertices. Hence, the number of pairs of adjacent yellow and blue vertices is $k(k - \lambda - 1)$. On the right-hand side of Eq. (6.19), we consider the blue vertices, which, by definition, are not adjacent to the red vertex. There are $N - k - 1$ blue vertices, since there are N total vertices in the graph, one of which is red and k of which are yellow. Each of the blue vertices is adjacent to μ yellow vertices, so there are $(N - k - 1)\mu$ pairs of yellow and blue vertices. The condition (6.19) comes from equating these expressions [309].

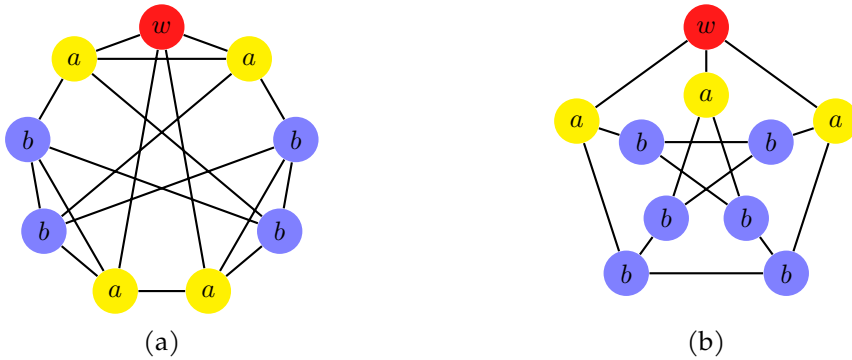


Figure 6.4. Two strongly regular graphs: (a) Paley graph with parameters $(9,4,1,2)$ (parametrization (6.24) for $\mu = 2$); (b) Petersen graph with parameters $(10,3,0,1)$. The trap vertex w is colored red. Identically evolving vertices have same transport properties and are identically colored and labeled.

The system evolves in a 3-dimensional subspace (see Appendix 6.B.2) spanned by the orthonormal basis states

$$|e_1\rangle = |w\rangle, \quad |e_2\rangle = \frac{1}{\sqrt{k}} \sum_{(i,w) \in E} |i\rangle, \quad |e_3\rangle = \frac{1}{\sqrt{N-k-1}} \sum_{(i,w) \notin E} |i\rangle. \quad (6.20)$$

This is also the basis we would obtain by grouping together the identically evolving vertices in the subsets $V_a = \{i \mid (i, w) \in E\}$ and $V_b = \{i \mid (i, w) \notin E\}$ (see Fig. 6.4) [309]. In this subspace

the reduced Hamiltonian is

$$H = \begin{pmatrix} k - i\kappa & -\sqrt{k} & 0 \\ -\sqrt{k} & k - \lambda & -\sqrt{\mu(k - \lambda - 1)} \\ 0 & -\sqrt{\mu(k - \lambda - 1)} & \mu \end{pmatrix}. \quad (6.21)$$

If the initial state is localized at a vertex $v \neq w$, then the transport efficiency is

$$\eta = \begin{cases} \frac{1}{k} & \text{if } (v, w) \in E, \\ \frac{1}{N - k - 1} & \text{if } (v, w) \notin E. \end{cases} \quad (6.22)$$

Instead, if the initial state is a superposition of two vertices one of which is adjacent to w and the other is not, i.e., $(v_1, w) \in E$ and $(v_2, w) \notin E$, then the transport efficiency

$$\eta_s = \frac{N - 1}{2k(N - k - 1)} \quad (6.23)$$

follows from Eq. (6.13).

A family of SRGs is the Paley graphs (see Fig. 6.4(a)), which are parametrized by

$$(N, k, \lambda, \mu) = (4\mu + 1, 2\mu, \mu - 1, \mu) \quad (6.24)$$

where N must be a prime power³ such that $N \equiv 1 \pmod{4}$. According to the parametrization (6.24), whether we consider an initial localized state or a superposition of two localized states, the transport efficiency on a Paley graph is $\eta = 1/2\mu$ (see Eqs. (6.22)–(6.23)), regardless of the fact that the vertices considered are adjacent or not to w .

6.3.3 Joined complete graphs

The transport efficiency on a complete graph, when the initial state is localized at a vertex $v \neq w$, is $\eta = 1/(N - 1)$ [304, 311]. Here we consider two complete graphs of $N/2$ vertices joined by a single edge (see Fig. 6.5). The two vertices, b_1 and b_2 , forming the “bridge” have degree $N/2$, whereas all the others have degree $N/2 - 1$. We denote each complete graph by $K_{N/2}^{(k)} = (V_k, E_k)$, with $k = 1, 2$, where $|V_1| = |V_2| = N/2$. Then, the resulting joined graph is such that $V = V_1 \cup V_2$ and $E = E_1 \cup E_2 \cup \{(b_1, b_2)\}$.

Grouping together the identically evolving vertices, we define the subsets $V_a = V_1 \setminus \{w, b_1\}$ and $V_c = V_2 \setminus \{b_2\}$ (see Fig. 6.5). The system evolves in a 4-dimensional subspace (see Appendix

³A prime power is a prime or integer power of a prime [314].

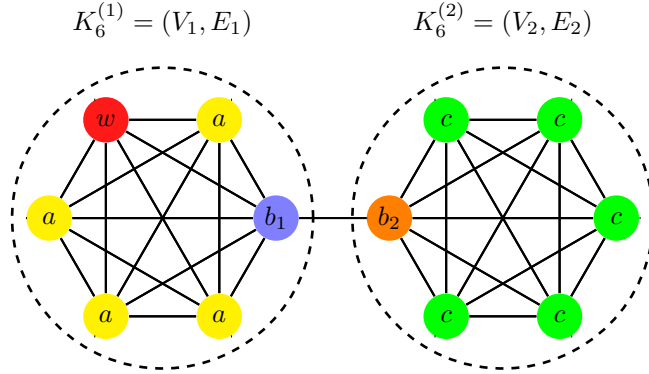


Figure 6.5. A graph with 12 vertices constructed by joining two complete graphs of 6 vertices by a single edge (b_1, b_2) , the bridge. The trap vertex $w \in V_1$ is colored red. Identically evolving vertices have same transport properties and are identically colored and labeled. The vertices b_1 and b_2 show the same transport efficiency even if they behave differently under the action of the Hamiltonian.

6.B.3) spanned by the orthonormal basis states

$$\begin{aligned}
 |e_1\rangle &= |w\rangle, \\
 |e_2\rangle &= \frac{1}{\sqrt{N/2-1}} \left(\sum_{i \in V_a} |i\rangle + |b_1\rangle \right), \\
 |e_3\rangle &= \frac{1}{\sqrt{(N-3)(N/2-1)}} \left[\sum_{i \in V_a} |i\rangle - (N/2-2)|b_1\rangle + (N/2-1)|b_2\rangle \right], \\
 |e_4\rangle &= \frac{1}{\sqrt{(N-3)[N(N/2-2)+1]}} \left[\sum_{i \in V_a} |i\rangle - (N/2-2)(|b_1\rangle + |b_2\rangle) - (N-3) \sum_{i \in V_c} |i\rangle \right]. \quad (6.25)
 \end{aligned}$$

We point out that this basis spans a subspace of dimension 4, thus smaller than the 5-dimensional subspace spanned by the basis defined by grouping together the identically evolving vertices [310]. In the subspace spanned by the basis states $\{|e_1\rangle, \dots, |e_4\rangle\}$ the reduced Hamiltonian is

$$H = \begin{pmatrix} N/2-1-i\kappa & -\sqrt{N/2-1} & 0 & 0 \\ -\sqrt{N/2-1} & \frac{N}{N-2} & -\frac{\sqrt{N-3}}{N/2-1} & 0 \\ 0 & -\frac{\sqrt{N-3}}{N/2-1} & \frac{1}{N-3} \left(\frac{N^2}{2} - 7 + \frac{1}{N/2-1} \right) & \frac{\sqrt{(N/2-1)[N(N/2-2)+1]}}{N-3} \\ 0 & 0 & \frac{\sqrt{(N/2-1)[N(N/2-2)+1]}}{N-3} & \frac{N/2-1}{N-3} \end{pmatrix}. \quad (6.26)$$

If the initial state is localized at a vertex $v \neq w$, then the transport efficiency is

$$\eta = \begin{cases} \frac{2(N-1)}{N(N-4)+2} & \text{if } v \in V_a, \\ \frac{1}{2} + \frac{N-3}{N(N-4)+2} & \text{if } v \in \{b_1, b_2\}, \\ \frac{2(N-3)}{N(N-4)+2} & \text{if } v \in V_c. \end{cases} \quad (6.27)$$

Assuming that each complete graph has $N/2 \geq 3$ vertices, then $\eta_c < \eta_a \leq \eta_b$, where the subscript refers to an initial state localized at vertex in V_c , in V_a , and in the bridge $\{b_1, b_2\}$, respectively. Instead, if the initial state is a superposition of two vertices, then

$$\eta_s(\theta) = \begin{cases} \frac{(N-2)[N+4(1+\cos\theta)]}{4[N(N-4)+2]} = \frac{1}{4} + O\left(\frac{1}{N}\right) & \text{if } v_1 \in V_a \wedge v_2 \in \{b_1, b_2\}, \\ \frac{2(N-2-\cos\theta)}{N(N-4)+2} = \frac{2}{N} + O\left(\frac{1}{N^2}\right) & \text{if } v_1 \in V_a \wedge v_2 \in V_c, \\ \frac{(N-2)[N-(N-4)\cos\theta]-4}{2[N(N-4)+2]} = \frac{1-\cos\theta}{2} + O\left(\frac{1}{N}\right) & \text{if } v_1 = b_1 \wedge v_2 = b_2, \\ \frac{N(N+2)+4(N-4)\cos\theta-16}{4[N(N-4)+2]} = \frac{1}{4} + O\left(\frac{1}{N}\right) & \text{if } v_1 \in \{b_1, b_2\} \wedge v_2 \in V_c. \end{cases} \quad (6.28)$$

We observe that for the superposition of $v_1 \in V_a$ and $v_2 \in V_c$ the transport efficiency $\eta_s(\pi)$ is equal to η for an initial state localized at $v \in V_a$. For the superposition of b_1 and b_2 , i.e., of the vertices of the bridge, we have $\eta_s(\pi) = 1$. This means that such state belongs to $\mathcal{I}(H, |w\rangle)$, indeed

$$\frac{1}{\sqrt{2}}(|b_1\rangle - |b_2\rangle) = \frac{1}{\sqrt{N-2}}(|e_2\rangle - \sqrt{N-3}|e_3\rangle). \quad (6.29)$$

For an initial state localized at b_1 or b_2 we have the same transport efficiency η_b (6.27). However, the two vertices b_1 and b_2 have different overlap with the basis states $|e_k\rangle$, so the transport efficiency (6.28) for the superposition of them is not given by Eq. (6.12).

6.3.4 Simplex of complete graphs

We call M -simplex of complete graphs what is formally known as the first-order truncated M -simplex lattice.⁴ It is obtained by replacing each of the $M+1$ vertices of a complete graph with a complete graph of M vertices (see Fig. 6.6). Each of the new M vertices is connected to one of the edges coming to the original vertex. The graph is regular, vertex transitive and there are $N = M(M+1)$ total vertices.

Grouping together the identically evolving vertices, we define the subsets V_a, V_c, V_d, V_e , and V_f ⁵ (see Fig. 6.6), having cardinality $|V_a| = |V_c| = |V_d| = |V_e| = M-1$, and $|V_f| = (M-1)(M-$

⁴The truncated M -simplex lattice is a generalization of the truncated tetrahedron lattice [315] and it is defined recursively. The graph of the zeroth order truncated M -simplex lattice is a complete graph of $M+1$ vertices. The graph for the $(n+1)$ th order lattice is obtained by replacing each of the vertices of the n th order graph with a complete graph of M vertices. The truncated simplex lattice has been studied in various problems, e.g., in statistical models [316], self-avoiding random walks [317], and spatial search [310, 318].

⁵The yellow vertices a are adjacent to w and belong to the same complete graph. The blue vertex b is adjacent to w but belongs to a different complete graph. The orange vertices c are adjacent to b and belong to the same complete graph.

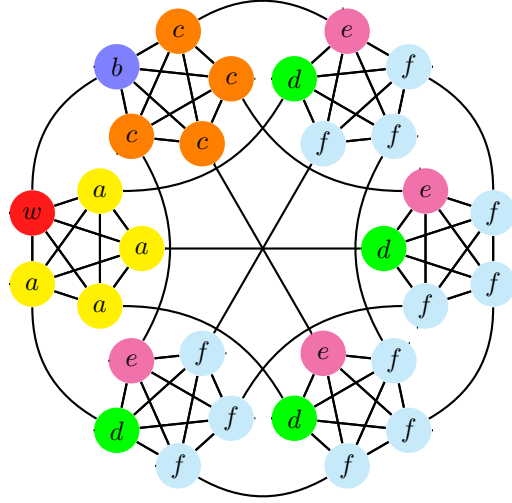


Figure 6.6. 5-simplex of complete graphs. The trap vertex w is colored red. Identically evolving vertices have same transport properties and are identically colored and labeled. The vertices in V_c and V_d show the same transport efficiency even if they behave differently under the action of the Hamiltonian.

2). Independently of M , the system evolves in a 5-dimensional subspace (see Appendix 6.B.4) spanned by the orthonormal basis states

$$\begin{aligned}
 |e_1\rangle &= |w\rangle, \\
 |e_2\rangle &= \frac{1}{\sqrt{M}} \left(\sum_{i \in V_a} |i\rangle + |b\rangle \right), \\
 |e_3\rangle &= \frac{\sqrt{M}}{\sqrt{(M-1)(M^2-2M+4)}} \left\{ \frac{M-2}{M} \left[\sum_{i \in V_a} |i\rangle - (M-1)|b\rangle \right] + \sum_{i \in V_c \cup V_d} |i\rangle \right\}, \\
 |e_4\rangle &= \frac{\sqrt{M^2-2M+4}}{\sqrt{(M-1)(M^3+2M^2-8M+16)}} \left\{ \frac{2(M-2)}{M^2-2M+4} \left[\sum_{i \in V_a} |i\rangle - (M-1)|b\rangle \right] \right. \\
 &\quad \left. - \frac{(M-2)^2}{M^2-2M+4} \sum_{i \in V_c \cup V_d} |i\rangle - 2 \sum_{i \in V_e} |i\rangle - \sum_{i \in V_f} |i\rangle \right\}, \\
 |e_5\rangle &= \frac{1}{M\sqrt{(M-1)(M-2)(M^3+2M^2-8M+16)}} \left\{ -4(M-2) \left[\sum_{i \in V_a} |i\rangle - (M-1)|b\rangle \right] \right. \\
 &\quad \left. + 2(M-2)^2 \sum_{i \in V_c \cup V_d} |i\rangle - M^2(M-2) \sum_{i \in V_e} |i\rangle + 2(M^2-2M+4) \sum_{i \in V_f} |i\rangle \right\}. \quad (6.30)
 \end{aligned}$$

The green vertices d , even if at distance 2 from w , like the vertices c , are adjacent to a , and so they form a different subset. The magenta vertices e are adjacent to c and belong to complete graphs other than the one the vertices c belong to. The cyan vertices f are adjacent to e and d .

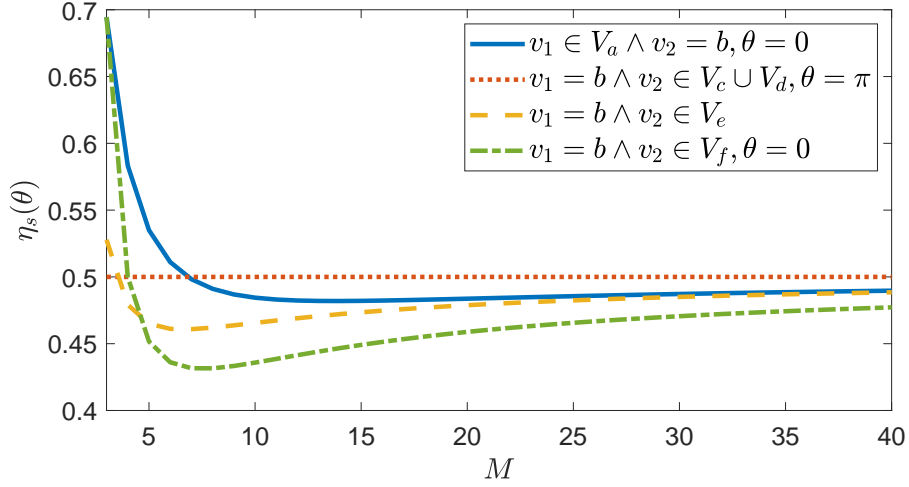


Figure 6.7. Transport efficiency $\eta_s(\theta)$ (6.33) as a function of M for different initial states $|\psi_0\rangle = (|v_1\rangle + e^{i\theta}|v_2\rangle)/\sqrt{2}$. M is the number of vertices in each of the $M + 1$ complete graphs forming the M -simplex. The initial states are the possible equal superposition of two vertices one of which is b .

Note that when the basis states include the vertices in V_c and V_d , they always involve the equal superposition of all the vertices in $V_c \cup V_d$. Thus, these vertices are equivalent for quantum transport, even if they behave differently under the action of the Hamiltonian. We point out that this basis spans a subspace of dimension 5, thus smaller than the 7-dimensional subspace spanned by the basis defined by grouping together the identically evolving vertices [310, 312]. In the subspace spanned by the basis states $\{|e_1\rangle, \dots, |e_5\rangle\}$ the reduced Hamiltonian is a symmetric tridiagonal matrix with cumbersome elements, so we store the main diagonal and the superdiagonal as follows

$$\begin{pmatrix} H_{1,1} & H_{1,2} \\ \vdots & \vdots \\ H_{n,n} & H_{n,n+1} \\ \vdots & \vdots \\ H_{5,5} & * \end{pmatrix} = \begin{pmatrix} M - i\kappa & -\sqrt{M} \\ \frac{3M-2}{M} & -\frac{\sqrt{(M-1)(M^2-2M+4)}}{M} \\ \frac{M^4-2M^3+4M^2-4M+8}{M(M^2-2M+4)} & \frac{\sqrt{M(M^3+2M^2-8M+16)}}{M^2-2M+4} \\ \frac{M(M^4-2M^3+20M^2-40M+64)}{(M^3+2M^2-8M+16)(M^2-2M+4)} & \frac{M(M+2)\sqrt{(M-2)(M^2-2M+4)}}{M^3+2M^2-8M+16} \\ \frac{(M+2)(M^3-4M+8)}{M^3+2M^2-8M+16} & * \end{pmatrix}, \quad (6.31)$$

where the $*$ denotes the missing element because its index exceeds the size of the matrix.

If the initial state is localized at a vertex $v \neq w$, then the transport efficiency is

$$\eta = \begin{cases} \frac{M^2 - 2}{M^2(M - 1)} & \text{if } v \in V_a, \\ \frac{M^2 - 2M + 2}{M^2} & \text{if } v = b, \\ \frac{2}{M^2} & \text{if } v \in V_c \cup V_d, \\ \frac{1}{M - 1} & \text{if } v \in V_e, \\ \frac{M^2 - 2M + 4}{M^2(M - 1)(M - 2)} & \text{if } v \in V_f. \end{cases} \quad (6.32)$$

Note that for an initial state localized at b , which is the only vertex adjacent to w which does not belong to the complete graph of w (see Fig. 6.6), we have $\eta_b \approx 1$ for large M . Instead, if the initial state is a superposition of two vertices, then

$$\eta_s(\theta) = \begin{cases} \frac{M(M^2 - 2M + 4) - 4 + 4(M - 1) \cos \theta}{2M^2(M - 1)} = \frac{1}{2} + O\left(\frac{1}{M}\right) & \text{if } v_1 \in V_a \wedge v_2 = b, \\ \frac{M^2 + 2M - 4 + 2(M - 2) \cos \theta}{2M^2(M - 1)} = \frac{1}{2M} + O\left(\frac{1}{M^2}\right) & \text{if } v_1 \in V_a \wedge v_2 \in V_c \cup V_d, \\ \frac{1}{M} + \frac{1}{M^2} & \text{if } v_1 \in V_a \wedge v_2 \in V_e, \\ \frac{M(M^2 - M - 4) + 8 - 4(M - 2) \cos \theta}{2M^2(M - 1)(M - 2)} = \frac{1}{2M} + O\left(\frac{1}{M^2}\right) & \text{if } v_1 \in V_a \wedge v_2 \in V_f, \\ \frac{M^2 - 2M + 4 - 2(M - 2) \cos \theta}{2M^2} = \frac{1}{2} + O\left(\frac{1}{M}\right) & \text{if } v_1 = b \wedge v_2 \in V_c \cup V_d, \\ \frac{1}{M^2} - \frac{1}{M} + \frac{M}{2(M - 1)} = \frac{1}{2} + O\left(\frac{1}{M}\right) & \text{if } v_1 = b \wedge v_2 \in V_e, \\ \frac{M(M^3 - 5M^2 + 11M - 12) + 8}{2M^2(M - 1)(M - 2)} + \frac{2}{M^2} \cos \theta = \frac{1}{2} + O\left(\frac{1}{M}\right) & \text{if } v_1 = b \wedge v_2 \in V_f, \\ \frac{1}{M^2} + \frac{1}{2(M - 1)} = \frac{1}{2M} + O\left(\frac{1}{M^2}\right) & \text{if } v_1 \in V_c \cup V_d \wedge v_2 \in V_e, \\ \frac{3M^2 - 8M + 8 + 2(M - 2)^2 \cos \theta}{2M^2(M - 1)(M - 2)} = \frac{3/2 + \cos \theta}{M^2} + O\left(\frac{1}{M^3}\right) & \text{if } v_1 \in V_c \cup V_d \wedge v_2 \in V_f, \\ \frac{1}{M^2} + \frac{1}{M} - \frac{1}{M - 1} + \frac{1}{2(M - 2)} = \frac{1}{2M} + O\left(\frac{1}{M^2}\right) & \text{if } v_1 \in V_e \wedge v_2 \in V_f. \end{cases} \quad (6.33)$$

Whenever the superposition of two vertices involves the vertex b , we have $\eta_s \approx 1/2$ for large M , and, in particular, $\eta_s(\pi) = 1/2$ for $v_1 = b \wedge v_2 \in V_c \cup V_d$, independently of M (see Fig. 6.7). Whenever the superposition involves a vertex in V_e , the transport efficiency does not depend on θ . Moreover, we observe that the equal superposition of the vertices in V_e belongs to $\mathcal{I}(H, |w\rangle)$, since

$$\frac{1}{\sqrt{M - 1}} \sum_{i \in V_e} |i\rangle = -\frac{1}{\sqrt{M^3 + 2M^2 - 8M + 16}} \left(2\sqrt{M^2 - 2M + 4} |e_4\rangle + M\sqrt{M - 2} |e_5\rangle \right), \quad (6.34)$$

and so this state provides $\eta = 1$.

In the M -simplex of complete graphs the total number vertices is $N = M(M + 1)$, so the asymptotic behavior of the transport efficiency must be understood according to $M = O(\sqrt{N})$.

6.4 Measures of connectivity

The vertex connectivity $v(G)$ and the edge connectivity $e(G)$ of a graph G are, respectively, the number of vertices or edges we must remove to make G disconnected [319]. These are the two most common measures of graph connectivity, and

$$v(G) \leq e(G) \leq \delta(G), \quad (6.35)$$

i.e., both $v(G)$ and $e(G)$ are upper bounded by the minimum degree of the graph $\delta(G)$ [51]. Another measure follows from the Laplace spectrum of the graph. The second-smallest eigenvalue $a(G)$ of the Laplacian of a graph G with $N \geq 2$ vertices is the algebraic connectivity [117, 273] and, to a certain extent, it is a good parameter to measure how well a graph is connected. In spectral graph theory it is well known, e.g., that a graph is connected if and only if its algebraic connectivity is different from zero. Indeed, the multiplicity of the Laplace eigenvalue zero of an undirected graph G is equal to the number of connected components of G [52]. For a complete graph we know that $v(K_N) = e(K_N) = N - 1$ and $a(K_N) = N$. Instead, for a noncomplete graph G we have $a(G) \leq v(G)$, and so $a(G) \leq e(G)$ [319].

Graph G	$\delta(G)$	$v(G) = e(G)$	$a(G)$
Complete K_N	$N - 1$	$N - 1$	N
Complete bipartite K_{N_1, N_2}	$\min(N_1, N_2)$	$\min(N_1, N_2)$	$\min(N_1, N_2)$
Strongly regular (Type I)	$(N - 1)/2$	$(N - 1)/2$	$(N - \sqrt{N})/2$
Joined complete $K_{N/2}$	$N/2 - 1$	1	$O(1/N)$
M -simplex	$M = O(\sqrt{N})$	$M = O(\sqrt{N})$	1

Table 6.1. The minimum degrees and vertex, edge, and algebraic connectivities of the graphs with N vertices considered in this work. For these graphs, the vertex and the edge connectivities are equal. Note that in the M -simplex of complete graphs $N = M(M + 1)$.

Results of the different measures of connectivity for each graph are shown in Table 6.1. Vertex, edge, and algebraic connectivities for the complete and the complete bipartite graphs are from [319]. The measures of connectivity for the M -simplex of complete graphs are from [310].

The vertex connectivity of a SRG is $v(G) = k$ [52] and the edge connectivity is $e(G) = k$. The latter follows from Eq. (6.35), since $\delta(G) = k$, or using the fact that if a graph has diameter 2, as the SRG has [320], then $e(G) = \delta(G)$ [51]. To assess the algebraic connectivity, we need the Laplace spectrum. The eigenvalues of the adjacency matrix A are

$$\frac{1}{2} \left[\lambda - \mu \pm \sqrt{(\lambda - \mu)^2 + 4(k - \mu)} \right], \quad k, \quad (6.36)$$

and the scaling of them with N depends on the type of SRG. Indeed, SRGs can be classified into two types [51, 313, 320]. Type I graphs, for which $(N - 1)(\mu - \lambda) = 2k$. This implies that $\lambda = \mu - 1$, $k = 2\mu$, and $N = 4\mu + 1$. They exists if and only if N is the sum of two squares. Examples include

the Paley graphs (see parametrization (6.24)). Type II graphs, for which $(\mu - \lambda)^2 + 4(k - \mu)$ is a perfect square d^2 , where d divides $(N - 1)(\mu - \lambda) - 2k$, and the quotient is congruent to $N - 1 \pmod{2}$. Type I graphs are also type II graphs if and only if N is a square [313]. The Paley graph (9,4,1,2) is an example of this (see Fig. 6.4(a)). Not all the SRGs of type II are known, only certain parameter families, e.g., the Latin square graphs [313], and certain graphs, e.g., the Petersen graph (see Fig. 6.4(b)), are. Hence, we consider the algebraic connectivity only for the SRGs of type I. According to the parametrization of the SRG of type I and to the fact that $D = kI$, the eigenvalues of $L = D - A$ are

$$0, \quad \frac{1}{2}(N \mp \sqrt{N}), \quad (6.37)$$

from which the algebraic connectivity is $a(G) = (N - \sqrt{N})/2$, since $\mu = (N - 1)/4$ and $k = (N - 1)/2$.

For the joined complete graphs we have $v(G) = e(G) = 1$, because of the bridge (see Fig. 6.5) [321]. The Laplace spectrum is

$$0, \frac{N}{2}, \frac{1}{4} \left[N + 4 \pm \sqrt{N(N + 8) - 16} \right], \quad (6.38)$$

from which the algebraic connectivity is $a(G) = [N + 4 - \sqrt{N(N + 8) - 16}]/4$.

Then, we assess whether connectivity of the graph may provide or not some bounds on the transport efficiency for an initial state localized at a vertex. First, we focus on the regular graphs considered in this work, for which $\delta(G) = v(G) = e(G)$ and this is equal to the degree. For a complete graph we have $1/a(G) \leq \eta = 1/(N - 1)$, and $1/(N - 1)$ is also the reciprocal of the degree. For a SRG of type I we have $\eta = 2/(N - 1) \leq 1/a(G)$ for $\mu \geq 1$, and $2/(N - 1)$ is also the reciprocal of the degree. Hence, from these two examples, we see that the reciprocal of the algebraic connectivity does not provide a common bound on η . For the M -simplex of complete graphs, we observe that $a(G) = 1$, from whose reciprocal we obtain the obvious upper bound $\eta \leq 1$. Note also that, in general, the transport efficiency for an initial state localized at vertex of a regular graph is not the reciprocal of the degree, as shown, e.g., by the transport efficiency on a general SRG (6.22) (degree k) and on the M -simplex (6.32) (degree M).

Now, we focus on the non-regular graphs. For the joined complete graphs the reciprocal of the vertex and edge connectivity provides the obvious bound $\eta \leq 1$, whereas neither the reciprocal of $\delta(G)$ nor that of $a(G)$ provide a unique bound on η . Indeed, they are an upper or lower bound on η depending on the initial state and the order of the graph (see Eq. (6.27)). For the CBG, the vertex, edge, and algebraic connectivity is $\min(N_1, N_2)$ and its reciprocal is an upper or lower bound on the transport efficiency (6.16) depending on the geometry of the graph. Indeed, we have $\eta_1 \leq \eta_2 \leq 1/\min(N_1, N_2)$ for $\alpha > 1/2$, i.e., $N_1 > N_2$, and $1/\min(N_1, N_2) = \eta_2 \leq \eta_1$ for $\alpha \leq 1/2$, i.e., $N_1 \leq N_2$.

In conclusion, just by focusing on the transport efficiency for an initial state localized at a vertex we observe that the connectivity is a poor indicator for the transport efficiency. First, because it does not provide any general lower or upper bound for estimating the transport efficiency, and transport efficiency and connectivity are generally uncorrelated (see Fig. 6.8). Second, because transport efficiency strongly depends on the initial state, or rather, on the overlap of this with the subspace spanned by the eigenstates of the Hamiltonian having non-zero overlap with the trap vertex, as shown in Sec. 6.3. Note that, analogously, we have found no general correlation between the transport efficiency and the normalized algebraic connectivity, which is the second-smallest eigenvalue of the normalized Laplacian matrix \mathcal{L} of elements $\mathcal{L}_{jk} = L_{jk}/\sqrt{\deg(j)\deg(k)}$ [322].

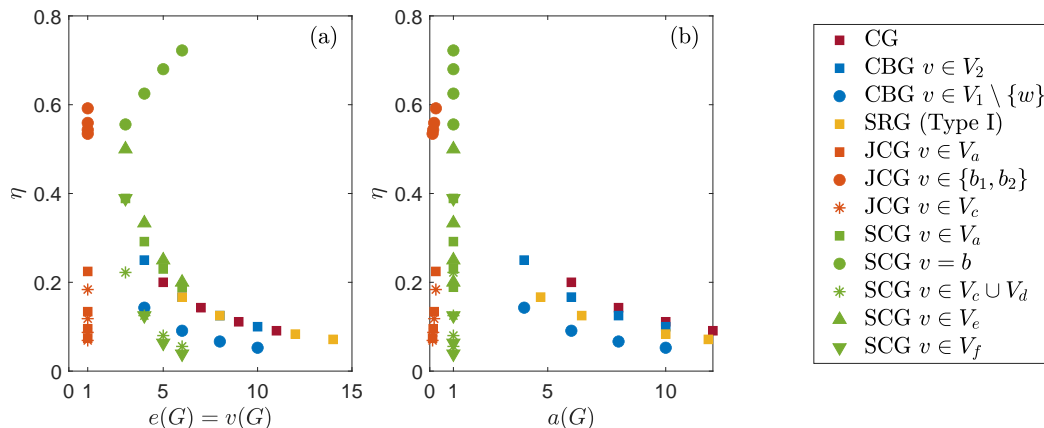


Figure 6.8. Scatter plot of the correlation between the transport efficiency η and (a) the edge or vertex connectivity, $e(G)$ and $v(G)$ respectively, or (b) the algebraic connectivity $a(G)$ (see also Table 6.1). Same color denotes results for the same graph: complete graph (CG, $N = 6, 8, 10, 12$), complete bipartite graph (CBG, $N = 12, 18, 24, 30$, $\alpha = 2/3$), strongly regular graphs of type I (SRG, $N = 13, 17, 25, 29$), joined complete graphs (JCG, $N = 12, 18, 24, 30$), and M -simplex of complete graphs (SCG, $M = 3, 4, 5, 6$). For a given a graph, different markers denote initial states localized at different vertices v . Note that for the SRG of type I $\eta = 1/2\mu = 2/(N - 1)$ independently of the fact that $(v, w) \in E$ or $(v, w) \notin E$. We observe some specific correlations between the transport efficiency and the connectivity for a given graph, but globally, among different graphs, transport efficiency and connectivity are uncorrelated.

6.5 Conclusions

In this chapter we have addressed the coherent dynamics of transport processes on graphs in the framework of continuous-time quantum walks. We have considered graphs having different properties in terms of regularity, symmetry, and connectivity and we have modeled the loss processes via the absorbing of the wave function component at a single trap vertex w . We have adopted the transport efficiency as a figure of merit to assess the transport properties of the system. In the ideal regime, as the one we have adopted, where there is no disorder nor decoherence processes during the transport, the transport efficiency η can be computed as the overlap of the initial state with the subspace $\Lambda(H, |w\rangle)$ spanned by the eigenstates of the Hamiltonian having non-zero overlap with the trap vertex. According to the dimensionality reduction method, we have determined the orthonormal basis of such subspace with no need to diagonalize the Hamiltonian. Therefore, any initial state which is a linear combination of such basis states provides the maximum transport efficiency $\eta = 1$. We have considered as the initial state either a state localized at a vertex or a superposition of two vertices, and computed the corresponding transport efficiency. Overall, the most promising graph seems to be the M -simplex of complete graphs, since it allows us to have a transport efficiency close to 1 for large M for an initially localized state. Transport with maximum efficiency is also possible on other graphs, if the walker is initially prepared in a suitable superposition state. However, the coherence of these preparations is likely to be degraded by noise, and the corresponding transport efficiency may be hard to be achieved in practice.

Our results suggest that connectivity of the graph is a poor indicator for the transport efficiency. Indeed, we observe some specific correlations between transport efficiency and connectivity for certain graphs, but in general they are uncorrelated. Moreover, transport efficiency depends on the overlap of the initial state with $\Lambda(H, |w\rangle)$ and the reciprocal of the measures of connectivity we have assessed does not provide a general and consistent either lower or upper bound on η . However, the topology of the graph is encoded in the Laplacian matrix, which contributes to defining the Hamiltonian. Thus, connectivity somehow affects the transport properties of the system in the sense that it affects the Hamiltonian.

On the other hand, the transport efficiency is the integrated probability of trapping in the limit of infinite time, thus other figures of merit for the transport properties, such as the transfer time, which is the average time required by the walker to get absorbed at the trap, and the survival probability might highlight the role of the connectivity of the graph, if any. Moreover, the role of the trap needs to be further investigated, considering more than one trap vertex, different trapping rates, and different trap location. Our analytical results are proposed as a reference for further studies on the transport properties of these systems and as a benchmark for studying environment-assisted quantum transport on such graphs. Indeed, our work paves the way for further investigation including the analysis of more realistic systems in the presence of noise.

Appendices

6.A Subspace of the eigenstates of the Hamiltonian with non-zero overlap with the trap

In this appendix we show that the subspace $\Lambda(H, |w\rangle)$ of the eigenstates of the Hamiltonian having nonzero overlap with the trap is equal to the subspace $\mathcal{I}(H, |w\rangle) = \text{span}(\{|H^k |w\rangle | k \in \mathbb{N}_0\})$ introduced in Sec. 6.2. This proof is from the *Supplementary information* of [311]. We report it for sake of completeness and because we refine a key point, not addressed in the original proof, about the right and the left inverse of a matrix.

Let $\Lambda(H, |w\rangle) = \text{span}(\{|\lambda_1\rangle, \dots, |\lambda_m\rangle\})$, where $H|\lambda_k\rangle = \lambda_k|\lambda_k\rangle$ and m is the minimum number of eigenstates of H having non-zero overlap with the trap, i.e., $\langle w|\lambda_k\rangle \neq 0$. In case of a degenerate eigenspace, more than one eigenstate belonging to it can have a non-zero overlap with $|w\rangle$, hence the need to find the minimum number m . The ambiguity is solved as follows. We choose the eigenstate from this degenerate eigenspace having the maximum overlap with $|w\rangle$, then we orthogonalize all the remaining eigenstates within such eigenspace with respect to it. After orthogonalizing, these eigenstates have zero overlap with $|w\rangle$ [304, 311].

Let $\dim(\mathcal{I}(H, |w\rangle)) = m_1$, $\dim(\Lambda(H, |w\rangle)) = m_2$, and N the dimension of the complete Hilbert space. First, we prove that $\mathcal{I}(H, |w\rangle) \subseteq \Lambda(H, |w\rangle)$, i.e., that any state $H^i |w\rangle \in \mathcal{I}(H, |w\rangle)$ also belongs to $\Lambda(H, |w\rangle)$:

$$H^i |w\rangle = \sum_{k=1}^N \langle \lambda_k | w \rangle H^i |\lambda_k\rangle = \sum_{k=1}^{m_2} \langle \lambda_k | w \rangle H^i |\lambda_k\rangle = \sum_{k=1}^{m_2} \langle \lambda_k | w \rangle \lambda_k^i |\lambda_k\rangle, \quad (6.39)$$

since $\langle \lambda_k | w \rangle = 0$ for $m_2 + 1 \leq k \leq N$. Any state $H^i |w\rangle$ can therefore be expressed as a linear combination of the eigenstates of the Hamiltonian having a non-zero overlap with the trap, so $H^i |w\rangle \in \Lambda(H, |w\rangle) \forall i \in \mathbb{N}_0$. Second, we prove that $\Lambda(H, |w\rangle) \subseteq \mathcal{I}(H, |w\rangle)$, i.e., that any state of $\Lambda(H, |w\rangle)$ can be expressed as a linear combination of the states of $\mathcal{I}(H, |w\rangle)$. We can write

$$|\lambda_j\rangle = \sum_{i=1}^{m_1} c_{ji} H^{i-1} |w\rangle = \sum_{k=1}^{m_2} \sum_{i=1}^{m_1} c_{ji} \lambda_k^{i-1} \langle \lambda_k | w \rangle |\lambda_k\rangle = \sum_{k=1}^{m_2} \sum_{i=1}^{m_1} c_{ji} M_{ik} |\lambda_k\rangle, \quad (6.40)$$

with matrix element $M_{ik} = \lambda_k^{i-1} \langle \lambda_k | w \rangle$, provided that $\sum_{i=1}^{m_1} c_{ji} M_{ik} = \delta_{jk}$. In terms of matrices, this condition is $C_{m_2 \times m_1} M_{m_1 \times m_2} = I_{m_2 \times m_2}$, which means that C is the left inverse of M , i.e., $C = M_L^{-1}$. Analogously, rewriting Eq. (6.39) and then using the first equality of Eq. (6.40), we have

$$H^{j-1} |w\rangle = \sum_{i=1}^{m_2} \langle \lambda_i | w \rangle \lambda_i^{j-1} |\lambda_i\rangle = \sum_{i=1}^{m_2} M_{ji} |\lambda_i\rangle = \sum_{i=1}^{m_2} \sum_{k=1}^{m_1} M_{ji} c_{ik} H^{k-1} |w\rangle, \quad (6.41)$$

provided that $\sum_{i=1}^{m_2} M_{ji} c_{ik} = \delta_{jk}$. In terms of matrices, this condition is $M_{m_1 \times m_2} C_{m_2 \times m_1} = I_{m_1 \times m_1}$, which means that C is the right inverse of M , i.e., $C = M_R^{-1}$. Therefore, M has a left and a right inverse, so M must be square, $m_1 = m_2 = m$, and $M_L^{-1} = M_R^{-1} = M^{-1} = C$ is unique [323]. The condition under which $\Lambda(H, |w\rangle) \subseteq \mathcal{I}(H, |w\rangle)$ is thus that M must be a $m \times m$ invertible matrix. The matrix M is invertible if $\det(M) \neq 0$. We define two $m \times m$ matrices, $V_{ij} = \lambda_j^{i-1}$ and the diagonal matrix $D_{ij} = \delta_{ij} \langle \lambda_j | w \rangle$, such that $M = VD$. Since $\langle \lambda_j | w \rangle = 0$ for $1 \leq j \leq m$, then $\det(V) \neq 0$. The matrix V is of the Vandermonde form, so $\det(V) = \prod_{1 \leq i < j \leq m} (\lambda_i - \lambda_j)$. This determinant is non-zero since all the states $|\lambda_k\rangle$, for $1 \leq k \leq m$, belong to different eigenspaces, so all the λ_k are different from each other. Hence, $\det(M) = \det(V) \det(D) \neq 0$, so M is always invertible and this condition ensures that $\Lambda(H, |w\rangle) \subseteq \mathcal{I}(H, |w\rangle)$. This concludes the proof that $\Lambda(H, |w\rangle) = \mathcal{I}(H, |w\rangle)$.

6.B Basis of $\mathcal{I}(H, |w\rangle)$ for each graph

In this appendix we analytically derive the orthonormal basis $\{|e_k\rangle\}$ spanning the subspace $\mathcal{I}(H, |w\rangle)$ for each graph considered. The first basis element is $|e_1\rangle = |w\rangle$, the trap vertex, and the k -th element $|e_k\rangle$ is obtained by orthonormalizing (O.N.) $H|e_{k-1}\rangle$ with respect to the subspace spanned by $\{|e_1\rangle, \dots, |e_{k-1}\rangle\}$. The procedure stops when we find the minimum m such that $H|e_m\rangle \in \text{span}(\{|e_1\rangle, \dots, |e_m\rangle\})$. The Hamiltonian (6.7) is the sum of the Laplacian matrix, generating the CTQW on the graph, and the trapping Hamiltonian (6.6), which projects onto the trap $|w\rangle$ with proper coefficient.

6.B.1 Complete bipartite graph

The Laplacian matrix of the CBG K_{N_1, N_2} is

$$L = N_2 \sum_{i \in V_1} |i\rangle\langle i| + N_1 \sum_{j \in V_2} |j\rangle\langle j| - \sum_{i \in V_1} \sum_{j \in V_2} (|i\rangle\langle j| + |j\rangle\langle i|), \quad (6.42)$$

since $\deg(i \in V_1) = N_2$ and $\deg(j \in V_2) = N_1$ (see Fig. 6.2). The basis states (6.14) are obtained as follows:

$$H|e_1\rangle = (N_2 - i\kappa)|w\rangle - \sum_{j \in V_2} |j\rangle = (N_2 - i\kappa)|e_1\rangle - \sqrt{N_2}|e_2\rangle \xrightarrow{\text{O.N.}} |e_2\rangle, \quad (6.43)$$

$$\begin{aligned} H|e_2\rangle &= \frac{N_1}{\sqrt{N_2}} \sum_{j \in V_2} |j\rangle - \frac{1}{\sqrt{N_2}} \sum_{i \in V_1} \sum_{j \in V_2} |i\rangle = N_1|e_2\rangle - \sqrt{N_2} \sum_{\substack{i \in V_1, \\ i \neq w}} |i\rangle - \sqrt{N_2}|e_1\rangle \\ &= N_1|e_2\rangle - \sqrt{N_2(N_1 - 1)}|e_3\rangle - \sqrt{N_2}|e_1\rangle \xrightarrow{\text{O.N.}} |e_3\rangle, \end{aligned} \quad (6.44)$$

$$H|e_3\rangle = \frac{N_2}{\sqrt{N_1 - 1}} \sum_{\substack{i \in V_1, \\ i \neq w}} |i\rangle - \frac{1}{\sqrt{N_1 - 1}} \sum_{i \in V_1} \sum_{\substack{j \in V_2, \\ j \neq w}} |j\rangle = N_2|e_3\rangle - \sqrt{N_2(N_1 - 1)}|e_2\rangle. \quad (6.45)$$

In conclusion, any state $H^k|w\rangle \in \text{span}(\{|e_1\rangle, |e_2\rangle, |e_3\rangle\}) \forall k \in \mathbb{N}_0$, thus the states (6.14) form an orthonormal basis for the subspace $\mathcal{I}(H, |w\rangle)$.

6.B.2 Strongly regular graph

The Laplacian matrix of the SRG with parameters (N, k, λ, μ) is

$$L = kI - \sum_{(j,i) \in E} |j\rangle\langle i|, \quad (6.46)$$

where $I = \sum_{i \in V} |i\rangle\langle i|$ is the identity. Indeed, in a SRG each vertex has degree k , so the diagonal degree matrix is $D = kI$ (see Fig. 6.4). The basis states (6.20) are obtained as follows:

$$H|e_1\rangle = (k - i\kappa)|e_1\rangle - \sum_{(j,w) \in E} |j\rangle = (k - i\kappa)|e_1\rangle - \sqrt{k}|e_2\rangle \xrightarrow{\text{O.N.}} |e_2\rangle. \quad (6.47)$$

To address the computation of the next basis states, a remark is due. The diameter of a connected SRG G , i.e., the maximum distance between two vertices of G , is 2 [320]. This means that, given a vertex w , we can group all the other vertices in two subsets as follows: the subset of the vertices at a distance 1 from w (adjacent); the subset of the vertices at a distance 2 from w (nonadjacent). Because of the structure of the SRG, where two (non)adjacent vertices have λ (μ) common adjacent vertices, in the following we face summations with repeated terms.

To determine the third basis state we consider

$$\begin{aligned} H|e_2\rangle &= k|e_2\rangle - \frac{1}{\sqrt{k}} \sum_{(i,w) \in E} \sum_{(j,i) \in E} |j\rangle \\ &= (k - \lambda)|e_2\rangle - \sqrt{k}|e_1\rangle - \sqrt{\mu(k - \lambda - 1)}|e_3\rangle \xrightarrow{\text{O.N.}} |e_3\rangle. \end{aligned} \quad (6.48)$$

To explain this, we have to focus on $\sum_{(i,w) \in E} \sum_{(j,i) \in E} |j\rangle$. The index of the first summation runs over the vertices i adjacent to w , whereas the index of the second summation runs over the vertices j adjacent to i . On the one hand, the vertex w is counted k times, because it has k adjacent vertices i , each of which, in turn, has $j = w$ among its adjacent vertices. On the other hand, the index of the second summation runs over the vertices adjacent and nonadjacent to w , because of the structure of the SRG. Each vertex j adjacent to w , i.e., $(j, w) \in E$, is connected to other λ vertices adjacent to w , so it is counted λ times. Each vertex j nonadjacent to w , i.e., $(j, w) \notin E$, is connected to μ vertices adjacent to w , so it is counted μ times. Thus we have

$$\begin{aligned} \sum_{(i,w) \in E} \sum_{(j,i) \in E} |j\rangle &= k|e_1\rangle + \lambda \sum_{(j,w) \in E} |j\rangle + \mu \sum_{(j,w) \notin E} |j\rangle \\ &= k|e_1\rangle + \lambda\sqrt{k}|e_2\rangle + \mu\sqrt{N - k - 1}|e_3\rangle. \end{aligned} \quad (6.49)$$

So, according to Eq. (6.19), we can write $\mu\sqrt{(N - k - 1)} = \sqrt{\mu k(k - \lambda - 1)}$, from which Eq. (6.48) follows.

Then, we consider

$$H|e_3\rangle = k|e_3\rangle - \frac{1}{\sqrt{N - k - 1}} \sum_{(i,w) \notin E} \sum_{(j,i) \in E} |j\rangle = \mu|e_3\rangle - \sqrt{\mu(k - \lambda - 1)}|e_2\rangle. \quad (6.50)$$

Again, to explain this, we have to focus on the term $\sum_{(i,w) \notin E} \sum_{(j,i) \in E} |j\rangle$ in the second equality. The index of the first summation runs over the vertices i nonadjacent to w , whereas the index of the second summation runs over the vertices j adjacent to i . Each vertex j nonadjacent to w , i.e., $(j, w) \notin E$, is connected to other $k - \mu$ vertices nonadjacent to w , so it is counted $k - \mu$ times. Each vertex j adjacent to w , i.e., $(j, w) \in E$, is connected to $k - \lambda - 1$ vertices nonadjacent to w , so it is

counted $k - \lambda - 1$ times. Thus we have

$$\begin{aligned} \sum_{(i,w) \notin E} \sum_{(j,i) \in E} |j\rangle &= (k - \lambda - 1) \sum_{(i,w) \in E} |i\rangle + (k - \mu) \sum_{(i,w) \notin E} |i\rangle \\ &= (k - \lambda - 1)\sqrt{k} |e_2\rangle + (k - \mu)\sqrt{N - k - 1} |e_3\rangle. \end{aligned} \quad (6.51)$$

So, according to Eq. (6.19), we can write $(k - \lambda - 1)\sqrt{k} = \sqrt{\mu(N - k - 1)(k - \lambda - 1)}$, from which Eq. (6.50) follows.

In conclusion, any state $H^k |w\rangle \in \text{span}(\{|e_1\rangle, |e_2\rangle, |e_3\rangle\}) \forall k \in \mathbb{N}_0$, thus the states (6.20) form an orthonormal basis for the subspace $\mathcal{I}(H, |w\rangle)$.

6.B.3 Joined complete graphs

The Laplacian matrix of the two complete graphs $K_{N/2}$ joined by a single edge (b_1, b_2) is

$$L = L_1 + L_2 + \underbrace{|b_1\rangle\langle b_1| + |b_2\rangle\langle b_2| - |b_1\rangle\langle b_2| - |b_2\rangle\langle b_1|}_{\text{bridge}}, \quad (6.52)$$

where

$$L_k = \left(\frac{N}{2} - 1\right) \sum_{i \in V_k} |i\rangle\langle i| - \sum_{(i,j) \in E_k} |i\rangle\langle j| \quad (6.53)$$

is the Laplacian matrix of the complete graph $K_{N/2}^{(k)}$, with $k = 1, 2$. The bridge introduces the edge between the vertices b_1 and b_2 and correctly makes the degree of such vertices be $N/2$ (see Fig. 6.5). Hence, $L|v\rangle = L_k|v\rangle$ for any vertex $v \in V_k \setminus \{b_k\}$. Instead, $L|b_k\rangle = (N/2)|b_k\rangle - \sum_{(i,b_k) \in E_k} |i\rangle - |b_{\bar{k}}\rangle$, where \bar{k} is the complement of k in $\{1, 2\}$.

Reasoning by symmetry, we introduce the subsets of the identically evolving vertices, i.e., the subsets containing the vertices which behave identically under the action of the Hamiltonian:

$$H|w\rangle = (N/2 - 1 - i\kappa)|w\rangle - \sum_{i \in V_a} |i\rangle - |b_1\rangle, \quad (6.54)$$

$$H \sum_{i \in V_a} |i\rangle = 2 \sum_{i \in V_a} |i\rangle - (N/2 - 2)(|w\rangle + |b_1\rangle), \quad (6.55)$$

$$H|b_1\rangle = N/2|b_1\rangle - \sum_{i \in V_a} |i\rangle - |w\rangle - |b_2\rangle, \quad (6.56)$$

$$H|b_2\rangle = N/2|b_2\rangle - \sum_{i \in V_c} |i\rangle - |b_1\rangle, \quad (6.57)$$

$$H \sum_{i \in V_c} |i\rangle = \sum_{i \in V_c} |i\rangle - (N/2 - 1)|b_2\rangle, \quad (6.58)$$

where $V_a = V_1 \setminus \{w, b_1\}$ and $V_c = V_2 \setminus \{b_2\}$. Note that the results of H applied on the vertices b_1 or b_2 are different, and this is the reason why they form different subsets. According to these

preliminary results, the basis states (6.25) are obtained as follows:

$$H |e_1\rangle = (N/2 - 1 - i\kappa) |w\rangle - \sum_{i \in V_a} |i\rangle - |b_1\rangle \xrightarrow{\text{O.N.}} |e_2\rangle, \quad (6.59)$$

$$H |e_2\rangle = \frac{1}{\sqrt{N/2 - 1}} \left[-(N/2 - 1) |w\rangle + \sum_{i \in V_a} |i\rangle + 2 |b_1\rangle - |b_2\rangle \right] \xrightarrow{\text{O.N.}} |e_3\rangle, \quad (6.60)$$

$$H |e_3\rangle = \frac{1}{\sqrt{(N-3)(N/2-1)}} \left[N/2 \sum_{i \in V_a} |i\rangle - (N^2/4 - 3) |b_1\rangle + (N^2/4 - 2) |b_2\rangle - (N/2 - 1) \sum_{i \in V_c} |i\rangle \right] \xrightarrow{\text{O.N.}} |e_4\rangle, \quad (6.61)$$

and it can be proved that

$$H |e_4\rangle = \frac{\sqrt{N/2 - 1}}{N - 3} \left(\sqrt{N(N/2 - 2) + 1} |e_3\rangle + \sqrt{N/2 - 1} |e_4\rangle \right). \quad (6.62)$$

In conclusion, any state $H^k |w\rangle \in \text{span}(\{|e_1\rangle, \dots, |e_4\rangle\}) \forall k \in \mathbb{N}_0$, thus the states (6.25) form an orthonormal basis for the subspace $\mathcal{I}(H, |w\rangle)$.

6.B.4 Simplex of complete graphs

The Laplacian matrix is defined as $L = D - A$. For a M -simplex of complete graphs the diagonal degree matrix is $D = MI$, since the graph is regular, and the adjacency matrix is

$$A = \sum_{m=1}^{M+1} A_{\text{intra}}^{(m)} + A_{\text{inter}}, \quad (6.63)$$

where

$$A_{\text{intra}}^{(m)} = \sum_{(i,j) \in E_m} |i^{(m)}\rangle \langle j^{(m)}| \quad (6.64)$$

is the intra-graph adjacency matrix, i.e., within the complete graph $K_M^{(m)}$, and

$$A_{\text{inter}} = \sum_{m=1}^{M+1} \sum_{i=1}^M |i^{(m)}\rangle \langle (M+1-i)^{(m')}|, \quad (6.65)$$

with $m' = 1 + \text{mod}(i + m - 1, M + 1)$, is the inter-graphs adjacency matrix, i.e., between different complete graphs. The index m labels the complete graphs $K_M^{(m)}$ forming the M -simplex. Note that Eq. (6.65) follows the labeling of the vertices in Fig. 6.9 and it is just one of the possible ways to computationally implement the inter-graphs contribution.

In this case, using the notion of adjacency and reasoning by symmetry to introduce the subsets of the identically evolving vertices provide a framework which, analytically, is simpler and clearer to deal with than using explicitly the Laplacian above defined. These subsets contain the vertices

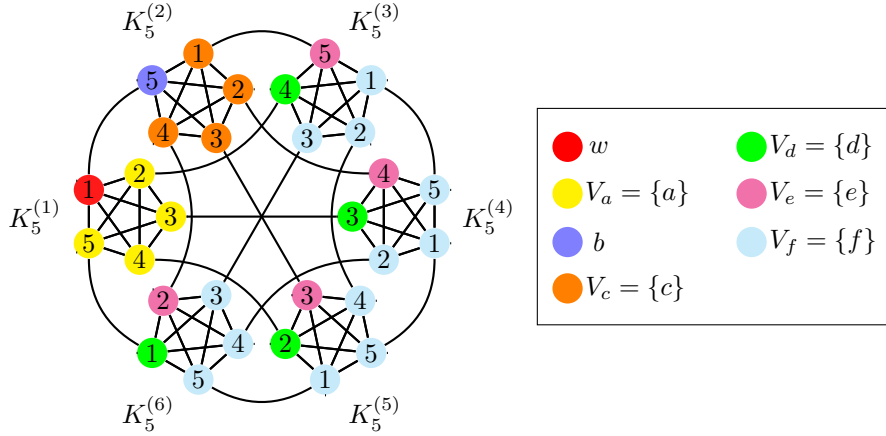


Figure 6.9. Labeling of vertices in a 5-simplex of complete graphs. The trap vertex w is colored red and assumed to be $|1\rangle$ in $K_5^{(1)}$. Same coloring denotes the subsets V_α of identically evolving vertices α , with $\alpha = w, a, b, c, d, e, f$ (see also Fig. 6.6). Note that each of the two vertices w and b forms a subset of one element, itself.

which behave identically under the action of the Hamiltonian:

$$H |w\rangle = (M - i\kappa) |w\rangle - \sum_{i \in V_a} |i\rangle - |b\rangle, \quad (6.66)$$

$$H \sum_{i \in V_a} |i\rangle = 2 \sum_{i \in V_a} |i\rangle - (M - 1) |w\rangle - \sum_{i \in V_d} |i\rangle, \quad (6.67)$$

$$H |b\rangle = M |b\rangle - |w\rangle - \sum_{i \in V_c} |i\rangle, \quad (6.68)$$

$$H \sum_{i \in V_c} |i\rangle = 2 \sum_{i \in V_c} |i\rangle - (M - 1) |b\rangle - \sum_{i \in V_e} |i\rangle, \quad (6.69)$$

$$H \sum_{i \in V_d} |i\rangle = M \sum_{i \in V_d} |i\rangle - \sum_{i \in V_a} |i\rangle - \sum_{i \in V_e} |i\rangle - \sum_{i \in V_f} |i\rangle, \quad (6.70)$$

$$H \sum_{i \in V_e} |i\rangle = M \sum_{i \in V_e} |i\rangle - \sum_{i \in V_c} |i\rangle - \sum_{i \in V_d} |i\rangle - \sum_{i \in V_f} |i\rangle, \quad (6.71)$$

$$H \sum_{i \in V_f} |i\rangle = 2 \sum_{i \in V_f} |i\rangle - (M - 2) \left(\sum_{i \in V_d} |i\rangle + \sum_{i \in V_e} |i\rangle \right). \quad (6.72)$$

Note that the results of H applied on the vertices in V_c or in V_d are different, and this is the reason why they form different subsets. According to these preliminary results, the basis states (6.30)

are obtained as follows:

$$H |e_1\rangle = (M - i\kappa) |w\rangle - \sum_{i \in V_a} |i\rangle - |b\rangle \xrightarrow{\text{O.N.}} |e_2\rangle, \quad (6.73)$$

$$H |e_2\rangle = \frac{1}{\sqrt{M}} \left(2 \sum_{i \in V_a} |i\rangle - M |w\rangle + M |b\rangle - \sum_{i \in V_c \cup V_d} |i\rangle \right) \xrightarrow{\text{O.N.}} |e_3\rangle, \quad (6.74)$$

$$H |e_3\rangle = \frac{\sqrt{M}}{\sqrt{(M-1)(M^2-2M+4)}} \left[\frac{M-4}{M} \sum_{i \in V_a} |i\rangle - (M-1)^2 |b\rangle + \frac{M^2-M+2}{M} \sum_{i \in V_c \cup V_d} |i\rangle \right. \\ \left. - 2 \sum_{i \in V_e} |i\rangle - \sum_{i \in V_f} |i\rangle \right] \xrightarrow{\text{O.N.}} |e_4\rangle, \quad (6.75)$$

$$H |e_4\rangle = \frac{1}{\sqrt{(M-1)(M^2-2M+4)(M^3+2M^2-8M+16)}} \left\{ (M^2-4) \left[\sum_{i \in V_a} |i\rangle - (M-1) |b\rangle \right] \right. \\ \left. + 2(M^2-M+2) \sum_{i \in V_c \cup V_d} |i\rangle - M(M^2-2M+8) \sum_{i \in V_e} |i\rangle \right. \\ \left. + (M-2)^2 \sum_{i \in V_f} |i\rangle \right\} \xrightarrow{\text{O.N.}} |e_5\rangle, \quad (6.76)$$

and it can be proved that

$$H |e_5\rangle = \frac{M+2}{M^3+2M^2-8M+16} \left[M \sqrt{(M-2)(M^2-2M+4)} |e_4\rangle + (M^3-4M+8) |e_5\rangle \right]. \quad (6.77)$$

In conclusion, any state $H^k |w\rangle \in \text{span}(\{|e_1\rangle, \dots, |e_5\rangle\}) \forall k \in \mathbb{N}_0$, thus the states (6.30) form an orthonormal basis for the subspace $\mathcal{I}(H, |w\rangle)$.

Part V

Finale

Chapter 7

Concluding remarks and perspectives

In this thesis we have presented and discussed the results of the research carried out during my PhD, which have been devoted to the theoretical study of continuous-time quantum walks (CTQWs) in the framework of quantum technologies. We have focused on the dynamics of CTQWs and on their potential application to quantum metrology and to modeling transport processes. The prototype model of CTQW on a graph G is the time evolution of a quantum walker whose allowed positions are the vertices of G and whose allowed paths are the edges between them. The state of the walker satisfies the Schrödinger equation with a Hamiltonian given by the Laplacian matrix L , which is the matrix representation of G and plays the role of the kinetic energy of the walker. Besides fundamental interest, understanding and characterizing the CTQW dynamics beyond the prototypical model, as done in the present thesis, may pave the way to further applications in modeling physical processes and in quantum technologies.

Regarding the dynamics, in Chapter 2 we have studied CTQWs generated by the Hamiltonian $H = L + \lambda L^2$, where the perturbation λL^2 is a convenient way to introduce next-nearest-neighbor hopping. We have considered cycle, complete, and star graphs, because paradigmatic models for connectivity and symmetry. After analytically solving the eigenproblem of each Laplacian matrix, we have assessed the time evolution of an initially localized walker, characterizing its dynamics in terms of probability distribution, mixing properties, inverse participation ratio, and coherence. We have observed that the perturbation strongly affects the CTQW in the cycle and in the star graph, whereas it is negligible in the complete graph. While the general quantum features of CTQWs are still present in their perturbed versions, novel effects emerge, such as the possibility of making the evolution on the star graph periodic for certain values of the perturbation parameter λ . In addition, we have addressed the optimal estimation of λ , determining the walker's preparations and the simple graphs that maximize the quantum Fisher information (QFI).

A quantum walker spreads ballistically on the line and on the two-dimensional square lattice, meaning that the variance of the position is proportional to the square of time, $\sigma^2 \propto t^2$, and so it spreads faster than its classical counterpart, $\sigma^2 \propto t$ (diffusive spread). In Chapter 3 we have answered the question whether the ballistic spread is a universal feature of CTQWs or not. Our results suggest that there exist limits to the envisaged universality. We have considered CTQWs on the regular tessellations of the Euclidean plane (triangular, square, and honeycomb lattices) and defined the CTQW Hamiltonian by spatially discretizing the Laplace operator according to the different geometries. Numerically computing the time evolution of an initially localized walker, we have observed that the walker spreads ballistically on Bravais lattices and

sub-ballistically, but still faster than diffusively, on non-Bravais lattices. After that, we have assumed that the walker is a (spinless) particle with charge q subjected to a perpendicular magnetic field. We have considered a vector potential \mathbf{A} in the symmetric gauge, which is known to break translational symmetry but to preserve the rotational one. Under the assumption of hopping only to nearest neighbors, we have proposed two approaches to define the CTQW Hamiltonian: (i) Introducing the Peierls phase-factors and (ii) spatially discretizing the original Hamiltonian in the continuum, $H = (\mathbf{p} - q\mathbf{A})^2/2m$. Numerically computing the time evolution of an initially localized walker, we have observed in both cases that the larger the magnitude of the magnetic field, the lower the variance of position. Also, the probability distribution of the walker is characterized by a trade-off between the circular symmetry, due to the gauge, and the symmetry of the underlying lattice. The differences between the two dynamics emerge over time. In (i) the walker eventually moves away from the initial site, while in (ii) its dynamics mimics periodic oscillations around the initial site and the effects of the Lorentz force. This is due to the fact that the Hamiltonian (i) attributes the Peierls phase-factor to the tunneling matrix elements of the free-particle Hamiltonian, thus it does not include the term \mathbf{A}^2 which is instead present in the Hamiltonian (ii) and, acting as a harmonic potential (symmetric gauge), confines the walker.

Regarding the applications of CTQWs in quantum metrology, we have studied their potential use in magnetometry and thermometry. In Chapter 4, we have put forward the idea of lattice quantum magnetometry. The probe is a charged spinless particle on a finite two-dimensional square lattice in the presence of a locally transverse magnetic field, either homogeneous or inhomogeneous, whose magnitude we want to estimate. Our scheme finds its root in CTQWs, but it does not exploit their dynamical properties, being based on ground-state measurements. According to our numerical results, the system has turned out to be of interest as a quantum magnetometer, providing non-negligible QFI with relevant peaks in a large range of configurations. Moreover, ultimate bounds to precision may be approached by position measurement, which is also robust against coarse-graining, i.e., reduction of resolution.

Employing the concept of QFI and graph theory, in Chapter 5 we have assessed the role of topology on the thermometric performance of a given system. The key idea is to use a finite system as a probe for estimating the temperature of an external environment. We have modeled the thermometer as a set of vertices for the CTQW of an excitation at thermal equilibrium, and evaluated the QFI of Gibbs states, providing analytical approximations that allow us to interpret the exact numerical results. The topology is inherently taken into account as the Hamiltonian of the system is the Laplacian matrix. Considering paradigmatic graphs and two-dimensional lattices, we have found that low connectivity is a resource to build precise thermometers working at low temperatures, whereas highly connected systems are suitable for higher temperatures. Our results suggest that quantum probes are particularly efficient in the low-temperatures regime, where the QFI reaches its maximum, and that it is the fragility of quantum coherence what makes the system a good sensor for temperature (a common feature in quantum probing).

Another field of application of CTQWs is the modeling of transport processes. In Chapter 6 we have modeled them as coherent CTQWs of an excitation, neglecting decoherence and disorder. To mimic what happens, e.g., in biological light-harvesting systems, where the excitation gets absorbed at the reaction center, we have assumed a single trap vertex accountable for the loss processes. We have considered graphs with different topological properties and the transport efficiency, the integrated probability of trapping in the limit of infinite time, as a figure of merit. By means of the dimensionality reduction method, which is based on the notion of Krylov subspace, we have analytically computed the transport efficiency for different initial states, localized or equal superposition of two vertices, and graphs, determining the subspace of states with maximum transport efficiency. Our results suggest that connectivity is a poor indicator for transport efficiency, because we have observed some specific correlations for certain graphs, but in general connectivity and transport efficiency are uncorrelated.

Future perspectives of the present work concern the study of CTQWs as open quantum systems. It is commonly believed that external noise is detrimental with respect to the ideal noiseless scenario, e.g., the random telegraph noise for spatial search [33], but it can actually be a resource, as observed, e.g., in environment-assisted quantum transport [302] and environment-assisted quantum search [324]. Including environmental noise in the model is necessary and desirable for at least two reasons. First, to have a more realistic model, even to be implemented on existing platform and near-term devices. Second, to study which applications are robust against noise or may even benefit from it. Further perspectives concerning the four pillars of quantum technologies are:

- i. **Quantum communication** To the best of our knowledge, applications of CTQWs to quantum cryptography are missing, while quantum direct communication protocols [325] and cryptographic protocols [326–329] based on discrete-time quantum walks have been proposed in recent years.
- ii. **Quantum simulation** Partially related to this area and its purpose of being a tool to design new materials, we mention that deep neural networks can use the density profiles formed in CTQWs to efficiently identify properties of a topological phase as well as phase transitions [330]. This may be used to identify quantum topological materials serving as a platform for new quantum technologies, such as fault-tolerant quantum computers.
- iii. **Quantum metrology and sensing** An experimental validation of the schemes proposed in Chapter 4 for magnetometry and Chapter 5 for thermometry would be desirable. The assumption we made in Chapter 5, i.e., having a system whose Hamiltonian is a Laplacian matrix, might seem unphysical, but actually CTQWs relative to the adjacency and Laplacian matrices are intimately related to quantum spin networks, respectively, in the XY and XYZ (isotropic Heisenberg model) interaction model, considering the single excitation subspace [331, 332]. As an example, the spin-1/2 XYZ quantum Heisenberg model can be realized with bosonic atoms loaded in the p band of an optical lattice in the Mott regime [333] or simulated in a trapped-ion system [334].
- iv. **Quantum computing** Despite the fact that CTQWs are universal for quantum computation and there are indications on how to compute using them [335], CTQWs have not received as much attention as the quantum circuit model or quantum annealing (suited for optimization tasks, but not universal). This is mainly due to the difficulties involved in dealing with their continuous-time nature and with the topology of the graphs. Physical platforms usually impose severe constraints on the arbitrariness of the connectivity one can implement. On the other hand CTQWs are a powerful tool and a basic subroutine for many quantum algorithms. In principle, we may implement the continuous-time evolution on a circuit model, thus on the existing platforms, by approximating the evolution operator as a set of quantum gates by using techniques like the Trotter-Suzuki decomposition. However, what generally makes the design of quantum circuits for CTQWs difficult is that (i) the evolution operator requires a time-dependent quantum circuit implementation and (ii) the CTQW does not act locally on vertices [336]. The global structure of a graph must be taken into account in designing quantum circuits, and the connectivity of the quantum processor is often a limit. In this regard, new opportunities may emerge from fully-connected programmable quantum computers in a trapped ion system [337]. Efficient implementations of CTQWs on quantum circuits have been realized for circulant graphs [338], others have been proposed for composite graphs [336], and possibilities have been explored to simulate CTQWs on IBM Q devices [339]. Finding efficient implementations may pave the way to a renewed interest in the algorithmic applications of CTQWs. We believe that algorithms based on CTQWs should be preferably designed taking into account limits and opportunities of near-term quantum

computing systems [340]. A way might be to identify CTQW problems that are highly reducible. The reduced Hamiltonian still reproduces the same dynamics as the original one that encodes the problem [311], but saves a significant amount of resources. As an example, the spatial search of a vertex on a complete graph of N vertices can be reduced to the CTQW on a weighted line of two vertices, independently of N . An overview of the dimensionality reduction approach to spatial search is offered in Ref. [341]. According to another proposal, this problem can be tackled by hybrid adiabatic–quantum-walk algorithms, even in the presence of noise [342].

Alongside this, CTQWs are now studied in frontier research topics. An approach based on convolutional neural network can determine the conditions (graph type and quantum system coherence) to achieve quantum advantage in particle transfer across networks [98]. Moreover, there is a proposal [343] of constructing a stochastic quantum walk, a form of decohered CTQW, between the global firing states of a quantum neural networks which shows the property of associative memory, an important feature of neural networks. Quantum stochastic walks on graphs mimicking neural networks are of use also in quantum state discrimination [344, 345]. Complex networks are another field of current interest and CTQWs have been investigated, e.g., to study connection instabilities and community structure [346], community detection [347], and link prediction [348].

List of publications

The contents of this thesis have been published as:

- L. Razzoli, L. Ghirardi, I. Siloi, P. Bordone, and M. G. A. Paris, [Physical Review A **99**, 062330 \(2019\)](#)
- L. Razzoli, M. G. A. Paris, and P. Bordone, [Physical Review A **101**, 032336 \(2020\)](#)
- A. Candeloro, L. Razzoli, S. Cavazzoni, P. Bordone, and M. G. A. Paris, [Physical Review A **102**, 042214 \(2020\)](#)
- L. Razzoli, M. G. A. Paris, and P. Bordone, [Entropy **23**, 85 \(2021\)](#)
- A. Candeloro, L. Razzoli, P. Bordone, and M. G. A. Paris, [Physical Review E **104**, 014136 \(2021\)](#)

Bibliography

- [1] *Quantum Manifesto, A New Era of Technology*, (May 2016) https://qt.eu/app/uploads/2018/04/93056_Quantum-Manifesto_WEB.pdf.
- [2] Y. Aharonov, L. Davidovich, and N. Zagury, *Physical Review A* **48**, 1687 (1993).
- [3] D. Aharonov, A. Ambainis, J. Kempe, and U. Vazirani, in *Proceedings of the 33rd Annual ACM Symposium on Theory of Computing* (ACM Press, New York, 2001), pp. 50–59.
- [4] A. Ambainis, E. Bach, A. Nayak, A. Vishwanath, and J. Watrous, in *Proceedings of the 33rd Annual ACM Symposium on Theory of Computing* (ACM Press, New York, 2001), pp. 37–49.
- [5] E. Farhi and S. Gutmann, *Physical Review A* **58**, 915 (1998).
- [6] A. M. Childs, E. Farhi, and S. Gutmann, *Quantum Information Processing* **1**, 35 (2002).
- [7] R. Portugal, *Quantum Walks and Search Algorithms* (Springer, New York, 2018).
- [8] S. E. Venegas-Andraca, *Quantum Information Processing* **11**, 1015 (2012).
- [9] J. Kempe, *Contemporary Physics* **44**, 307 (2003).
- [10] J. Wang and K. Manouchehri, *Physical Implementation of Quantum Walks* (Springer, New York, 2013).
- [11] D. D’Alessandro, *Reports on Mathematical Physics* **66**, 85 (2010).
- [12] T. G. Wong, L. Tarrataca, and N. Nahimov, *Quantum Information Processing* **15**, 4029 (2016).
- [13] J. Du, H. Li, X. Xu, M. Shi, J. Wu, X. Zhou, and R. Han, *Physical Review A* **67**, 042316 (2003).
- [14] R. Côté, A. Russell, E. E. Eyler, and P. L. Gould, *New Journal of Physics* **8**, 156 (2006).
- [15] P. M. Preiss, R. Ma, M. E. Tai, A. Lukin, M. Rispoli, P. Zupancic, Y. Lahini, R. Islam, and M. Greiner, *Science* **347**, 6227 (2015).
- [16] H. B. Perets, Y. Lahini, F. Pozzi, M. Sorel, R. Morandotti, and Y. Silberberg, *Physical Review Letters* **100**, 170506 (2008).
- [17] A. Peruzzo, M. Lobino, J. C. Matthews, N. Matsuda, A. Politi, K. Poulios, X.-Q. Zhou, Y. Lahini, N. Ismail, K. Wörhoff, et al., *Science* **329**, 1500 (2010).
- [18] H. Tang, X.-F. Lin, Z. Feng, J.-Y. Chen, J. Gao, K. Sun, C.-Y. Wang, P.-C. Lai, X.-Y. Xu, Y. Wang, et al., *Science Advances* **4**, eaat3174 (2018).
- [19] H. Tang, C. Di Franco, Z.-Y. Shi, T.-S. He, Z. Feng, J. Gao, K. Sun, Z.-M. Li, Z.-Q. Jiao, T.-Y. Wang, et al., *Nature Photonics* **12**, 754 (2018).
- [20] Z. Yan, Y.-R. Zhang, M. Gong, Y. Wu, Y. Zheng, S. Li, C. Wang, F. Liang, J. Lin, Y. Xu, et al., *Science* **364**, 753 (2019).

-
- [21] M. Gong, S. Wang, C. Zha, M.-C. Chen, H.-L. Huang, Y. Wu, Q. Zhu, Y. Zhao, S. Li, S. Guo, et al., *Science* **372**, 948 (2021).
- [22] M. Christandl, N. Datta, A. Ekert, and A. J. Landahl, *Physical Review Letters* **92**, 187902 (2004).
- [23] M. Christandl, N. Datta, T. C. Dorlas, A. Ekert, A. Kay, and A. J. Landahl, *Physical Review A* **71**, 032312 (2005).
- [24] V. M. Kendon and C. Tamon, *Journal of Computational and Theoretical Nanoscience* **8**, 422 (2011).
- [25] R. Alvir, S. Dever, B. Lovitz, J. Myer, C. Tamon, Y. Xu, and H. Zhan, *Journal of Algebraic Combinatorics* **43**, 801 (2016).
- [26] A. M. Childs, *Physical Review Letters* **102**, 180501 (2009).
- [27] A. M. Childs, D. Gosset, and Z. Webb, *Science* **339**, 791 (2013).
- [28] Y. Lahini, G. R. Steinbrecher, A. D. Bookatz, and D. Englund, *npj Quantum Information* **4**, 1 (2018).
- [29] R. Herrman and T. S. Humble, *Physical Review A* **100**, 012306 (2019).
- [30] V. Kendon, *Interface Focus* **10**, 20190143 (2020).
- [31] A. M. Childs and J. Goldstone, *Physical Review A* **70**, 022314 (2004).
- [32] S. Chakraborty, L. Novo, A. Ambainis, and Y. Omar, *Physical Review Letters* **116**, 100501 (2016).
- [33] M. Cattaneo, M. A. Rossi, M. G. A. Paris, and S. Maniscalco, *Physical Review A* **98**, 052347 (2018).
- [34] S. Chakraborty, L. Novo, and J. Roland, *Physical Review A* **102**, 032214 (2020).
- [35] J. K. Gamble, M. Friesen, D. Zhou, R. Joynt, and S. Coppersmith, *Physical Review A* **81**, 052313 (2010).
- [36] D. Tamascelli and L. Zanetti, *Journal of Physics A: Mathematical and Theoretical* **47**, 325302 (2014).
- [37] M. Krok, K. Rycerz, and M. Bubak, in *International Conference on Computational Science* (Springer, Cham, 2019), pp. 17–30.
- [38] E. Campos, S. E. Venegas-Andraca, and M. Lanzagorta, *Scientific Reports* **11**, 1 (2021).
- [39] P. Arrighi, V. Nesme, and M. Forets, *Journal of Physics A: Mathematical and Theoretical* **47**, 465302 (2014).
- [40] G. Di Molfetta and P. Arrighi, *Quantum Information Processing* **19**, 1 (2020).
- [41] O. Mülken and A. Blumen, *Physics Reports* **502**, 37 (2011).
- [42] D. A. Chisholm, G. García-Pérez, M. A. Rossi, G. M. Palma, and S. Maniscalco, *New Journal of Physics* **23**, 033031 (2021).
- [43] M. Mohseni, P. Rebentrost, S. Lloyd, and A. Aspuru-Guzik, *The Journal of Chemical Physics* **129**, 174106 (2008).
- [44] M. B. Plenio and S. F. Huelga, *New Journal of Physics* **10**, 113019 (2008).
- [45] Y. Lahini, M. Verbin, S. D. Huber, Y. Bromberg, R. Pugatch, and Y. Silberberg, *Physical Review A* **86**, 011603(R) (2012).
- [46] A. Beggi, L. Razzoli, P. Bordone, and M. G. A. Paris, *Physical Review A* **97**, 013610 (2018).
- [47] A. Altland and M. R. Zirnbauer, *Physical Review Letters* **77**, 4536 (1996).

- [48] M. Delvecchio, F. Petiziol, and S. Wimberger, *Condensed Matter* **5**, 4 (2020).
- [49] L. Seveso, C. Benedetti, and M. G. A. Paris, *Journal of Physics A: Mathematical and Theoretical* **52**, 105304 (2019).
- [50] F. Zatelli, C. Benedetti, and M. G. A. Paris, *Entropy* **22**, 1321 (2020).
- [51] D. B. West, *Introduction to Graph Theory*, 2nd ed. (Prentice Hall, Upper Saddle River, NJ, 2001).
- [52] A. E. Brouwer and W. H. Haemers, *Spectra of Graphs* (Springer Science + Business Media, New York, 2011).
- [53] C. W. Helstrom, *Quantum Detection and Estimation Theory* (Academic Press, 1976).
- [54] A. S. Holevo, *Statistical structure of quantum theory* (Springer, 2001).
- [55] M. G. A. Paris, *International Journal of Quantum Information* **7**, 125 (2009).
- [56] S. Barnett, *Quantum information*, Vol. 16 (Oxford University Press, 2009).
- [57] H. E. Brandt, *American Journal of Physics* **67**, 434 (1999).
- [58] C. W. Helstrom, *Physics letters A* **25**, 101 (1967).
- [59] H. Yuen and M. Lax, *IEEE Transactions on Information Theory* **19**, 740 (1973).
- [60] C. W. Helstrom and R. Kennedy, *IEEE Transactions on Information Theory* **20**, 16 (1974).
- [61] S. L. Braunstein and C. M. Caves, *Physical Review Letters* **72**, 3439 (1994).
- [62] S. L. Braunstein, C. M. Caves, and G. J. Milburn, *Annals of Physics (NY)* **247**, 135 (1996).
- [63] A. Monras, *Physical Review A* **73**, 033821 (2006).
- [64] M. Sarovar and G. J. Milburn, *Journal of Physics A: Mathematical and General* **39**, 8487 (2006).
- [65] M. Hotta, T. Karasawa, and M. Ozawa, *Journal of Physics A: Mathematical and General* **39**, 14465 (2006).
- [66] A. Fujiwara, *Physical Review A* **63**, 042304 (2001).
- [67] A. Fujiwara and H. Imai, *Journal of Physics A: Mathematical and General* **36**, 8093 (2003).
- [68] A. Monras and M. G. A. Paris, *Physical Review Letters* **98**, 160401 (2007).
- [69] V. D'Auria, C. de Lisio, A. Porzio, S. Solimeno, and M. G. A. Paris, *Journal of Physics B: Atomic, Molecular and Optical Physics* **39**, 1187 (2006).
- [70] P. Grangier, R. E. Slusher, B. Yurke, and A. LaPorta, *Physical Review Letters* **59**, 2153 (1987).
- [71] B. R. Frieden, *Optics Communications* **271**, 71 (2007).
- [72] H. Cramér, *Mathematical methods of statistics* (Princeton University Press, 1999).
- [73] E. L. Lehmann and G. Casella, *Theory of Point Estimation* (Springer Science & Business Media, New York, 2006).
- [74] H. L. Van Trees, *Detection, Estimation, and Modulation Theory, Part I: Detection, Estimation, and Linear Modulation Theory* (John Wiley & Sons, New York, 2004).
- [75] W. K. Newey and D. McFadden, in *Handbook of Econometrics*, edited by R. F. Engle and D. L. McFadden (Elsevier, Amsterdam, 1994), Vol. IV, Chap. 36, pp. 2112–2245, Theorem 3.3.
- [76] S. Amari and H. Nagaoka, *Methods of Information Geometry*, Vol. 191 (American Mathematical Society, Providence, RI, 2007).
- [77] L. Seveso, M. A. C. Rossi, and M. G. A. Paris, *Physical Review A* **95**, 012111 (2017).

- [78] L. Seveso and M. G. A. Paris, *Physical Review A* **98**, 032114 (2018).
- [79] L. Seveso, F. Albarelli, M. G. Genoni, and M. G. A. Paris, *Journal of Physics A: Mathematical and Theoretical* **53**, 02LT01 (2019).
- [80] B. Teklu, S. Olivares, and M. G. Paris, *Journal of Physics B: Atomic, Molecular and Optical Physics* **42**, 035502 (2009).
- [81] S. Olivares and M. G. Paris, *Journal of Physics B: Atomic, Molecular and Optical Physics* **42**, 055506 (2009).
- [82] I. J. Myung, *Journal of Mathematical Psychology* **47**, 90 (2003).
- [83] D. Bures, *Transactions of the American Mathematical Society* **135**, 199 (1969).
- [84] J. Dittmann, *Journal of Physics A: Mathematical and General* **32**, 2663 (1999).
- [85] M. J. W. Hall, *Physics Letters A* **242**, 123 (1998).
- [86] M. Hübner, *Physics Letters A* **163**, 239 (1992).
- [87] R. Jozsa, *Journal of Modern Optics* **41**, 2315 (1994).
- [88] P. B. Slater, *Journal of Physics A: Mathematical and General* **29**, L271 (1996).
- [89] P. B. Slater, *Physics Letters A* **244**, 35 (1998).
- [90] A. Uhlmann, *Reports on Mathematical Physics* **9**, 273 (1976).
- [91] H.-J. Sommers and K. Zyczkowski, *Journal of Physics A: Mathematical and General* **36**, 10083 (2003).
- [92] B. R. Rao, R. Srikanth, C. M. Chandrashekar, and S. Banerjee, *Physical Review A* **83**, 064302 (2011).
- [93] F. Caruso, *New Journal of Physics* **16**, 055015 (2014).
- [94] I. Siloi, C. Benedetti, E. Piccinini, J. Piilo, S. Maniscalco, M. G. A. Paris, and P. Bordone, *Physical Review A* **95**, 022106 (2017).
- [95] M. A. C. Rossi, C. Benedetti, M. Borrelli, S. Maniscalco, and M. G. A. Paris, *Physical Review A* **96**, 040301(R) (2017).
- [96] M. A. C. Rossi, M. Cattaneo, M. G. A. Paris, and S. Maniscalco, *Quantum Measurements and Quantum Metrology* **5**, 40 (2018).
- [97] L. De Santis, G. Coppola, C. Antón, N. Somaschi, C. Gómez, A. Lemaître, I. Sagnes, L. Lanco, J. C. Loredó, O. Krebs, and P. Senellart, *Physical Review A* **99**, 022312 (2019).
- [98] A. A. Melnikov, L. E. Fedichkin, R.-K. Lee, and A. Alodjants, *Advanced Quantum Technologies* **3**, 1900115 (2020).
- [99] V. Kendon, *International Journal of Quantum Information* **4**, 791 (2006).
- [100] T. G. Wong and A. Ambainis, *Physical Review A* **92**, 022338 (2015).
- [101] T. G. Wong and D. A. Meyer, *Physical Review A* **93**, 062313 (2016).
- [102] P. Philipp, L. Tarrataca, and S. Boettcher, *Physical Review A* **93**, 032305 (2016).
- [103] M. Delvecchio, C. Groiseau, F. Petiziol, G. S. Summy, and S. Wimberger, *Journal of Physics B: Atomic, Molecular and Optical Physics* **53**, 065301 (2020).
- [104] A. Ahmadi, R. Belk, C. Tamon, and C. Wendler, *Quantum Information & Computation* **3**, 611 (2003).
- [105] N. Inui, K. Kasahara, Y. Konishi, and N. Konno, *Fluctuation and Noise Letters* **5**, L73 (2005).
- [106] M. A. Jafarizadeh and S. Salimi, *Annals of Physics (NY)* **322**, 1005 (2007).

- [107] S. Salimi, *Annals of Physics (NY)* **324**, 1185 (2009).
- [108] X.-P. Xu, *Journal of Physics A: Mathematical and Theoretical* **42**, 115205 (2009).
- [109] C. Moore and A. Russell, in *International Workshop on Randomization and Approximation Techniques in Computer Science (Springer, 2002)*, pp. 164–178.
- [110] D. J. Thouless, *Physics Reports* **13**, 93 (1974).
- [111] B. Kramer and A. MacKinnon, *Reports on Progress in Physics* **56**, 1469 (1993).
- [112] G.-L. Ingold, A. Wobst, C. Aulbach, and P. Hänggi, *The European Physical Journal B - Condensed Matter and Complex Systems* **30**, 175 (2002).
- [113] T. Baumgratz, M. Cramer, and M. B. Plenio, *Physical Review Letters* **113**, 140401 (2014).
- [114] R. M. Gray, *Foundations and Trends® in Communications and Information Theory* **2**, 155 (2006).
- [115] T. Endo, S. Osano, K. Toyoshima, and Y. Hirayoshi, *Journal of the Physical Society of Japan* **78**, 064004 (2009).
- [116] K. R. Parthasarathy, in *Stochastics in Finite and Infinite Dimensions*, edited by T. Hida, R. L. Karandikar, H. Kunita, B. S. Rajput, S. Watanabe, and J. Xiong (Springer, New York, 2001), pp. 361–377.
- [117] M. Fiedler, *Czechoslovak Mathematical Journal* **23**, 298 (1973).
- [118] Y. Alavi, G. Chartrand, O. R. Oellermann, and A. J. Schwenk, *Graph Theory, Combinatorics, and Applications* **2**, 871 (1991).
- [119] A. Marsden, Eigenvalues of the laplacian and their relationship to the connectedness of a graph, University of Chicago, REU, 2013, available at <http://math.uchicago.edu/~may/REU2013/REUPapers/Marsden.pdf> (unpublished).
- [120] R. A. Horn and C. R. Johnson, *Matrix Analysis* (Cambridge University Press, Cambridge, 2012).
- [121] D. A. Meyer, *Journal of Statistical Physics* **85**, 551 (1996).
- [122] T. D. Mackay, S. D. Bartlett, L. T. Stephenson, and B. C. Sanders, *Journal of Physics A: Mathematical and General* **35**, 2745 (2002).
- [123] G. Abal, R. Donangelo, F. L. Marquezino, and R. Portugal, *Mathematical Structures in Computer Science* **20**, 999 (2010).
- [124] I. Foulger, S. Gnutzmann, and G. Tanner, *Physical Review A* **91**, 062323 (2015).
- [125] A. M. Childs and Y. Ge, *Physical Review A* **89**, 052337 (2014).
- [126] I. G. Karafyllidis, *Journal of Computational Science* **11**, 326 (2015).
- [127] H. Bougroua, H. Aissaoui, N. Chancellor, and V. Kendon, *Physical Review A* **94**, 062331 (2016).
- [128] K. Eckert, J. Mompart, G. Birkel, and M. Lewenstein, *Physical Review A* **72**, 012327 (2005).
- [129] A. Schreiber, A. Gábris, P. P. Rohde, K. Laiho, M. Štefaňák, V. Potoček, C. Hamilton, I. Jex, and C. Silberhorn, *Science* **336**, 55 (2012).
- [130] Y.-C. Jeong, C. Di Franco, H.-T. Lim, M. Kim, and Y.-H. Kim, *Nature Communications* **4**, 1 (2013).
- [131] M. A. Jafarizadeh and R. Sufiani, *Physica A: Statistical Mechanics and its Applications* **381**, 116 (2007).
- [132] P. Arrighi, G. Di Molfetta, I. Márquez-Martín, and A. Pérez, *Physical Review A* **97**, 062111 (2018).

-
- [133] C. Benedetti, F. Buscemi, P. Bordone, and M. G. A. Paris, *Physical Review A* **93**, 042313 (2016).
- [134] L. Wang, L. Wang, and Y. Zhang, *Physical Review A* **90**, 063618 (2014).
- [135] İ. Yalçinkaya and Z. Gedik, *Physical Review A* **92**, 042324 (2015).
- [136] I. Buluta and F. Nori, *Science* **326**, 108 (2009).
- [137] J. Dalibard, F. Gerbier, G. Juzeliūnas, and P. Öhberg, *Reviews of Modern Physics* **83**, 1523 (2011).
- [138] O. Boada, L. Novo, F. Sciarrino, and Y. Omar, *Physical Review A* **95**, 013830 (2017).
- [139] P. Arnault and F. Debbasch, *Physica A: Statistical Mechanics and its Applications* **443**, 179 (2016).
- [140] L. Razzoli, L. Ghirardi, I. Siloi, P. Bordone, and M. G. A. Paris, *Physical Review A* **99**, 062330 (2019).
- [141] J. M. Harris, J. L. Hirst, and M. J. Mossinghoff, *Combinatorics and Graph Theory*, 2nd ed. (Springer, New York, 2008).
- [142] E. W. Weisstein, Lattice Graph, *MathWorld*, <http://mathworld.wolfram.com/LatticeGraph.html>.
- [143] F. Harary, *Graph Theory and Theoretical Physics* (Academic Press, London, 1967).
- [144] M. R. T. Dale, *Applying Graph Theory in Ecological Research* (Cambridge University Press, Cambridge, UK, 2017).
- [145] L. M. Chen, *Digital and Discrete Geometry: Theory and Algorithms* (Springer, New York, 2014).
- [146] H. S. M. Coxeter, *Introduction to Geometry*, 2nd ed. (John Wiley & Sons, New York, 1969).
- [147] E. W. Weisstein, Tessellation, *MathWorld*, <http://mathworld.wolfram.com/Tessellation.html>.
- [148] D. Wells, *The Penguin Dictionary of Curious and Interesting Geometry* (Penguin, London, 1991).
- [149] E. W. Weisstein, Schläfli Symbol, *MathWorld*, <http://mathworld.wolfram.com/SchlaefliSymbol.html>.
- [150] N. W. Ashcroft and N. D. Mermin, *Solid State Physics* (Harcourt College Publishers, New York, 1976).
- [151] M. Abramowitz and I. A. Stegun, *Handbook of mathematical functions: with formulas, graphs, and mathematical tables* (Dover, New York, 1970).
- [152] M. Woodward and F. Muir, *Stanford Exploration Project* **38**, 195 (1984).
- [153] B. Hamilton and S. Bilbao, in *Proceedings of Meetings on Acoustics*, Vol. 19, 1 (ASA, Montréal, Canada, 2013), p. 015120.
- [154] J. H. Conway, H. Burgiel, and C. Goodman-Strauss, *The Symmetries of Things* (AK Peters, Wellesley, MA, 2008).
- [155] H. Zhu, M. Hayashi, and L. Chen, *Physical Review A* **97**, 022342 (2018).
- [156] T. G. Wong, *Quantum Information Processing* **15**, 675 (2016).
- [157] J. A. Izaac, J. B. Wang, and Z. J. Li, *Physical Review A* **88**, 042334 (2013).
- [158] T. G. Wong, *Journal of Physics A: Mathematical and Theoretical* **49**, 484002 (2016).
- [159] R. Shankar, *Principles of Quantum Mechanics*, 2nd ed. (Plenum Press, New York, 1994).

- [160] D. Tong, ArXiv e-prints (2016), [arXiv:1606.06687](https://arxiv.org/abs/1606.06687).
- [161] Y. Aharonov and D. Bohm, *Physical Review* **115**, 485 (1959).
- [162] M. Aidelsburger, *Artificial Gauge Fields with Ultracold Atoms in Optical Lattices* (Springer, New York, 2015).
- [163] B. A. Bernevig and T. L. Hughes, *Topological Insulators and Topological Superconductors* (Princeton University Press, Princeton, NJ, 2013).
- [164] D. R. Hofstadter, *Physical Review B* **14**, 2239 (1976).
- [165] R. P. Feynman, R. B. Leighton, and M. Sands, *Mainly Electromagnetism and Matter*, The Feynman Lectures on Physics Vol. 2 (Basic Books, New York, 2011).
- [166] R. P. Feynman, R. B. Leighton, and M. Sands, *Quantum Mechanics*, The Feynman Lectures on Physics Vol. 3 (Basic Books, New York, 2011).
- [167] R. Peierls, *Zeitschrift für Physik* **80**, 763 (1933).
- [168] R. L. Burden and J. D. Faires, *Numerical Analysis*, 9th ed. (Cengage Learning, Boston, 2010).
- [169] S. Butenko and P. M. Pardalos, *Numerical Methods and Optimization: An Introduction* (CRC Press, Boca Raton, FL, 2014).
- [170] M. Shashkov, *Conservative Finite-Difference Methods on General Grids* (CRC Press, New York, 1996).
- [171] A. Samarskii, V. Tishkin, A. Favorskii, and M. Y. Shashkov, *Differential Equations* **17**, 854 (1981).
- [172] A. Samarskii, V. Tishkin, A. Favorskii, and M. Y. Shashkov, *Differential Equations* **18**, 881 (1982).
- [173] R. Aris, *Vectors, Tensors and the Basic Equations of Fluid Mechanics* (Dover, New York, 1962).
- [174] K. F. Riley, M. P. Hobson, and S. J. Bence, *Mathematical Methods for Physics and Engineering* (Cambridge University Press, Cambridge, UK, 2006).
- [175] J. J. Sakurai and J. Napolitano, *Modern Quantum Mechanics*, 2nd ed. (Addison-Wesley, San Francisco, CA, 2011).
- [176] C. L. Degen, F. Reinhard, and P. Cappellaro, *Reviews of Modern Physics* **89**, 035002 (2017).
- [177] G. Salvatori, A. Mandarino, and M. G. A. Paris, *Physical Review A* **90**, 022111 (2014).
- [178] L. A. Correa, M. Mehboudi, G. Adesso, and A. Sanpera, *Physical Review Letters* **114**, 220405 (2015).
- [179] M. G. A. Paris, *Journal of Physics A: Mathematical and Theoretical* **49**, 03LT02 (2015).
- [180] A. H. Kiilerich, A. De Pasquale, and V. Giovannetti, *Physical Review A* **98**, 042124 (2018).
- [181] J. Taylor, P. Cappellaro, L. Childress, L. Jiang, D. Budker, P. Hemmer, A. Yacoby, R. Walsworth, and M. Lukin, *Nature Physics* **4**, 810 (2008).
- [182] C. Degen, *Applied Physics Letters* **92**, 243111 (2008).
- [183] K. Jensen, N. Leefer, A. Jarmola, Y. Dumeige, V. M. Acosta, P. Kehayias, B. Patton, and D. Budker, *Physical Review Letters* **112**, 160802 (2014).
- [184] L. Ghirardi, I. Siloi, P. Bordone, F. Troiani, and M. G. A. Paris, *Physical Review A* **97**, 012120 (2018).
- [185] F. Troiani and M. G. A. Paris, *Physical Review Letters* **120**, 260503 (2018).
- [186] S. Danilin, A. V. Lebedev, A. Vepsäläinen, G. B. Lesovik, G. Blatter, and G. Paraoanu, *npj Quantum Information* **4**, 29 (2018).

-
- [187] A. Smirne, S. Cialdi, G. Anelli, M. G. A. Paris, and B. Vacchini, *Physical Review A* **88**, 012108 (2013).
- [188] C. Benedetti, F. Buscemi, P. Bordone, and M. G. A. Paris, *Physical Review A* **89**, 032114 (2014).
- [189] M. G. A. Paris, *Physica A: Statistical Mechanics and its Applications* **413**, 256 (2014).
- [190] G. L. Giorgi, F. Galve, and R. Zambrini, *Physical Review A* **94**, 052121 (2016).
- [191] C. Benedetti and M. G. A. Paris, *Physics Letters A* **378**, 2495 (2014).
- [192] M. A. Rossi and M. G. A. Paris, *Physical Review A* **92**, 010302 (2015).
- [193] F. Galve, J. Alonso, and R. Zambrini, *Physical Review A* **96**, 033409 (2017).
- [194] D. Tamascelli, C. Benedetti, S. Olivares, and M. G. A. Paris, *Physical Review A* **94**, 042129 (2016).
- [195] M. Bina, F. Grasselli, and M. G. A. Paris, *Physical Review A* **97**, 012125 (2018).
- [196] F. Cosco, M. Borrelli, F. Plastina, and S. Maniscalco, *Physical Review A* **95**, 053620 (2017).
- [197] C. Benedetti, F. S. Sehdaran, M. H. Zandi, and M. G. A. Paris, *Physical Review A* **97**, 012126 (2018).
- [198] M. Bina, I. Amelio, and M. Paris, *Physical Review E* **93**, 052118 (2016).
- [199] A. Schreiber, A. Gábris, P. P. Rohde, K. Laiho, M. Štefaňák, V. Potoček, C. Hamilton, I. Jex, and C. Silberhorn, in *Proceedings of the 2012 Conference on Lasers and Electro-Optics (CLEO)* (IEEE, San Jose, CA, 2012), pp. 1–2.
- [200] A. Beggi, I. Siloi, C. Benedetti, E. Piccinini, L. Razzoli, P. Bordone, and M. G. A. Paris, *European Journal of Physics* **39**, 065401 (2018).
- [201] E. Piccinini, C. Benedetti, I. Siloi, M. G. A. Paris, and P. Bordone, *Computer Physics Communications* **215**, 235 (2017).
- [202] B. C. Travaglione and G. J. Milburn, *Physical Review A* **65**, 032310 (2002).
- [203] M. Ezawa, *Physics Letters A* **375**, 3610 (2011).
- [204] L. D. Landau and E. M. Lifshitz, *Quantum mechanics: non-relativistic theory*, 3rd ed., Vol. 3 (Pergamon Press, 1977).
- [205] A. P. Hines and P. Stamp, *Physical Review A* **75**, 062321 (2007).
- [206] H. De Raedt and K. Michielsen, *Computers in Physics* **8**, 600 (1994).
- [207] I. Apellaniz, I. Urizar-Lanz, Z. Zimborás, P. Hyllus, and G. Tóth, *Physical Review A* **97**, 053603 (2018).
- [208] F. Giazotto, T. T. Heikkilä, A. Luukanen, A. M. Savin, and J. P. Pekola, *Reviews of Modern Physics* **78**, 217 (2006).
- [209] V. Mukherjee, A. Zwick, A. Ghosh, X. Chen, and G. Kurizki, *Communications Physics* **2**, 162 (2019).
- [210] M. H. Partovi, *Physics Letters A* **137**, 440 (1989).
- [211] C. Jarzynski, *Physical Review Letters* **78**, 2690 (1997).
- [212] S. Mukamel, *Physical Review Letters* **90**, 170604 (2003).
- [213] U. Seifert, *Physical Review Letters* **95**, 040602 (2005).
- [214] A. Cuccoli, V. Tognetti, P. Verrucchi, and R. Vaia, *Physical Review B* **46**, 11601 (1992).
- [215] M. B. Plenio and V. Vedral, *Contemporary Physics* **39**, 431 (1998).

- [216] T. M. Nieuwenhuizen and A. E. Allahverdyan, *Physical Review E* **66**, 036102 (2002).
- [217] K. Jacobs, *Physical Review E* **86**, 040106(R) (2012).
- [218] H. Gharibyan and M. Tegmark, *Physical Review E* **90**, 032125 (2014).
- [219] R. Alicki, *Open Systems & Information Dynamics* **21**, 1440002 (2014).
- [220] F. Plastina, A. Alecce, T. J. G. Apollaro, G. Falcone, G. Francica, F. Galve, N. Lo Gullo, and R. Zambrini, *Physical Review Letters* **113**, 260601 (2014).
- [221] F. Brandao, M. Horodecki, N. Nelly, J. Oppenheim, and S. Wehner, *Proceedings of the National Academy of Sciences* **112**, 3275 (2015).
- [222] F. Binder, S. Vinjanampathy, K. Modi, and J. Goold, *Physical Review E* **91**, 032119 (2015).
- [223] M. Brunelli, A. Xuereb, A. Ferraro, G. De Chiara, N. Kiesel, and M. Paternostro, *New Journal of Physics* **17**, 035016 (2015).
- [224] M. Borrelli, J. V. Koski, S. Maniscalco, and J. P. Pekola, *Physical Review E* **91**, 012145 (2015).
- [225] M. Esposito, M. A. Ochoa, and M. Galperin, *Physical Review Letters* **114**, 080602 (2015).
- [226] M. Olshanii, *Physical Review Letters* **114**, 060401 (2015).
- [227] J. P. Pekola, *Nature Physics* **11**, 118 (2015).
- [228] J. C. Gallop, L. Hao, and P. Reed, *Applied Superconductivity* **5**, 285 (1997).
- [229] J. M. Courty, A. Heidmann, and M. Pinard, *The European Physical Journal D - Atomic, Molecular, Optical and Plasma Physics* **17**, 399 (2001).
- [230] D. Kleckner and D. Bouwmeester, *Nature* **444**, 75 (2006).
- [231] A. Schliesser, R. Riviere, G. Anetsberger, O. Arcizet, and T. J. Kippenberg, *Nature Physics* **4**, 415 (2008).
- [232] C. A. Regal, J. D. Teufel, and K. W. Lehnert, *Nature Physics* **4**, 555 (2008).
- [233] T. Rocheleau, T. Ndukum, C. Macklin, J. B. Hertzberg, A. A. Clerk, and K. C. Schwab, *Nature* **463**, 72 (2010).
- [234] A. D. O'Connell, M. Hofheinz, M. Ansmann, R. C. Bialczak, M. Lenander, E. Lucero, M. Neeley, D. Sank, H. Wang, M. Weides, J. Wenner, J. M. Martinis, and A. N. Cleland, *Nature* **464**, 697 (2010).
- [235] M. Bruderer and D. Jaksch, *New Journal of Physics* **8**, 87 (2006).
- [236] T. M. Stace, *Physical Review A* **82**, 011611(R) (2010).
- [237] M. Brunelli, S. Olivares, and M. G. A. Paris, *Physical Review A* **84**, 032105 (2011).
- [238] M. Brunelli, S. Olivares, M. Paternostro, and M. G. A. Paris, *Physical Review A* **86**, 012125 (2012).
- [239] U. Marzolino and D. Braun, *Physical Review A* **88**, 063609 (2013).
- [240] K. D. B. Higgins, B. W. Lovett, and E. M. Gauger, *Physical Review B* **88**, 155409 (2013).
- [241] M. Mehboudi, M. Moreno-Cardoner, G. D. Chiara, and A. Sanpera, *New Journal of Physics* **17**, 055020 (2015).
- [242] S. Jevtic, D. Newman, T. Rudolph, and T. M. Stace, *Physical Review A* **91**, 012331 (2015).
- [243] M. Jarzyna and M. Zwierz, *Physical Review A* **92**, 032112 (2015).
- [244] A. De Pasquale, D. Rossini, R. Fazio, and V. Giovannetti, *Nature Communications* **7**, 12782 (2016).
- [245] A. De Pasquale, K. Yuasa, and V. Giovannetti, *Physical Review A* **96**, 012316 (2017).

- [246] S. Razavian and M. G. A. Paris, *Physica A: Statistical Mechanics and its Applications* **525**, 825 (2019).
- [247] S. Razavian, C. Benedetti, M. Bina, Y. Akbari-Kourbolagh, and M. G. A. Paris, *The European Physical Journal Plus* **134**, 284 (2019).
- [248] M. T. Mitchison, T. Fogarty, G. Guarnieri, S. Campbell, T. Busch, and J. Goold, *Physical Review Letters* **125**, 080402 (2020).
- [249] M. R. Jorgensen, P. P. Potts, M. G. A. Paris, and J. B. Brask, *Physical Review Research* **2**, 033394 (2020).
- [250] B. B. Mandelbrot, *Journal of Mathematical Physics* **5**, 164 (1964).
- [251] R. McFee, *American Journal of Physics* **41**, 230 (1973).
- [252] C. Kittel, *American Journal of Physics* **41**, 1211 (1973).
- [253] C. Kittel, *Physics Today* **41**, 93 (1988).
- [254] B. B. Mandelbrot, *Physics Today* **42**, 71 (1989).
- [255] H. B. Prosper, *American Journal of Physics* **61**, 54 (1993).
- [256] T. C. P. Chui, R. Swanson, M. J. Adriaans, J. A. Nissen, and J. A. Lipa, *Physical Review Letters* **69**, 3005 (1992).
- [257] G. S. Boltachev and J. W. P. Schmelzer, *The Journal of Chemical Physics* **133**, 134509 (2010).
- [258] J. Uffink and J. van Lith, *Foundations of Physics* **29**, 655 (1999).
- [259] L. D. Landau and E. M. Lifshitz, *Statistical Physics* (Pergamon, London, 1980).
- [260] G. D. J. Phillies, *American Journal of Physics* **52**, 629 (1984).
- [261] J. Liu, H. Yuan, X.-M. Lu, and X. Wang, *Journal of Physics A: Mathematical and Theoretical* **53**, 023001 (2019).
- [262] P. Zanardi, L. C. Venuti, and P. Giorda, *Physical Review A* **76**, 062318 (2007).
- [263] P. Zanardi, P. Giorda, and M. Cozzini, *Physical Review Letters* **99**, 100603 (2007).
- [264] P. P. Potts, J. B. Brask, and N. Brunner, *Quantum* **3**, 161 (2019).
- [265] A. S. Baimuratov, I. D. Rukhlenko, V. K. Turkov, A. V. Baranov, and A. V. Fedorov, *Scientific Reports* **3**, 1 (2013).
- [266] W. Lechner, P. Hauke, and P. Zoller, *Science Advances* **1**, e1500838 (2015).
- [267] S. E. Nigg, N. Lörch, and R. P. Tiwari, *Science Advances* **3**, e1602273 (2017).
- [268] L. Buffoni and M. Campisi, *Quantum Science and Technology* **5**, 035013 (2020).
- [269] J. Marshall, D. Venturelli, I. Hen, and E. G. Rieffel, *Physical Review Applied* **11**, 044083 (2019).
- [270] Y. Aharonov, S. Massar, and S. Popescu, *Physical Review A* **66**, 052107 (2002).
- [271] K. Temme, T. J. Osborne, K. G. Vollbrecht, D. Poulin, and F. Verstraete, *Nature* **471**, 87 (2011).
- [272] S. Nakayama, A. Soeda, and M. Muraio, *Physical Review Letters* **114**, 190501 (2015).
- [273] N. M. M. De Abreu, *Linear Algebra and its Applications* **423**, 53 (2007).
- [274] C. W. Wu, *Linear Multilinear Algebra* **53**, 203 (2005).
- [275] D. de Caen, *Discrete Mathematics* **185**, 245 (1998).
- [276] B. Elspas and J. Turner, *Journal of Combinatorial Theory* **9**, 297 (1970).

- [277] M. J. Golin and Y. C. Leung, in *International Workshop on Graph-Theoretic Concepts in Computer Science* (Springer, Berlin, Heidelberg, 2004), pp. 296–307.
- [278] E. W. Weisstein, Circulant Graph, *MathWorld*, <https://mathworld.wolfram.com/CirculantGraph.html>.
- [279] E. W. Weisstein, Complete Bipartite Graph, *MathWorld*, <https://mathworld.wolfram.com/CompleteBipartiteGraph.html>.
- [280] L. Razzoli, M. G. A. Paris, and P. Bordone, *Physical Review A* **101**, 032336 (2020).
- [281] E. W. Weisstein, Grid Graph, *MathWorld*, <https://mathworld.wolfram.com/GridGraph.html>.
- [282] E. W. Weisstein, Torus Grid Graph, *MathWorld*, <https://mathworld.wolfram.com/TorusGridGraph.html>.
- [283] L. Euler, *Commentarii academiae scientiarum Petropolitanae*, 128 (1741).
- [284] J. M. Aldous and R. J. Wilson, *Graphs and Applications: An Introductory Approach* (Springer-Verlag, London, 2003).
- [285] S. Barik, R. B. Bapat, and S. Pati, *Applicable Analysis and Discrete Mathematics* **9**, 39 (2015).
- [286] E. Agliari, A. Blumen, and O. Mülken, *Journal of Physics A: Mathematical and Theoretical* **41**, 445301 (2008).
- [287] S. Salimi, *Quantum Information Processing* **9**, 75 (2010).
- [288] Z. Darázs, A. Anishchenko, T. Kiss, A. Blumen, and O. Mülken, *Physical Review E* **90**, 032113 (2014).
- [289] X. Li, H. Chen, M. Wu, Y. Ruan, Z. Liu, and J. Tan, *Quantum Information Processing* **19**, 1 (2020).
- [290] A. Rai, G. S. Agarwal, and J. H. Perk, *Physical Review A* **78**, 042304 (2008).
- [291] A. Blumen, V. Bierbaum, and O. Mülken, *Physica A: Statistical Mechanics and its Applications* **371**, 10 (2006).
- [292] O. Mülken, V. Pernice, and A. Blumen, *Physical Review E* **76**, 051125 (2007).
- [293] X.-P. Xu, W. Li, and F. Liu, *Physical Review E* **78**, 052103 (2008).
- [294] S. Yalouz and V. Pouthier, *Physical Review E* **97**, 022304 (2018).
- [295] O. Mülken, A. Blumen, T. Amthor, C. Giese, M. Reetz-Lamour, and M. Weidemüller, *Physical Review Letters* **99**, 090601 (2007).
- [296] E. Agliari, O. Muelken, and A. Blumen, *International Journal of Bifurcation and Chaos* **20**, 271 (2010).
- [297] O. Mülken and A. Blumen, *Physical Review E* **71**, 016101 (2005).
- [298] O. Mülken and A. Blumen, *Physical Review E* **73**, 066117 (2006).
- [299] N. Lambert, Y.-N. Chen, Y.-C. Cheng, C.-M. Li, G.-Y. Chen, and F. Nori, *Nature Physics* **9**, 10 (2013).
- [300] M. Mohseni, Y. Omar, G. S. Engel, and M. B. Plenio, *Quantum effects in biology* (Cambridge University Press, 2014).
- [301] O. Mülken, V. Bierbaum, and A. Blumen, *The Journal of Chemical Physics* **124**, 124905 (2006).
- [302] P. Rebentrost, M. Mohseni, I. Kassal, S. Lloyd, and A. Aspuru-Guzik, *New Journal of Physics* **11**, 033003 (2009).

- [303] A. Olaya-Castro, C. F. Lee, F. F. Olsen, and N. F. Johnson, *Physical Review B* **78**, 085115 (2008).
- [304] F. Caruso, A. W. Chin, A. Datta, S. F. Huelga, and M. B. Plenio, *The Journal of Chemical Physics* **131**, 09B612 (2009).
- [305] S. Hoyer, M. Sarovar, and K. B. Whaley, *New Journal of Physics* **12**, 065041 (2010).
- [306] L. Novo, M. Mohseni, and Y. Omar, *Scientific Reports* **6**, 18142 (2016).
- [307] A. Adronov and J. M. Fréchet, *Chemical Communications*, 1701 (2000).
- [308] D. S. Bradshaw and D. L. Andrews, *Polymers* **3**, 2053 (2011).
- [309] J. Janmark, D. A. Meyer, and T. G. Wong, *Physical Review Letters* **112**, 210502 (2014).
- [310] D. A. Meyer and T. G. Wong, *Physical Review Letters* **114**, 110503 (2015).
- [311] L. Novo, S. Chakraborty, M. Mohseni, H. Neven, and Y. Omar, *Scientific Reports* **5**, 1 (2015).
- [312] T. G. Wong, *Quantum Information Processing* **14**, 1767 (2015).
- [313] P. J. Cameron and J. H. Van Lint, *Designs, graphs, codes and their links*, Vol. 3 (Cambridge University Press, 1991).
- [314] E. W. Weisstein, Prime Power, *MathWorld*, <https://mathworld.wolfram.com/PrimePower.html>.
- [315] D. R. Nelson and M. E. Fisher, *Annals of Physics (NY)* **91**, 226 (1975).
- [316] D. Dhar, *Journal of Mathematical Physics* **18**, 577 (1977).
- [317] D. Dhar, *Journal of Mathematical Physics* **19**, 5 (1978).
- [318] Y. Wang, S. Wu, and W. Wang, *Physical Review A* **101**, 062333 (2020).
- [319] M. Fiedler, *Banach Center Publications* **25**, 57 (1989).
- [320] L. W. Beineke, R. J. Wilson, P. J. Cameron, et al., *Topics in algebraic graph theory*, Vol. 102 (Cambridge University Press, 2004).
- [321] G. Chartrand and P. Zhang, *A first course in graph theory* (Dover Publications, 2012).
- [322] F. R. Chung and F. C. Graham, *Spectral graph theory*, 92 (American Mathematical Soc., 1997).
- [323] S. Banerjee and A. Roy, *Linear algebra and matrix analysis for statistics* (CRC Press, 2014).
- [324] L. Novo, S. Chakraborty, M. Mohseni, and Y. Omar, *Physical Review A* **98**, 022316 (2018).
- [325] S. Srikara and C. Chandrashekar, *Quantum Information Processing* **19**, 1 (2020).
- [326] C. Vlachou, J. Rodrigues, P. Mateus, N. Paunković, and A. Souto, *International Journal of Quantum Information* **13**, 1550050 (2015).
- [327] C. Vlachou, W. Krawec, P. Mateus, N. Paunković, and A. Souto, *Quantum Information Processing* **17**, 1 (2018).
- [328] J. Shi, H. Chen, F. Zhou, L. Huang, S. Chen, and R. Shi, *International Journal of Theoretical Physics* **58**, 1337 (2019).
- [329] A. A. Abd El-Latif, B. Abd-El-Atty, M. Amin, and A. M. Ilyyasu, *Scientific Reports* **10**, 1 (2020).
- [330] Y. Ming, C.-T. Lin, S. D. Bartlett, and W.-W. Zhang, *npj Computational Materials* **5**, 1 (2019).
- [331] S. Bose, *Physical Review Letters* **91**, 207901 (2003).

- [332] S. Bose, A. Casaccino, S. Mancini, and S. Severini, *International Journal of Quantum Information* **7**, 713 (2009).
- [333] F. Pinheiro, G. M. Bruun, J.-P. Martikainen, and J. Larson, *Physical Review Letters* **111**, 205302 (2013).
- [334] T. Graß and M. Lewenstein, *EPJ Quantum Technology* **1**, 1 (2014).
- [335] V. Kendon, *ArXiv e-prints* (2020), [arXiv:2004.01329](https://arxiv.org/abs/2004.01329).
- [336] T. Loke and J. Wang, *Journal of Physics A: Mathematical and Theoretical* **50**, 055303 (2017).
- [337] K. Wright, K. Beck, S. Debnath, J. Amini, Y. Nam, N. Grzesiak, J.-S. Chen, N. Pisenti, M. Chmielewski, C. Collins, et al., *Nature Communications* **10**, 1 (2019).
- [338] X. Qiang, T. Loke, A. Montanaro, K. Aungskunsiri, X. Zhou, J. L. O'Brien, J. B. Wang, and J. C. Matthews, *Nature Communications* **7**, 1 (2016).
- [339] A. K. Madhu, A. A. Melnikov, L. E. Fedichkin, A. Alodjants, and R.-K. Lee, *ArXiv e-prints* (2020), [arXiv:2012.14386](https://arxiv.org/abs/2012.14386).
- [340] A. D. Córcoles, A. Kandala, A. Javadi-Abhari, D. T. McClure, A. W. Cross, K. Temme, P. D. Nation, M. Steffen, and J. M. Gambetta, *Proceedings of the IEEE* **108**, 1338 (2019).
- [341] C.-F. Chiang, *Quantum Information Processing* **19**, 1 (2020).
- [342] J. G. Morley, N. Chancellor, S. Bose, and V. Kendon, *Physical Review A* **99**, 022339 (2019).
- [343] M. Schuld, I. Sinayskiy, and F. Petruccione, *Physical Review A* **89**, 032333 (2014).
- [344] N. Dalla Pozza and F. Caruso, *Physics Letters A* **384**, 126195 (2020).
- [345] N. Dalla Pozza and F. Caruso, *Physical Review Research* **2**, 043011 (2020).
- [346] D. I. Tsomokos, *Physical Review A* **83**, 052315 (2011).
- [347] M. Faccin, P. Migdał, T. H. Johnson, V. Bergholm, and J. D. Biamonte, *Physical Review X* **4**, 041012 (2014).
- [348] J. P. Moutinho, A. Melo, B. Coutinho, I. A. Kovács, and Y. Omar, *ArXiv e-prints* (2021), [arXiv:2112.04768](https://arxiv.org/abs/2112.04768).